Extensions of some approximate Riemann Solvers for the computation of mixed incompressible-compressible flows

Victor Courtin

université PARIS-SACLAY

Extensions of some approximate Riemann Solvers for the computation of mixed incompressible-compressible flows

Extension de quelques solveurs de Riemann approchés pour la simulation d'écoulements compressibles-incompressibles

Thèse de doctorat de l'université Paris-Saclay

Ecole doctorale n°574, Mathématiques Hadamard, EDMH
Spécialité de doctorat: Mathématiques appliquées
Graduate School : Mathématiques Référent : Université de Versailles-Saint-Quentin-en-Yvelines

Thèse préparée dans les unités de recherche **LMV**(Université Paris-Saclay, UVSQ, CNRS) et **ONERA**(Ministère des Armées), sous la direction de **Christophe CHALONS**, Professeur des universités, la co-direction de **Florent RENAC**, Ingénieur de recherche, et les co-encadrements de **Jean-Christophe BONIFACE**, Ingénieur de recherche, et **Cédric CONTENT**, Ingénieur de recherche

Thèse soutenue à Meudon, le 16 décembre 2024, par

Victor COURTIN

Composition du jury

Membres du jury avec voix délibérative

Aymeric VIÉ Professeur, CNRS, CentraleSupelec, Université Paris-Saclay	Président
Rémi ABGRALL Professeur, Université de Zurich	Rapporteur & examinateur
Pierre-Henri MAIRE Directeur de recherche, CEA/CESTA, Université Bordeaux 1	Rapporteur & examinateur
Marica PELANTI Professeur assistante, ENSTA, Institut Polytechnique de Paris	Examinatrice
Vincent PERRIER Directeur de recherche, INRIA, Université de Pau et des Pays de l'Adour	Examinateur

THESE DE DOCTORAT
NNT : 2024UPASM041

université PARIS-SACLAY | ÉCOLE DOCTORALE de mathématiques Hadamard (EDMH)

Titre: Extension de quelques solveurs de Riemann approchés pour la simulation d'écoulements compressibles-incompressibles

Mots clés: Mécanique des fluides numériques, Régime bas-Mach, Fluide compressible, Fluide incompressible, Stabilité au sens de von Neumann, Méthode des volumes finis.

Résumé: Dans cette thèse, on s'intéresse à la simulation d'écoulements compressibles à l'aide de méthodes numériques implicites de type solveurs de Riemann, telles que la méthode de Roe ou le schéma HLLC. L'objectif est de développer des extensions faible nombre de Mach afin de préserver la précision des solutions discrètes dans la limite bas Mach. Ce type d'écoulement est souvent rencontré dans la simulation de configurations industrielles, caractérisées par la présence de zones plus ou moins étendues à faible vitesse.

On se focalise sur la composante hyperbolique des équations de Navier-Stokes, qui constitue le cœur du problème d'analyse numérique abordé dans cette thèse, les équations d'Euler. On y expose une analyse approfondie et détaillée retraçant un sujet de recherche vieux de plusieurs décennies, qui présente encore d'importants défis, même pour ce modèle académique. La littérature recense un grand nombre d'extensions possibles pour le schéma de Roe, qui sont généralement faciles à implémenter. Ces extensions consistent à modifier certains termes de la dissipation numérique, en amplifiant ou diminuant leur contribution dans la limite faible nombre de Mach (on parle de « rescaling » de la dissipation numérique). Elles permettent par ailleurs d'obtenir une solution discrète compressible approchant la solution analytique issue de la théorie du potentiel pour le problème incompressible, sans pour autant introduire une détérioration des résultats dans le régime compressible. La capture des ondes de choc pour les écoulements transsoniques et supersoniques reste quasiment inchangée. Cependant, il existe plusieurs études suggérant de faire preuve de vigilance quant au choix de la formulation de ce type de correction. Il est connu de la littérature que des pertes de stabilité numérique sont généralement observées, ainsi que des risques d'apparition de problèmes de découplage vitesse-pression, détériorant fortement la précision globale de la solution discrète dans les faibles vitesses. Ces travaux se fondent sur deux corrections très différentes du schéma de Roe, issues de la littérature scientifique, et qui présentent des propriétés discrètes distinctes. La première approche, proposée par C.-C. Rossow, amplifie les sauts de pression en introduisant une vitesse artificielle du son, tandis que la seconde, développée par F. Rieper, vise à uniquement atténuer les sauts de vitesse. Ces deux approches illustrent deux stratégies majeures fréquemment utilisées dans les extensions à faible nombre de Mach. Nous commençons tout d'abord par l'analyse asymptotique discrète de l'approche proposée par C.-C. Rossow non publiée dans la littérature, en abordant également la formulation de la condition de stabilité au sens de von Neumann. On montre que cette correction évite l'écueil du découplage vitesse-pression. Ensuite, nous présentons une méthode numérique, visant à construire des phases implicites exactes nécessaires à l'intégration temporelle, en utilisant la différentiation algorithmique et un solveur direct. Ces techniques nous permettent de contourner la contrainte très stricte de stabilité sur le pas de temps, et d'obtenir des solutions discrètes en quelques centaines d'itérations, et ce même pour des écoulements à très faible nombre de Mach. La généralisation de ces travaux au schéma HLLC se fait ensuite en poursuivant l'analyse de la structure d'onde faite par M. Pelanti.

Ces travaux révèlent une profonde similarité entre les dissipations numériques de ces méthodes. En particulier, nous dérivons un formalisme commun entre ces deux schémas, afin de simplifier les analyses, et la transposition d'une correction d'un solveur de Riemann approché à l'autre, au sens d'une relation très claire entre les deux méthodes. Cette analyse nous permet en particulier de dériver le schéma HLLC-Rossow, mais également d'expliciter l'expression de la matrice de viscosité du schéma HLLC, qui exhibe une ressemblance intéressante avec celle du schéma Roe.

Title: Extensions of some approximate Riemann Solvers for the computation of mixed incompressible-compressible flows

Keywords: CFD, Low-Mach number flows, Compressible flows, Incompressible flows, Finite volume method, von Neumann stability condition.

Abstract:

In this thesis, we focus on the simulation of compressible flows using implicit Godunov-type methods, such as the Roe method or the HLLC scheme. The objective is to develop low Mach number extensions that preserve the accuracy of discrete solutions in the low Mach number limit. This type of flow is frequently encountered in the simulation of industrial configurations, which are often characterized by the presence of more or less extensive low-speed areas.

We focus on the hyperbolic component of the Navier-Stokes equations, which form the core of the numerical analysis problem addressed in this thesis, the Euler equations. We present an in-depth and detailed analysis of research topic that has been the subject of investigations for decades, and which continues to present significant challenges, even for this academic model. A review of the literature reveals a large number of possible extensions to the Roe scheme, which are generally easy to implement. These involve modifying specific terms of the numerical dissipation, either by amplifying or by diminishing their contribution in the low Mach number limit (also known as a rescaling of the numerical dissipation). They also enable us to obtain a discrete compressible solution that approaches the analytical solution derived from potential theory for the incompressible problem, without introducing any deterioration in the results in the compressible regime. The capture of shock waves for transonic and supersonic flows remains almost unaltered. However, there are a number of studies suggesting that care should be taken in the choice of formulation for this type of correction. It is well documented in the literature that losses in numerical stability are generally observed, as well as the risk of velocity-pressure decoupling problems appearing, which can significantly deteriorate the overall accuracy of the discrete solution for low-speed flows.

This work is based on two very different corrections of the Roe scheme, taken from the scientific literature, and highlighting distinct discrete properties. The first approach, proposed by C.-C. Rossow, amplifies pressure jumps by introducing an artificial speed of sound, whereas the second approach, developed by F. Rieper, aims to attenuate velocity jumps exclusively. These two approaches illustrate two major strategies frequently used in low-Mach extensions. We begin with a discrete asymptotic analysis of the approach proposed by C.-C. Rossow, which has not been published in the literature, including the formulation of the von Neumann stability condition. It is demonstrated that this correction avoids the issue of pressure- velocity decoupling. Next, we present a numerical method for constructing the exact implicit phases required for time integration, using algorithmic differentiation and a direct solver. These techniques enable us to bypass the very strict stability constraint on the time step, thereby facilitating the acquisition of discrete solutions within a few hundred iterations, even for very low Mach number flows. The generalization of this work to the HLLC scheme is then made by continuing the wave structure analysis carried out by M. Pelanti. This work demonstrates a significant similarity between the numerical dissipations of these methods. In particular, a common formalism between these two schemes is derived, with the aim of simplifying the analyses, and transposing of a correction from one approximate Riemann solver to the other, in the sense of a very clear relationship between the two methods. In particular, this analysis enables us to derive the HLLC-Rossow scheme, but also to clarify the expression of the viscosity matrix of the HLLC scheme, which exhibits an interesting resemblance to that of the Roe scheme.

Remerciements

En sortant de mon stage de fin d'étude, j'écrivais dans mes notes " Bien que mon esprit soit désormais libre des questions qui l'ont occupé pendant ces 6 derniers mois, je ne souhaiterais qu'une chose : pouvoir y répondre."

Pour commencer ces remerciements, j'aimerais tout d'abord exprimer ma sincère gratitude envers mes directeurs de thèse, F.Renac et C. Chalons, ainsi qu'envers mes encadrants de thèse, J.C. Boniface et C. Content. Je vous remercie de m'avoir retenu pour cette thèse, et de m'avoir offert cette chance : celle d'avoir le temps pour pouvoir répondre à des questions profondes et pourtant si fréquentes dans la pratique. Les premières pensées qui me viennent en tête en écrivant ces lignes sont d'abord une rectification : ~~"avoir le temps"~~ car ce n'est pas tout à fait vrai, mais aussi un mélange d'humilité et de gratitude envers ces personnes. J'espère ne pas avoir été un étudiant trop audacieux dans mes choix, notamment lorsque je défendais avec conviction ce qui me semblait pertinent, plutôt que d'admettre soudainement d'autres points de vue. J'espère toutefois avoir atténué ce trait de ma personnalité par mon engagement sans faille dans ce projet de recherche, en m'y consacrant pleinement, et en suivant par exemple le rythme de J.C. lors de ses journées ponctuelles de 14 heures sur site. Je vous remercie sincèrement pour le temps que vous m'avez consacré, malgré des agendas parfois chargés, ainsi que pour la confiance que vous m'avez témoigné tout au long de la réalisation de ces travaux.

Dans un second temps, je souhaiterais exprimer ma profonde reconnaissance à l'ensemble des membres de mon jury de thèse. Leur expertise et leur présence lors de ma soutenance m'honorent particulièrement, d'autant plus que les discussions qui ont suivi ont suscité de nouvelles réflexions enrichissantes sur des travaux pourtant trop bien connus par l'auteur de ces travaux. Je tiens tout particulièrement à exprimer ma sincère gratitude envers R. Abgrall et P.H. Maire, qui ont accepté d'endosser le rôle de rapporteurs et ont entrepris, avec une grande rigueur, l'évaluation scientifique du manuscrit de thèse.

Cette thèse s'est déroulée au sein des bureaux de deux équipes de l'ONERA, H2T et CLEF, où de nombreuses personnes ont contribué, directement ou indirectement, à un cadre professionnel convivial, et parfois même attentionné. Tout au long de mon doctorat, j'ai eu la chance de bénéficier d'un environnement social précieux, pour lequel je suis profondément reconnaissant envers tous mes collègues, et dans lequel ont notamment eu lieu des discussions scientifiques particulièrement enrichissantes (HPC, voilure tournante, multi-espèces, compilateurs, programmation, etc.). Cette environnement m'a été bénéfique lors des moments de doute. Cependant, par souci de concision, il m'est difficile de nommer individuellement toutes les personnes associées à cette environnement. Qu'il s'agisse des anciens doctorants, qui ont été pour certains des compagnons de travail lors des longues journées, des jeunes chercheurs, dont l'énergie débordante et les plaisanteries incessantes apportaient une touche de légèreté, ou encore des membres permanents, jonglant de manière impressionnante entre de nombreux projets, qu'ils soient toujours actifs ou partis vers d'autres horizons, je tiens à tous les remercier. L'ensemble de ces personnes a contribué, de manière indirecte, par leur bonne humeur, leurs gestes quotidiens et leur soutien, à l'aboutissement de la synthèse de ces travaux.

Enfin, mes dernières pensées se tournent vers ma famille, à qui j'exprime toute ma reconnaissance pour leur soutien constant pendant ces années de travail intenses. Plus particulièrement à ma compagne, qui a en plus toléré que je ramène à la maison cette addiction, parfois trop proche de l'obsession.
Merci infiniment à eux.

Victor Courtin
Vélizy, Janvier 2025

" ... nous sommes comme des nains assis sur des épaules de géants. Si nous voyons plus de choses et plus lointaines qu'eux, ce n'est pas à cause de la perspicacité de notre vue, ni de notre grandeur, c'est parce que nous sommes élevés par eux."

– Bernard de Chartres, XIIe siècle

Conformément aux recommandations ministérielles relatives à la promotion de la francophonie, les mémoires de thèse doivent inclure une proportion significative de contenu rédigé en français.
En réponse à cette exigence, l'introduction de la thèse, présentant le cadre général des travaux ainsi que la structure du document, a été traduite en français et intégrée au début de ce mémoire. De manière similaire, la conclusion et les perspectives de recherche seront également adaptées et incluses dans cette version francophone.
Ces deux sections traduites précèdent donc le sommaire du document (page 16), lequel expose le contenu du manuscrit, intégralement rédigé en anglais.

Introduction générale à la thèse (traduction)

Contexte

Ce travail de doctorat a été réalisé dans le département Aérodynamique, Aéroélasticité, Acoustique de l'ONERA. Dans ce département, les études et recherches sont menées dans les domaines de la modélisation, des simulations numériques et expérimentales, couvrant un large éventail de technologies et de physique des fluides. En particulier, les activités de recherche et développement portent sur le développement de méthodes de calcul avancées pour la simulation numérique des écoulements à grand nombre de Reynolds. De nombreux écoulements complexes en aéronautique sont caractérisés par des régimes mixtes compressibles et incompressibles.

La simulation numérique des écoulements aérodynamiques dans les régimes compressible et incompressible nécessite des méthodes numériques intrinsèquement différentes. Ceci est principalement dû à la nature distincte des équations aux dérivées partielles (EDP) associées, le régime compressible est régi par des systèmes d'équations hyperboliques alors que les équations pour le régime incompressible sont elliptiques. L'étude des écoulements aérodynamiques a notamment mis en évidence l'importance du développement de solveurs « compressibles », capables de capturer efficacement les ondes de choc inhérentes aux écoulements compressibles à grande vitesse. C'est précisément ce à quoi ont historiquement répondu les méthodes de type upwind (schéma décentré en amont) [1], dont font partie les *solveurs de Riemann* [2]. Au cours des dernières décennies, les *solveurs de Riemann approchés* [3, 4] ont fait l'objet de nombreuses études dans la littérature, en tant qu'outils clés pour la formulation de schémas capturant efficacement les chocs. Ces méthodes numériques ont suscité un intérêt croissant en raison de leur simplicité, de leur précision et de leur robustesse. Aujourd'hui, elles sont couramment utilisées pour la simulation d'un large éventail d'applications en dynamique des fluides numériques (CFD), pour un spectre de vitesse allant du régime subsonique au régime hypersonique.

Cependant, dans le cadre des écoulements à faible vitesse, le régime compressible à faible nombre de Mach soulève un certain nombre de défis numériques important, qui ont été déjà fréquemment abordés dans la littérature au cours des dernières décennies. Dans la limite bas-Mach, il est déjà bien établi que les schémas upwind standard discrétisant les équations d'Euler compressibles se confrontent à de nombreux inconvénients et problèmes. Ces problèmes découlent de la sensibilité des schémas compressibles au nombre de Mach local, comme indiqué ci-dessous :

(i) Le système linéaire est mal conditionné, ce qui affecte significativement la vitesse de convergence des solveurs itératifs et, par conséquent, l'efficacité des schémas implicites.

(ii) Une rigidité numérique qui impose un pas de temps excessivement petit, rendant prohibitif le nombre d'itérations du solveur CFD.

(iii) Les solutions discrètes souffrent de sévères pertes de précision [5, 6].

L'origine de la perte de précision (iii) a été clairement examinée par Guillard et Viozat, dans le travail de référence [7]. Une analyse dimensionnelle des équations met en évidence l'existence de deux régimes asymptotiques dans la limite à faible nombre de Mach $M_\star$. En temps court, les équations sans dimension, indiquées ci-dessous, se comportent comme *une limite asymptotique acoustique* ($\mathcal{A}_c$), tandis

qu'en temps long, elles correspondent à ce que l'on appelle *une limite asymptotique incompressible* ($\mathcal{I}_{nc}$). Dans l'échelle des temps longs, les équations passent d'une nature hyperbolique à une nature elliptique, démontrant ainsi une *limite singulière* de ces équations. En outre, l'analyse fonctionnelle indique qu'une solution des équations compressibles présente un comportement complexe dans la limite bas-Mach, puisqu'elle peut être décrite comme une superposition de ces deux régimes, avec des interactions acoustiques-incompressibles [8–10].

$$(\mathcal{A}_c)\begin{cases} \frac{1}{M_\star}\partial_t\rho + \nabla\cdot(\rho\boldsymbol{\mathcal{U}}) & = 0 \\ \frac{1}{M_\star}\partial_t(\rho\boldsymbol{\mathcal{U}}) + \nabla\cdot(\rho\boldsymbol{\mathcal{U}}\otimes\boldsymbol{\mathcal{U}}) + \frac{1}{{M_\star}^2}\boldsymbol{\nabla p} & = \mathbf{0} \\ \frac{1}{M_\star}\partial_t(\rho E) + \nabla\cdot(\rho\boldsymbol{\mathcal{U}}(E+\frac{p}{\rho})) & = 0 \end{cases} \qquad (\mathcal{I}_{nc})\begin{cases} \partial_t\rho + \nabla\cdot(\rho\boldsymbol{\mathcal{U}}) & = 0 \\ \partial_t(\rho\boldsymbol{\mathcal{U}}) + \nabla\cdot(\rho\boldsymbol{\mathcal{U}}\otimes\boldsymbol{\mathcal{U}}) + \frac{1}{{M_\star}^2}\boldsymbol{\nabla p} & = \mathbf{0} \\ \partial_t(\rho E) + \nabla\cdot(\rho\boldsymbol{\mathcal{U}}(E+\frac{p}{\rho})) & = 0 \end{cases}$$

Pour chacune des deux limites, l'analyse en nombre de Mach fournit des caractérisations du comportement asymptotique de la solution, ce qui permet d'identifier précisément les causes des pertes de précision des solutions discrètes [7]. Dans la limite à faible nombre de Mach, il est démontré que ces méthodes numériques introduisent des fluctuations de pression d'ordre incorrect, mettant ainsi en évidence une discrétisation inappropriée des équations compressibles, ce qui entraîne un écart notable entre les solutions continues et discrètes. Comme le souligne Turkel dans ses travaux, cette détérioration peut également être attribuée au comportement asymptotique incorrect de la dissipation à valeur matricielle du schéma numérique pour les schémas de type Roe [11–13].

Au cours des trois dernières décennies, de nombreuses études ont été menées dans la littérature afin d'identifier des méthodes efficaces permettant d'obtenir un schéma précis dans la limite bas-Mach. L'approche la plus ancienne et la plus emblématique, initiée dans les années 1990, consiste à introduire des *préconditionneurs locaux à faible vitesse* [11, 14–16]. L'objectif de ces méthodes est d'accélérer la convergence vers l'état stationnaire en améliorant le conditionnement du système d'équations et d'obtenir des solutions discrètes précises. Cependant, les préconditionneurs bas-Mach modifient les équations en un système pseudo-instationnaire, ce qui nécessite donc une reformulation complète du solveur CFD. En particulier, toutes les conditions aux limites basées sur les variables caractéristiques ou les invariants de Riemann doivent être soigneusement réécrites. De plus, l'extension aux problèmes instationnaires n'est pas triviale, et la précision temporelle peut être perdue sans une attention particulière. Notez que cette approche ne sera pas prise en compte dans le cadre de ce travail de thèse et ne sera donc pas discutée dans la suite.
À l'opposée, des méthodes plus récentes et prometteuses se sont concentrées sur la définition de nouveaux schémas qui, de part leur construction, sont intrinsèquement bien adaptés aux écoulements à faible nombre de Mach. Ces schémas utilisent une décomposition d'opérateurs et des techniques de relaxation, comme le soulignent [17–19]. Cependant, de telles approches ne seront pas abordées dans ce travail, car l'objectif principal de cette thèse concerne les méthodes numériques couramment utilisées dans le domaine aéronautique, et qui ont déjà été largement adaptées à un niveau industriel pour traiter des écoulements compressibles complexes.
Depuis les années 2000, la littérature fait état d'un intérêt croissant pour une approche différente qui, bien que non conventionnelle, sera désignée ici par souci de clarté sous le nom de « termes de stabilisation corrigés ». Ces techniques ont émergé progressivement à la suite des préconditionneurs locaux à faible vitesse et consistent à adapter la dissipation numérique des schémas de type solveur de Riemann approché pour le régime compressible, en fonction du nombre de Mach. Ces corrections présentent l'avantage d'être moins intrusives dans les codes de calcul existants que les préconditionneurs basse vitesse, et de préserver la consistance en temps avec les équations. L'approche vise à modifier

certaines entrées spécifiques de la dissipation matricielle du schéma, en amplifiant ou en diminuant leur contribution (rééquilibrage/rescaling) dans la limite bas-Mach. Par conséquent, ces techniques offrent une nouvelle interprétation du schéma, permettant de maintenir la précision pour les faibles vitesses (iii) et de retrouver le schéma original au point sonique. L'introduction initiale de ces méthodes dans la littérature a été présentée dans les travaux de Guillard-Viozat [7] avec le schéma de Roe-Turkel. Cette approche a largement inspiré de nombreux développements,comme en témoigne la littérature, avec l'émergence d'un grand nombre d'extensions à faible nombre de Mach pour les schémas de type Roe et HLL.

Cependant, des études récentes ont souligné que de telles modifications doivent être introduites avec prudence. En effet, bien que la formulation de ces corrections améliore la précision des solutions discrètes, elle engendre généralement d'autres problèmes numériques, tels que des pertes de stabilité numérique [9], des problèmes de *découplage vitesse-pression* [20, 21], ainsi que des incohérences dans le traitement des phénomènes acoustiques dans les écoulements à faible nombre de Mach [22, 23]. La définition d'une extension robuste et stable aux écoulements turbulents complexes sur des maillages non structurés reste un sujet de recherche encore actif.

Les objectifs de cette thèse

Cette thèse porte sur la simulation des équations d'Euler compressibles pour les gaz parfaits, en utilisant des méthodes numériques compressibles implicites, modifiées par des techniques de stabilisation corrigées.

L'objectif est de contribuer à l'analyse théorique et numérique des méthodes pour les écoulements à faible nombre de Mach, avec une attention particulière portée à deux solveurs de Riemann approchés couramment utilisés dans les applications en dynamique des fluides numériques : *la méthode de Roe* [3], et *Le schéma HLLC* [4, 24].

La but de ce travail est de proposer des extensions faible nombre de Mach, robustes et stables, qui répondent au problème de précision (iii) pour les écoulements faiblement compressibles, tout en maintenant la précision dans la capture des ondes de choc.

De plus, ce travail de doctorat examinera également la stabilité au sens de von Neumann de ces schémas, afin d'aborder le second problème (ii) rencontré dans la limite bas-Mach.

Démarche scientifique

Dans le but d'atteindre ces objectifs, les travaux de doctorat se sont d'abord concentrés sur le schéma de Roe, pour lequel il existe une littérature très abondante, traitant de divers types d'analyse discrète et d'extensions possibles à faible nombre de Mach. À titre de première étape préliminaire, deux approches distinctes et bien documentées de rééquilibrage de la dissipation à valeur matricielle font l'objet d'une analyse approfondie. Tout d'abord, nous avons considéré *la correction de Rieper* [25], une extension bien connue qui a été largement analysée et discutée dans de nombreux articles. Cette correction se distingue par la formulation d'une discrétisation spatiale permettant de retrouver asymptotiquement

une contrainte de divergence nulle pour le régime incompressible ($\mathcal{I}_{nc}$). Puis, *l'approche de la vitesse du son artificielle* proposée par Rossow [26, 27], qui présente des similitudes formelles avec les préconditionneurs à faible vitesse. Ces deux extensions introduisent des rééquilibrages distincts de la dissipation à valeur matricielle dans le régime subsonique, en modifiant spécifiquement différentes entrées de la matrice de dissipation. Cependant, à notre connaissance, les propriétés discrètes de l'approche de la vitesse du son artificielle de Rossow n'ont pas encore été analysées dans la littérature.

Ensuite, ce travail de doctorat s'est concentré sur une mise en regard des différentes méthodologies de rééquilibrage utilisées pour *le schema HLLC*, et plus généralement pour *les schémas de type HLL*. L'état de l'art pour les corrections des schémas de type HLL souligne qu'une partie de la littérature traitant des modifications de *Le schéma de Roe* a été fréquemment utilisée comme une source d'inspiration. Ceci s'explique par le fait que le schéma de Roe bénéficie d'une littérature plus conséquente concernant les extensions à faible nombre de Mach, y compris les préconditionneurs à faible vitesse, en comparaison avec d'autres schémas proposés, tels que le schéma de Jameson, par exemple. Un nombre considérable d'articles ont traité de l'extension des schémas de dissipation matricielle modifiés pour les schémas de type Roe aux schémas de type HLL. Toutefois, une revue de la littérature met en évidence un manque de formalisme comparable entre les deux types de solveurs de Riemann approchés lors de la dérivation des corrections à faible nombre de Mach. Cela a, en général, contribuer à un grand éparpillement des formulations des corrections, et a de légères différences dans les corrections propagées d'un type de solveur de Riemann approchés à l'autre. Néanmoins, cela a démontré que ces deux types de méthodes peuvent être corrigés avec des extensions qui semblent familières.
Dans ce travail, notre approche consiste à identifier progressivement un formalisme unifié permettant d'exprimer les flux Roe et HLLC d'une manière mathématiquement analogue. L'objectif est d'essayer d'éliminer les différences fondamentales qui apparaissent dans la formulation des *schémas de Roe et de HLLC* [3, 4], pour ensuite étudier l'existence d'extensions globales à faible nombre de Mach pour ces deux solveurs de Riemann approchés. L'approche impliquera la recherche d'un cadre plus efficace et plus général pour l'étude de ces deux solveurs de Riemann approchés, qui permettra des comparaisons algébriques, malgré les divergences déjà connues.

Les résultats numériques présentés dans cette thèse ont été obtenus en développant un code de recherche bidimensionnel, utilisant une méthode des volumes finis centrée sur les cellules dans des maillages structurés. Afin de contourner la condition de stabilité stricte pour les schémas explicites (ii), une composante clé de la procédure numérique repose sur une intégration temporelle implicite efficace. Dans ce travail, un schéma d'Euler implicite linéarisé est considéré :

$$(\frac{V}{\Delta t}\boldsymbol{\mathcal{I}} + \boldsymbol{\partial_{W^n}\mathcal{R}^n})\,(\boldsymbol{W^{n+1}} - \boldsymbol{W^n}) = -\boldsymbol{\mathcal{R}^n}.$$

Un effort considérable a été investi au développement de schémas implicites pertinents, en s'appuyant sur des outils modernes tels que *Tapenade* : un outil de différentiation automatique/algorithmique [28], ainsi que des bibliothèques optimisées de décomposition LU. La matrice jacobienne exacte du bilan de flux $\boldsymbol{\partial_{W^n}\mathcal{R}^n}$ requise pour l'intégration temporelle est obtenue grâce à l'utilisation de *Tapenade* ainsi que de techniques de coloration de maillage, introduites pour construire efficacement cette matrice. Afin de contourner la lenteur prohibitive de la convergence des solveurs itératifs, liée aux problèmes de conditionnement (i), une *factorisation LU creuse* (solveur direct), fournie par les bibliothèques Intel, est utilisée à chaque itération pour résoudre le système linéaire. De plus, pour des écoulements stationnaires, une stratégie CFL adaptative a été développée, permettant d'augmenter le nombre de CFL et d'atteindre des valeurs importantes qui compensent la condition de stabilité stricte typiquement rencontrée dans le régime bas-Mach. Ainsi, le schéma d'Euler implicite linéarisés tend asymptotiquement à se comporter comme une méthode quasi-Newton, nécessitant alors d'être résolue à l'aide d'une

méthode efficace. La sélection de ces techniques est d'une importance fondamentale, car leur combinaison permet une construction rapide et efficace de la *phase implicite exacte*, aboutissant à des schémas notablement stables. En particulier, dans ce travail, la condition de stabilité de von Neumann sera formulée en fonction du rayon spectral de la dissipation à valeur matricielle, conformément à l'analyse de stabilité de Birken-Meister effectuée dans [29].

Résultats

Les principales contributions de ce travail de doctorat sont les suivantes :

---

1. Le développement d'un code de recherche générique qui peut être facilement utilisé pour évaluer une variété d'extensions à faible nombre de Mach de schémas compressibles, ainsi qu'une discrétisation temporelle implicite efficace incorporant une reconstruction MUSCL du deuxième ou du troisième ordre en l'espace.
2. L'introduction et l'évaluation d'un nouveau critère de stabilité numérique.
3. Le développement d'une approche plus efficace pour le calcul des écoulements compressibles stationnaires à très faible nombre de Mach, donnant lieu à une accélération significative du taux de convergence vers la solution stationnaire.
4. L'analyse discrète de l'approche de la vitesse du son artificielle de Rossow.
5. La proposition d'un formalisme unifié, obtenu à partir d'une analyse basée sur les structures d'ondes de la *méthode de Roe* et du *schéma HLLC*, conduisant à la notion d'extensions globales à faible nombre de Mach pour les deux solveurs de Riemann approchés. Ce dernier point est en particulier discuté et illustré par la dérivation de l'approche de la vitesse du son artificielle de Rossow appliquée au schéma HLLC (c'est-à-dire le schéma HLLC-Rossow).

Structure du document

Le premier chapitre introduit le sujet de la thèse en décrivant les cadres théoriques et numériques sur lesquels ce travail est basé. Dans les sections suivantes, les différentes notations utilisées dans le manuscrit sont introduites. Le premier chapitre traite de l'approche numérique et des méthodes numériques utilisées pour le calcul des écoulements compressibles à faible nombre de Mach. Enfin, quelques aperçus sont donnés sur la construction de *schémas implicites exacts* grâce à l'utilisation de la Différenciation Automatique par Transformation de Source (AD-ST) mise en œuvre dans *Tapenade* et *les méthodes de coloration de maillage.*

Le deuxième chapitre est consacré au *schéma de Roe.* Une fois la construction de ce solveur de Riemann approché rappelée, l'attention est progressivement attirée sur deux formalismes équivalents permettant d'exprimer le flux numérique. Ces formalismes sont d'une part soit la forme d'onde simple caractérisant les solveurs de Riemann approchés, soit d'autre part la forme de viscosité artificielle, couramment rencontrée dans la littérature, et qui fait intervenir la dissipation à valeur matricielle du

schéma de Roe. Ensuite, *la correction de Rieper* et *l'approche de la vitesse du son artificielle de Rossow* sont introduits et certains cadres d'analyse proposés par Turkel et Guillard-Viozat sont discutés.

Le troisième chapitre correspond à un article soumis au Journal of Computational Physics, relatif à l'analyse discrète de *l'approche de la vitesse du son artificielle de Rossow*. Quelques cas tests simples sont considérés pour la comparaison des propriétés discrètes de l'approche de la vitesse du son artificielle avec *la correction de Rieper* et le *schéma de Roe-Turkel*. En particulier, l'article vise à examiner différents types d'analyse asymptotique des extensions à faible nombre de Mach qui ont déjà été décrits dans la littérature au cours des dernières décennies. L'objectif était d'examiner et d'évaluer des questions spécifiques qui ont été précédemment identifiées dans la littérature, dans le but de présenter des preuves numériques à l'appui de leur véracité ou non. Dans cet article, nous discutons également de la convergence des solutions discrètes vers l'état stable, de la condition de stabilité de von Neumann du schéma de Roe modifié, et nous passons en revue les développements récents concernant l'acoustique dans les écoulements à faible nombre de Mach.

Le chapitre 4 porte sur les *schémas du type HLL*. Après avoir rappelé la construction du schéma *HLLC*, nous examinons les différentes formes qui ont été proposées dans la littérature, en incorporant à ce schéma des extensions à faible nombre de Mach. Cette présentation se conclut par le travail récent de M. Pelanti, se focalisant sur la structure d'ondes du schéma HLLC, lequel a été ensuite approfondi dans ce travail de doctorat pour la dérivation du *schéma HLLC-Rossow*.

Le dernier chapitre est consacré à la poursuite de l'analyse des structures d'ondes de ces deux solveurs de Riemann. En effet, les résultats de Pelanti indiquent qu'un nombre limité de similitudes entre les deux structures d'ondes est suffisant pour étendre certaines corrections formulées pour le schéma de Roe au schéma HLLC. Cependant, le mécanisme exact par lequel cela se produit n'est pas encore clair. L'objectif de ce chapitre est de présenter une série d'hypothèses qui tentent d'expliquer pourquoi les schémas de Roe et HLLC peuvent être corrigés avec une approche identique (la vitesse du son artificielle, la correction de Rieper, ...etc...). Afin d'atteindre cet objectif, une activité de recherche a été consacrée au développement d'un formalisme unifié qui peut faciliter une analyse discrète complète des extensions à faible nombre de Mach de ces schémas compressibles. Une forme de dissipation à valeur matricielle du schéma HLLC est introduite. Une attention particulière est accordée à l'étude de la relation entre les deux dissipations matricielles correspondantes aux schémas de type Roe ou HLLC, grâce à l'application d'une certaine condition de consistance.

Liste des communications

ECCOMAS 2024, *Lisbonne*, communication orale, V. Courtin, J.C. Boniface, *Numerical investigations of the artificial speed of sound approach for compressible low-Mach number flows.*

JCP Soumission papier août 2024, V. Courtin, J.C. Boniface, *Analysis of the Rossow's Artificial Speed of Sound Approach for the Computation of Compressible Flows in the Incompressible Limit.*

Conclusion et perspectives des travaux (traduction)

Remarques finales

Le travail de doctorat s'est principalement concentré sur la formulation de corrections à faible nombre de Mach pour les schémas de volumes finis Roe et HLLC, dans le but d'améliorer ces deux méthodes numériques pour la simulation d'écoulements compressibles, pour une gamme de régimes allant de très faiblement compressible au régime transsonique. L'objectif était de démontrer que la formulation de ces méthodes numériques peut être modifiée et généralisée sans compromettre leur précision dans le régime compressible, tout en préservant la qualité des solutions discrètes compressibles pour les écoulements presque incompressibles. Les objectifs de cette thèse étaient doubles : premièrement, contribuer à l'analyse numérique de ces méthodes en apportant de nouvelles perspectives dans la formulation de corrections bas-Mach numériquement stables ; deuxièmement, proposer une correction robuste et efficace pour ces schémas.

Dans ce contexte, nous avons développé une méthodologie basée sur un examen approfondi des différentes approches proposées dans la littérature afin de rééquilibrer les termes de la dissipation numérique, en mettant un accent particulier sur le schéma de Roe. L'examen des approches existantes dans la littérature, complété par leur analyse à l'aide de diverses techniques, fournit une vue d'ensemble cruciale de ce sujet de recherche difficile, comme principalement exposé dans la première partie de cette thèse. Malgré des décennies de recherche active, ce sujet demeure partiellement ouvert, avec certains de ses aspects nécessitant à ce jour encore des investigations plus approfondies. L'une des principales difficultés sous-jacentes réside dans la présence simultanée de deux échelles de temps, l'une acoustique et l'une incompressible, qui caractérisent les solutions compressibles dans la limite à faible nombre de Mach. Les défis inhérents reposent sur la formulation d'une dissipation modifiée à valeur matricielle, permettant à la solution discrète d'approcher avec précision la solution dans les limites des deux échelles de temps, tout en évitant l'introduction de problèmes secondaires tels que les problèmes de découplage vitesse-pression.

En se concentrant sur les modifications du vecteur de dissipation du schéma de Roe dans le cas général (c'est-à-dire indépendamment du maillage ou des types d'éléments), le chapitre 2 a révélé qu'il existe deux approches distinctes pour résoudre le problème de précision dans la limite des faibles nombres de Mach. Ces deux approches sont mises en évidence dans cette thèse avec la correction de Rieper et l'approche de la vitesse du son artificielle de Rossow, qui, soit centre asymptotiquement le gradient de pression du premier ordre dans les équations, soit au contraire, évite de centrer asymptotiquement les gradients de pression. Les deux approches présentent des avantages et des inconvénients distincts dans le cas général
Comme démontré dans la dernière section du deuxième chapitre, le développement d'une troisième approche, fondée sur le centrage asymptotique des gradients de pression du premier ordre, s'avère insuffisamment robuste et par conséquent inefficace, en raison de l'introduction de problèmes secondaires plus significatifs que ceux des deux autres approches. Il a été montré que cette correction produit des niveaux d'entropie parasites excessivement importants aux points d'arrêt, entraînant ainsi en une grave détérioration de la précision globale de la solution discrète. De plus, l'analyse asymptotique de la troisième approche met en évidence des caractéristiques communes avec la correction de Rossow, indiquant que ce type de corrections est également sujet à des incohérences similaires dans la limite

de l'échelle de temps acoustique. On pourrait considérer ces recherches sur une troisième approche comme la preuve qu'il est difficilement possible de faire mieux que les deux approches que l'on trouve déjà dans la littérature.

Dans le chapitre 3, nous avons effectué l'analyse asymptotique pour le schéma de Roe modifié selon l'approche de la vitesse du son artificielle de Rossow et avons réalisé une analyse détaillée de cette correction. Il a été prouvé qu'à l'échelle de temps incompressible, les solutions discrètes sont caractérisées par des fluctuations de pression quadratiques en espace, et qu'elles ne vérifient pas non plus, de manière asymptotique, une contrainte discrète de divergence nulle sur le terme dominant de la vitesse. Nous avons également démontré que la correction de Rossow n'est pas sensible à des problèmes de découplage vitesse-pression. Le schéma reste précis même sur un maillage très étiré, contrairement à la correction de Rieper.
De plus, nous montrons que l'analyse de stabilité de von Neumann de ce schéma aboutit à une condition de stabilité plus stricte dans la limite bas-Mach que celle initialement prédit par Rossow, cette correction se comporte de manière analogue au schéma de Roe-Turkel. Ainsi, le pas de temps est contraint d'être excessivement petit dans la limite bas-Mach, ce qui la rend pénalisante pour certaines applications de la CFD.
Afin de contourner la rigidité de la contrainte de stabilité, une approche numérique robuste et stable est présentée, reposant sur une intégration temporelle implicite avec un schéma d'Euler implicite linéarisé. Les principaux éléments clés de cette approche sont la différenciation algorithmique, l'utilisation de bibliothèques de décomposition LU rapide, une nouvelle condition de stabilité numérique ainsi que la formulation d'une méthode de pseudo-continuité vers une méthode de quasi-Newton. Cela conduit au développement de schémas implicites très stables qui permettent l'utilisation de grands nombres CFL et qui, de manière remarquable, ne nécessitent que quelques centaines d'itérations pour obtenir une convergence quadratique vers les solutions stationnaires, et ce même pour des écoulements à très faible nombre de Mach allant jusqu'à 10^{-6}.
Ce travail aborde également les interactions acoustiques incompressibles caractérisant les solutions discrètes compressibles dans la limite incompressible. Nous montrons que les solutions discrètes présentent des perturbations acoustiques permanentes dans la limite à faible vitesse, même pour le problème stationnaire, caractérisé par des impulsions acoustiques générées à des temps très courts et dissipées à des temps plus longs. Nous avons constaté que l'intensité de ces perturbations acoustiques est liée à la modification des sauts de la composante normale de la vitesse à l'interface de la cellule.

La deuxième partie de cette thèse a été consacrée au schéma HLLC. L'examen approfondi des approches existantes met en évidence de nombreuses similitudes entre les corrections appliquées aux schéma de HLLC et de Roe. Afin de généraliser l'analyse réalisée dans la première partie concernant le schéma de Roe au schéma HLLC, nous proposons une poursuite de l'analyse menée par Pelanti en nous concentrant sur les similitudes entre les deux structures d'ondes des deux solveurs de Riemann. Cette recherche a abouti à la formulation d'un cadre commun visant à analyser et à simplifier la dérivation des corrections appliquées aux deux vecteurs de dissipation. En effet, nous avons établi une nouvelle expression pour le vecteur de dissipation associé au schéma HLLC, qui peut être facilement interprétée comme une généralisation de la forme de Liu-Vinokur pour le schéma de Roe, également désignée dans la littérature sous le nom de décomposition de Weiss-Smith, au schéma HLLC.
En guise d'application, deux approches ont été proposées pour dériver des corrections « identiques » à faible nombre de Mach pour ces deux schémas. Ces approches se distinguent par leur capacité à identifier les similitudes entre les deux schémas, lesquelles servent de fondement clé pour la transposition de la correction du vecteur de dissipation d'une méthode à l'autre.
En particulier, cela a permis de généraliser l'approche de la vitesse du son artificielle de Rossow au

schéma HLLC, appelé schéma HLLC-Rossow. Il est démontré par des preuves numériques que ce schéma HLLC-Rossow restitue exactement les mêmes propriétés discrètes que celles du schéma de Roe-Rossow. Des solutions discrètes précises sont obtenues dans la limite bas-Mach, et le schéma ne pressente pas les problèmes de découplage vitesse-pression fréquemment observés avec d'autres corrections. Même en considérant un maillage fortement étiré, nous n'avons pas réussi à déclencher ce problème numérique, ce qui témoigne du comportement robuste de ce schéma modifié.

Perspectives

A la lumière des résultats présentés ci-dessus, plusieurs limitations et perspectives d'approfondissement ont été identifiées et sont maintenant discutées.
Tout d'abord, l'approche numérique développée dans ce travail constitue une composante cruciale de cette thèse, car elle a permis des investigations approfondies en simplifiant l'acquisition de résultats grâce à l'utilisation de phase implicite exacte. Néanmoins, cette approche est limitée à une certaine densité de maillage puisque les solveurs directs deviennent prohibitifs en termes de mémoire lorsque le nombre de cellules augmente. Une première perspective serait de reproduire cette approche en considérant des solveurs itératifs tels qu'un solveur GMRES. En procédant ainsi, il serait possible d'évaluer les difficultés liées à ces problèmes mal conditionnés dans la limite faible nombre de Mach, en particulier en ce qui concerne la nécessité d'une résolution précise de ces systèmes linéaires très raides.
Deuxièmement, ce travail s'est principalement concentré sur la formulation des corrections du vecteur de dissipation concernant l'échelle de temps incompressible. Cependant, cela ne correspond qu'à un aspect du problème de précision rencontré dans les écoulements à faible nombre de Mach. La prise en compte de la limite acoustique s'avère indispensable dans la formulation des corrections destinées au régime à faible nombre de Mach. À ce jour, à notre connaissance, la formulation d'une correction capable de résoudre les problèmes de précision dans les deux limites asymptotiques demeure une question importante dans la littérature, nécessitant des recherches encore plus approfondies. Cela s'explique par le fait que, d'une part, la première approche, bien qu'efficace, présente des problèmes majeurs de découplage vitesse-pression, et que d'autre part, la seconde approche, tout en évitant ce problème de découplage, implique des incohérences dans la limite acoustique. Nous pourrions donc suggérer que ces deux défis majeurs ne peuvent pas être facilement contournés, soit l'existence de solutions en damier, ou soit les incohérences dans la limite acoustique, doivent être traités et résolus pour obtenir un schéma compressible qui reste précis dans le cas général, tel que les écoulements instationnaires à faible nombre de Mach.
Troisièmement, le formalisme commun introduit pour les schémas HLLC et Roe est ouvert à d'autres investigations pour un examen approfondi. L'intérêt réside dans la dérivation de vecteurs de dissipation numérique modifiés et dans la recherche d'une analyse asymptotique commune entre les deux solveurs de Riemann approchés. Dans le chapitre 5, des preuves numériques montrent que la correction appliquée aux schémas de Roe ou HLLC présente exactement le même comportement en ce qui concerne la condition de stabilité, la précision de la solution discrète mais aussi le problème de découplage vitesse-pression. Bien que cela ne soit pas illustré dans cette thèse, on peut souligner ici, pour des recherches ultérieures, que les incohérences dans la limite acoustique ont également été observées numériquement pour le schéma HLLC-Rossow. Il convient également de noter que des tendances similaires ont été observées par Pelanti, qui a étendu la correction du schéma de Roe-Turkel au schéma HLLC, en signalant que les différences entre les deux solutions discrètes sont peu visibles. La réponse à tous ces comportements peut être trouvée dans l'analyse asymptotique, dont quelques éléments sont partagés ci-dessous comme pistes intéressantes pour des recherches ultérieures. Contrairement à l'approche standard appliquée au schéma de Roe, l'analyse asymptotique pour le HLLC est longue et nécessite de

faire une série de choix dans l'analyse dimensionnelle, comme discuté précédemment dans la section 4.2.4 avec par exemple la définition de S_*. En outre, il faut effectuer plusieurs développement de Taylor pour simplifier les expressions. Cependant, une idée clé peut être facilement déduite de la décomposition de la matrice $\boldsymbol{\mathcal{M}}^{\boldsymbol{HLLC}}$ en une matrice commune et une matrice de déviation ($\boldsymbol{\mathcal{M}}_c$, : $\boldsymbol{\mathcal{M}}_d$). Ceci montre que, dans le vecteur de dissipation associé au schéma HLLC, il existe une partie commune et facilement associable aux termes présents dans le vecteur de dissipation du schéma de Roe, mais également d'autres termes supplémentaires qui eux ne présentent aucune correspondance. Les détails manquants relatifs au rôle de ces termes supplémentaires constitueraient une information précieuse pour un formalisme unifié, et mériteraient de faire l'objet de recherches plus approfondies.
Quatrièmement, il serait bénéfique d'examiner également les liens étroits potentiels avec d'autres travaux existants dans le but d'étendre l'analyse. Par exemple, l'expression de type AUSM du schéma HLLC proposée par Kitamura-Shima dans [30], ou le schéma JST, qui sont tous deux des schémas couramment utilisés pour les applications industrielles.

En conclusion, la formulation d'une correction faible nombre de Mach pour les schémas Roe ou HLLC reste un sujet actif et ouvert à de nouvelles recherches. Néanmoins, elle devrait être étudiée simultanément afin d'éviter l'éparpillement des formulations, avec une attention spécifique aux problèmes secondaires introduits par les corrections.

Contents

List of Figures

General introduction

Context

This Ph-D work was carried out in the Aerodynamics, Aeroelasticity, Acoustics department of ONERA. In this department, study and research are conducted in the fields of modeling, numerical and experimental simulations, covering a wide range of technologies and physics of fluids. In particular, research and development activities address the development of advanced computational methods and the numerical simulation of high-Reynolds number flows. Many complex flows in aeronautics are characterized by mixed compressible and incompressible regimes.

The numerical simulation of aerodynamic flows in the compressible and incompressible regimes requires intrinsically different numerical methods. This is mainly due to distinct nature of the associated partial differential equations (PDEs), the compressible regime is governed by hyperbolic systems of equations whereas equations for the incompressible regime are elliptic. The study of aerodynamic flows has in particular demonstrated the significance of the development of "compressible" solvers, aiming at capturing efficiently shock waves that are inherent to compressible high speed flows. This is precisely what has historically been addressed by upwind methods [1], including *Riemann solvers* [2]. Over the past few decades, *Approximate Riemann Solvers* [3,4] have been extensively studied in the literature as valuable tools for designing efficient *shock-capturing schemes*. These numerical methods have gained an increasing interest due to their simplicity, accuracy, and robustness. Nowadays, they are routinely employed for the simulation of a wide range of applications in computational fluid dynamics (CFD), from the subsonic to the hypersonic regime.

However, when looking at low-speed flows, the compressible regime at very low Mach number presents significant numerical challenges that have been discussed for several decades in the literature. In the low Mach number limit, it is already well-established that standard upwind schemes discretizing the compressible Euler equations are facing numerous drawbacks and issues. These issues stem from the sensitivity of compressible schemes to the local Mach number, as listed below:

(i) The linear system is ill-conditioned, which has a significant impact on the convergence speed of iterative solvers and, as a result, on the efficiency of implicit schemes.

(ii) A numerical stiffness that constrains the time step to be exceedingly small, making prohibitive the number of iterations of the CFD solver.

(iii) The discrete solutions suffer from severe losses of accuracy [5,6].

The origin of the loss of accuracy (iii) has been clearly addressed by Guillard and Viozat, in the work of reference [7]. A dimensional analysis of the equations highlights the existence of two asymptotic regimes for a vanishing Mach number $M_\star$. In short times, the dimensionless equations indicated below behave as *an acoustic asymptotic limit* ($\mathcal{A}_c$), while in long times, they corresponds to the so-called *incompressible asymptotic limit* ($\mathcal{I}_{nc}$). In the long time scale, the equations change from a hyperbolic to an elliptic nature, demonstrating therefore a *singular limit* of these equations. Furthermore, the functional analysis indicates that a solution of the compressible equations exhibits a complex behavior

in the low Mach number limit, since it can be described as a superposition of these two regimes, with acoustic-incompressible interactions [8–10].

$$(\mathcal{A}_c)\begin{cases} \frac{1}{M_\star}\partial_t\rho + \nabla\cdot(\rho\boldsymbol{\mathcal{U}}) & = 0 \\ \frac{1}{M_\star}\partial_t(\rho\boldsymbol{\mathcal{U}}) + \nabla\cdot(\rho\boldsymbol{\mathcal{U}}\otimes\boldsymbol{\mathcal{U}}) + \frac{1}{{M_\star}^2}\boldsymbol{\nabla p} & = \mathbf{0} \\ \frac{1}{M_\star}\partial_t(\rho E) + \nabla\cdot(\rho\boldsymbol{\mathcal{U}}(E+\frac{p}{\rho})) & = 0 \end{cases} \qquad (\mathcal{I}_{nc})\begin{cases} \partial_t\rho + \nabla\cdot(\rho\boldsymbol{\mathcal{U}}) & = 0 \\ \partial_t(\rho\boldsymbol{\mathcal{U}}) + \nabla\cdot(\rho\boldsymbol{\mathcal{U}}\otimes\boldsymbol{\mathcal{U}}) + \frac{1}{{M_\star}^2}\boldsymbol{\nabla p} & = \mathbf{0} \\ \partial_t(\rho E) + \nabla\cdot(\rho\boldsymbol{\mathcal{U}}(E+\frac{p}{\rho})) & = 0 \end{cases}$$

For each of the two limits, the Mach number analysis provides characterizations of the asymptotic behavior of the solution, making it possible to clearly identify the causes of accuracy losses in discrete solutions [7]. In the low Mach number range, it is demonstrated that these numerical methods introduce pressure fluctuations of the incorrect order, which highlights an inappropriate discretization of the compressible equations, since this leads to an significant discrepancy between the continuous and discrete solutions. As pointed-out by Turkel, this deterioration can also be attributed to the incorrect asymptotic behavior of the matrix-valued dissipation of the numerical scheme for Roe-type schemes [11–13].

Over the past three decades, numerous studies have been conducted in the literature with the objective of identifying effective methods for obtaining an accurate scheme within the low Mach number limit. The oldest and most emblematic approach, developed in the 1990s, consists in introducing *local low-speed preconditioners* [11, 14–16]. The objective of these methods is to accelerate the convergence to the steady state by enhancing the conditioning of the system of equations, and to get accurate discrete solutions. However, low Mach number preconditioners modify the equations into a pseudo-unsteady system, thus requiring a complete reformulation of the CFD solver. In particular, all boundary conditions based on the characteristic variables or Riemann invariants must be rewritten with care. In addition, the extension to unsteady problems is not trivial, and the time accuracy can be lost without special care. Note that this approach will not be considered in this Ph-D work, and therefore will not be further discussed.

In contrast, promizing methods have focused on defining new schemes that, by construction, are well suited to low Mach number flows. These schemes make use of an operator decomposition and relaxation techniques, as highlighted in [17–19]. However, such approaches will not be used in this work, as the main concern of this thesis is related to numerical methods that are commonly employed for aeronautical applications and have already been readily scaled up to an industrial level for complex compressible flows.

Since the 2000s, the literature has documented an increased interest for a different approach that, although unconventional, will be referred to here as "corrected stabilization terms" for the sake of convenience. These techniques have gradually emerged in the continuation of local low-speed preconditioners and consist in adapting the numerical dissipation of approximate Riemann solver-type schemes for the compressible regime, to the Mach number regime. These corrections offer the advantage of being less intrusive into existing computational codes than low-speed preconditioners, and do not require to modify the governing equations. The approach aims at modifying some specific entries in the matrix-valued dissipation of the scheme, by either amplifying or diminishing their contribution (rescaling) in the low Mach number limit. Consequently, these techniques offer a novel interpretation of the scheme that maintains accuracy at low speeds (iii), and returns to the original scheme at the sonic point. The initial introduction of these methods into the literature was presented in the work of Guillard-Viozat [7] for a so-called Roe-Turkel scheme. This approach has significantly inspired many developments reported in the literature, with the emergence of a large number of low-Mach number extensions for Roe and HLL-type schemes.

Nevertheless, recent studies have indicated that such modifications should be introduced carefully. Although the formulation of these corrections improves the accuracy of the discrete solutions, it also introduces in general other numerical issues such as numerical stability losses [9], *spurious pressure-checkerboard mode problems* [20, 21], and even inconsistencies in the treatment of acoustic phenomena in low Mach number flows [22, 23]. The definition of a robust and stable extension to complex turbulent flows using an unstructured mesh remains a topic of ongoing research.

Objectives of this thesis

This thesis is dedicated to the simulation of the *compressible Euler equations for perfect gases* with *implicit compressible numerical methods*, modified by techniques of *corrected stabilization terms*.

The objective is to contribute to the theoretical and numerical analysis of numerical methods for low Mach number flows, with a focus on two widely used approximate Riemann solvers in CFD applications: *the Roe method* [3], and *the HLLC scheme* [4, 24].

The aim of this work is to propose robust and stable low Mach number extensions that address the accuracy issue (iii) for weakly compressible flows, while maintaining accuracy in capturing shock waves.

Furthermore, this Ph-D work will also discuss the von Neumann stability of these schemes, to tackle the second issue (ii), encountered in the low Mach number limit.

Scientific approach

To achieve these aforementioned objectives, the Ph-D work has first focused on the *Roe scheme*, for which a very large literature is available, addressing several type discrete analysis, and low Mach-number extensions. As a preliminary step, two distinct well-documented rescaling approaches of the matrix-valued dissipation are subjected to detailed examination. First, we have considered *the Rieper's fix* [25], a well-known correction that has been extensively analyzed and discussed in numerous papers. This correction is especially characterized by a discretization corresponding to the incompressible asymptotic regime ($\mathcal{I}_{nc}$), in which the free divergence constraint is enforced. Second, *the artificial speed of the sound approach* according to Rossow introduced in [26, 27], which exhibits formal similarities with low-speed preconditioners. Both of these extensions introduce a distinct rescaling of the matrix-valued dissipation in the subsonic regime, specifically modifying different entries of the matrix dissipation. Nevertheless, to the best of our knowledge, the discrete properties of the artificial speed of the sound approach of Rossow have not yet been discussed in the literature.

Next, this Ph-D work has focused on a comprehensive examination of different rescaling methodologies used for *the HLLC scheme*, and more generally for *HLL-type schemes*. An overview of the state of the art concerning the corrections of HLL-type schemes shows that part of the literature dealing with modifications of *the Roe scheme* has been frequently used as a source of inspiration. This is due to the fact that the Roe scheme has a larger literature investigating low Mach number extensions, including local low-speed preconditioners, than other proposed schemes as the Jameson scheme for instance. A considerable number of papers have addressed the extension of modified matrix-dissipation schemes

for Roe-type schemes to HLL-type schemes. However, a review of the literature reveals a lack of comparable formalism in deriving low Mach number corrections between the two types of approximate Riemann solvers. This has, in general, resulted in a large scattering of proposed corrections, and slight differences in the corrections transposed from one type of approximate Riemann solver to the other. Nevertheless, this has also demonstrated that these two types of approximate Riemann solvers can be corrected with extensions that may appear familiar.
In this work, our approach is to progressively identify a unified formalism that can be used to express the Roe and HLLC fluxes in a way that is mathematically analogous. The objective is to attempt to eliminate the fundamental differences that arise in the formulation of *the Roe and the HLLC scheme* [3, 4], to then investigate the existence of global low-Mach number extensions for the two approximate Riemann solvers. The approach will entail the pursuit of a more efficient and comprehensive framework for the study of these two approximate Riemann solvers, which will enable algebraic comparisons, despite already known discrepancies.

The numerical results presented in this thesis were obtained by developing a two-dimensional research code, using a cell-centered finite-volume method in structured meshes. In order to circumvent the stringent stability condition for the explicit schemes (ii), a crucial component of the numerical procedure relies on an efficient implicit time-integration. In this work, a linearized backward-Euler time stepping scheme is considered:

$$(\frac{V}{\Delta t}\boldsymbol{\mathcal{I}} + \boldsymbol{\partial_{W^n}\mathcal{R}^n})\,(\boldsymbol{W^{n+1}} - \boldsymbol{W^n}) = -\boldsymbol{\mathcal{R}^n}.$$

A significant effort has been dedicated to the development of efficient implicit schemes, using modern tools such as *Tapenade*: an Automatic/Algorithmic Differentiation tool [28] and fast LU decomposition libraries. The exact Jacobian matrix of the flux balance $\boldsymbol{\partial_{W^n}\mathcal{R}^n}$ required for the time integration is obtained through the use of *Tapenade*, and some mesh coloring methods, introduced to effectively build the exact Jacobian matrix. In order to circumvent the prohibitive slow convergence of iterative solvers due to the ill-conditioned problems (i), a *sparse LU-factorization* (direct solver) provided by the Intel libraries is employed at each iteration to solve the linear system. Additionally, an adaptive CFL strategy is formulated allowing to increase the CFL number, and to achieve large values that overcome the stringent stability condition typically encountered in the low Mach number regime. So, the linearized backward-Euler scheme behaves as a very stiff quasi-Newton method, requiring to be solved with a robust method. The selection of these techniques is of significant importance, as their combination facilitates a fast and efficient construction of the *exact implicit stage*, resulting in notably stable schemes. In particular, in this work, the von Neumann stability condition will be based on the spectral radius of the matrix-valued dissipation according to the stability analysis of Birken-Meister conducted in [29].

Results

The main achievements of this Ph-D work are the following:

---

1. The development of a generic research code that can be readily used to evaluate a variety of low Mach number extensions of compressible schemes, along with an efficient implicit time-discretization incorporating second or third order MUSCL reconstruction in space.

2. The introduction and the evaluation of a new numerical stability criteria.

3. The development of a more efficient approach for the computation of steady-state compressible flows at very low Mach numbers, giving rise to a significant acceleration in the convergence rate towards the steady state.

4. The discrete analysis of the artificial speed of the sound approach according to Rossow.

5. The proposition of a unified formalism, achieved from an analysis based on the wave structures of the *Roe's method* and the *HLLC scheme*, leading to the definition of global low Mach-number extensions of the two approximate Riemann solvers. This latter point is in particular discussed and illustrated by deriving the artificial speed of the sound approach of Rossow applied to the HLLC scheme (i.e. HLLC-Rossow scheme).

Chapter contents

The first chapter introduces the topic of the thesis by outlining the theoretical and numerical frameworks on which this work is based. Throughout the following sections, the various notations used in the manuscript are introduced. The first chapter deals with the numerical approach and the numerical methods used for the computation of low Mach-number compressible flows. Finally, some insights are given into the construction of *exact implicit schemes* through the use of Automatic Differentiation by Source Transformation (AD-ST) implemented in *Tapenade* and *mesh coloring methods*.

The second chapter is dedicated to the *Roe scheme*. Once the construction of this approximate Riemann solver has been reminded, the attention is progressively drawn to two equivalent formalisms that can be used to express the numerical flux. These formalisms are either the simple wave form characterizing approximate Riemann solvers, or the artificial viscosity form, commonly encountered in the literature and which involves the matrix-valued dissipation of the Roe scheme. Then, *the Rieper's fix* and *the artificial speed of the sound approach of Rossow* are introduced and some framework analysis proposed by Turkel and Guillard-Viozat are discussed.

The third chapter corresponds to a paper submitted to the Journal of Computational Physics, related to the discrete analysis of *the Rossow's artificial speed of the sound approach*. Some simple test cases are considered for the comparison of the discrete properties of the artificial speed of the sound approach with *the Rieper's fix* and the *Roe-Turkel scheme*. In particular, the paper aimed at reviewing different types of asymptotic analysis of low-Mach number extensions that have been already described in the literature. The objective was to examine and evaluate specific issues that have been previously identified in the literature, with the aim of either presenting numerical evidence to support their veracity or not. In this paper, we also discuss the convergence of discrete solutions towards the steady state, the von Neumann stability condition of the modified Roe scheme, and we provide a review of recent developments regarding acoustics in low Mach number flows.

The chapter 4 deals with the *HLL-type scheme*. After recalling the construction of the *HLLC scheme*, we look at the different forms that have been proposed in the literature, incorporating low Mach number extensions into this scheme. This presentation ends by addressing a recent work by M. Pelanti, focusing on the wave structure of the HLLC scheme, which was further developed in this Ph-D work for the derivation of *the HLLC-Rossow scheme*.

The final chapter is devoted to the pursuit of the analysis of the wave structures of these two Riemann

solvers. Indeed, Pelanti's findings indicate that a limited number of similarities between the two wave structures is sufficient to extend some corrections formulated for the Roe scheme to the HLLC scheme. However, the exact mechanism by which this occurs remains unclear. The objective of this chapter is to present a series of assumptions that attempt to explain why the Roe and HLLC schemes can be corrected with the identical approach (artificial speed of sound, low-Mach number fix, ...). In order to achieve this objective, a research activity was dedicated to the development of a unified formalism that can make easier a comprehensive discrete analysis of low-Mach number extensions of these compressible schemes. A matrix-valued dissipation form of the HLLC scheme is introduced. A particular attention is paid on finding out the relationship between the corresponding two matrix-valued dissipations for the Roe and HLLC types of Riemann solver, within the use of a certain consistency condition.

List of communications

ECCOMAS 2024, *Lisbon*, oral communication, V. Courtin, J.C. Boniface, *Numerical investigations of the artificial speed of sound approach for compressible low-Mach number flows.*

JCP Paper submitted in august 2024, V. Courtin, J.C. Boniface, *Analysis of the Rossow's Artificial Speed of Sound Approach for the Computation of Compressible Flows in the Incompressible Limit.*

1 - Theoretical and numerical frameworks

Contents

This chapter introduces the general framework of first-order non-linear conservation laws, outlining the theoretical and numerical foundations on which this Ph-D work is based. The theoretical framework regarding non-linear hyperbolic systems of conservation laws is first reminded, and the compressible Euler equations are introduced. Next, the attention is drawn on the simulation of low-speed flows, where the theoretical background and the numerical difficulties are introduced (sections 1.3 and 1.4). Then, the discrete framework is addressed, in which a finite-volume method is introduced for the space discretization of the Euler equations. The final section presents some insight into the construction of *implicit schemes* using an *exact Jacobian* through the use of automatic differentiation and *mesh coloring methods*.

1.1 . Non-linear conservation laws and weak entropy solution

The following section is dedicated to a short overview of non-linear hyperbolic conservation laws. Particular attention is paid to illustrate some fundamental ideas and the underlying motivations. The following section briefly reminds the mathematical framework by means of well-known examples, definitions, and theorems given in reference books [31–34].

1.1.1 . Hyperbolic conservation laws

Let $\boldsymbol{x}$ be an arbitrary space variable in $\mathbb{R}^d$ and t be the time variable in $\mathbb{R}_+$. In the following, we are interested to find the solution of an initial value problem (i.e. Cauchy problem) described by partial derivative equations (PDE):

$$\left|\begin{array}{ll} \boldsymbol{w} : \mathbb{R}_+ \times \mathbb{R}^d \to \mathbb{R}^p & \begin{cases} \partial_t \boldsymbol{w} + \nabla_{\boldsymbol{x}} \cdot \boldsymbol{f}(\boldsymbol{w}) = \mathbf{0} \\ \boldsymbol{w}(0, \boldsymbol{x}) = \boldsymbol{w_0}(\boldsymbol{x}) \end{cases} \\ \boldsymbol{f}(\boldsymbol{w}) : \mathbb{R}^p \to \mathbb{R}^{p \times d} & \end{array}\right. , \tag{1.1}$$

In the case $p = 1 = d$, (1.1) reduces to a more classical non-linear scalar advection equation, related to an initial condition w_0, according to a flux function f.

Solutions to this type of partial differential equation (PDE) are distinguished by their wave-like propagation behavior, characterized by a finite speed of propagation [35]. System (1.1) is hyperbolic if the flux Jacobian matrix $\partial_{\boldsymbol{w}} \boldsymbol{f}$ has only real eigenvalues and is diagonalizable.

Considering the multidimensional case with the Cauchy problem (1.1) ($p \neq 1 \neq d$), the initial condition $\boldsymbol{w_0}$ is now assumed to belong to the space of locally bounded measurable functions $\mathbf{L}^\infty_{loc}(\mathbb{R}^d)^p$. Additionally, we temporarily assume for the moment that the initial value problem (1.1) admits a classical solution which is $\boldsymbol{w} \in \mathbf{C}^1(\mathbb{R}_+ \times \mathbb{R}^d)^p$. The Cauchy problem can therefore be equivalently written under the form of a variational problem. By multiplying the partial derivative in (1.1) by a test function $\boldsymbol{\varphi} \in \mathbf{C}^1_{\mathrm{c}}(\mathbb{R}_+ \times \mathbb{R}^d)^p$ and integrating the product in domain $\mathbb{R}_+ \times \mathbb{R}^d$, the Green's theorem leads to:

$$\int_0^\infty \int_{\mathbb{R}^d} \boldsymbol{w} \cdot \partial_t \boldsymbol{\varphi} + \sum_{j=1}^{d} \boldsymbol{f_j}(\boldsymbol{w}) \cdot \partial_{x_j} \boldsymbol{\varphi} \, \mathrm{d}x dt + \int_{\mathbb{R}^d} \boldsymbol{w_0}(\boldsymbol{x}) \cdot \boldsymbol{\varphi}(0, \boldsymbol{x}) \mathrm{d}x = \mathbf{0} \quad \forall \boldsymbol{\varphi} \in \mathbf{C}^1_{\mathrm{c}}(\mathbb{R}_+ \times \mathbb{R}^d)^p. \tag{1.2}$$

As long as the solution $\boldsymbol{w}$ is smooth, then the two problems, either (1.2) or (1.1), are equivalent. The variational problem (1.2) has the advantage of introducing a more fundamental formulation, in which the definition of a solution $\boldsymbol{w}$ exists in a larger domain and allows discontinuities. The expression entails a more general framework in which the solution $\boldsymbol{w}$ retains its mathematical significance especially if it is defined in $\mathbf{L}^\infty_{\mathrm{loc}}(\mathbb{R}_+ \times \mathbb{R}^d)^p$. The solution can be thus found in a larger functional space, but at the cost of a more general definition. In this context, the more general definition is a weak solution in the sense of distributions, including both classical and weak solutions.

Definition 1.1.1 (Weak solution in the sense of distributions) *Assuming that the initial condition $\boldsymbol{w_0} \in \mathbf{L}^\infty_{loc}(\mathbb{R}^d)^p$, a function $\boldsymbol{w}$ is called a weak solution of the Cauchy problem (1.1) if $\boldsymbol{w}(t, \boldsymbol{x}) \in \mathbb{R}^p$ almost everywhere and satisfies (1.2) for any function $\varphi \in \mathbf{C}^\infty_c(\mathbb{R}_+ \times \mathbb{R}^d)^p$.*

A particular interest is retained for weak solutions in the sense of distributions that remain piecewise smooth while exhibiting propagating discontinuities. The underlying reason can be easily understood with the preceding scalar example of the Burger's equation. To clarify the question, the initial condition is modified to illustrate the essential aspects of a potential solution in the presence of a discontinuity. By transposing the initial value problem to the critical time at which the discontinuity emerges, the next initial condition is introduced

$$w_0(x) = \begin{cases} 1 & \text{if } x < 1 \\ 0 & \text{if } x > 1 \end{cases}.$$

The objective is now to investigate potential solutions to the problem. A relevant insight can be deduced by considering the linear advection equation with $f(w) = aw$. In such a case, the time evolution appears easily interpreted, as the solution is only a simple translation of the initial condition with:

$$w(t, x) = \begin{cases} 1 & \text{if } (x-1)/t < a \\ 0 & \text{if } (x-1)/t > a \end{cases}.$$

With regard to the Burger's equation, it seems reasonable to suggest that the observed behavior, which corresponds to a propagating discontinuity, can be deduced in the context of a nonlinear case. However, in contrast to the linear case, the quasi-linear form does not explicitly provide the speed of the shock. As indicated in [33], the speed of the shock can be determined by integrating the conservation law in an infinitesimal rectangle. In the case of the Burger's equation, this implies that admissible shocks are propagating at a speed $1/2$:

$$w(t,x) = \begin{cases} 1 & \text{if } (x-1)/t < 1/2 \\ 0 & \text{if } (x-1)/t > 1/2 \end{cases}.$$

The following theorem provides a characterization of admissible weak solutions in the sense of distributions.

Theorem 1.1.1 (The Rankine-Hugoniot condition) *Assuming that the initial condition* $\boldsymbol{w_0} \in \mathbf{L}^{\infty}_{loc}(\mathbb{R}^d)^p$, *and* $\boldsymbol{w} : \mathbb{R}_+ \times \mathbb{R}^d \to \mathbb{R}^p$ *is a* $\mathbf{C}^1$ *solution except on a finite number of smooth orientable surfaces in the* ($\boldsymbol{x}$,t)*-space.*
Then, $\boldsymbol{w}$ *is a weak solution of (1.1) in the sense of distributions on* $\mathbb{R}_+ \times \mathbb{R}$ *if and only if the two following conditions are satisfied:*
(i) $\boldsymbol{w}$ *is a classical solution of (1.1) in the domains where* $\boldsymbol{w}$ *is* $\mathbf{C}^1$.
(ii) $\boldsymbol{w}$ *satisfies the jump conditions*

$$n_t(\boldsymbol{w}^+ - \boldsymbol{w}^-) + \sum_{j=1}^{d} \left[\boldsymbol{f_j}(\boldsymbol{w}^+) - \boldsymbol{f_j}(\boldsymbol{w}^-)\right] n_{x_j} = \mathbf{0}, \tag{1.3}$$

along the surfaces of discontinuity, where $\boldsymbol{n} = (n_t, n_{x_1}, ..., n_{x_d})$ *is the associated normal vector and*

$$\boldsymbol{w}^{\pm}(t,\boldsymbol{x}) = \lim_{\epsilon \to 0^+} \boldsymbol{w}((t,\boldsymbol{x}) \pm \epsilon \boldsymbol{n})$$

Note that in the case of a classical solution, the jump condition (ii) is obviously automatically satisfied. This theorem introduces a more advanced mathematical framework in which solutions can still be characterized even if they are prone to develop discontinuities. However, the uniqueness of the weak solution is not guaranteed in the absence of additional criteria. This can be easily understood by considering the initial condition

$$w_0(x) = \begin{cases} 0 & \text{if } x < 0 \\ 1 & \text{if } x > 0 \end{cases}.$$

Two potential solutions satisfying the theorem 1.1.1 exist, either a weak admissible solution corresponding to a propagating shock wave, or a classical solution corresponding to a rarefaction wave. Although, the continuous solution appears to be more natural, as suggested by the orientation of the characteristic curves in the smooth part of the domain.

1.1.2 . Entropic weak solutions

The preceding example has illustrated that the uniqueness of the solution is not guaranteed by theorem 1.1.1. An additional criterion is required. As demonstrated in [31, 36, 37], a mathematical approach for defining a criterion is to consider that the unique admissible solution to the problem should also be related in some sense to solutions as the limit of vanishing viscosity. Therefore, the relevant solution will be identified as the asymptotic limit of solutions to the following Cauchy problem

$$\begin{cases} \partial_t \boldsymbol{w_\epsilon} + \nabla_{\boldsymbol{x}} \cdot \boldsymbol{f}(\boldsymbol{w_\epsilon}) = \epsilon\, \Delta \boldsymbol{w_\epsilon} \\ \boldsymbol{w_\epsilon}(0,\boldsymbol{x}) = \boldsymbol{w_0}(\boldsymbol{x}) \end{cases}, \quad \text{for } \epsilon \to 0^+. \tag{1.4}$$

Definition 1.1.2 (Entropy function and entropy-fluxes) *A convex function $\eta : \mathbb{R}^d \to \mathbb{R}$ is called an entropy for the system of conservation laws (1.1) if there exist d functions $\xi_i : \mathbb{R}^d \to \mathbb{R}$, $1 \leq i \leq d$, called entropy fluxes, such that:*

$$\sum_{k=1}^{p} \partial_{w_k} \eta(\boldsymbol{w})\, \partial_{w_j} f_{i,k}(\boldsymbol{w}) = \partial_{w_j}\, \xi_i(\boldsymbol{w}), \qquad 1 \leq i \leq d \qquad 1 \leq j \leq p$$

The interest of such definition relies on the following characterization of the asymptotic limit of the solutions $\boldsymbol{w_\epsilon}$ of the viscous problem (1.4).

Theorem 1.1.2 (Characterization of viscous limit) *Let $\boldsymbol{w} \in \mathbf{L}^\infty_{loc}(\mathbb{R}_+ \times \mathbb{R}^d)^p$ be the limit, in the sense of distributions, of smooth viscous solutions of the problem (1.4) when $\epsilon \to 0^+$, in the sense that there exists $C > 0$ such that for all non negative ϵ, we have $||\boldsymbol{w_\epsilon}||_{L^\infty_{loc}(\mathbb{R}_+ \times \mathbb{R}^d)^p} \leq C$.*
Then, the solution $\boldsymbol{w}$ is a weak solution of (1.1), and, for all pairs $(\eta, \xi_1, ..., \xi_d)$ of entropy and entropy-fluxes (1.1.2), and for all positive functions $\varphi \in \mathbf{C}^1_0(\mathbb{R}_+ \times \mathbb{R}^d)^p$, the solution $\boldsymbol{w}$ also satisfies:

$$\int_0^\infty \int_{\mathbb{R}^d} \eta(\boldsymbol{w})\, \partial_t \boldsymbol{\varphi} + \sum_{i=1,d} \xi_i(\boldsymbol{w})\, \partial_{x_i} \boldsymbol{\varphi}\; dxdt \quad + \quad \int_{\mathbb{R}^d} \eta(\boldsymbol{w_0}(\boldsymbol{x}))\, \varphi(0, \boldsymbol{x})\, dx \geq 0$$

Since $\boldsymbol{w}$ is a weak solution, by integrating by part the above inequality, the next equation can be obtained:

$$\partial_t \eta(\boldsymbol{w}) + \sum_{i=1}^{d} \partial_{x_i} \xi_i(\boldsymbol{w}) \leq 0, \quad a.e.$$

Finally, weak entropy solutions are characterized by satisfying additional inequations for all entropy functions and entropy fluxes as defined in the definition 1.1.2. We shall no go any further into the details of the mathematical theory, as our objective, in the following sections, is to define and sufficiently characterize the approximated low Mach-number flow solutions with numerical schemes. However, for the sake of clarity, we will conclude this section with a final theorem summarizing the mathematical definition of solutions of interest. The well-posedness nature of these problems, concerning the existence and the uniqueness of weak entropy solution are subsequently not discussed in the remaining of this section. For a more extended introduction, the reader is referred to [31].

Theorem 1.1.3 (A weak entropy solution) *Assuming that the initial condition $\boldsymbol{w_0} \in \mathbf{L}^\infty_{loc}(\mathbb{R}^d)^p$, and $\boldsymbol{w} : \mathbb{R}_+ \times \mathbb{R}^d \to \mathbb{R}^p$ is a $\mathbf{C}^1$ solution except on a finite number of smooth orientable surfaces in the ($\boldsymbol{x}$,t)-space.*
Then, $\boldsymbol{w}$ is a weak entropy solution of (1.1) in the sense of distributions on $\mathbb{R}_+ \times \mathbb{R}^d$ if and only if the three following hold:
(i) $\boldsymbol{w}$ is a classical solution of (1.1) in the domains where $\boldsymbol{w}$ is $\mathbf{C}^1$.
(ii) $\boldsymbol{w}$ satisfies the jump conditions

$$n_t(\boldsymbol{w}^+ - \boldsymbol{w}^-) + \sum_{j=1}^{d} \left[\boldsymbol{f_j}(\boldsymbol{w}^+) - \boldsymbol{f_j}(\boldsymbol{w}^-)\right] n_{x_j} = \mathbf{0}, \tag{1.5}$$

along the surfaces of discontinuity, where $\boldsymbol{n} = (n_t, n_{x_1}, ..., n_{x_d})$ *is the associated normal vector and*

$$\boldsymbol{w}^{\pm}(\boldsymbol{x}, t) = \lim_{\epsilon \to 0^+} \boldsymbol{w}\big((\boldsymbol{x}, t) \pm \epsilon \boldsymbol{n}\big)$$

(iii) for all entropy and entropy-fluxes $(\eta, \xi_1, ..., \xi_d)$*, the inequality of jump conditions is satisfied:*

$$n_t\big(\eta(\boldsymbol{w}^+) - \eta(\boldsymbol{w}^+)\big) + \sum_{j=1}^{d} \left[\xi_j(\boldsymbol{w}^+) - \xi_j(\boldsymbol{w}^-\right] n_{x_j} \leq 0 \tag{1.6}$$

1.2 . The multidimensional compressible Euler equations for perfect gas

The following section introduces the compressible Euler equations in Eulerian coordinates. These equations correspond to a nonlinear system of conservation laws, describing the fundamental principles of mass, momentum, and total energy conservation for the dynamics of compressible, inviscid and adiabatic flows, excluding viscous effects. The scope of this Ph-D work intentionally excludes the compressible Navier-Stokes equations because viscous effects will not be considered in the asymptotic analysis in the low Mach number limit. The discrete analysis of compressible schemes in the low Mach number limit and the inherent accuracy and stability issues are related to the hyperbolic part of the Navier-Stokes equations. A direct confrontation with these equations introduces unnecessary complexity and raise questions concerning the interaction of the discretizations of the convective and viscous fluxes, which may not be readily apparent.

Let $\Omega \subset \mathbb{R}^d$ be an open and bounded set. The compressible Euler equations are formulated in the integral form as follows

$$\left| \begin{array}{l} \boldsymbol{w} : \mathbb{R}_+ \times \Omega \to \Omega^a \subset \mathbb{R}^{(2+d)} \\ \\ \boldsymbol{f}(\boldsymbol{w}) : \Omega^a \to \mathbb{R}^{(2+d)\times d} \end{array} \right. \qquad d_t \int_{\Omega} \boldsymbol{w}\, d\Omega + \int_{\partial\Omega} \boldsymbol{f}(\boldsymbol{w}) \cdot \boldsymbol{n}\, dS = \boldsymbol{0}, \tag{1.7}$$

where Ω^a is the set of admissible states that will be given below, $\boldsymbol{n}$ is the unit outward normal vector $\subset \mathbb{R}^d$, and the boundary of the domain is denoted by $\partial\Omega$. The conservative variables $\boldsymbol{w}$ and the flux function $\boldsymbol{f}(\boldsymbol{w})$ are given by:

$$\boldsymbol{w} = \begin{pmatrix} \rho \\ \rho\boldsymbol{\mathcal{U}} \\ \rho E \end{pmatrix} \qquad \boldsymbol{f}(\boldsymbol{w}) = \begin{pmatrix} \rho\boldsymbol{\mathcal{U}}^t \\ \rho\boldsymbol{\mathcal{U}} \otimes \boldsymbol{\mathcal{U}} + p\, \boldsymbol{I_d} \\ \rho\boldsymbol{\mathcal{U}}^t(E + \frac{p}{\rho}) \end{pmatrix}, \tag{1.8}$$

where ρ is the density, $\boldsymbol{\mathcal{U}}$ is the velocity vector, E is the specific energy, defined as the sum of the internal and kinetic energies $E = e + \frac{|\boldsymbol{\mathcal{U}}|^2}{2}$, with the specific internal energy denoted by e. The system is closed by considering the equation of state for a perfect gas expressed as

$$p = (\gamma - 1)\, \rho e, \tag{1.9}$$

where the ratio of specific heat γ is assumed constant and $\gamma > 1$. The speed of sound for a perfect gas is defined as:

$$c = \sqrt{\frac{\gamma p}{\rho}}. \tag{1.10}$$

In order to be consistent with the physics of fluids, in (1.8), the flow solution $\boldsymbol{w}$ is assumed to belong to the convex set of admissible states defined as:

$$\Omega^a = \left\{ \boldsymbol{w} \in \mathbb{R}^{2+d} \quad | \quad \rho > 0 \text{ and } e > 0 \right\}. \tag{1.11}$$

1.2.1 . Hyperbolicity

From a mathematical perspective, the compressible Euler equations (1.8) constitute a non-linear hyperbolic system of equations. The following section provides a brief overview of the considerations related to the hyperbolic theory. It is of particular interest to introduce the notations that will be used throughout the remainder of the manuscript. The notations are introduced as general as possible, with special interest on the one-dimensional "projected" compressible Euler equations, which are introduced below. This provides a relevant formalism, adapted to the introduction of numerical methods for the simulation of compressible flows in curvilinear meshes. The attention will be progressively drawn to Riemann solvers, and more precisely to approximate Riemann solvers, which are both studied with the hyperbolic theory.

Let us introduce the quasi-linear form of the compressible Euler equations to determine the characteristic structure of the equations. For smooth solutions, the conservative form reduces to

$$\partial_t \boldsymbol{w} + \nabla_{\boldsymbol{x}} \cdot \boldsymbol{f}(\boldsymbol{w}) \;=\; \partial_t \boldsymbol{w} + \sum_{j=1}^{d} \partial_{\boldsymbol{w}} \boldsymbol{f_j}\, \partial_{x_j} \boldsymbol{w} \;=\; \boldsymbol{0}, \tag{1.12}$$

where the expression of the flux function is given in (1.13). In the two-dimensional case, the quasi-linear form is based on the definitions of the two Jacobian matrices of the flux components

$$\boldsymbol{f_1}(\boldsymbol{w}) = \begin{pmatrix} \rho u \\ \rho u^2 + p \\ \rho u v \\ \rho u (E + \frac{p}{\rho}) \end{pmatrix} \qquad \text{and} \qquad \boldsymbol{f_2}(\boldsymbol{w}) = \begin{pmatrix} \rho v \\ \rho u v \\ \rho v^2 + p \\ \rho v (E + \frac{p}{\rho}) \end{pmatrix}. \tag{1.13}$$

Expressions of the corresponding Jacobian matrix are not explicitly written in this manuscript, but can be found in Toro's textbook [34].
In the context of multidimensional hyperbolic problems, it is often necessary to make a compromise with regard to the dimension, since these studies are commonly reformulated in the framework of one-dimensional problems. The reason lies in the fact that the two Jacobian matrices associated with the functions $\boldsymbol{f_1}(\boldsymbol{w})$ and $\boldsymbol{f_2}(\boldsymbol{w})$, do not have a common diagonalisation basis, and different eigenvalues. Consequently, the diagonalization of the system equations in the multidimensional case is not as straightforward as it would be in the scalar case.

A first approach commonly employed to circumvent this difficulty consists in studying the multidimensional Euler equations, introducing the projected equations over an arbitrary vector, as indicated in the following references [8, 31, 33].

Let us introduce $\boldsymbol{n} = (n_1, n_2)^T$, an arbitrary unit vector of $\mathbb{R}^2$, and define $\xi = \boldsymbol{x} \cdot \boldsymbol{n}$, the projected spatial variable onto the direction $\boldsymbol{n}$. The projected equations are simply formulated using the projected flux,

defined as $\boldsymbol{f}(\boldsymbol{w},\boldsymbol{n}) = \boldsymbol{f}(\boldsymbol{w})\cdot\boldsymbol{n}$, with respect to the new spatial variable ξ, as indicated next

$$\partial_t \boldsymbol{w} + \partial_\xi \boldsymbol{f}(\boldsymbol{w},\boldsymbol{n}) = \boldsymbol{0} \quad \text{with} \quad \boldsymbol{f}(\boldsymbol{w},\boldsymbol{n}) = \begin{pmatrix} \rho\mathcal{U}_n \\ \rho\boldsymbol{\mathcal{U}}\,\mathcal{U}_n + p\boldsymbol{n} \\ \rho\mathcal{U}_n(E+\dfrac{p}{\rho}) \end{pmatrix}. \tag{1.14}$$

where $\mathcal{U}_n = \boldsymbol{\mathcal{U}}\cdot\boldsymbol{n}$. Therefore, the quasi-linear form is defined as

$$\partial_t \boldsymbol{w} + \boldsymbol{A}(\boldsymbol{w},\boldsymbol{n})\,\partial_\xi \boldsymbol{w} = \boldsymbol{0} \quad \text{with} \quad \boldsymbol{A}(\boldsymbol{w},\boldsymbol{n}) = n_1\,\partial_x \boldsymbol{f_1}(\boldsymbol{w}) + n_2\,\partial_y \boldsymbol{f_2}(\boldsymbol{w}).$$

The interest of the projected equations is to get a one-dimensional problem (1.16) in which the definitions and properties of a scalar hyperbolic system of equations can be recovered. Under these considerations, it becomes possible to diagonalize the Jacobian matrix. Consequently, the multidimensional system (1.12) is said hyperbolic if and only if the one-dimensional projected equations are hyperbolic for any unit vector $\boldsymbol{n}$. For the compressible Euler equations, the matrix $\boldsymbol{A}(\boldsymbol{w},\boldsymbol{n})$ has $d+2$ real eigenvalues given by

$$\lambda_1(\boldsymbol{w},\boldsymbol{n}) = \mathcal{U}_n - c \qquad \lambda_2(\boldsymbol{w},\boldsymbol{n}) = \lambda_{d+1}(\boldsymbol{w},\boldsymbol{n}) = \mathcal{U}_n \qquad \lambda_{d+2}(\boldsymbol{w},\boldsymbol{n}) = \mathcal{U}_n + c\ , \tag{1.15}$$

which are indexed in an increasing order, and the corresponding eigenvectors are the vectors $(\boldsymbol{r_k})_{k=1,\dots,d+2}$, representing the columns of the matrix $\boldsymbol{R} = (\boldsymbol{r}_k(\boldsymbol{w},\boldsymbol{n}))_k$, form a basis of $\mathbb{R}^{d+2}$.

In the following sections, a special emphasis is put on the associated Riemann problems, formulated as follows

$$\begin{cases} \partial_t \boldsymbol{w} + \boldsymbol{A}(\boldsymbol{w},\boldsymbol{n})\,\partial_\xi \boldsymbol{w} = \boldsymbol{0} \\ \\ \boldsymbol{w}(0,\xi) = \begin{cases} \boldsymbol{w_l} \text{ if } \xi < 0 \\ \\ \boldsymbol{w_r} \text{ if } \xi > 0 \end{cases} \end{cases}, \tag{1.16}$$

since the solutions provided by these problems offer a valuable information, that can be used to introduce robust numerical shock-capturing methods, also known as approximate Riemann solvers, which are commonly encountered in the literature.
It can be demonstrated that these problems admit the existence of a unique solution, provided that the two initial states $\boldsymbol{w_l}$ and $\boldsymbol{w_r}$ are close in a special norm [31]. The solution of (1.16) will involve up to four constant states $(\boldsymbol{w_l}, \boldsymbol{w_l^*}, \boldsymbol{w_r^*}, \boldsymbol{w_r})$, where the two intermediate states $(\boldsymbol{w_l^*}, \boldsymbol{w_r^*})$ must be determined.

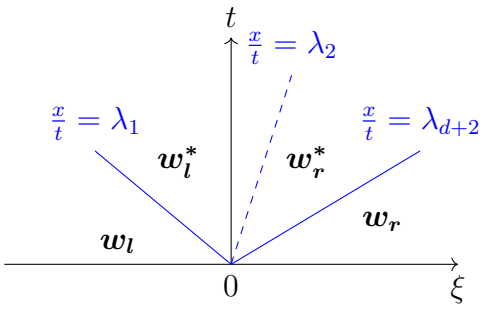

Figure 1.1: An example of solution for the Riemann problem associated with the Euler flux

As observed in the Fig. 1.1, the first and last waves, illustrated with blue solid curves, represent the truly nonlinear waves associated with the acoustic waves λ_1 and λ_{d+2}, similar to those observed in the

scalar case. These waves may consist in shock waves or in rarefaction waves depending on the initial states $(\boldsymbol{w_l}, \boldsymbol{w_r})$. In contrast, the intermediate waves, depicted by a dashed blue line, represent linearly degenerate fields, corresponding to simple waves resulting in contact discontinuities.
The exact solution can be computed using the approach described in [34]. However, due to the strong non-linearity of the flux function, the algorithm requires the application of Newton's methods.

1.2.2 . Compressibility and Mach number

The aim of this section is to introduce the Mach number, which is a fundamental dimensionless quantity characterizing the compressibility of the fluid. This can be formulated by considering the Euler equations

$$\begin{cases} \partial_t \rho & + \nabla_{\boldsymbol{x}} \cdot (\rho \boldsymbol{\mathcal{U}}) & = 0 \\ \partial_t (\rho \boldsymbol{\mathcal{U}}) & + \nabla_{\boldsymbol{x}} \cdot (\rho \boldsymbol{\mathcal{U}} \otimes \boldsymbol{\mathcal{U}}) + \nabla_{\boldsymbol{x}}\, p & = \mathbf{0} \\ \partial_t (\rho E) & + \nabla_{\boldsymbol{x}} \cdot \left(\rho \boldsymbol{\mathcal{U}} (E + \frac{p}{\rho}) \right) & = 0 \end{cases} . \tag{1.17}$$

As can be observed from the first equation, the absence of a free divergence constraint allows to the fluid to exhibit a variable density throughout the domain. Assuming smooth solutions, the continuity equation in (1.17) can be equivalently written as

$$-\frac{1}{\rho} \left(\partial_t \rho + \boldsymbol{\mathcal{U}} \cdot \nabla_{\boldsymbol{x}} \rho \right) = -\frac{1}{\rho}\, D_t \rho = \nabla_{\boldsymbol{x}} \cdot \boldsymbol{\mathcal{U}},$$

where D_t is the material derivative operator. It can be observed that, compressible flows exhibit a rate of change of density in response to the deformation of the fluid particle. This expression can be also associated to pressure disturbances, since the pressure and fluid density are related for compressible flows. Manipulating the continuity equation, the following relationship between the pressure and the velocity divergence can be derived

$$-\frac{1}{\rho c^2}\, D_t p = \nabla_{\boldsymbol{x}} \cdot \boldsymbol{\mathcal{U}}.$$

In the following, an appropriate scaling is employed to derive a local Mach number, as a scaling factor arising in the continuity equation. Introducing the following non-dimensional quantities

$$\hat{x} = \frac{x}{l_r} \qquad \hat{t} = \frac{u_r t}{l_r} \qquad \hat{\rho} = \frac{\rho}{\rho_r} \qquad \hat{\boldsymbol{\mathcal{U}}} = \frac{\boldsymbol{\mathcal{U}}}{u_r} \qquad \hat{p} = \frac{p}{\rho_r u_r^2},$$

where (l_r, t_r) are respectively a characteristic length and a characteristic time scale, and the other characteristic quantities are defined for instance as the maximum of the values in the fluid domain, with $\rho_r = \max_{\boldsymbol{x}} \rho$ and $u_r = \max_{\boldsymbol{x}} |\boldsymbol{\mathcal{U}}|$. Consequently, the non-dimensional form of the continuity equation written for the pressure is formulated as follows

$$-M^2\, \frac{1}{\hat{\rho}}\, D_{\hat{t}}\, \hat{p} = \nabla_{\hat{\boldsymbol{x}}} \cdot \hat{\boldsymbol{\mathcal{U}}}, \tag{1.18}$$

introducing in particular the following local Mach number M, defined as $M = u_r/c$, as weight of the material derivative associated to the pressure. As the local Mach number decreases, the compressibility asymptotically vanishes as the left-hand side of the equation goes to zero. Then, a free divergence constraint is found in the low Mach number limit, using this formal scaling.

In contrast to compressible flows equations, the incompressible Euler equations for a fluid with a constant density are formulated as follows

$$\begin{cases} \nabla_{\boldsymbol{x}} \cdot \boldsymbol{\mathcal{U}} & = 0 \\ \rho\Big(\partial_t(\boldsymbol{\mathcal{U}}) + (\boldsymbol{\mathcal{U}} \cdot \nabla_{\boldsymbol{x}})\, \boldsymbol{\mathcal{U}}\Big) + \nabla_{\boldsymbol{x}} p & = \mathbf{0} \\ \rho & = \text{cst} \end{cases} . \tag{1.19}$$

Note that, the pressure remains independent of the fluid density and is only related to the free divergence constraint. These equations are different of the compressible formulation, in terms of modeling but also in terms of mathematical properties. This latter point will be discussed in the two following sections.

1.3 . A review of the behavior of compressible solutions for low-speed flows

The gas dynamic equations introduced in section 1.2 for a perfect gas (1.9) enable the modeling of a large range of physical flow features, depending on the effects of the compressibility of the flow. The description of the compressibility of the flow is characterized by the Mach number, a fundamental quantity defined as a dimensionless ratio of the convective speed and the speed of sound. Based on the value of the Mach number, it is of common practice to categorize compressible flows into at least three distinct regimes. For $M < 0.8$, the flow is subsonic, and numerical solutions can be considered as smooth. For $0.8 < M < 1.2$, the flow is transonic. Here, for the sake of brevity, higher Mach number flows (i.e. $M > 1.2$) will be classified as supersonic.

The main concern of this work, is mainly related to weakly compressible flows in the subsonic and low Mach number regimes. These flows have the advantage of exhibiting relatively predictable behavior, characterized by moderate velocity and pressure gradients. Compressible effects are not sufficiently significant to trigger shock waves for this flows. As a consequence, the fluid exhibits a continuous evolution of physical quantities.
In the following, we shall give a particular interest to low-speed flows, which are typically characterized by lower Mach numbers such as $M < 0.3$. For many decades, low-speed flows have raised profound questions concerning the gap between two theoretical frameworks: the incompressible flows theory and the compressible flows theory. Indeed, as the Mach number decreases, the velocity also decreases, resulting in smaller disturbances of the divergence of the fluid particles. This is illustrated by the normalized equation (1.18), which allows low-speed flows to be interpreted as almost incompressible flows.
Two significant and closely related issues, in the study of low Mach number flows, originates from this observation. First, in what sense compressible solutions are related to incompressible solutions in the low Mach-number limit? This question has notably motivated the development of a mathematical theory, also known as low Mach number flows theory, which attempts to describe the asymptotic behavior of the compressible solution [8, 38–42].
The second issue is related to the discretization of the compressible equations, for the simulation of weakly compressible flows with compressible numerical methods, such as Riemann solvers. Indeed, in general, the simulation of low Mach number flows requires a particular attention since Riemann solvers are not able to provide accurate results (see for instance [6, 7]). The discrete compressible solutions may even be inconsistent, since they do not recover incompressible flow features, as it will be illustrated in the following chapters. This thesis addresses the second issue.
The objective of the next section is threefold. The initial objective is to discuss some of the common methods used for the discretization of compressible flows in the low Mach-number range. Next, the

significant mathematical discrepancies between the two systems of fluid equations will be reminded. Finally, the asymptotic behavior of the exact solution of the compressible Euler equations in the low Mach-number limit will be presented.

A first approach to deal with low Mach number flows relies on simplifying the governing set of equations by deriving reduced models, as indicated for instance in the first chapter of the Viozat's thesis [43]. In general, this approach provides simpler models that are easier to analyze and simulate, but is specifically restricted to low-speed flows. Note that, this approach is discussed here, but not retained in this work.
A second approach, as indicated in some textbooks (see, for instance [44,45]), consists in approximating low Mach number flows by the incompressible equations. This results in a sudden change in the governing fluid equations and leads to neglecting the extremely small disturbances in the divergence of fluid velocities. From a practical standpoint, the incompressible model offers significant advantages without compromising accuracy, with respect to the aerodynamic coefficients considered [45]. It is interesting to see that numerous authors have investigated the legitimacy of such assumption. From a mathematical point of view, does the compressible solution converge to the incompressible one when the Mach tends to zero?

In order to initiate the discussion, some fundamental differences in the natures of the two fluid equations are reminded, as the two pressure fields cannot be easily reconciled in their mathematical interpretation. As previously mentioned, the set of the compressible fluid equations (1.17) is an hyperbolic system of conservation laws. The pressure and density terms are related to acoustics, as they may produce small fluctuations propagating in the field at a different speed. For the normalized Euler equations, as the Mach number decreases, the speed of sound increases. Then, the two acoustic eigenvalues λ_1 and λ_{d+2}, defined as $\mathcal{U}_n \pm c$, go to infinity when $M \to 0$. This indicates that, in the low Mach number limit, the compressible equations (1.17) are no longer hyperbolic, and thus admit a singular limit.
In opposition to the compressible equations (1.17), the incompressible equations (1.19) are characterized by a constant density throughout the domain, with especially a pressure field defined as the Lagrange multiplier associated to the free-divergence constraint [46]. As it will be shown in the next section, this incompressible pressure is solution of an elliptic equation.
In order to introduce efficient numerical methods approximating the continuous solution, it is necessary to give some mathematical insight, illustrating the behavior of the compressible solutions in the low Mach number limit. The remainder of this section is devoted to that purpose.

The second chapter of Madja's book [8] relates the works of numerous authors, including Madja and Klainerman, providing a thorough overview of the complexities involved in the theoretical analysis of exact compressible solutions. A normalization process for the barotropic Euler equations is employed to formally establish the mathematical relationship between compressible and incompressible solutions. Barotropic flows have the advantage of modeling the pressure as function of the density only, as indicated by the corresponding equation of state

$$p = A\rho^{\gamma} \qquad \text{with A} > 0\text{, a scalar coefficient.}$$

The normalized compressible fluid equations are then formulated for the two normalized pressure and velocity variables $(p,\boldsymbol{\mathcal{U}})$ as follows

$$\begin{cases} \dfrac{1}{\gamma p^{\lambda}}\, D_t p^{\lambda} + \nabla \boldsymbol{\mathcal{U}}^{\boldsymbol{\lambda}} = 0 \\ \rho^{\lambda}\, D_t \boldsymbol{\mathcal{U}}^{\boldsymbol{\lambda}} + \lambda^2 \nabla p^{\lambda} = \mathbf{0} \end{cases}. \quad \text{where} \quad \lambda = \frac{1}{M\sqrt{\gamma A}},$$

where the exponents λ denotes the dependence of the solution in λ which now acts as a parameter, with the initial condition

$$p^\lambda(0,\boldsymbol{x}) = p_0^\lambda(\boldsymbol{x}) \qquad\qquad \boldsymbol{\mathcal{U}^\lambda}(0,\boldsymbol{x}) = \boldsymbol{\mathcal{U}_0^\lambda}(\boldsymbol{x}).$$

Assuming that the normalized solution $(p^\lambda, \boldsymbol{\mathcal{U}^\lambda})$ can be expanded in an asymptotic expansion in power of λ, Majda performed an asymptotic analysis of the compressible solution. This analysis shows that the incompressible Euler equations have solutions which approximate solutions of the compressible Euler equations provided that the Mach number is small. It has been demonstrated that, for well-chosen initial conditions, belonging to a specific class of well-prepared initial conditions [8, 10]

$$\begin{cases} p_0^\lambda(\boldsymbol{x}) = P_0 + O(\frac{1}{\lambda^2})(x) \\ \\ \boldsymbol{\mathcal{U}_0^\lambda}(\boldsymbol{x}) = \boldsymbol{\mathcal{U}_0^\infty}(\boldsymbol{x}) + O(\frac{1}{\lambda})(x) \end{cases} \quad \text{with} \quad \begin{cases} \nabla \cdot \boldsymbol{\mathcal{U}_0^\infty} = 0 \\ \\ P_0 = \text{cst} \end{cases}.$$

Then, the existence of incompressible solutions can be obtained by passing to the limit the compressible solutions $(p^\lambda, \boldsymbol{\mathcal{U}^\lambda})$ for a vanishing Mach number (Theorem 2.4) (i.e. $\lambda \to +\infty$). However, this result describes the behavior of the leading-order term of the compressible solution in the formal asymptotic analysis. For higher order terms, the correct asymptotic expansion of compressible solution exhibits a more complex behavior, which contains a fast scale component (Theorem 2.5). Madja explicitly wrote the symbolic decomposition to illustrate the following behavior of the compressible solution in the low Mach number limit:

$$\{\text{Comp. Euler eq.}\} \quad = \quad \{\text{Incomp. Euler eq.}\} \quad + \quad M\,\{\text{Linear acoustic eq.}\} \quad + \quad \mathcal{O}(M^2)$$

This symbolic decomposition, along with the associated theoretical insights, clarifies the implications of replacing the compressible fluid equations with their incompressible counterparts.

Another interesting discussion can be found in the review of Guillard-Nkonga [9]. It is stated that most of the theoretical analyses and results published in the literature generally concern simplified equation of states, such as the barotropic gas previously mentioned. However, there are some mathematical evidence demonstrating that, in the low Mach number limit, the compressible solution cannot be directly identified as the solution of the incompressible equations. The solution appears to be, at least, decomposed as a sum of a fast acoustic component and a slow component solution of the incompressible equations. The authors have presented a founded discussion of this subject, which is worth of being reported hereafter.
An important literature has been dedicated to this topic. It appears that this decomposition is related to the complex behavior of the compressible models in the low Mach number regime. The crucial point to understand is that, in general, the strong limit solution of the compressible Euler (or Navier-Stokes) model is not described by the corresponding incompressible equations. In the case of barotropic flows, the functional analysis shows that two limits exist, representing two very different systems from a mathematical point of view. At the incompressible time-scale, based on the flow velocity, the incompressible system is elliptic in nature, and thus represents a singular limit since the mathematical nature of the system changes from hyperbolic to elliptic. While at the acoustic time scale, based on the speed of sound, the acoustic system is hyperbolic and describes the propagation of acoustic waves. Both limits are relevant, and numerical experiments (as illustrated later in chapter 3) show that we have at the same time incompressible and acoustic phenomena. In the physical world, the two limits co-exist and superpose.

1.4 . Formal derivations of the asymptotic behavior of the continuous solutions in the low Mach number limit

A normalization process is a particular type of dimensionless scaling, using some specific relationships between the reference quantities. The normalization process aims at making all physical terms of the same order of magnitude (of the order of unity), characterizing the respective weight of these different terms by the occurrence of scaling coefficients, as factors of the different normalized physical terms. In this section, we discuss two normalizations of the compressible Euler equations, corresponding either on a convective time scale, or on an acoustic time scale. Note that the two time scales could be combined into a single analysis. However, in the following, for the sake of clarity, a single-time-scale asymptotic analysis is conducted for each of these two aforementioned normalization processes, as done in [7,47].

1.4.1 . Normalisation for the incompressible time scale

The analysis is carried out starting from the conservative form of the Euler equations. In the following, for each physical quantity q, a reference quantity is introduced q_r and the associated dimensionless quantity will be denoted as $\hat{q}$ such as the following equality holds $q = \hat{q}q_r$. The divergence and gradient operator are replaced using $\nabla = \hat{\nabla}/l_r$, where l_r is the reference length and the time derivative is reformulated upon substitution $\partial_t = \frac{\partial_{\hat{t}}}{t_r}$, with t_r being the reference time. After simplifications, the non-dimensional Euler equations can be expressed as follows

$$\begin{cases} \left(\frac{l_r}{t_r u_r}\right)\partial_{\hat{t}}\hat{\rho} & + \nabla_{\hat{\boldsymbol{x}}}\cdot(\hat{\rho}\hat{\boldsymbol{\mathcal{U}}}) & = 0 \\ \left(\frac{l_r}{t_r u_r}\right)\partial_{\hat{t}}(\hat{\rho}\hat{\boldsymbol{\mathcal{U}}}) & + \nabla_{\hat{\boldsymbol{x}}}\cdot(\hat{\rho}\hat{\boldsymbol{\mathcal{U}}}\otimes\hat{\boldsymbol{\mathcal{U}}}) + \left(\frac{p_r}{\rho_r u_r^2}\right)\nabla_{\hat{\boldsymbol{x}}}\,\hat{p} & = \mathbf{0} \\ \left(\frac{l_r}{t_r u_r}\right)\left(\frac{E_r}{H_r}\right)\partial_{\hat{t}}(\hat{\rho}\hat{E}) & + \nabla_{\hat{\boldsymbol{x}}}\cdot\left(\hat{\rho}\hat{\boldsymbol{\mathcal{U}}}\hat{H}\right) & = 0 \end{cases} \tag{1.20}$$

where ρ_r, u_r, p_r are the reference quantities for the primitive variables and E_r, H_r are respectively reference quantities for the specific total energy and enthalpy $H = E + \frac{p}{\rho}$.

As mentioned before, the normalization process requires all normalized quantities to be of the same order of magnitude, of the order of unity. The following results are known from asymptotic theory [11,48]

$$\rho \simeq \mathcal{O}(1), \quad c \simeq \mathcal{O}(\frac{1}{M}), \quad \text{when} \quad M \to 0.$$

Assuming perfect gas, the gradient of pressure field behaves as follows

$$p \simeq \rho c^2 \simeq \mathcal{O}(\frac{1}{M^2}) \quad \text{and} \quad \nabla p \simeq \mathcal{O}(\frac{1}{M^2}) \quad \text{as} \quad M \to 0. \tag{1.21}$$

Thus, the pressure gradient is the dominating term of the equations. This asymptotic behavior can be reproduced in the normalization process. In this framework analysis, the reference quantities must verify certain relationships, as described below. An asymptotic reference state is defined from a density ρ_∞, a velocity u_∞, a reference sound velocity c_∞ independent of u_∞ and a reference length l_r. The reference quantities are then introduced with the following definitions

$$\begin{aligned} &\rho_r = \rho_\infty, \qquad u_r = u_\infty, \qquad c_r = c_\infty, \qquad p_r = \rho_r c_r^2, \qquad t_r = \frac{l_r}{u_r} \\ \implies \qquad &p_r = \rho_\infty c_\infty^2 \qquad \text{and} \qquad t_r = \frac{l}{u_\infty}. \end{aligned} \tag{1.22}$$

Then

$$\frac{l_r}{t_r u_r} = 1, \qquad \frac{p_r}{\rho_r u_r^2} = \frac{c_\infty^2}{u_\infty^2} = \frac{1}{M_\infty^2}.$$

Next, we also demand that the normalized total specific enthalpy returns to the same formulation as for the original equations with $H = E + \frac{p}{\rho}$. So, considering $H = \hat{H} H_r$, we get

$$\hat{H} = \left(\frac{H_r}{E_r}\right) \hat{E} + \left(\frac{p_r}{\rho_r H_r}\right) \frac{\hat{p}}{\hat{\rho}}. \tag{1.23}$$

Therefore, the following relationship must be satisfied for the reference quantities

$$E_r = H_r \qquad \text{and} \qquad H_r = \frac{p_r}{\rho_r} = c_\infty^2. \tag{1.24}$$

With the choice of reference quantities (1.22) and (1.24), we can see that

$$\hat{\rho} = \frac{\rho}{\rho_\infty} \simeq \mathcal{O}(1), \quad \hat{\boldsymbol{\mathcal{U}}} = \frac{\boldsymbol{\mathcal{U}}}{u_\infty} \simeq \mathcal{O}(1), \quad \hat{p} = \frac{p}{\rho_\infty c_\infty^2} \simeq \mathcal{O}(1), \quad \hat{H} = \frac{H}{c_\infty^2} \simeq \mathcal{O}(1) \text{ when } M_\infty \to 0. \tag{1.25}$$

By comparing the orders of magnitude of the various terms in the limit $M_\infty \to 0$, we also see that

$$\begin{cases} \underbrace{\partial_{\hat{t}} \hat{\rho}}_{\mathcal{O}(1)} + \underbrace{\nabla_{\hat{\boldsymbol{x}}} \cdot (\hat{\rho} \hat{\boldsymbol{\mathcal{U}}})}_{\mathcal{O}(1)} = 0, \\ \underbrace{\partial_{\hat{t}} (\hat{\rho} \hat{\boldsymbol{\mathcal{U}}})}_{\mathcal{O}(1)} + \underbrace{\nabla_{\hat{\boldsymbol{x}}} \cdot \left(\hat{\rho} \hat{\boldsymbol{\mathcal{U}}} \otimes \hat{\boldsymbol{\mathcal{U}}}\right)}_{\mathcal{O}(1)} + \frac{1}{M_\infty^2} \underbrace{\nabla_{\hat{\boldsymbol{x}}} \hat{p}}_{\mathcal{O}(1)} = \mathbf{0}, \\ \underbrace{\partial_{\hat{t}} (\hat{\rho} \hat{E})}_{\mathcal{O}(1)} + \underbrace{\nabla_{\hat{\boldsymbol{x}}} \cdot \left(\hat{\rho} \hat{\boldsymbol{\mathcal{U}}} \hat{H}\right)}_{\mathcal{O}(1)} = 0, \end{cases} \tag{1.26}$$

Therefore, in the momentum equation, we can clearly see that, in the asymptotic limit, the pressure gradient becomes a dominant term over all other terms, and particularly over the convection

$$\frac{1}{M_\infty^2} \hat{\nabla} \hat{p} \simeq \mathcal{O}(\frac{1}{M_\infty^2}) >> \hat{\nabla} \cdot (\hat{\rho} \hat{\boldsymbol{\mathcal{U}}} \otimes \hat{\boldsymbol{\mathcal{U}}}) \simeq \mathcal{O}(1) \quad \text{when} \quad M_\infty \to 0.$$

We can also observe that the normalized equation of state for pressure is no longer expressed exactly as for the closure of the original equations

$$p = (\gamma - 1) \rho e = (\gamma - 1) \rho \left[E - \frac{|\boldsymbol{\mathcal{U}}|^2}{2} \right]. \tag{1.27}$$

Indeed, normalizing the equation of state with the same reference quantities, we have

$$\hat{p} \;=\; (\gamma - 1) \left(\frac{\rho_r}{p_r}\right) \hat{\rho} \left[\hat{E}_r E - u_r^2 \frac{|\hat{\boldsymbol{\mathcal{U}}}|^2}{2} \right].$$

Then

$$\hat{p} \;=\; (\gamma - 1) \hat{\rho} \left[\hat{E} - M_\infty^2 \frac{|\hat{\boldsymbol{\mathcal{U}}}|^2}{2} \right], \tag{1.28}$$

since $E_r = H_r = \frac{p_r}{\rho_r}$, then $\frac{\rho_r E_r}{p_r} = 1$ and thus $\frac{\rho_r u_r^2}{p_r} = M_\infty^2$. Another consequence of normalization (1.26) is that the normalized aerodynamic variables (density, velocity, pressure) depend explicitly on

the reference Mach number M_∞. So the solutions to this system of normalized equations have to be found in the form of asymptotic expansions in powers of M_∞

$$\left\{\begin{array}{rcl} \hat{\rho}(\hat{t},\hat{\boldsymbol{x}}) & = & \hat{\rho}_0(\hat{t},\hat{\boldsymbol{x}}) + \hat{\rho}_1(\hat{t},\hat{\boldsymbol{x}})M_\infty + \hat{\rho}_2(\hat{t},\hat{\boldsymbol{x}})M_\infty^2 + \mathcal{O}(M_\infty^3) \\ \hat{\boldsymbol{\mathcal{U}}}(\hat{t},\hat{\boldsymbol{x}}) & = & \hat{\boldsymbol{\mathcal{U}}}_0(\hat{t},\hat{\boldsymbol{x}}) + \hat{\boldsymbol{\mathcal{U}}}_1(\hat{t},\hat{\boldsymbol{x}})M_\infty + \hat{\boldsymbol{\mathcal{U}}}_2(\hat{t},\hat{\boldsymbol{x}})M_\infty^2 + \mathcal{O}(M_\infty^3) \\ \hat{p}(\hat{t},\hat{\boldsymbol{x}}) & = & \hat{p}_0(\hat{t},\hat{\boldsymbol{x}}) + \hat{p}_1(\hat{t},\hat{\boldsymbol{x}})M_\infty + \hat{p}_2(\hat{t},\hat{\boldsymbol{x}})M_\infty^2 + \mathcal{O}(M_\infty^3) \end{array}\right. \tag{1.29}$$

It has been shown in [43, 47], by replacing the primitive variables into the system of normalized equations (1.26) by these asymptotic expansions, and comparing the terms according to the different orders of magnitude in these developments, that the pressure field is characterized by

$$\nabla_{\hat{\boldsymbol{x}}}\,\hat{p}_0 = \mathbf{0} \text{ at order } \mathcal{O}(\frac{1}{M_\infty^2}) \quad \text{and} \quad \nabla_{\hat{\boldsymbol{x}}}\,\hat{p}_1 = \mathbf{0} \text{ at order } \mathcal{O}(\frac{1}{M_\infty}),$$

and, at order $\mathcal{O}(1)$, the system reduces to the following set of incompressible equations

$$\left\{\begin{array}{l} \nabla_{\hat{\boldsymbol{x}}}\cdot\hat{\boldsymbol{\mathcal{U}}}_0 = 0 \\ \hat{\rho}_0\left[\partial_{\hat{t}}\,\hat{\boldsymbol{\mathcal{U}}}_0 + \nabla_{\hat{\boldsymbol{x}}}\cdot\left(\hat{\boldsymbol{\mathcal{U}}}_{\mathbf{0}}\otimes\hat{\boldsymbol{\mathcal{U}}}_{\mathbf{0}}\right)\right] + \nabla_{\hat{\boldsymbol{x}}}\,\hat{p}_2 = \mathbf{0} \\ \hat{\rho}_0 = cst \end{array}\right. . \tag{1.30}$$

Therefore, it can be stated that $\hat{p}_0$ and $\hat{p}_1$ are only functions of time and then, the normalized pressure is constant in space up to a fluctuation of order M_∞^2, with

$$\hat{p}(\hat{t},\hat{\boldsymbol{x}}) = \hat{p}_0(\hat{t}) + \hat{p}_1(\hat{t})M_\infty + \hat{p}_2(\hat{t},\hat{\boldsymbol{x}})M_\infty^2 + \mathcal{O}(M_\infty^3), \tag{1.31}$$

where $\hat{p}_0(\hat{t})$ is the ambient thermodynamic pressure and $\hat{p}_2(\hat{t},\hat{\boldsymbol{x}})$ represents the incompressible pressure disturbances. This fundamental behavior of the pressure field must be reproduced in the incompressible limit at the discrete level. Additionally, the incompressible pressure is the solution of an elliptic equation, since, by taking the divergence of the second equation in (1.30), and using $\nabla_{\hat{\boldsymbol{x}}}\cdot\hat{\boldsymbol{\mathcal{U}}}_0 = 0$, we see that $\hat{p}_2$ is the solution of a Poisson-like equation

$$\Delta_{\hat{\boldsymbol{x}}}\,\hat{p}_2 = -\hat{\rho}_0\nabla_{\hat{\boldsymbol{x}}}\cdot\left[\nabla_{\hat{\boldsymbol{x}}}\cdot\left(\hat{\boldsymbol{\mathcal{U}}}_{\mathbf{0}}\otimes\hat{\boldsymbol{\mathcal{U}}}_{\mathbf{0}}\right)\right].$$

This shows that the incompressible equations (1.30) are also elliptic in nature, representing therefore a singular limit in contrast to the compressible system, of hyperbolic nature.

1.4.2 . Normalization for the acoustic time scale

The accoustic normalization is defined from a reference time based on the speed of sound. So in the definitions (1.22), we set $t_r = \frac{l_r}{c_\infty}$. Therefore, equations (1.20) take the following normalized form

$$\left\{\begin{array}{l} \frac{1}{M_\infty}\partial_{\hat{t}}\hat{\rho} + \nabla_{\hat{\boldsymbol{x}}}\cdot(\hat{\rho}\hat{\boldsymbol{\mathcal{U}}}) = 0 \\ \frac{1}{M_\infty}\partial_{\hat{t}}(\hat{\rho}\hat{\boldsymbol{\mathcal{U}}}) + \nabla_{\hat{\boldsymbol{x}}}\cdot\left(\hat{\rho}\hat{\boldsymbol{\mathcal{U}}}\otimes\hat{\boldsymbol{\mathcal{U}}}\right) + \frac{1}{M_\infty^2}\nabla_{\hat{\boldsymbol{x}}}\,\hat{p} = \mathbf{0} \\ \frac{1}{M_\infty}\partial_{\hat{t}}(\hat{\rho}\hat{E}) + \nabla_{\hat{\boldsymbol{x}}}\cdot\left(\hat{\rho}\hat{\boldsymbol{\mathcal{U}}}\hat{H}\right) = 0 \end{array}\right. . \tag{1.32}$$

By inserting the expansions (1.29) into this system and by comparing the terms according to the different orders of magnitude, we find that

$$\nabla_{\hat{\boldsymbol{x}}}\,\hat{p}_0 = \mathbf{0} \text{ at order } \mathcal{O}(\frac{1}{M_\infty^2}), \tag{1.33}$$

but, at order $\mathcal{O}(\frac{1}{M_\infty})$, we get the following system

$$\begin{cases} \partial_{\hat{t}}\,\hat{\rho}_0 = 0 \\ \partial_{\hat{t}}(\hat{\rho}_0\hat{\boldsymbol{\mathcal{U}}}_0) + \nabla_{\hat{\boldsymbol{x}}}\,\hat{p}_1 = \mathbf{0} \\ \partial_{\hat{t}}\,(\hat{\rho}_0\hat{E}_0) = 0 \end{cases}, \tag{1.34}$$

while, at order $\mathcal{O}(1)$

$$\begin{cases} \partial_{\hat{t}}\,\hat{\rho}_1 + \nabla_{\hat{\boldsymbol{x}}}(\hat{\rho}_0\hat{\boldsymbol{\mathcal{U}}}_0) = 0 \\ \partial_{\hat{t}}(\hat{\rho}\hat{\boldsymbol{\mathcal{U}}})^{[1]} + \nabla_{\hat{\boldsymbol{x}}}\cdot\left(\hat{\rho}_0\hat{\boldsymbol{\mathcal{U}}}_{\mathbf{0}}\otimes\hat{\boldsymbol{\mathcal{U}}}_{\mathbf{0}}\right) + \nabla_{\hat{\boldsymbol{x}}}\,\hat{p}_2 = \mathbf{0} \\ \hat{\partial}_{\hat{t}}\,(\hat{\rho}\hat{E})^{[1]} + \nabla_{\hat{\boldsymbol{x}}}\cdot\left(\hat{\rho}_0\hat{\boldsymbol{\mathcal{U}}}_0\hat{H}_0\right) = 0 \end{cases}. \tag{1.35}$$

In this system, the shorthand notation of Rieper [25] has been used and reads for the momentum equation $(\hat{\rho}\hat{\boldsymbol{\mathcal{U}}})^{[1]} = (\hat{\rho}\hat{\boldsymbol{\mathcal{U}}})_0 + (\hat{\rho}\hat{\boldsymbol{\mathcal{U}}})_1$, whereas for the energy equation $(\hat{\rho}\hat{E})^{[1]} = \hat{\rho}_0\hat{E}_1 + \hat{E}_0\hat{\rho}_1$.
So for this acoustic time scale, the 0-state leading-order pressure $\hat{p}_0$, is constant in space (1.33) and also in time (1.34) since

$$\hat{p}_0 = (\gamma-1)\hat{\rho}_0\hat{E}_0.$$

Then, the pressure field is only constant up to a fluctuation in space at the first order at the acoustic time scale

$$\hat{p}(\hat{t},\hat{\boldsymbol{x}}) = \hat{p}_0 + \hat{p}_1(\hat{t},\hat{\boldsymbol{x}})M_\infty + \mathcal{O}(M_\infty^2). \tag{1.36}$$

From the normalized equation of state (1.28), a constant leading order $\hat{p}_0$ in space also entails the product $\hat{\rho}_0\hat{E}_0$ to be constant in space. Next, to simplify the analysis, we assume that the leading-order density $\hat{\rho}_0$ is constant in space (i.e. $\nabla_{\hat{\boldsymbol{x}}}\hat{\rho}_0 = 0$), as commonly done in the literature (see for instance [7, 9, 25]). Then, the leading-order total enthalpy is also constant in space

$$\nabla_{\hat{\boldsymbol{x}}}\hat{H}_0 = 0 \quad \text{since} \quad \hat{H}_0 = \hat{E}_0 + \frac{\hat{p}_0}{\hat{\rho}_0}.$$

Therefore, at the order $\mathcal{O}(1)$, the energy equation in (1.35) can be simplified and formulated for the first-order pressure term $\hat{p}_1$. Using the definitions of the above leading-order enthalpy $\hat{H}_0$, we get

$$\partial_{\hat{t}}\hat{p}_1 + \hat{c}_0^2\,\nabla_{\hat{\boldsymbol{x}}}\cdot\left(\hat{\rho}_0\hat{\boldsymbol{\mathcal{U}}}_0\right) = 0, \tag{1.37}$$

since $\hat{p}_1 = (\gamma-1)(\hat{\rho}\hat{E})^{[1]}$ and $\hat{H}_0 = \hat{c}_0^2/(\gamma-1)$, with $\hat{c}_0$ being to the ambient surrounding speed of sound. An interesting result can be expressed by taking the divergence of the second equation of the system (1.34), and using (1.37). Then, we see that the normalized disturbance pressure at order $\mathcal{O}(\infty)$, $\hat{p}_1$ verifies the following linear wave equation (second-order hyperbolic)

$$\frac{\partial^2\hat{p}_1}{\partial\hat{t}^2} - \hat{c}_0^2\,\hat{\nabla}^2\hat{p}_1 = 0. \tag{1.38}$$

Thus, we find that the system (1.34) with equation (1.37) is hyperbolic in nature. Moreover, at the acoustic time scale, it can be observed that the normalized pressure is characterized by an acoustic fluctuation (1.36) of an order of magnitude greater than the incompressible pressure fluctuation (1.31).

1.5 . The finite volume method

In this section, we briefly introduce the computational framework used to discretize the compressible Euler equations. We have considered a two-dimensional cell-centered finite volume-method, first implemented in a existing research code used throughout this Ph-D work. As discussed in the following, finite-volume methods offer a robust formulation particularly suited to the approximation of hyperbolic systems of conservation laws. Finite-volume methods are discrete approximations based on the integral form of the equations (1.7) in the fluid domain, described by local balance equations and flow exchanges in each cell of the computational domain.

Let's introduce a mesh discretizing the fluid domain $\Omega = \bigcup_I \Omega_I$. By integrating the conservation laws (1.1) on each cell Ω_I, we get:

$$|\Omega_I|\, d_t(\boldsymbol{w_I}(t)) + \int_{\partial\Omega_I} \boldsymbol{f}(\boldsymbol{w}) \cdot \boldsymbol{n}\; dS = \boldsymbol{0}. \quad \text{with} \quad \boldsymbol{w_I}(t) = \frac{1}{|\Omega_I|}\int_{\Omega_I} \boldsymbol{w}(t,\boldsymbol{x})\, d\Omega,$$

where $\partial\Omega_I$ denotes the boundary of cell Ω_I, and $|\Omega_I|$ is a d-dimensional measure of Ω_I. The discrete solution is assumed to be a piecewise constant approximation of $\boldsymbol{w_I}$ in each computational cell, denoted as $\boldsymbol{W_I}(t)$ in cell Ω_I. The flux $\boldsymbol{f}(\boldsymbol{w})$ at interfaces is not uniquely defined and is thus approximated by a numerical flux $\boldsymbol{\mathcal{F}}$, function of the two constant approximations $\boldsymbol{W_I}$ and $\boldsymbol{W_J}$ and the unit normal vector $\boldsymbol{n}$

$$\boldsymbol{\mathcal{F}}\big(\boldsymbol{W_I}(t), \boldsymbol{W_J}(t), \boldsymbol{n_{IJ}}\big),$$

where the vector $\boldsymbol{n_{IJ}}$ is the unit outward normal vector at the cell interfaces $\Omega_I \cap \Omega_J$ pointed towards the neighboring cells Ω_J, and $\mathcal{V}(I)$ is the set of the indices J of neighboring cells to Ω_I. The expression of numerical flux balance can be simplified by introducing δ_{IJ}, the measure of the interface $\Omega_I \cap \Omega_J$. This leads to the well known formulation of the semi-discretized scheme in space as formulated with

$$|\Omega_I|\, d_t(\boldsymbol{W_I}(t)) + \sum_{J\in\mathcal{V}(I)} \delta_{IJ}\boldsymbol{\mathcal{F}}\big(\boldsymbol{W_I}(t), \boldsymbol{W_J}(t), \boldsymbol{n_{IJ}}\big) = \boldsymbol{0}, \tag{1.39}$$

The equations are then fully-discretized in time and space, by considering for instance the forward Euler method:

$$\boldsymbol{W_I^{n+1}} = \boldsymbol{W_I^n} - \frac{\Delta t}{|\Omega_I|}\boldsymbol{R_I^n} \quad \text{with} \quad \boldsymbol{R_I^n} = \sum_{J\in\mathcal{V}(I)} \delta_{IJ}\boldsymbol{\mathcal{F}}(\boldsymbol{W_I^n}, \boldsymbol{W_J^n}, \boldsymbol{n_{IJ}}), \tag{1.40}$$

where $\boldsymbol{R_I^n}$ is the explicit numerical flux balance for the time t^n.

In this Ph-D work, we shall consider Godunov-type schemes, which are numerical methods associating the definition of the numerical fluxes with the solution of Riemann problems (1.16). In particular, we shall consider numerical fluxes associated with approximate Riemann solvers. These numerical fluxes have several advantages in comparison to exact Riemann solvers, but also some drawbacks that will be discussed later in chapters 2 and 3. In addition, they are significantly easier to implement and faster to evaluate, whereas exact solvers typically require more theoretical analysis, often involving Newton methods for solving non-linear equations [33, 34], making such methods prohibitively time-consuming.

1.6 . Kodef: a research code for two-dimensional compressible Euler equations

During the first year of the Ph-D program, a significant effort was devoted to the development of a novel functionality within the existing research code, enabling the definition and the implementation of efficient implicit stages. This development became an important foundation for this thesis, as it has allowed for the rapid generation of numerical results for a large number of numerical schemes. In particular, this has substantially contributed to the investigations presented in the following chapters. The computations presented in this work were obtained using this research code, implementing a cell-centered finite volume method, as described above, in structured mesh with quadrangle elements. Depending on the flow configurations, MUSCL reconstruction methods [49] with slope limiters could be applied in order to improve the overall accuracy in space. The effectiveness of this development relies on the use of automatic/algorithmic differentiation tools based on source transformation, the so-called Tapenade [28]. This tool proved to be a valuable alternative strategy to approximated implicit stages, particularly in the context of investigation for low Mach number corrections. Although the literature has reported numerous approximated implicit stages (see for instance [50–54] among others), we could suggest that, for compressible schemes in the low Mach number limit, standard approximated implicit stages should also required a particular attention to stability issues. This is due to the fact that, the efficiency of the implicit stage must also be taken into account as since the number of iterations required to converge with machine precision levels may become excessively large due to the stringent stability condition. To circumvent this difficulty, a potential solution consist in considering implicit schemes that remain stable even when large CFL number are used. Such schemes can be in particular obtained by considering an exact Jacobian matrix with a relevant time-integration scheme, as discussed below. The objective of this section is to provide details regarding the implicit schemes developped in this work. However, there is an important need to avoid a redundant presentation with the chapter 3.5.2. Thus, in this section we adopt a more global description of the numerical approach refereeing to sections in chapter 3 for additional information.

Linearized backward Euler scheme, and pseudo time integration methods

We have considered a linearized backward-Euler time stepping scheme. For a uniform mesh, this can be formulated as

$$\left(\boldsymbol{\mathcal{I}} + \partial_{\boldsymbol{W^n}} \boldsymbol{R^n}\right)\left(\boldsymbol{W}^{n+1} - \boldsymbol{W}^{n}\right) = -\boldsymbol{R^n} \quad \text{with} \quad \boldsymbol{\mathcal{I}} = \mathbf{diag}\left(\frac{|\Omega_I|}{\Delta t}\right) \quad \text{and} \quad \boldsymbol{R^n} = (\boldsymbol{R_I^n})_I, \tag{1.41}$$

where in the left-hand side, a Jacobian matrix has to be provided, $\boldsymbol{W}^n$ denotes the vector of conservative variables, and $\boldsymbol{R^n}$ is the vector of the explicit numerical flux balances at the time t^n, with $\boldsymbol{R_I^n}$ defined in (1.40).

For steady flows, it is of common practice to introduce a pseudo-time integration method in order to accelerate the convergence of the discrete solution to the steady-state. A local time stepping method [55] was considered, consisting in modifying the definition of the diagonal matrix I in the left-hand side of (1.41) with

$$\boldsymbol{\mathcal{I}} = \mathbf{diag}\left(\frac{|\Omega_I|}{\Delta t_I}\right).$$

In the above expression, Δt_I is a local time step defined in each computational cell Ω_I. This technique yields a pseudo-time integration method since the information contained in each cell propagates according to different time steps, thus expressing a numerical method more closely related to a fixed-point problem than to an evolution problem. In this Ph-D work, rather than examining features of the long-time behavior of unsteady solutions, we usually adopted another approach consisting in examining steady solutions obtained through a fixed-point problem. For steady inviscid flows, there is no ambiguity between the two discrete solutions: the long time behavior of the unsteady solution converges to

the result as the steady method, characterized as a steady-state solution. However, it should be noted that, for unsteady viscous flows, this is no longer the case as for instance discussed in [56, p3-4].
In addition to the local time stepping method, in order to improve the convergence rate, a pseudo transient continuation method was formulated, and was strongly inspired from the work of Crivellini-Bassi [57]. Its definition is given in section 3.5.2. This pseudo transient continuation method aims at progressively increasing the CFL number as long as the normalized explicit residuals decrease. The use of very large CFL numbers leads to a vanishing contribution of the diagonal matrix $\boldsymbol{\mathcal{I}}$ in the left-hand side of (1.41), resulting in a method that asymptotically resolves a Newton method, as indicated next

$$\partial_{\boldsymbol{W}^n}\boldsymbol{R}^n\left(\boldsymbol{W}^{n+1}-\boldsymbol{W}^n\right)=-\boldsymbol{R}^n,$$

corresponding to the case of an infinite CFL number.
The construction of the exact Jacobian matrix $\partial_{\boldsymbol{W}^n}\boldsymbol{R}^n$ was obtained by using Tapenade, which produces the differentiated Fortran routine corresponding to the computation of the differentiated explicit flux balance $\boldsymbol{R}^n$. Both are denoted as "RHS.f90" and "RHS_d.f90" in Fig.1.2 representing a typical illustration of how Tapenade operates in the research code.

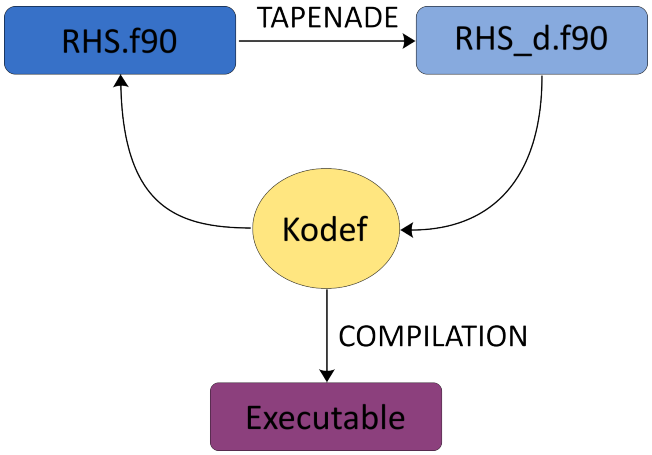

Figure 1.2: Representation of how Tapenade operates in the research Code

At each iteration, an iterative algorithm was applied to build the exact Jacobian matrix $\partial_{\boldsymbol{W}^n}\boldsymbol{R}^n$, which consisted in multiple calls to the differentiated code while storing the information in a sparse format matrix. The iterative algorithm is described in detail in section 3.5.1. A few algorithms can also be found in Poulain's thesis [58]. Once the Jacobian matrix had been built, the system is resolved using a sparse LU factorization provided by the Intel-MKL libraries. We considered a direct solver, instead of iterative solvers [59], to circumvent the issue with ill-conditioned problem which severely deteriorate the convergence rate of these methods in the low Mach number limit.
The introduction of the iterative algorithm corresponds mainly to the key stage of new development in the research code, which became somewhat challenging when further optimisations were considered. However, these optimisations were implemented and have allowed to significantly reduce the run-time needed to construct the Jacobian matrix, as indicated below.

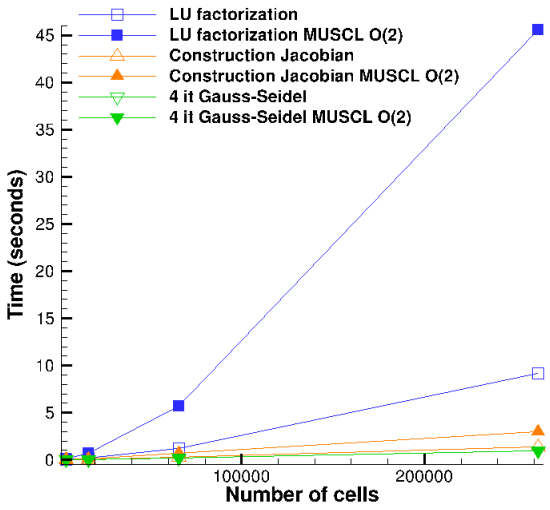

Figure 1.3: Sequential time required for the construction of the Jacobian matrix

In Fig. 1.3, the time required to construct the exact Jacobian matrix is compared with the run-time consumed by the direct solver to solve the system on the left-hand side of (1.40) and the run-time needed by a Symmetric Gauss-Seidel method with only four forward and backward diagonal sweeps used to invert the same implicit system. In this figure, they are respectively denoted as 'Construction Jacobian', 'LU factorization' or '4 it Gauss-Seidel'. These observations were made for various mesh densities, reaching up to 262,000 cells, using the same first-and second-order scheme in space. In particular, the second-order scheme, which required to evaluate five neighboring cells in the x- and y-directions, is represented in the Fig.1.3 with solid symbols. As it can be observed, the time require for construction of the Jacobian matrix associated with the second-order scheme is more easily comparable to the time needed by the iterative solver whereas the direct solver. This shows that, for this research code, the use of AD proves to be an efficient tool for formulating an exact implicit stage, as it does not require intensive CPU-resources in comparison to a direct solver.

2 - The Roe scheme: introduction, review and analysis for low Mach number flows

Contents

The second chapter is dedicated to an in-depth examination of *the Roe scheme* [3], an approximate Riemann solver based on a linearization of the initial system (2.1). The Roe scheme has been the subject of considerable interest in the literature for decades, due to its simplicity and robustness in handling complex flows in industrial applications.

The first objective of the chapter is to present an overview of the approach proposed by Roe for the construction of an approximate Riemann solver. Then, fundamental considerations underlying *the Roe-type linearization* are reminded, and the different choices for the derivation of an approximate Riemann solver are discussed.

The second objective is to give more details regarding the relations between the approximate Riemann problem, the numerical flux, and the artificial viscosity, which are crucial features in this work. In the following sections, the numerical flux is derived with a compact formulation in order to illustrate two simple and equivalent interpretations of the Roe flux. These formulations correspond either to a simple wave solver or to an artificial viscosity method involving a matrix-valued dissipation. The interpretation of the numerical flux as a corrected simple centered scheme with a viscosity matrix has provided an interesting framework for the asymptotic analysis, particularly following pioneering works by Turkel in the 90's [5, 60, 61]. This formulation is discussed in section 2.3, where it is explained why the Roe's matrix-valued dissipation fails in computing low Mach number flows.

The third objective is to introduce three equivalent formulations of the dissipation vector characterized by a matrix-valued dissipation, which will be essential in this work, particularly in chapter 3. These

different formulations of dissipation vector have been used in the literature in different ways to derive low Mach corrections. The last section presents two interesting corrections [25, 26] that have been considered as potential foundations for this Ph-D work. In particular, they could serve as prospective candidates for categorizing low-Mach number corrections into two approaches that have been implicitly discussed in the literature on several occasions.

2.1 . The Roe-type linearization

The initial methodology proposed by Godunov [2] to formulate a relevant numerical flux is based on the exact resolution of the Riemann problem, defined at each mesh interface. Locally at each interface, the exact Riemann problem (2.1) can be written as follows

$$\begin{cases} \partial_t \boldsymbol{w} + \boldsymbol{A}(\boldsymbol{w}, \boldsymbol{n})\, \partial_\xi \boldsymbol{w} = \boldsymbol{0} \\ \boldsymbol{w}(0,\xi) = \begin{cases} \boldsymbol{w_l} & \text{If } \xi < 0 \\ \boldsymbol{w_r} & \text{If } \xi > 0 \end{cases} \end{cases}, \tag{2.1}$$

with the objective of formulating a numerical flux defined as the evaluation of the exact solution of (2.1) by the flux function, resulting in the so-called Godunov scheme. This constitutes the fundamental concept underlying the construction of Riemann solvers. In opposition to the Godunov scheme, Roe was among the first contributors to propose numerical methods based on approximate Riemann problems, obtained through the linearization of the initial system. Indeed, Roe in [3] proposed an approach to construct a linearized Jacobian matrix with constant coefficients, denoted as $\boldsymbol{A^{Roe}}$, which is computed locally at the interface between the left and right states $\boldsymbol{w_l}$ and $\boldsymbol{w_r}$. As a result, this introduces an approximate problem of (2.1). Nowadays, this approach is known as the Roe-type linearization and is first discussed in this chapter. The construction of a linearized matrix $\boldsymbol{A^{Roe}}$ requires to satisfy a number of properties in order to introduce an appropriate linearized problem substituting (2.1). In most cases, the derivation requires lengthy calculations. However, once constructed, the approximate Riemann problem can be written as follows

$$\begin{cases} \partial_t \boldsymbol{w} + \boldsymbol{A^{Roe}}(\boldsymbol{w_l}, \boldsymbol{w_r}, \boldsymbol{n}) \partial_\xi \boldsymbol{w} = \boldsymbol{0} \\ \boldsymbol{w}(0,\xi) = \begin{cases} \boldsymbol{w_l} & \text{If } \xi < 0 \\ \boldsymbol{w_r} & \text{If } \xi > 0 \end{cases} \end{cases}. \tag{2.2}$$

The approximate Riemann problem (2.2) is significantly more easy to solve, given that the Jacobian matrix has constant coefficients. Therefore, a solution can be derived from the spectral properties of the matrix $\boldsymbol{A^{Roe}}$, through the application of linear Hyperbolic Theory. However, in order to ensure consistency between the problems (2.1) and (2.2), Roe prescribed the following constraints on the linearized Jacobian matrix.

Consistency: $\boldsymbol{A^{Roe}}(\boldsymbol{w}, \boldsymbol{w}, \boldsymbol{n}) = \boldsymbol{A}(\boldsymbol{w}, \boldsymbol{n}) \quad \forall \boldsymbol{w} \in \Omega^a \ , \ \boldsymbol{n} \in \mathbb{S}^{d-1}$

Conservation Condition: $\boldsymbol{A^{Roe}}(\boldsymbol{w_l}, \boldsymbol{w_r}, \boldsymbol{n})\ (\boldsymbol{w_r} - \boldsymbol{w_l}) = \boldsymbol{f}(\boldsymbol{w_r}, \boldsymbol{n}) - \boldsymbol{f}(\boldsymbol{w_l}, \boldsymbol{n})$

Hyperbolicity: $\boldsymbol{A^{Roe}}(\boldsymbol{w_l}, \boldsymbol{w_r}, \boldsymbol{n})$ has $d+2$ real eigenvalues and distinct eigenvectors

In order to obtain a matrix $\boldsymbol{A^{Roe}}$ that satisfies the *conservation condition*, Roe introduced a parameter vector $\boldsymbol{v}$ aiming at decomposing easily the jumps of the physical flux and conservative variables

$$\Delta \boldsymbol{f}(\boldsymbol{w}, \boldsymbol{n}) = \boldsymbol{f}(\boldsymbol{w_r}, \boldsymbol{n}) - \boldsymbol{f}(\boldsymbol{w_l}, \boldsymbol{n}) \qquad \text{and} \qquad \Delta \boldsymbol{w} = \boldsymbol{w_r} - \boldsymbol{w_l}.$$

Introducing the two matrices $\boldsymbol{B}(\boldsymbol{v_l}, \boldsymbol{v_r})$ and $\boldsymbol{C}(\boldsymbol{v_l}, \boldsymbol{v_r}, \boldsymbol{n})$ in $\mathbb{R}^{(d+2)\times(d+2)}$, with $\boldsymbol{B}$ an invertible matrix, the existence of $\boldsymbol{A^{Roe}}$ approximating the Jacobian matrix $\boldsymbol{A}(\boldsymbol{w}, \boldsymbol{n})$ can be deduced from the two matrices $\boldsymbol{B}$ and $\boldsymbol{C}$ with

$$\begin{cases} \Delta \boldsymbol{w} = \boldsymbol{B}(\boldsymbol{v_l}, \boldsymbol{v_r}) \Delta \boldsymbol{v} \\ \Delta \boldsymbol{f}(\boldsymbol{w}, \boldsymbol{n}) = \boldsymbol{C}(\boldsymbol{v_l}, \boldsymbol{v_r}, \boldsymbol{n}) \Delta \boldsymbol{v} \end{cases} \implies \Delta \boldsymbol{f}(\boldsymbol{w}) = \overbrace{\boldsymbol{C}(\boldsymbol{v_l}, \boldsymbol{v_r}, \boldsymbol{n}) \Big(\boldsymbol{B}(\boldsymbol{v_l}, \boldsymbol{v_r}) \Big)^{-1}}^{\boldsymbol{A^{Roe}}(\boldsymbol{w_l}, \boldsymbol{w_r}, \boldsymbol{n})} \Delta \boldsymbol{w}, \tag{2.3}$$

where matrix $\boldsymbol{A^{Roe}}(\boldsymbol{w_l}, \boldsymbol{w_r}, \boldsymbol{n})$ introduced in (2.2) with expression (2.3) indicates the dependencies of the Roe matrix to the two initial conservative states. Observing that, in the case of the compressible Euler equations, the conservative variables $\boldsymbol{w}$ and the flux function $\boldsymbol{f}(\boldsymbol{w}, \boldsymbol{n})$ are quadratic functions of parameter vector $\boldsymbol{v} = \sqrt{\rho}(1, \boldsymbol{\mathcal{U}}, H)^t$, Roe proposed a constant matrix $\boldsymbol{A^{Roe}}(\boldsymbol{w_l}, \boldsymbol{w_r}, \boldsymbol{n})$ using averaged states, that are nowadays the so-called Roe averages, as indicated next

$$\tilde{\boldsymbol{w}}(\boldsymbol{w_l}, \boldsymbol{w_r}) = (\tilde{\rho}, \tilde{\boldsymbol{\mathcal{U}}}, \tilde{H})^t \quad \text{with} \quad \tilde{\rho} = \sqrt{\rho_l \rho_r} \quad \text{and for the other components} \quad \tilde{\cdot} = \frac{\sqrt{\rho_l}\ \cdot_l + \sqrt{\rho_r}\ \cdot_r}{\sqrt{\rho_l} + \sqrt{\rho_r}}. \tag{2.4}$$

As mentioned by Roe [3], the choice of parameter vector is not unique and many others could have been chosen. In particular, as demonstrated by Harten-Lax-van Leer in [4] (Theorem 2.1), the existence of a convex entropy function ensures the existence of a Roe-type linearization, satisfying the three above conditions. However, Roe suggested the parameter vector $\boldsymbol{v}$ as it has significant properties. Once constructed, the Roe-type linearization allows the approximate Jacobian matrix $\boldsymbol{A^{Roe}}$ to be interpreted as a direct evaluation of the exact Jacobian matrix, as indicated by the two right-hand side expressions

$$\boldsymbol{A^{Roe}}(\boldsymbol{w_l}, \boldsymbol{w_r}, \boldsymbol{n}) = \boldsymbol{A^{Roe}}(\tilde{\boldsymbol{w}}(\boldsymbol{w_l}, \boldsymbol{w_r}), \boldsymbol{n}) = \boldsymbol{A}(\tilde{\boldsymbol{w}}(\boldsymbol{w_l}, \boldsymbol{w_r}), \boldsymbol{n}).$$

Then, the *hyperbolicity condition* for $\boldsymbol{A^{Roe}}(\tilde{\boldsymbol{w}}, \boldsymbol{n})$ is derived from $\boldsymbol{A}(\boldsymbol{w}, \boldsymbol{n})$, as the spectral properties of the Jacobian matrix involved in the initial Riemann problem (2.1) are preserved.

In a second paper, Roe-Pike [62] demonstrated that $\boldsymbol{v}$ is the unique parameter vector that yields this mathematical interpretation of $\boldsymbol{A^{Roe}}$. The authors also present a second approach for deriving an approximate Riemann problem preserving the original wave structure of the initial problem (2.1). It should be mentioned that, for the compressible Euler equations, the two approaches are equivalent.

Nevertheless, as mentioned in the original paper [3], the linearization process has also several severe drawbacks that have been addressed in the literature, for instance a risk to not capture the admissible entropy solution within the weak solutions. Additionally, the Roe method is known to not preserve the set of physical states (1.11), and thus, can compute intermediate states with negative density (see for instance Vinokur [63], Einfeldt et al. [64], and also Batten et al. [65] for the positivity preserving). Entropy fixes have been proposed in the literature [66] to recover a more consistent behavior of the numerical method [67], and are briefly discussed in section 2.4.1.

2.2 . Expressions of the numerical flux

This section examines the relationship between Godunov-type methods and the associated numerical flux expressions. It focuses on approximate Riemann solvers, such as the Roe scheme, which defines an approximate Riemann problem by introducing a linearized Jacobian matrix with constant coefficients, substituting the physical Jacobian matrix. In the context of finite-volume schemes, there exist several

possible formulations for the numerical flux $\boldsymbol{\mathcal{F}^{Roe}}$. Although these formulations are all equivalent, they nonetheless implicitly highlight different interpretations of the numerical flux.
The following subsections present two formulations of the Roe scheme: the first is *the simple wave form*, which typically characterizes numerical fluxes associated with simple approximate Riemann solvers, and the second is *the artificial viscosity form*, which encompasses a wider class of numerical schemes, that are not Godunov-type methods for instance. In particular, the Roe flux can be regarded as a stabilization of the simple centered scheme with a matrix-valued dissipation, which in addition allows for sharp capture of discontinuities without oscillations.
To this aim, we provide details regarding the derivation of the relation between the approximate Riemann problem and the expression of the numerical flux, but also for the equivalence between these two formalisms. The analysis presented in these sections introduces fundamental concepts, which are used in next chapters, to establish a unified formalism for the Roe and HLLC schemes.
The section first indicates how to build the exact solution $\boldsymbol{\omega}^{Roe}$ of the approximated Riemann problem (2.2) using the linear hyperbolic theory. Then, the Godunov method is applied using $\boldsymbol{\omega}^{Roe}$ in order to examine and to identify common features and differences with the Roe scheme.

2.2.1 . The simple wave form for the Roe scheme

Considering the approximate Riemann problem obtained by the Roe method, the problem involves a Jacobian matrix with constant coefficients

$$\begin{cases} \partial_t \boldsymbol{w} + \boldsymbol{A^{Roe}}(\tilde{\boldsymbol{w}}, \boldsymbol{n})\partial_\xi \boldsymbol{w} = \boldsymbol{0} \\ \boldsymbol{w}(0,\xi) = \begin{cases} \boldsymbol{w_l} & \text{If } \xi < 0 \\ \boldsymbol{w_r} & \text{If } \xi > 0 \end{cases} \end{cases},$$

where the solution can be constructed using the spectral properties of $\boldsymbol{A^{Roe}}(\tilde{\boldsymbol{w}}, \boldsymbol{n})$. Introducing the eigenvalues and the left and right eigenvectors denoted as follows

$$\text{for } 1 \leq k \leq d+2 \qquad \begin{cases} \tilde{\boldsymbol{l}}_k \boldsymbol{A^{Roe}}(\tilde{\boldsymbol{w}}, \boldsymbol{n}) & = \tilde{\boldsymbol{l}}_k \tilde{\lambda}_k & \tilde{\boldsymbol{L}}, \tilde{\boldsymbol{R}} \in \mathbb{R}^{(d+2)\times(d+2)} \\ \boldsymbol{A^{Roe}}(\tilde{\boldsymbol{w}}, \boldsymbol{n})\tilde{\boldsymbol{r}}_{\boldsymbol{k}} & = \tilde{\lambda}_k \tilde{\boldsymbol{r}}_{\boldsymbol{k}} & \tilde{\boldsymbol{R}}\,\tilde{\boldsymbol{L}} = \tilde{\boldsymbol{L}}\,\tilde{\boldsymbol{R}} = \boldsymbol{I_{d+2}} = \mathbf{diag}(1,...,1) \end{cases}, \quad (2.5)$$

the eigenvalues are indexed in an increasing order with especially $\tilde{\lambda}_2$ with multiplicity d, the columns of the matrix $\boldsymbol{R}$ correspond to the right eigenvectors $(\tilde{\boldsymbol{r}}_{\boldsymbol{k}})_{k=1,...,d+2}$, whereas the rows of $\boldsymbol{L}$ represent the left eigenvectors $(\tilde{\boldsymbol{l}}_{\boldsymbol{k}})_{k=1,...,d+2}$. For the sake of brevity, the dependence on the average state $\tilde{\boldsymbol{w}}$ for the eigenvectors is omitted in (2.5). From the linear hyperbolic theory, the exact solution of this approximate Riemann problem is a self-similar solution which can be formulated as

$$\boldsymbol{\omega^{Roe}}(\frac{\xi}{t}; \boldsymbol{w_l}, \boldsymbol{w_r}, \boldsymbol{n}) = \begin{cases} \boldsymbol{w_l} & \text{if} \quad \frac{\xi}{t} < \tilde{\lambda}_1 \\ \boldsymbol{w_l^*} & \text{if} \quad \tilde{\lambda}_1 < \frac{\xi}{t} < \tilde{\lambda}_2 \\ \boldsymbol{w_r^*} & \text{if} \quad \tilde{\lambda}_2 < \frac{\xi}{t} < \tilde{\lambda}_{d+2} \\ \boldsymbol{w_r} & \text{if} \quad \tilde{\lambda}_{d+2} < \frac{\xi}{t} \end{cases}. \quad (2.6)$$

The structure of the solution involves three simple waves separating four constant states, and which are associated with the three characteristic speeds $\tilde{\lambda}_1$, $\tilde{\lambda}_2$ and $\tilde{\lambda}_{d+2}$. As long as the hyperbolicity condition holds, the characteristic approach can be applied and therefore the two intermediate states $\boldsymbol{w_l^*}$ and $\boldsymbol{w_r^*}$ are derived from the spectral properties of $\boldsymbol{A^{Roe}}$. By decomposing the jump of the conservative variables in the eigenvectors basis $(\tilde{\boldsymbol{r}}_{\boldsymbol{k}})_{k=1,...,d+2}$

$$\Delta \boldsymbol{w} = (\boldsymbol{w_r} - \boldsymbol{w_l}) = \tilde{\boldsymbol{R}}\,\tilde{\boldsymbol{\alpha}} \qquad \Leftrightarrow \qquad \tilde{\boldsymbol{\alpha}} = \tilde{\boldsymbol{L}}\,\Delta \boldsymbol{w} \quad , \quad (2.7)$$

the expressions of $\boldsymbol{w}_l^*$ and $\boldsymbol{w}_r^*$ are deduced from the associated coordinates $\tilde{\boldsymbol{\alpha}} = (\tilde{\alpha}_k)_{k=1,\dots,d+2}$ and the structure of the approximate Riemann problem (2.6). Indeed, by introducing in the left-hand side of (2.7) the different jumps for the conservative variables occurring in the fan waves (2.6), and expanding the right-hand side as follows

$$\Delta \boldsymbol{w} = (\boldsymbol{w}_l^* - \boldsymbol{w}_l) + (\boldsymbol{w}_r^* - \boldsymbol{w}_l^*) + (\boldsymbol{w}_r - \boldsymbol{w}_r^*) = \tilde{\boldsymbol{R}}\,\boldsymbol{\alpha} = \tilde{\alpha}_1 \tilde{\boldsymbol{r}}_{\boldsymbol{1}} + \sum_{k=2}^{d+1} \tilde{\alpha}_k \tilde{\boldsymbol{r}}_{\boldsymbol{k}} + \tilde{\alpha}_{d+2} \tilde{\boldsymbol{r}}_{\boldsymbol{d+2}},$$

then, the different jumps of the conservative variables can be associated with their simple waves, as indicated next

$$\begin{aligned} \Delta \boldsymbol{w} = &\quad (\boldsymbol{w}_l^* - \boldsymbol{w}_l) &+ &\quad (\boldsymbol{w}_r^* - \boldsymbol{w}_l^*) &+ &\quad (\boldsymbol{w}_r - \boldsymbol{w}_r^*) \\ = &\quad \tilde{\alpha}_1 \tilde{\boldsymbol{r}}_{\boldsymbol{1}} &+ &\quad \sum_{k=2}^{d+1} \tilde{\alpha}_k \tilde{\boldsymbol{r}}_{\boldsymbol{k}} &+ &\quad \tilde{\alpha}_{d+2} \tilde{\boldsymbol{r}}_{\boldsymbol{d+2}} \end{aligned} \quad . \tag{2.8}$$

The expression (2.8) clearly exhibits the change of rate between the conservative states across each wave, and consequently identifies the explicit path connecting $\boldsymbol{w}_l$ to $\boldsymbol{w}_r$ in the fan waves (2.6). Therefore, the expressions for $\boldsymbol{w}_l^*$ and $\boldsymbol{w}_r^*$ are deduced from (2.7). There are three equivalent definitions to express the intermediate states $(\boldsymbol{w}_l^*, \boldsymbol{w}_r^*)$. We shall consider in the following

$$\boldsymbol{w}_l^* = \boldsymbol{w}_l + \tilde{\alpha}_1 \tilde{\boldsymbol{r}}_{\boldsymbol{1}} \qquad\qquad \boldsymbol{w}_r^* = \boldsymbol{w}_r - \tilde{\alpha}_{d+2} \tilde{\boldsymbol{r}}_{\boldsymbol{d+2}} \quad . \tag{2.9}$$

To explicitly highlight the differences between the exact Riemann solver and the Roe solver, the original Godunov method is first formulated for the approximate Riemann problem (2.2). Although the approach leads to an inappropriate numerical flux $\boldsymbol{\mathcal{F}}^{\boldsymbol{God-A^{Roe}}}$ which does not correctly discretize the original problem (2.1), its extension to the original problem (2.1) is instructive. Specifically, the extension of $\boldsymbol{\mathcal{F}}^{\boldsymbol{God-A^{Roe}}}$ to the original problem (2.1) provides a simple interpretation of the numerical flux $\boldsymbol{\mathcal{F}}^{\boldsymbol{Roe}}$. The Godunov flux for the linearized problem (2.2) is given by

$$\boldsymbol{\mathcal{F}}^{\boldsymbol{God-A^{Roe}}}(\boldsymbol{w}_l, \boldsymbol{w}_r, \boldsymbol{n}) = \begin{cases} \boldsymbol{A}^{\boldsymbol{Roe}}(\tilde{\boldsymbol{w}}, \boldsymbol{n})\, \boldsymbol{w}_l & \text{if } 0 < \tilde{\lambda}_1 \\ \boldsymbol{A}^{\boldsymbol{Roe}}(\tilde{\boldsymbol{w}}, \boldsymbol{n})\, \boldsymbol{w}_l^* & \text{if } \tilde{\lambda}_1 < 0 < \tilde{\lambda}_2 \\ \boldsymbol{A}^{\boldsymbol{Roe}}(\tilde{\boldsymbol{w}}, \boldsymbol{n})\, \boldsymbol{w}_r^* & \text{if } \tilde{\lambda}_2 < 0 < \tilde{\lambda}_{d+2} \\ \boldsymbol{A}^{\boldsymbol{Roe}}(\tilde{\boldsymbol{w}}, \boldsymbol{n})\, \boldsymbol{w}_r & \text{if } \tilde{\lambda}_{d+2} < 0 \end{cases} , \tag{2.10}$$

where the exact solution $\boldsymbol{\omega}^{\boldsymbol{Roe}}$ is directly used in the flux function associated with the linearized problem. The structure of the expression (2.10) is referred to as the simple wave form, as it consists of simple discontinuities. This designation arises because the value of the numerical flux is uniquely determined by $\boldsymbol{\omega}^{\boldsymbol{Roe}}$ with respect to the orientation of the fan waves. Although (2.10) defines a consistent numerical flux with the initial Riemann problem (2.1), yet it fails to satisfy the standard requirement for an upwind scheme. Indeed, assuming a supersonic flow, where all eigenvalues are positive (i.e. $0 < \tilde{\lambda}_1$), then the flux differs from the value $\boldsymbol{f}(\boldsymbol{w}_l, \boldsymbol{n})$. To fit the expression of the numerical flux (2.10) with the initial Riemann problem, the first requirement is to enforce the standard definition of an upwind flux. Additionally, it is necessary to modify the intermediate terms in (2.10) in order to maintain the jump conditions across each wave, which were originally satisfied. The Roe flux thus reads

$$\boldsymbol{\mathcal{F}}^{\boldsymbol{Roe}}(\boldsymbol{w}_l, \boldsymbol{w}_r, \boldsymbol{n}) = \begin{cases} \boldsymbol{f}(\boldsymbol{w}_l, \boldsymbol{n}) & \text{if } 0 < \tilde{\lambda}_1 \\ \boldsymbol{f}_l^* \cdot \boldsymbol{n} & \text{if } \tilde{\lambda}_1 < 0 < \tilde{\lambda}_2 \\ \boldsymbol{f}_r^* \cdot \boldsymbol{n} & \text{if } \tilde{\lambda}_2 < 0 < \tilde{\lambda}_{d+2} \\ \boldsymbol{f}(\boldsymbol{w}_r, \boldsymbol{n}) & \text{if } \tilde{\lambda}_{d+2} < 0 \end{cases} . \tag{2.11}$$

The two intermediate fluxes $(\boldsymbol{f}_{\boldsymbol{l}}^{*} \cdot \boldsymbol{n}, \boldsymbol{f}_{\boldsymbol{r}}^{*} \cdot \boldsymbol{n})$ must be chosen in order to guarantee locally each jump condition, and therefore, globally *the conservation condition*

$$\begin{aligned} \Delta \boldsymbol{f}(\boldsymbol{w}, \boldsymbol{n}) = \boldsymbol{A}^{\boldsymbol{Roe}}(\tilde{\boldsymbol{w}}, \boldsymbol{n}) \Delta \boldsymbol{w} &= \sum_{k=1}^{d+2} \tilde{\lambda}_k \tilde{\alpha}_k \tilde{\boldsymbol{r}}_{\boldsymbol{k}} \\ &= \tilde{\lambda}_1 (\boldsymbol{w}_{\boldsymbol{l}}^{*} - \boldsymbol{w}_{\boldsymbol{l}}) + \tilde{\lambda}_2 (\boldsymbol{w}_{\boldsymbol{r}}^{*} - \boldsymbol{w}_{\boldsymbol{l}}^{*}) + \tilde{\lambda}_{d+2} (\boldsymbol{w}_{\boldsymbol{r}} - \boldsymbol{w}_{\boldsymbol{r}}^{*}) \end{aligned} \quad . \tag{2.12}$$

These two expressions can be derived either by expanding the left- and right-hand sides of (2.12) across each wave, as similarly performed for the intermediate states (2.8). Otherwise, this can be done in a more straightforward manner, by noticing that the following relationships hold from (2.9)

$$\begin{aligned} \boldsymbol{A}^{\boldsymbol{Roe}}(\tilde{\boldsymbol{w}}, \boldsymbol{n})\, \boldsymbol{w}_{\boldsymbol{l}}^{*} = \boldsymbol{A}^{\boldsymbol{Roe}}(\tilde{\boldsymbol{w}}, \boldsymbol{n})\, (\boldsymbol{w}_{\boldsymbol{l}} + \tilde{\alpha}_1 \tilde{\boldsymbol{r}}_{\boldsymbol{1}}) &= \boldsymbol{A}^{\boldsymbol{Roe}}(\tilde{\boldsymbol{w}}, \boldsymbol{n})\, \boldsymbol{w}_{\boldsymbol{l}} + \tilde{\lambda}_1 \tilde{\alpha}_1 \tilde{\boldsymbol{r}}_{\boldsymbol{1}} \\ \boldsymbol{A}^{\boldsymbol{Roe}}(\tilde{\boldsymbol{w}}, \boldsymbol{n})\, \boldsymbol{w}_{\boldsymbol{r}}^{*} = \boldsymbol{A}^{\boldsymbol{Roe}}(\tilde{\boldsymbol{w}}, \boldsymbol{n})\, (\boldsymbol{w}_{\boldsymbol{r}} - \tilde{\alpha}_{d+2} \tilde{\boldsymbol{r}}_{\boldsymbol{d+2}}) &= \boldsymbol{A}^{\boldsymbol{Roe}}(\tilde{\boldsymbol{w}}, \boldsymbol{n})\, \boldsymbol{w}_{\boldsymbol{r}} - \tilde{\lambda}_{d+2} \tilde{\alpha}_{d+2} \tilde{\boldsymbol{r}}_{\boldsymbol{d+2}} \end{aligned} \quad , \tag{2.13}$$

and applying the same substitutions in (2.13) as those employed in (2.10). This can be concisely expressed in the definition of the Roe flux as follows

$$\boldsymbol{\mathcal{F}}^{\boldsymbol{Roe}}(\boldsymbol{w}_{\boldsymbol{l}}, \boldsymbol{w}_{\boldsymbol{r}}, \boldsymbol{n}) = \begin{cases} \boldsymbol{f}(\boldsymbol{w}_{\boldsymbol{l}}, \boldsymbol{n}) & \text{if } 0 < \tilde{\lambda}_1 \\ \boldsymbol{f}(\boldsymbol{w}_{\boldsymbol{l}}, \boldsymbol{n}) + \tilde{\lambda}_1 \, (\boldsymbol{w}_{\boldsymbol{l}}^{*} - \boldsymbol{w}_{\boldsymbol{l}}) & \text{if } \tilde{\lambda}_1 < 0 < \tilde{\lambda}_2 \\ \boldsymbol{f}(\boldsymbol{w}_{\boldsymbol{r}}, \boldsymbol{n}) - \tilde{\lambda}_{d+2} \, (\boldsymbol{w}_{\boldsymbol{r}} - \boldsymbol{w}_{\boldsymbol{r}}^{*}) & \text{if } \tilde{\lambda}_2 < 0 < \tilde{\lambda}_{d+2} \\ \boldsymbol{f}(\boldsymbol{w}_{\boldsymbol{r}}, \boldsymbol{n}) & \text{if } \tilde{\lambda}_{d+2} < 0 \end{cases} \quad . \tag{2.14}$$

2.2.2 . The artificial viscosity form of the Roe scheme

It is noteworthy that the Roe flux is not frequently discussed in the literature using the simple wave form. However, this is a more appropriate formalism for a comparative study between the Roe and HLL-type schemes. In contrast, the formulation of the Roe flux is more frequently introduced as an artificial viscosity method [68,69], expressing explicitly a correction stabilizing the centered discretization, which is inherently unstable for convective equations. Although these two potential mathematical interpretations of the Roe flux are equivalent, the artificial viscosity form provides a larger framework enabling algebraic comparisons between different schemes [70]. In the following, the derivation of the artificial viscosity form is carried out by starting from expressions (2.11) and (2.13), and writing it as a first-order upwind scheme

$$\boldsymbol{\mathcal{F}}^{\boldsymbol{Roe}}(\boldsymbol{w}_{\boldsymbol{l}}, \boldsymbol{w}_{\boldsymbol{r}}, \boldsymbol{n}) = \boldsymbol{f}(\boldsymbol{w}_{\boldsymbol{l}}) \cdot \boldsymbol{n} + \sum_{k=1}^{d+2} \tilde{\lambda}_k^{-} \, \tilde{\alpha}_k \tilde{\boldsymbol{r}}_{\boldsymbol{k}} = \boldsymbol{f}(\boldsymbol{w}_{\boldsymbol{r}}) \cdot \boldsymbol{n} - \sum_{k=1}^{d+2} \tilde{\lambda}_k^{+} \, \tilde{\alpha}_k \tilde{\boldsymbol{r}}_{\boldsymbol{k}} \quad ,$$

where the exponents $\pm$ denote the positive $\cdot^{+}$ and negative part $\cdot^{-}$ of a scalar quantity

$$a^{+} = \max(a, 0), \qquad \text{and} \qquad a^{-} = \min(a, 0) \quad .$$

By averaging the two expressions of $\boldsymbol{\mathcal{F}}^{\boldsymbol{Roe}}(\boldsymbol{w}_{\boldsymbol{l}}, \boldsymbol{w}_{\boldsymbol{r}}, \boldsymbol{n})$, and using $a^{+} - a^{-} = |a|$ to simplify the result, the following conservative formulation for the numerical flux is obtained:

$$\begin{aligned} \boldsymbol{\mathcal{F}}^{\boldsymbol{Roe}}(\boldsymbol{w}_{\boldsymbol{l}}, \boldsymbol{w}_{\boldsymbol{r}}, \boldsymbol{n}) &= \frac{\boldsymbol{f}(\boldsymbol{w}_{\boldsymbol{l}}) \cdot \boldsymbol{n} + \boldsymbol{f}(\boldsymbol{w}_{\boldsymbol{r}}) \cdot \boldsymbol{n}}{2} \quad - \quad \frac{1}{2} \sum_{k=1}^{d+2} |\tilde{\lambda}_k| \, \tilde{\alpha}_k \tilde{\boldsymbol{r}}_{\boldsymbol{k}} \\ &= \frac{\boldsymbol{f}(\boldsymbol{w}_{\boldsymbol{l}}) \cdot \boldsymbol{n} + \boldsymbol{f}(\boldsymbol{w}_{\boldsymbol{r}}) \cdot \boldsymbol{n}}{2} \quad - \quad \frac{1}{2} \, |\boldsymbol{A}^{\boldsymbol{Roe}}(\tilde{\boldsymbol{w}}, \boldsymbol{n})| \, \Delta \boldsymbol{w} \end{aligned} \quad .$$

This gives the commonly used expression for the Roe scheme. The expressions of the numerical dissipation of Godunov-type methods are of particular interest, as depending on the definition of the

numerical dissipation, valuable properties could be enforced into the scheme [68, 71, 72]. In particular, Godunov-type methods highlight an appropriate amount of numerical dissipation allowing to obtain efficient shock-capturing methods that are monotone and easily comparable to other schemes.
However, in contrast to the previous derivation of $\boldsymbol{\mathcal{F}^{Roe}}$, it is also interesting to examine the viscosity matrix associated with the Godunov flux for the linearized system, since this provides insight between the two approaches. Therefore, the Roe flux is once again derived as an extension required to make consistent the expression of the numerical flux $\boldsymbol{\mathcal{F}^{God-A^{Roe}}}$ with the initial problem.
Following the characteristic approach [31], the approximate solution $\boldsymbol{\omega^{Roe}}$ in (2.2) is equivalently rewritten in a more compact form. In order to proceed, the left and right conservative states are projected on the eigenvector basis $(\tilde{\boldsymbol{r}}_{\boldsymbol{k}})_k$ as done in (2.7), and the coordinates of the jumps of the conservative variables are written as $\tilde{\alpha}_k = \tilde{\alpha}_{k_r} - \tilde{\alpha}_{k_l}$. By expressing the solution $\boldsymbol{\omega^{Roe}}$ and using the left and right coordinates in the right eigenvector basis, the numerical flux can be also formulated as

$$\boldsymbol{\mathcal{F}^{God-A^{Roe}}}(\boldsymbol{w_l}, \boldsymbol{w_r}, \boldsymbol{n}) = \boldsymbol{A^{Roe}}(\tilde{\boldsymbol{w}}, \boldsymbol{n})\, \boldsymbol{\omega^{Roe}}(0_+; \boldsymbol{w_l}, \boldsymbol{w_r}, \boldsymbol{n}) \;=\; \sum_{k=1}^{d+2} \tilde{\alpha}_{l_k} \tilde{\lambda}_k^+ \tilde{\boldsymbol{r}}_{\boldsymbol{k}} \;+\; \sum_{k=1}^{d+2} \tilde{\alpha}_{r_k} \tilde{\lambda}_k^- \tilde{\boldsymbol{r}}_{\boldsymbol{k}} \quad .$$

This expression further simplifies using the hyperbolicity of the matrix $\boldsymbol{A^{Roe}}$, resulting in

$$\boldsymbol{\mathcal{F}^{God-A^{Roe}}}(\boldsymbol{w_l}, \boldsymbol{w_r}, \boldsymbol{n}) = \quad = \quad \boldsymbol{A^{Roe}}(\tilde{\boldsymbol{w}}, \boldsymbol{n})^+ \boldsymbol{w_l} \quad + \quad \boldsymbol{A^{Roe}}(\tilde{\boldsymbol{w}}, \boldsymbol{n})^- \boldsymbol{w_r} \quad , \tag{2.15}$$

which highlights the upstream differencing behavior of the flux. The expression of the Godunov flux associated with the linearized Riemann problem is reformulated as a centered term corrected by a viscosity matrix

$$\boldsymbol{\mathcal{F}^{God-A^{Roe}}}(\boldsymbol{w_l}, \boldsymbol{w_r}, \boldsymbol{n}) \;=\; \underbrace{\boldsymbol{A^{Roe}}(\tilde{\boldsymbol{w}}, \boldsymbol{n}) \left(\frac{\boldsymbol{w_l} + \boldsymbol{w_r}}{2} \right)}_{\text{centered term}} \;-\; \underbrace{\frac{1}{2} |\boldsymbol{A^{Roe}}(\tilde{\boldsymbol{w}}, \boldsymbol{n})| \, (\boldsymbol{w_r} - \boldsymbol{w_l})}_{\text{matrix-valued dissipation}} \quad , \tag{2.16}$$

where the artificial viscosity introduced by the Godunov method is clearly expressed for a problem defined with a matrix of constant coefficients. To correlate this expression to the original Riemann problem (2.1), the expression (2.16) must be adapted. As previously mentioned, for a supersonic flow where all eigenvalues are positive (i.e. $0 < \tilde{\lambda}_1$), the expression (2.16) reduces to $\boldsymbol{A^{Roe}}(\tilde{\boldsymbol{w}}, \boldsymbol{n})\boldsymbol{w_l}$, because of

$$\begin{aligned} \boldsymbol{A^{Roe}}(\tilde{\boldsymbol{w}}, \boldsymbol{n})(\boldsymbol{w_l} + \boldsymbol{w_r}) &= \boldsymbol{A^{Roe}}(\tilde{\boldsymbol{w}}, \boldsymbol{n})^+ (\boldsymbol{w_l} + \boldsymbol{w_r}) \, , \\ -|\boldsymbol{A^{Roe}}(\tilde{\boldsymbol{w}}, \boldsymbol{n})| \Delta \boldsymbol{w} &= -\boldsymbol{A^{Roe}}(\tilde{\boldsymbol{w}}, \boldsymbol{n})^+ (\boldsymbol{w_r} - \boldsymbol{w_l}) \end{aligned} \quad .$$

These relationships suggest to modify the centered term of (2.16), this gives

$$\boldsymbol{\mathcal{F}^{Roe}}(\boldsymbol{w_l}, \boldsymbol{w_r}, \boldsymbol{n}) = \frac{\boldsymbol{f}(\boldsymbol{w_l}, \boldsymbol{n}) + \boldsymbol{f}(\boldsymbol{w_r}, \boldsymbol{n})}{2} - \frac{1}{2} |\boldsymbol{A^{Roe}}(\tilde{\boldsymbol{w}}, \boldsymbol{n})| \, \Delta \boldsymbol{w} \quad , \tag{2.17}$$

and by using the *conservation condition*, it can be observed that the above expression recovers the correct behavior for supersonic flows. Expressions (2.16) and (2.17) show that, the Godunov flux applied for the linearized problem and the Roe flux defined for the initial problem, are characterized by an identical matrix-valued dissipation.

2.3 . Asymptotic behavior of the numerical dissipation

In this section, the analysis is limited to the two-dimensional case (i.e., $d = 2$) and subsonic flows. The objective of this analysis is twofold: first, the modified equations associated with the first-order Roe

scheme are introduced; second, the asymptotic behavior of the scheme in the low-Mach number limit is investigated. To this end, an asymptotic analysis of the matrix-valued dissipation due to Turkel [11] is considered, as this framework analysis explains the failure of Roe-Type schemes to accurately approximate low Mach number flows. This analysis is based on the study of the modified equations, which have been widely considered in the literature (see, for instance, [10,43,73–75]). These equations have been identified as a potentially valuable tool for gaining a deeper insight into the behavior of the numerical scheme. This is related to the fact that these continuous equations, corresponding to equations with second-order numerical viscosity terms, are approximated at the second-order in space by the first-order scheme. These continuous equations are in general easier to manipulate than fully discrete or semi-discretized equations.

2.3.1 . The truncation error of the Roe scheme

Considering a uniform Cartesian 2D mesh with a constant grid spacing h, the semi-discrete Roe scheme in space can be formulated, after rearranging terms, in the following compact form

$$h\, d_t(\boldsymbol{W_I}(t)) + \frac{1}{2}\sum_{J\in\mathcal{V}(I)}\Big(\boldsymbol{f}(\boldsymbol{w_J},\boldsymbol{n_{IJ}}) - |\boldsymbol{A^{Roe}}(\tilde{\boldsymbol{w}}_{\boldsymbol{IJ}},\boldsymbol{n_{IJ}})|\,\Delta_{IJ}\boldsymbol{w}\Big) = \boldsymbol{0}, \tag{2.18}$$

with the same notations introduced in (1.39), and $\Delta_{IJ}\boldsymbol{w} = \boldsymbol{w_J} - \boldsymbol{w_I}$.
As indicated in Viozat's thesis [43, Sec. 2.5], in the case of subsonic flows, the exact solution can be assumed smooth and sufficiently differentiable, so that an analysis of the truncation error can be performed. By replacing the exact solution in the discrete equation (2.18) and using Taylor expansions, the truncation error in space for the Roe scheme is given by

$$\boldsymbol{\epsilon_I} = \frac{h}{2}\Big(\partial_x\big(|\boldsymbol{A}(\boldsymbol{w_I})|\,\partial_x\boldsymbol{w_I}\big) + \partial_y\big(|\boldsymbol{B}(\boldsymbol{w_I})|\,\partial_y\boldsymbol{w_I}\big)\Big) + \mathcal{O}(h^2), \tag{2.19}$$

where $\boldsymbol{A}$ and $\boldsymbol{B}$ are the corresponding Jacobian matrices to the flux function. Then, in a uniform Cartesian mesh, the first-order Roe scheme solves at the second order in space the following modified equations

$$\partial_t\boldsymbol{w} + \partial_x\boldsymbol{f_1}(\boldsymbol{w}) + \partial_y\boldsymbol{f_2}(\boldsymbol{w}) = \frac{h}{2}\Big(\partial_x\big(|\boldsymbol{A}(\boldsymbol{w_I})|\,\partial_x\boldsymbol{w_I}\big) + \partial_y\big(|\boldsymbol{B}(\boldsymbol{w_I})|\,\partial_y\boldsymbol{w_I}\big)\Big), \tag{2.20}$$

which, under some assumptions made for instance in [43, Sec. 2.5], could be simplified for some flows into

$$\partial_t\boldsymbol{w} + \partial_x\boldsymbol{f_1}(\boldsymbol{w}) + \partial_y\boldsymbol{f_2}(\boldsymbol{w}) = \frac{h}{2}\Big(|\boldsymbol{A}(\boldsymbol{w_I})|\,\partial^2_{x^2}\boldsymbol{w_I} + |\boldsymbol{B}(\boldsymbol{w_I})|\,\partial^2_{y^2}\boldsymbol{w_I}\Big). \tag{2.21}$$

2.3.2 . Asymptotic behavior of matrix-valued dissipation schemes

The origin of the inaccuracy of the Roe scheme to approximate correctly low Mach number flows can be easily understood from the analysis introduced by Turkel [11,61], considering the modified equations (2.21). In this section, we investigate the asymptotic behavior of the artificial viscosity introduced in the right-hand side of the Euler equations (2.21), comparing with the asymptotic behavior of convective and pressure terms on the left-hand side. As suggested by several authors, in order to greatly simplify the analysis, the modified equations are first reformulated using a convenient change of variables based on entropy [60,61,76,77], defined as follows

$$\boldsymbol{d\tilde{w}_0} = (d\Phi, du, dv, dS)^T, \tag{2.22}$$

where $d\Phi = \dfrac{dp}{\rho c}$ is proportional to the pressure, and $dS = \dfrac{dp - c^2 d\rho}{\rho c}$ to the entropy. Note that this analysis can also be conducted using standard sets of variables, such as the compressible variables as

outlined by Viozat [43], or the primitive variables as discussed by Miczek et al. in [12]. However, the introduction of the symmetrizing variables (2.22) offers significant advantages, as it symmetrizes the two Jacobian matrices and also substantially simplifies their expressions. We first begin by expressing the modified equations associated with the first-order Roe scheme (2.21) in the entropic variables

$$\partial_t \tilde{\boldsymbol{w}}_{\mathbf{0}} + \tilde{\boldsymbol{A}}_{\mathbf{0}}(\tilde{\boldsymbol{w}}_{\mathbf{0}})\partial_x \tilde{\boldsymbol{w}}_{\mathbf{0}} + \tilde{\boldsymbol{B}}_{\mathbf{0}}(\tilde{\boldsymbol{w}}_{\mathbf{0}})\partial_y \tilde{\boldsymbol{w}}_{\mathbf{0}} = \frac{h}{2}\Big(|\tilde{\boldsymbol{A}}_{\mathbf{0}}|\partial^2_{x^2}\tilde{\boldsymbol{w}}_{\mathbf{0}} + |\tilde{\boldsymbol{B}}_{\mathbf{0}}|\partial^2_{y^2}\tilde{\boldsymbol{w}}_{\mathbf{0}}\Big), \tag{2.23}$$

where the Jacobian matrices in the x- and y-directions are expressed within the following similarity transformations

$$\tilde{\boldsymbol{A}}_{\mathbf{0}}(\tilde{\boldsymbol{w}}_{\mathbf{0}}) = \partial_{\boldsymbol{w}}\tilde{\boldsymbol{w}}_{\mathbf{0}}\ \boldsymbol{A}(\boldsymbol{w})\ \partial_{\tilde{\boldsymbol{w}}_{\mathbf{0}}}\boldsymbol{w} \qquad \text{and} \qquad \tilde{\boldsymbol{B}}_{\mathbf{0}}(\tilde{\boldsymbol{w}}_{\mathbf{0}}) = \partial_{\boldsymbol{w}}\tilde{\boldsymbol{w}}_{\mathbf{0}}\ \boldsymbol{B}(\boldsymbol{w})\ \partial_{\tilde{\boldsymbol{w}}_{\mathbf{0}}}\boldsymbol{w},$$

where the two matrices corresponding to the change of variables are given by

$$\partial_{\boldsymbol{w}}\,\tilde{\boldsymbol{w}}_{\mathbf{0}} = \begin{pmatrix} \frac{\gamma-1}{2}\frac{|\boldsymbol{\mathcal{U}}|^2}{\rho c} & (1-\gamma)\frac{u}{\rho c} & (1-\gamma)\frac{v}{\rho c} & \frac{(\gamma-1)}{\rho c} \\ \frac{-u}{\rho} & \frac{1}{\rho} & 0 & 0 \\ \frac{-v}{\rho} & 0 & \frac{1}{\rho} & 0 \\ \frac{1}{\rho c}\left(\frac{\gamma-1}{2}|\boldsymbol{\mathcal{U}}|^2 - c^2\right) & (1-\gamma)\frac{u}{\rho c} & (1-\gamma)\frac{v}{\rho c} & \frac{(\gamma-1)}{\rho c} \end{pmatrix}, \quad \partial_{\tilde{\boldsymbol{w}}_{\mathbf{0}}}\boldsymbol{w} = \begin{pmatrix} \frac{\rho}{c} & 0 & 0 & \frac{-\rho}{c} \\ \frac{\rho u}{c} & \rho & 0 & \frac{-\rho u}{c} \\ \frac{\rho v}{c} & 0 & \rho & \frac{-\rho v}{c} \\ \frac{\rho H}{c} & \rho u & \rho v & \frac{-\rho}{c}\frac{|\boldsymbol{\mathcal{U}}|^2}{2} \end{pmatrix}. \tag{2.24}$$

Next, to simplify the analysis, a general expression of the Jacobian matrix is used with

$$\tilde{\boldsymbol{A}}_{\mathbf{0}}(\boldsymbol{n}) = n_x\tilde{\boldsymbol{A}}_{\mathbf{0}}(\tilde{\boldsymbol{w}}_{\mathbf{0}}) + n_y\tilde{\boldsymbol{B}}_{\mathbf{0}}(\tilde{\boldsymbol{w}}_{\mathbf{0}}) = \begin{pmatrix} \mathcal{U}_n & cn_x & cn_y & 0 \\ cn_x & \mathcal{U}_n & 0 & 0 \\ cn_y & 0 & \mathcal{U}_n & 0 \\ 0 & 0 & 0 & \mathcal{U}_n \end{pmatrix}, \tag{2.25}$$

where $\boldsymbol{n}$ is an arbitrary unit vector $\boldsymbol{n} = (n_x, n_y)^t$. As it can be observed, the symmetrizing variables have the advantage of yielding sparse and simple expressions. Then, upon substitution of $\boldsymbol{n}$ by one of the two canonical vectors of $\mathbb{R}^2$ in (2.25), we recover the expressions of the Jacobian matrix in the x- or y-direction. In order to derive the absolute value of the two artificial viscosity matrices arising in the right-hand side of equation (2.23), we consider the following diagonalisations

$$|\tilde{\boldsymbol{A}}_{\mathbf{0}}(\tilde{\boldsymbol{w}}_{\mathbf{0}})| = \partial_{\boldsymbol{w}}\tilde{\boldsymbol{w}}_{\mathbf{0}}\left[\boldsymbol{R}_{\boldsymbol{x}}|\boldsymbol{\Lambda}_{\boldsymbol{x}}|\boldsymbol{L}_{\boldsymbol{x}}\right]\ \partial_{\tilde{\boldsymbol{w}}_{\mathbf{0}}}\boldsymbol{w} \qquad \text{and} \qquad |\tilde{\boldsymbol{B}}_{\mathbf{0}}(\tilde{\boldsymbol{w}}_{\mathbf{0}})| = \partial_{\boldsymbol{w}}\tilde{\boldsymbol{w}}_{\mathbf{0}}\left[\boldsymbol{R}_{\boldsymbol{y}}|\boldsymbol{\Lambda}_{\boldsymbol{y}}|\boldsymbol{L}_{\boldsymbol{y}}\right]\partial_{\tilde{\boldsymbol{w}}_{\mathbf{0}}}\boldsymbol{w},$$

where the two matrices $\boldsymbol{\Lambda}_{\boldsymbol{x}}$ and $\boldsymbol{\Lambda}_{\boldsymbol{y}}$ are the diagonal matrices of the eigenvalues of the Jacobian matrices $\tilde{\boldsymbol{A}}_{\mathbf{0}}$ and $\tilde{\boldsymbol{B}}_{\mathbf{0}}$, respectively.

$$\boldsymbol{\Lambda}_{\boldsymbol{x}} = \mathrm{diag}(u-c, u, u, u+c) \qquad \text{and} \qquad \boldsymbol{\Lambda}_{\boldsymbol{y}} = \mathrm{diag}(v-c, v, v, v+c).$$

Hence, for the Jacobian matrix expressed with (2.25), we get the diagonalization $|\tilde{\boldsymbol{A}}(\boldsymbol{w})(\boldsymbol{n})| = \boldsymbol{R}(\boldsymbol{n})|\boldsymbol{\Lambda}(\boldsymbol{n})|\boldsymbol{L}(\boldsymbol{n})$ (see for instance the section 18.5 in [33]). Then, using this general formalism, the eigenvectors in en-

tropic variables are given by

$$\tilde{\boldsymbol{R}}_{\boldsymbol{0}}(\boldsymbol{n}) = \begin{pmatrix} c & c & 0 & 0 \\ cn_x & -cn_x & -n_y & 0 \\ cn_y & -cn_y & n_x & 0 \\ 0 & 0 & 0 & 1 \end{pmatrix}, \quad \text{and} \quad \tilde{\boldsymbol{L}}_{\boldsymbol{0}}(\boldsymbol{n}) = \begin{pmatrix} \frac{1}{2c} & \frac{n_x}{2c} & \frac{n_y}{2c} & 0 \\ \frac{1}{2c} & -\frac{n_x}{2c} & -\frac{n_y}{2c} & 0 \\ 0 & -n_y & n_x & 0 \\ 0 & 0 & 0 & 1 \end{pmatrix}. \tag{2.26}$$

where $\tilde{\boldsymbol{R}}_{\boldsymbol{0}}(\boldsymbol{n})$ and $\tilde{\boldsymbol{L}}_{\boldsymbol{0}}(\boldsymbol{n})$ are respectively the matrices of the right and left eigenvectors. So, the two definitions of the artificial viscosity matrices in the x- or y-direction, respectively $|\tilde{\boldsymbol{A}}_{\boldsymbol{0}}|$ and $|\tilde{\boldsymbol{B}}_{\boldsymbol{0}}|$, can be derived from

$$|\tilde{\boldsymbol{A}}_{\boldsymbol{0}}(\boldsymbol{n})| = \tilde{\boldsymbol{R}}_{\boldsymbol{0}}(\boldsymbol{n})|\boldsymbol{\Lambda}(\boldsymbol{n})|\tilde{\boldsymbol{L}}_{\boldsymbol{0}}(\boldsymbol{n}) = \begin{pmatrix} c & n_x\mathcal{U}_n & n_y\mathcal{U}_n & 0 \\ n_x\mathcal{U}_n & c\left(n_x^2 + n_y^2|M_n|\right) & n_x n_y c\left(1-|M_n|\right) & 0 \\ n_y\mathcal{U}_n & n_x n_y c\left(1-|M_n|\right) & c\left(n_y^2 + n_x^2|M_n|\right) & 0 \\ 0 & 0 & 0 & |\mathcal{U}_n| \end{pmatrix}, \tag{2.27}$$

where $M_n = \dfrac{\mathcal{U}_n}{c}$ is the directional Mach number. It is worth mentioning that the above expression is restricted to subsonic flows, for which the explicit expression of the absolute value of the two acoustic eigenvalues is known, with $|\boldsymbol{\Lambda}(\boldsymbol{n})| = \mathrm{diag}(c-\mathcal{U}_n, |\mathcal{U}_n|, |\mathcal{U}_n|, \mathcal{U}_n + c)$. Looking at the physical terms of the Euler equations, corresponding to the quasi-linear form of the left-hand side of (2.23) with matrix $\tilde{\boldsymbol{A}}_{\boldsymbol{0}}(\boldsymbol{n})$ defined in (2.25), it can be shown that the matrix coefficients have the following asymptotic behavior

$$\tilde{\boldsymbol{A}}_{\boldsymbol{0}}(\boldsymbol{n}) \simeq \begin{pmatrix} \mathcal{O}(1) & \mathcal{O}(\frac{1}{M}) & \mathcal{O}(\frac{1}{M}) & 0 \\ \mathcal{O}(\frac{1}{M}) & \mathcal{O}(1) & \mathcal{O}(1) & 0 \\ \mathcal{O}(\frac{1}{M}) & \mathcal{O}(1) & \mathcal{O}(1) & 0 \\ 0 & 0 & 0 & \mathcal{O}(1) \end{pmatrix} \quad \text{when} \quad M \longrightarrow 0. \tag{2.28}$$

In contrast, regarding the right-hand side of (2.21), we see that the following asymptotic behavior is found

$$|\tilde{\boldsymbol{A}}_{\boldsymbol{0}}(\boldsymbol{n})| \simeq \begin{pmatrix} \mathcal{O}(\frac{1}{M}) & \mathcal{O}(1) & \mathcal{O}(1) & 0 \\ \mathcal{O}(1) & \mathcal{O}(\frac{1}{M}) & \mathcal{O}(\frac{1}{M}) & 0 \\ \mathcal{O}(1) & \mathcal{O}(\frac{1}{M}) & \mathcal{O}(\frac{1}{M}) & 0 \\ 0 & 0 & 0 & \mathcal{O}(1) \end{pmatrix} \quad \text{when} \quad M \longrightarrow 0. \tag{2.29}$$

As pointed-out by Turkel [11], in the limit of the vanishing Mach number, it can be observed that the modified equations (2.21) are characterized by unbalanced coefficients between the convective and pressure terms and the entries of the matrix dissipation. This is illustrated in more details in the following, for the case of the Roe scheme, or more generally for any scheme using the flux Jacobian matrix as matrix-valued dissipation. It is shown that unbalanced entries of the matrix dissipation may

cause either excessive or insufficient amount of dissipation, as illustrated for instance with

$$\Big(|\tilde{\boldsymbol{A}}_{\boldsymbol{0}}(\boldsymbol{n})|\Big)_{1,1} \gg \Big(\tilde{\boldsymbol{A}}_{\boldsymbol{0}}(\boldsymbol{n})\Big)_{1,1} \quad \text{and} \quad \Big(|\tilde{\boldsymbol{A}}_{\boldsymbol{0}}(\boldsymbol{n})|\Big)_{1,2} \ll \Big(\tilde{\boldsymbol{A}}_{\boldsymbol{0}}(\boldsymbol{n})\Big)_{1,2}.$$

As shown by Viozat in [43] (lemma 2.5.1), by taking into account the asymptotic behaviors of these matrix coefficients and expanding the modified equations (2.23), it can be observed that, for a fixed mesh, a decrease in the Mach number results in an increase in the truncation error. This can be pointed out for instance with the equation for the longitudinal velocity component by extracting the scalar contributions in the second component:

$$\Big(\partial_t \tilde{\boldsymbol{w}}_{\boldsymbol{0}}\Big)_2 + \Big(\tilde{\boldsymbol{A}}_{\boldsymbol{0}}(\boldsymbol{e_0})\partial_x \tilde{\boldsymbol{w}}_{\boldsymbol{0}}\Big)_2 + \Big(\tilde{\boldsymbol{A}}_{\boldsymbol{0}}(\boldsymbol{e_1})\partial_y \tilde{\boldsymbol{w}}_{\boldsymbol{0}}\Big)_2 = \frac{h}{2}\Big(|\tilde{\boldsymbol{A}}_{\boldsymbol{0}}(\boldsymbol{e_1})|\partial^2_{x^2} \tilde{\boldsymbol{w}}_{\boldsymbol{0}}\Big)_2 + \frac{h}{2}\Big(|\tilde{\boldsymbol{A}}_{\boldsymbol{0}}(\boldsymbol{e_2})|\partial^2_{y^2} \tilde{\boldsymbol{w}}_{\boldsymbol{0}}\Big)_2. \quad (2.30)$$

We know from the asymptotic theory [11, 48] that

$$\Phi \simeq \mathcal{O}(M), \qquad u \simeq \mathcal{O}(1), \qquad v \simeq \mathcal{O}(1). \quad (2.31)$$

Hence, expanding the matrix-vector products in equation (2.30), the left-hand side behaves asymptotically as follows

$$\underbrace{\partial_t u}_{\mathcal{O}(1)} + \Big(\underbrace{c}_{\mathcal{O}(1/M)} \underbrace{\partial_x \Phi}_{\mathcal{O}(M)} + \underbrace{u}_{\mathcal{O}(1)} \underbrace{\partial_x u}_{\mathcal{O}(1)} \Big) + \Big(\underbrace{c}_{\mathcal{O}(1/M)} \underbrace{\partial_y \Phi}_{\mathcal{O}(M)} + \underbrace{v}_{\mathcal{O}(1)} \underbrace{\partial_y v}_{\mathcal{O}(1)} \Big) \simeq \mathcal{O}(1). \quad (2.32)$$

In contrast, the behavior of the right-hand side of (2.30) is formally given by

$$\frac{h}{2}\Big(|\tilde{\boldsymbol{A}}_{\boldsymbol{0}}(\boldsymbol{e_1})|\partial^2_{x^2} \tilde{\boldsymbol{w}}_{\boldsymbol{0}}\Big)_2 + \frac{h}{2}\Big(|\tilde{\boldsymbol{A}}_{\boldsymbol{0}}(\boldsymbol{e_2})|\partial^2_{y^2} \tilde{\boldsymbol{w}}_{\boldsymbol{0}}\Big)_2 \simeq \frac{h}{2}\mathcal{O}(1/M). \quad (2.33)$$

Then, equations (2.32 - 2.33) illustrate an incorrect scaling of the matrix-valued dissipation in comparison to the physical terms, thus resulting in a large increase of the truncation error.
Following Turkel in [11], a criterion for a consistent amount of dissipation can be determined by introducing generic second-order terms in the right-hand side of the modified equations

$$\partial_t \tilde{\boldsymbol{w}}_{\boldsymbol{0}} + \tilde{\boldsymbol{A}}_{\boldsymbol{0}}(\tilde{\boldsymbol{w}}_{\boldsymbol{0}})\partial_x \tilde{\boldsymbol{w}}_{\boldsymbol{0}} + \tilde{\boldsymbol{B}}_{\boldsymbol{0}}(\tilde{\boldsymbol{w}}_{\boldsymbol{0}})\partial_y \tilde{\boldsymbol{w}}_{\boldsymbol{0}} = \boldsymbol{Q_x}(\tilde{\boldsymbol{w}}_{\boldsymbol{0}})\partial^2_{x^2} \tilde{\boldsymbol{w}}_{\boldsymbol{0}} + \boldsymbol{Q_y}(\tilde{\boldsymbol{w}}_{\boldsymbol{0}})\partial^2_{y^2} \tilde{\boldsymbol{w}}_{\boldsymbol{0}}, \quad (2.34)$$

where $\boldsymbol{Q_x}$ and $\boldsymbol{Q_y}$ represent some matrix-valued dissipations in the x- and y-directions, respectively. More generally, such generic matrix dissipation can be expressed with $\boldsymbol{Q}(\boldsymbol{n}) = n_x \boldsymbol{Q_x} + n_y \boldsymbol{Q_y}$ in a manner analogous to $\tilde{\boldsymbol{A}}_{\boldsymbol{0}}(\boldsymbol{n})$. Then, expanding all matrix-vector products in (2.34), and looking at the individual asymptotic behaviors of all terms, it is found that in the low Mach number limit, the entries of a consistent matrix-valued dissipation should have the following behavior

$$\boldsymbol{Q}(\boldsymbol{n}) \simeq \begin{pmatrix} \mathcal{O}(\frac{1}{M^2}) & \mathcal{O}(\frac{1}{M}) & \mathcal{O}(\frac{1}{M}) & 0 \\ \mathcal{O}(\frac{1}{M}) & \mathcal{O}(1) & \mathcal{O}(1) & 0 \\ \mathcal{O}(\frac{1}{M}) & \mathcal{O}(1) & \mathcal{O}(1) & 0 \\ 0 & 0 & 0 & \mathcal{O}(1) \end{pmatrix} \quad \text{when} \quad M \longrightarrow 0. \quad (2.35)$$

This outcome has been identified by Turkel as a necessary condition for the convergence of a general preconditioner. Yet, this result actually indicates the maximum allowed dissipation for a matrix-valued dissipation scheme discretizing the Euler equations. In the case of the Roe scheme, it can be observed that the four central entries of the viscosity matrix $|\tilde{\boldsymbol{A}}_{\boldsymbol{0}}(\boldsymbol{n})|$ with the asymptotic behavior (2.28) exceed the allowed limit given by (2.35). In addition, it is also notable that the pressure equation (first row) demonstrates a lack of dissipation.

2.4 . Different forms of the dissipation vector related to the artificial viscosity

Several possible formulations can be derived for the dissipation vector corresponding to the Roe scheme

$$\boldsymbol{\mathcal{F}^{Roe}}(\boldsymbol{w_l}, \boldsymbol{w_r}, \boldsymbol{n}) = \frac{\boldsymbol{f}(\boldsymbol{w_l}, \boldsymbol{n}) + \boldsymbol{f}(\boldsymbol{w_r}, \boldsymbol{n})}{2} - \frac{1}{2} \underbrace{|\boldsymbol{A^{Roe}}(\tilde{\boldsymbol{w}}, \boldsymbol{n})| \, \Delta \boldsymbol{w}}_{\boldsymbol{d^{Roe}}} \quad ,$$

where $\boldsymbol{d^{Roe}}$ denotes the dissipation vector associated with the matrix dissipation $|\boldsymbol{A^{Roe}}|$ and the jump of the conservative variables $\Delta \boldsymbol{w}$. In the following, three different formulations of the dissipation vector $\boldsymbol{d^{Roe}}$, which have been used in the literature to introduce low-Mach number corrections to the Roe scheme, are reminded for the two-dimensional case ($d = 2$). These different formulations were considered in this Ph-D work to illustrate distinct discrete framework analyses. The first formulation is a classical decomposition of the dissipation vector, allowing to better describe the influence of low Mach number corrections on the wave structure of the Riemann problem. The second formulation gives a more compact expression, leading to a more comprehensive framework analysis of the effect of low Mach number corrections on discrete properties of the numerical solution in the incompressible limit. A third formulation was developed especially for theoretical investigations, enabling an algebraic comparison between different low Mach number corrections. This formulation turned out to be also essential to introduce similar corrections to approximate Riemann solvers such as the Roe and HLLC schemes. This latter point is discussed in detail in the last chapter.

2.4.1 . The Harten-Hyman form

The Roe scheme is not entropy stable and may fail to capture the entropy weak solution, as mentioned in [3,66]. To address this issue, Roe prescribed the use of an empirical mechanism to easily control the amount of numerical dissipation in the scheme. In this work, the first decomposition is referred to as the Harten-Hyman form [66]. This was achieved with the objective of deriving a mechanism that controls and avoids a vanishing numerical dissipation, commonly known as an entropy fix. This decomposition is based on the hyperbolicity of the Roe matrix, which significantly simplifies the expression of the dissipation vector, with no need of a diagonalization to define the absolute value of the Roe matrix, as reminded below

$$\boldsymbol{d^{Roe}} = |\boldsymbol{A^{Roe}}(\tilde{\boldsymbol{w}}, \boldsymbol{n})| \Delta \boldsymbol{w} = \sum_{k=1}^{4} |\tilde{\lambda}_k| \tilde{\alpha}_k \tilde{\boldsymbol{r}}_{\boldsymbol{k}}. \tag{2.36}$$

This expression reduces significantly the algebra required to compute the flux balance using the Roe flux. The definition of the different terms arising in the decomposition (2.36) reads

$$\tilde{\lambda}_1 = \tilde{\mathcal{U}}_n - c \qquad \tilde{\lambda}_2 = \tilde{\mathcal{U}}_n \qquad \tilde{\lambda}_3 = \tilde{\mathcal{U}}_n \qquad \tilde{\lambda}_4 = \tilde{\mathcal{U}}_n + c \quad , \tag{2.37}$$

$$\tilde{\alpha}_1 = \frac{\Delta p - \tilde{\rho}\tilde{c}\Delta \mathcal{U}_n}{2\tilde{c}^2} \qquad \tilde{\alpha}_2 = \Delta \rho - \frac{\Delta p}{\tilde{c}^2} \qquad \tilde{\alpha}_3 = \tilde{\rho} \Delta \tilde{\mathcal{U}}_t \qquad \tilde{\alpha}_4 = \frac{\Delta p + \tilde{\rho}\tilde{c}\Delta \mathcal{U}_n}{2\tilde{c}^2} \quad , \tag{2.38}$$

$$\tilde{\boldsymbol{r}}_{\boldsymbol{1}} = \begin{pmatrix} 1 \\ \tilde{u} - \tilde{c}\, n_x \\ \tilde{v} - \tilde{c}\, n_y \\ \tilde{H} - \tilde{c}\, \tilde{\mathcal{U}}_n \end{pmatrix} \qquad \tilde{\boldsymbol{r}}_{\boldsymbol{2}} = \begin{pmatrix} 1 \\ \tilde{u} \\ \tilde{v} \\ \frac{|\tilde{\mathcal{U}}|^2}{2} \end{pmatrix} \qquad \tilde{\boldsymbol{r}}_{\boldsymbol{3}} = \begin{pmatrix} 0 \\ -n_y \\ n_x \\ \tilde{\mathcal{U}}_t \end{pmatrix} \qquad \tilde{\boldsymbol{r}}_{\boldsymbol{4}} = \begin{pmatrix} 1 \\ \tilde{u} + \tilde{c}\, n_x \\ \tilde{v} + \tilde{c}\, n_y \\ \tilde{H} + \tilde{c}\, \tilde{\mathcal{U}}_n \end{pmatrix} \quad . \tag{2.39}$$

In these expressions, $\mathcal{U}_n = \boldsymbol{\mathcal{U}} \cdot \boldsymbol{n}$ and $\mathcal{U}_t$ stand for the normal and tangential velocity components, respectively, and the tilde symbol previously introduced denotes the Roe average. In order to fully describe the eigenspaces of the dissipation matrix $\boldsymbol{A^{Roe}}(\tilde{\boldsymbol{w}}, \boldsymbol{n})$, we also give the corresponding left

eigenvectors, with the following expressions

$$\tilde{\boldsymbol{l}}_{\mathbf{1}} = \begin{pmatrix} \frac{\tilde{\mathcal{U}}_n}{2\tilde{c}} + \frac{\gamma-1}{4}\frac{|\tilde{\mathcal{U}}|^2}{\tilde{c}^2} \\ -\frac{n_x}{2\tilde{c}} - \frac{\gamma-1}{2}\frac{\tilde{u}}{\tilde{c}^2} \\ -\frac{n_y}{2\tilde{c}} - \frac{\gamma-1}{2}\frac{\tilde{v}}{\tilde{c}^2} \\ \frac{\gamma-1}{2\tilde{c}^2} \end{pmatrix}^t \quad \tilde{\boldsymbol{l}}_{\mathbf{2}} = \begin{pmatrix} 1 - \frac{\gamma-1}{2}\frac{|\tilde{\mathcal{U}}|^2}{\tilde{c}^2} \\ (\gamma-1)\frac{\tilde{u}}{\tilde{c}^2} \\ (\gamma-1)\frac{\tilde{v}}{\tilde{c}^2} \\ -\frac{\gamma-1}{\tilde{c}^2} \end{pmatrix}^t \quad \tilde{\boldsymbol{l}}_{\mathbf{3}} = \begin{pmatrix} -\tilde{\mathcal{U}}_t \\ -n_y \\ n_x \\ 0 \end{pmatrix}^t \quad \tilde{\boldsymbol{l}}_{\mathbf{4}} = \begin{pmatrix} -\frac{\tilde{\mathcal{U}}_n}{2\tilde{c}} + \frac{\gamma-1}{4}\frac{|\tilde{\mathcal{U}}|^2}{\tilde{c}^2} \\ \frac{n_x}{2\tilde{c}} - \frac{\gamma-1}{2}\frac{\tilde{u}}{\tilde{c}^2} \\ \frac{n_y}{2\tilde{c}} - \frac{\gamma-1}{2}\frac{\tilde{v}}{\tilde{c}^2} \\ \frac{\gamma-1}{2\tilde{c}^2} \end{pmatrix}^t . \quad (2.40)$$

As can be observed in (2.36 - 2.37), near the sonic point, one of the acoustic eigenvalues $(\tilde{\lambda}_1, \tilde{\lambda}_4)$ tends to zero, and is thus responsible of a vanishing contribution in the sum (2.36). In [66], in order to prevent the entropic instability of the Roe scheme, a so-called entropy fix was proposed based on a local regularization of the absolute value of $\tilde{\lambda}_1$ and $\tilde{\lambda}_4$ with a continuous differentiable approximation, as indicated next with

$$\Psi(|\lambda|) = \begin{cases} |\lambda| & \text{if} \quad |\lambda| \geq \delta_h \quad \text{(no regularization)} \\ \dfrac{\lambda^2 + \delta_h^2}{2\delta_h} & \text{if} \quad |\lambda| < \delta_h \end{cases} , \quad (2.41)$$

where δ_h is an empirical parameter, adjustable according to the case and is commonly introduced as a percentage of the spectral radius of $|\boldsymbol{A}^{\boldsymbol{Roe}}|$. Modifying the acoustic eigenvalues introduces an artificial viscosity into the scheme, and therefore contributes to define an approximation of a viscous problem. This idea has been widely studied in the literature, and has demonstrated relevance and efficiency. It is common practice to control and introduce more numerical dissipation in the scheme thanks to this type of correction. Numerous formulations for the entropy fix have been proposed, see for instance the review of Pelanti-Quartapelle-Vigevano [67]. Note that it is a common practice to also apply the entropy fix on the intermediate eigenvalues $(\tilde{\lambda}_2, \tilde{\lambda}_3)$, for preventing the occurrence of the carbuncle phenomena in high-Mach number flows or instabilities near the stagnation point.

The decomposition (2.36) has been considered by numerous authors, including [7, 25, 78–81] among others, with the purpose of introducing a modified dissipation vector $\boldsymbol{d}^{\boldsymbol{Roe-X}}$, corrected by a X-correction, improving the accuracy of the Roe scheme for low-speed flows. In general, the correction entails modifications in terms $(\tilde{\alpha}_k, \tilde{\lambda}_k, \tilde{\boldsymbol{r}}_{\boldsymbol{k}})_k$. Practically, this offers the advantage of a straightforward implementation, as it requires only minor adjustments to the original routine, keeping a strong similarity with the original Roe scheme. Nevertheless, this simplicity can be misleading. Indeed, substituting one of the terms $(\tilde{\alpha_k}, \tilde{\lambda_k}, \tilde{r_k})_k$ results in the definition of a new viscosity matrix that differs from the original one $|\boldsymbol{A}^{\boldsymbol{Roe}}|$. Specifically, such modifications yields a new matrix-valued dissipation:

$$\boldsymbol{d}^{\boldsymbol{Roe-X}} = |\boldsymbol{D}(\tilde{\boldsymbol{w}}, \boldsymbol{n})| \Delta \boldsymbol{w} \quad ,$$

and then, this modification raises questions about the consequences on the spectral properties of the viscosity matrix $|\boldsymbol{D}|$, in particular regarding the formulation of the entropy fix. This should be generally applied with care since the question is not frequently addressed in the literature, except in few papers [13, 82].

2.4.2 . The Liu-Vinokur form

The second decomposition has been popularized in the work of Weiss-Smith [14], in which a preconditioning method was derived for the unsteady compressible Navier-Stokes equations. This explains why this form is sometimes referred to as the Weiss-Smith form in the literature, although this is not

correct. Indeed, as accurately pointed-out by Hope-Collins-Di-Mare in [75], this decomposition has been first introduced by Liu-Vinokur in [83]. Li-Gu in [21] have developed an interesting and relevant framework to study low Mach number corrections for the Roe scheme, based on the following decomposition of the dissipation vector, involving simple expressions and providing a physical interpretation. After some algebra, the dissipation vector can also be expanded as follows

$$\boldsymbol{d^{Roe}} = |\tilde{\mathcal{U}}_n| \begin{pmatrix} \Delta\rho \\ \Delta\rho u \\ \Delta\rho v \\ \Delta\rho E \end{pmatrix} + \delta\mathcal{U}_n \begin{pmatrix} \tilde{\rho} \\ \tilde{\rho}\tilde{u} \\ \tilde{\rho}\tilde{v} \\ \tilde{\rho}\tilde{H} \end{pmatrix} + \delta p \begin{pmatrix} 0 \\ n_x \\ n_y \\ \tilde{\mathcal{U}}_n \end{pmatrix} \quad . \tag{2.42}$$

As it can be observed, this expression introduces a concise decomposition of $\boldsymbol{d^{Roe}}$, as the formulation reduces to a sum of three vectors instead of four regarding the Harten-Hyman form (2.36). As described in [14, 21], the dissipation vector may be read as the sum of a basic upwind term, a velocity interface term and a pressure interface term, respectively. The three scalar coefficients arising in decomposition (2.42) are respectively the absolute value of the normal velocity at the cell interface, denoted as $|\tilde{\mathcal{U}}_n|$, and the two last coefficients $\delta\mathcal{U}_n$ and δp are simply expressed as follows

$$\begin{aligned} \delta\mathcal{U}_n = \quad & (\frac{|\tilde{\lambda_4}| + |\tilde{\lambda_1}|}{2} - |\tilde{\lambda_2}|)\frac{\Delta p}{\tilde{\rho}\tilde{c}^2} \quad + \quad (\frac{|\tilde{\lambda_4}| - |\tilde{\lambda_1}|}{2})\frac{\Delta\mathcal{U}_n}{\tilde{c}} \\ \delta p = \quad & (\frac{|\tilde{\lambda_4}| + |\tilde{\lambda_1}|}{2} - |\tilde{\lambda_2}|)\tilde{\rho}\Delta\mathcal{U}_n \quad + \quad (\frac{|\tilde{\lambda_4}| - |\tilde{\lambda_1}|}{2})\frac{\Delta p}{\tilde{c}} \end{aligned} \quad , \tag{2.43}$$

with the absolute values of the eigenvalues. The form (2.42 - 2.43) has several interests. First this decomposition provides a compact expression, as it requires less algebraic operations than the Hathen-Hyman form (2.36 - 2.39) to be evaluated. Second, Li-Gu have shown that this expression can be used to introduce a comprehensive framework analysis for the study of low-Mach corrections of the Roe scheme. Indeed, in [21], fifteen low-Mach corrections were proposed, and have been all reformulated within the unified formalism (2.42 - 2.43), allowing preliminary investigations of the discrete properties of their respective low Mach corrections. All these proposed corrections of the Roe scheme were respectively reinterpreted as a simple modification of the scalar coefficients $(|\tilde{\mathcal{U}}_n|, \delta\mathcal{U}_n, \delta p)$. The noteworthy feature of such approach is to provide a very clear and suitable formalism, allowing to easily review but also to compare different corrections in order to investigate their corresponding discrete properties in the low Mach number limit, as illustrated in a next section.

2.4.3 . The matrix form

This third decomposition starts from the matrix-valued dissipation form, expanding all terms of the dissipation vector $\boldsymbol{d^{Roe}}$ into jumps of some dependent primitive variables. This arbitrary choice of dependent variables is made considering the jumps that naturally emerged in the definition of the coordinates $\tilde{\boldsymbol{\alpha}} = (\tilde{\alpha}_k)_k$. This formulation does not appears particularly interesting for the evaluation of the Roe flux in comparison with the two previous decompositions (2.36) and (2.42), but on the other hand, is of particular interest for a more theoretical study of the dissipation vector. A similar formulation has been considered by Rossow [26, 27] to compare different schemes, and especially for deriving a low-Mach correction of the Roe scheme, termed as the artificial speed of sound approach, discussed in the next section and thoroughly analyzed in the chapter 3. For this formulation, the dissipation vector is expressed as the following matrix-vector product

$$\boldsymbol{d^{Roe}} = \boldsymbol{\mathcal{M}^{Roe}}(\tilde{\boldsymbol{w}}, \boldsymbol{n}) \begin{pmatrix} \Delta\rho \\ \boldsymbol{\Delta\mathcal{U}} \\ \Delta\mathcal{U}_n \\ \Delta p \end{pmatrix} \quad , \tag{2.44}$$

where the matrix $\boldsymbol{\mathcal{M}^{Roe}}$ is defined by

$$\boldsymbol{\mathcal{M}^{Roe}} = \begin{pmatrix} |\tilde{\mathcal{U}}_n| & 0 & 0 & \frac{\tilde{\rho}B}{\tilde{c}} & \frac{A}{\tilde{c}^2} \\ |\tilde{\mathcal{U}}_n|\tilde{u} & |\tilde{\mathcal{U}}_n|\tilde{\rho} & 0 & \frac{\tilde{\rho}\tilde{u}B}{\tilde{c}} + A\tilde{\rho}n_x & \frac{Bn_x}{\tilde{c}} + \frac{A\tilde{u}}{\tilde{c}^2} \\ |\tilde{\mathcal{U}}_n|\tilde{v} & 0 & |\tilde{\mathcal{U}}_n|\tilde{\rho} & \frac{\tilde{\rho}\tilde{v}B}{\tilde{c}} + A\tilde{\rho}n_y & \frac{Bn_y}{\tilde{c}} + \frac{A\tilde{v}}{\tilde{c}^2} \\ \frac{|\tilde{\mathcal{U}}_n||\tilde{\mathcal{U}}|^2}{2} & |\tilde{\mathcal{U}}_n|\tilde{\rho}\tilde{u} & |\tilde{\mathcal{U}}_n|\tilde{\rho}\tilde{v} & \frac{\tilde{\rho}\tilde{H}B}{\tilde{c}} + A\tilde{\rho}\tilde{\mathcal{U}}_n & \frac{B\tilde{\mathcal{U}}_n}{\tilde{c}} + \frac{A\tilde{H}}{\tilde{c}^2} + \frac{|\mathcal{U}_n|}{\gamma-1} \end{pmatrix} , \quad (2.45)$$

with coefficients A and B already observed in the definition of the Liu-Vinokur form (2.42 - 2.43)

$$A = \frac{|\tilde{\lambda}_1| + |\tilde{\lambda}_4|}{2} - |\tilde{\lambda}_2| \qquad B = \frac{|\tilde{\lambda}_4| - |\tilde{\lambda}_1|}{2} \quad . \quad (2.46)$$

2.5 . Two interesting rescaling of the numerical dissipation

It is of great importance to pursue the analysis of some published low Mach extensions of the Roe scheme, as originally undertaken in the work of Li-Gu [21], in order to provide a more comprehensive and a finer analysis. Indeed, despite decades of active research and numerous proposals for low Mach number corrections for the Roe scheme, with in particular new corrections still being reported in recent years, resolving the accuracy problem remains a challenging topic especially when no mesh considerations are introduced. The challenge lies in resolving this problem without introducing side issues, that too frequently affect the efficacy of the numerical methods to provide accurate solution in the general case. It has been found essential to try to summarize this topic, given the somewhat disorganized state of the literature on the subject presenting a large scattering of the formulations, whereas the underlying numerical mechanisms are not yet fully mastered.
This section presents two interesting corrections of the Roe scheme, considering the Liu-Vinokur form, that have been already published in the literature. The following corrections are reviewed in a common framework as a starting point of this thesis work: the Rieper's fix [25] and the Rossow's artificial speed of sound approach [27]. The underlying objective of this presentation is to illustrate that a multitude of corrections proposed for the Roe scheme can be essentially categorized into two distinct approaches, which effectively resolve the accuracy problem. On the one hand, corrections that amplify the pressure jumps (for instance the Rossow's artificial speed of sound), and, on the other hand, corrections that reduce the normal velocity jumps (like the Rieper's fix).
In addition, some computations considering a baseline test case were performed as a first assessment of these two corrections. The objective was to investigate the impact of such corrections on the capture of shock waves in the compressible regime and the overall accuracy of the discrete solutions, in direct comparison with solutions obtained with the original Roe scheme. It should be noted that, this has already been discussed in the literature to some extent, since these two corrections have been used in numerous papers, thereby demonstrating their efficiency in the compressible regime. Nevertheless, these results are also presented here to illustrate the practical application of an efficient implicit scheme based on the use of Automatic Differentiation [28], which has required a significant effort during the first year of this Ph-D work. Indeed, as illustrated below, by combining this development with a local time-stepping method and a pseudo-transient continuation method, steady-state solutions can be obtained with quadratic convergence due to an adaptive and progressively increasing CFL. All

these developments and the rigorous stability condition discussed in chapter 3 are of a significant importance in this work, as it has greatly facilitated a series of numerical investigations. In particular, the numerical assessments carried out in the compressible regime, presented in the following, turned out to be useful to discuss of a third approach, that was investigated in this thesis work. Although this investigated third approach is interesting, as it effectively addresses the accuracy problem, it also proved to be unsatisfying due to an excessively modified dissipation vector. This latter point will be discussed in the last subsection.

2.5.1 . The Roe scheme

In order to provide more compact expressions, the definitions of the normal interface velocity $\delta\mathcal{U}_n$ and the interface pressure δp introduced in (2.43) for the Roe scheme, are first reformulated as

$$\begin{pmatrix} \delta\mathcal{U}_n \\ \\ \delta p \end{pmatrix} = \begin{pmatrix} \frac{B}{\tilde{c}} & \frac{A}{\tilde{\rho}\tilde{c}^2} \\ \\ A\tilde{\rho} & \frac{B}{\tilde{c}} \end{pmatrix} \begin{pmatrix} \Delta\mathcal{U}_n \\ \\ \Delta p \end{pmatrix} \quad ,$$

with the two coefficients A and B defined in (2.46). Next, the discrete asymptotic properties of modified Roe schemes can be derived using this compact form, with a particular attention paid to the asymptotic behavior of the semi-discretized scheme in space, following the approach of Guillard-Viozat [7]. The comparison of these modified Roe schemes with the original scheme is performed based on the analysis of coefficients ($\delta\mathcal{U}_n$, δp). This allows avoiding a redundant and lenghty presentation of the detailed discrete analysis already published in the literature (see [7] or [25]), which are additionally discussed in chapter 3 devoted to the discrete analysis of the properties of the Roe-Rossow scheme.
Using the standard normalization process at the incompressible time-scale, introduced in section 1.4.1, the normalized dissipation vector can be expressed as follows

$$\hat{\boldsymbol{d}} = |\tilde{\mathcal{U}_n}| \begin{pmatrix} 1 & 0 & 0 \\ 0 & 1 & 0 \\ 0 & 0 & 1 \end{pmatrix} \begin{pmatrix} \Delta\rho \\ \Delta(\rho\boldsymbol{\mathcal{U}}) \\ \Delta(\rho E) \end{pmatrix} + \delta\check{\mathcal{U}}_n \begin{pmatrix} 1 & 0 & 0 \\ 0 & 1 & 0 \\ 0 & 0 & 1 \end{pmatrix} \begin{pmatrix} \tilde{\rho} \\ \tilde{\rho}\tilde{\boldsymbol{\mathcal{U}}} \\ \tilde{\rho}\tilde{H} \end{pmatrix} + \delta\check{p} \begin{pmatrix} 0 & 0 & 0 \\ 0 & 1 & 0 \\ 0 & 0 & \epsilon \end{pmatrix} \begin{pmatrix} 0 \\ \boldsymbol{n} \\ \tilde{\mathcal{U}_n} \end{pmatrix}, \quad (2.47)$$

where ϵ denotes the reference Mach number arising from the normalization process, and $(\delta\check{\mathcal{U}}_n, \delta\check{p})$ are two coefficients defined with the normalized quantities $(\delta\hat{\mathcal{U}}_n, \delta\hat{p})$ not given herein. All terms arising in the right-hand side of (2.47) are normalized quantities, and where for the sake of brevity, the symbol $\hat{\cdot}$ previously introduced for the description of normalized quantities has been omitted. The normalization process applied to the Roe flux expressed with the Liu-Vinokur form yields the following expressions for the two scalar coefficients

$$\textbf{(Roe)} \quad \delta\check{\mathcal{U}}_n = \frac{1}{\epsilon}(1-\epsilon\frac{|\tilde{\mathcal{U}_n}|}{\tilde{c}})\frac{\Delta p}{\tilde{\rho}\tilde{c}} + \epsilon\frac{\tilde{\mathcal{U}_n}\Delta\mathcal{U}_n}{\tilde{c}} \qquad \delta\check{p} = \frac{1}{\epsilon}\frac{\tilde{\mathcal{U}_n}\Delta p}{\tilde{c}} + \frac{1}{\epsilon}(1-\epsilon\frac{|\tilde{\mathcal{U}_n}|}{\tilde{c}})\tilde{\rho}\tilde{c}\Delta\mathcal{U}_n \quad . \quad (2.48)$$

These reference expressions will be next compared to the modified Roe schemes introduced in the following sections.

Some computations were performed for the NACA0012 airfoil, at inflow Mach number $M = 0.85$ with incidence $\alpha = 1°$, in a structured C-type mesh with 279x60 nodes, represented in Fig.2.1a, with 151 nodes discretizing the solid wall. A usual slip condition is applied at the wall. Due to the reduced extension downstream of the computational mesh (20 chords), a subsonic outflow condition is imposed with a prescribed pressure. Finally, at the inlet boundary, a characteristic farfield boundary condition is applied.
A computation was first performed for a reference solution, corresponding to the Roe scheme using a second-order MUSCL reconstruction with the van Albada limiter, also referred to as "Roe MUSCL

$O(2)$" in the figures. Note that no entropy fix needed to be activated in these computations, neither in the next cases for the Rieper's fix nor for the artificial speed of sound.
Figure 2.1b shows the Mach number contours of the discrete solution. Figure 2.1c illustrates the convergence history of the l^2-norms of the normalized explicit residuals with respect to the evolution of the CFL value, as depicted by the red curve. Considering a uniform initial condition, a local time stepping method combined with an adaptive CFL is applied in order to quickly converge to the steady-state solution. The detailed formulation of the adaptive CFL strategy is given in chapter 3. The computation is initially set to a CFL = 6 (higher value results in unstabilities that could not be damped). At a prescribed iteration 15, the adaptive CFL starts with a prescribed CFL = 20. In the following iterations, the normalized residuals decrease, resulting in a progressive increase of the CFL number around the 400th iteration, which then begins to fluctuate. At the 600th iteration, the CFL number suddenly increases, from 25 to 110 at the 800th iteration. This indicates the beginning of a quadratic convergence to the zero machine precision, with very large values of the CFL number reached.
Next figures 2.1d and 2.1e depict the entropy S and Mach number distributions at the solid wall. It can be observed that a spurious entropy is produced at the stagnation point, in addition of the usual increase in entropy across the shock waves. By increasing the space accuracy of the scheme, an expected significant reduction of the spurious entropy can be observed, together with a less dissipated numerical shock structure, in comparison with the first-order Roe scheme (denoted as "Roe O(1)" in the figures), with a sharper shock waves as shown in Fig. 2.1e.

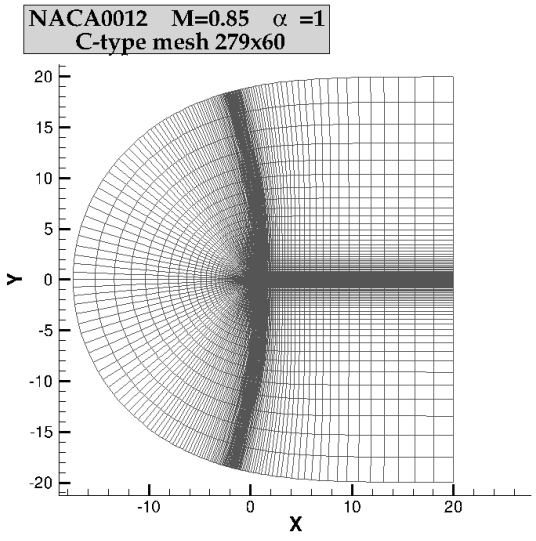

(a) C-type mesh for the NACA0012

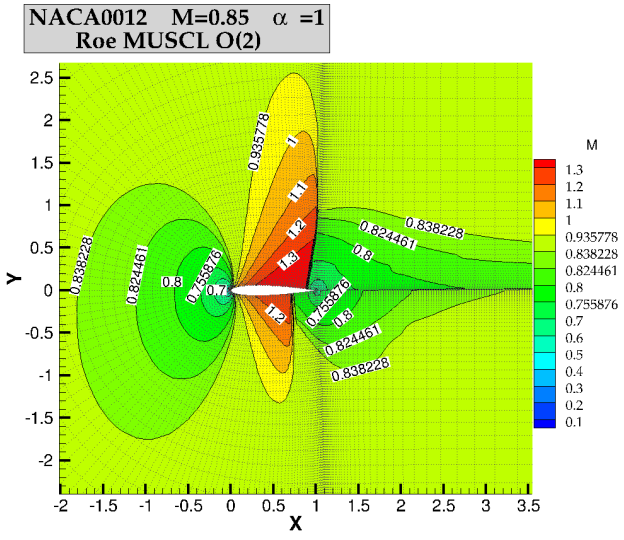

(b) Vertex-centered contours of the Mach number in the vicinity of the airfoil

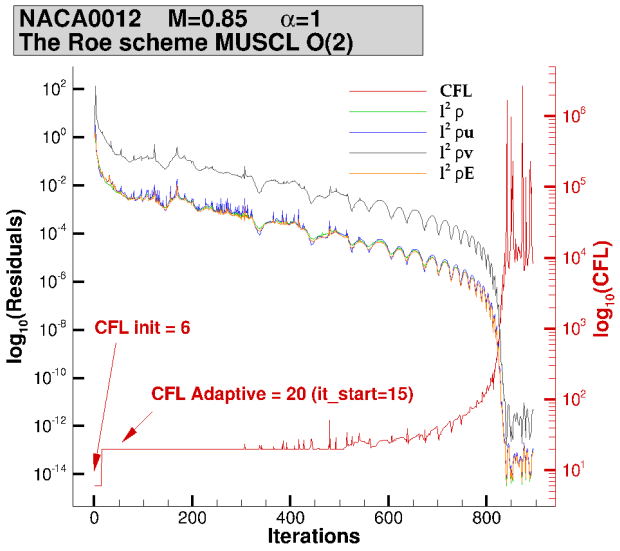

(c) Convergence history for residuals and the CFL

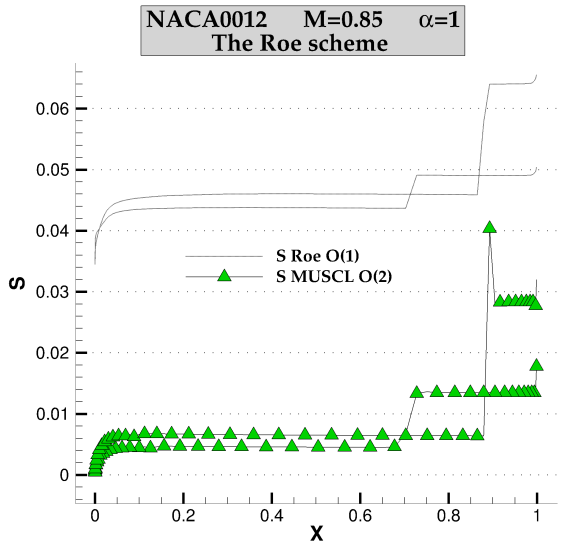

(d) Production of spurious entropy at the wall

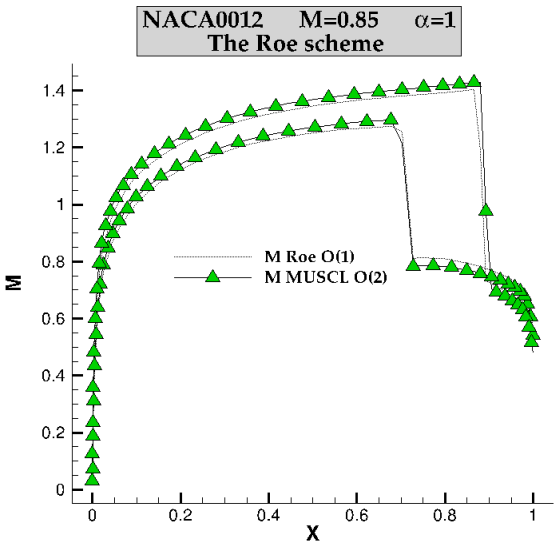

(e) Mach number at the wall

Figure 2.1: Roe scheme with MUSCL reconstruction O(2), NACA0012 airfoil at $M = 0.85$ $\alpha = 1°$

2.5.2 . The Rieper's fix

The Rieper's fix [25] (also referred to as the Roe-Rieper scheme in the manuscript) is a well-documented correction in the literature that emerged in the pursuit of the pioneering works of Guillard-Murrone [84], Thornber [85] and Dellacherie [10, 20, 86]. The original formulation was developed using the Harten-Hyman form (2.36 - 2.39), with the objective to cancel out the contribution of the directional velocity jump $\Delta\mathcal{U}_n$ in the low Mach number limit. This is achieved with the purpose of recovering asymptotically a discrete divergence-free constraint in the discrete analysis, by simply modifying the definitions of the coordinates $\tilde{\alpha}_1$ and $\tilde{\alpha}_4$ as follows

$$\tilde{\alpha}_1 = \frac{\Delta p - \tilde{\rho}\tilde{c}z\Delta\mathcal{U}_n}{2\tilde{c}^2}, \qquad \tilde{\alpha}_4 = \frac{\Delta p + \tilde{\rho}\tilde{c}z\Delta\mathcal{U}_n}{2\tilde{c}^2},$$

where z is a low Mach number fix. The Rieper's fix can be readily reinterpreted within the Liu-Vinokur decomposition, as demonstrated by Li-Gu [21], this reads for any flow regimes

$$\begin{pmatrix} \delta\mathcal{U}_n \\ \delta p \end{pmatrix} = \begin{pmatrix} \frac{B^{Rieper}}{\tilde{c}} & \frac{A}{\tilde{\rho}\tilde{c}^2} \\ A^{Rieper}\tilde{\rho} & \frac{B}{\tilde{c}} \end{pmatrix} \begin{pmatrix} \Delta\mathcal{U}_n \\ \Delta p \end{pmatrix} \quad \text{with} \quad \begin{cases} A^{Rieper} = z\,\dfrac{|\tilde{\lambda_4}| + |\tilde{\lambda_1}|}{2} - |\tilde{\lambda_2}| \\ B^{Rieper} = z\,\dfrac{|\tilde{\lambda_4}| - |\tilde{\lambda_1}|}{2} \end{cases}, \tag{2.49}$$

where z is interpreted as a rescaling coefficient, defined as a local interface Mach number with $z = \min(\frac{|\tilde{\mathcal{U}_n}|+|\tilde{\mathcal{U}_t}|}{\tilde{c}}, 1)$. The discrete analysis conducted by Rieper [25] for the compressible Euler equations, assuming a perfect gas, clearly shows that the absence of an asymptotically centered pressure gradient $p^{(1)}$ in the momentum equations is responsible for the incorrect order of the pressure disturbance (see for instance equations $(U^{(0)})$ and $(E^{(0)})$ above the section 2.3 in [25]). The main feature of this approach consists in delaying the first occurrence of these dissipative terms in the asymptotic expansion by introducing a rescaling coefficient z to let the pressure gradient $p^{(1)}$ in the momentum equations without any dissipation at the order $\mathcal{O}(1/\epsilon)$. Indeed, for subsonic flows, the two normalized scalar coefficients for the Rieper's fix are given by

$$\textbf{(Rieper)} \quad \delta\check{\mathcal{U}}_n = \frac{1}{\epsilon}(1 - \epsilon\frac{|\tilde{\mathcal{U}_n}|}{\tilde{c}})\frac{\Delta p}{\tilde{\rho}\tilde{c}} + \epsilon^2\, z\frac{\tilde{\mathcal{U}_n}\Delta\mathcal{U}_n}{\tilde{c}}, \quad \delta\check{p} = \frac{1}{\epsilon}\frac{\tilde{\mathcal{U}_n}\Delta p}{\tilde{c}} + (z - \frac{|\tilde{\mathcal{U}_n}|}{\tilde{c}})\tilde{\rho}\tilde{c}\Delta\mathcal{U}_n, \tag{2.50}$$

where the contributions of the term $\Delta\hat{\mathcal{U}}_n$ in the coefficient $\delta\check{p}$ has been reduced, in comparison to the original Roe scheme (2.48). Note that an asymptotically centered pressure gradient $p^{(1)}$ would also be achieved by maintaining the scalar coefficient $\delta\check{\mathcal{U}}_n$ unchanged. Nevertheless, this type of approach, which asymptotically centers the pressure gradient, typically leads to the occurrence of checkerboard mode problems [20, 21, 87], contaminating discrete solutions. Indeed, non-constant solutions, such as four-field solutions, also satisfy a zero discrete gradient operator (see equation (32) and figure 1 in [7]). In practice, this potential risk of pressure-velocity decoupling is often encountered, with a discrete solution converging towards a non-physical solution, as it is demonstrated in the next chapter for the steady-state problem.

Although this low-Mach correction introduces a simple modification of the Roe flux, it is also interesting to look at the consequences on the asymptotic behavior of the modified artificial viscosity matrix, which provides further insights into the correction. In particular, this indicates that relatively straightforward modifications usually yield significant discrepancies in the matrix-valued dissipation for the modified numerical flux

$$\boldsymbol{\mathcal{F}}^{\mathbf{Rieper}}(\boldsymbol{w_l}, \boldsymbol{w_r}, \boldsymbol{n}) = \frac{\boldsymbol{f}(\boldsymbol{w_l}, \boldsymbol{n}) + \boldsymbol{f}(\boldsymbol{w_r}, \boldsymbol{n})}{2} - \frac{1}{2}|\boldsymbol{A}^{\mathbf{Rieper}}(\tilde{\boldsymbol{w}}, \boldsymbol{n})|\,\Delta\boldsymbol{w}$$

Following the analysis exposed in section 2.3.2, the matrix-valued dissipation can be formulated in the entropic variables as follows

$$|\tilde{\boldsymbol{A}}_{\mathbf{0}}^{\mathbf{Rieper}}| = \begin{pmatrix} c & n_x z\mathcal{U}_n & n_y z\mathcal{U}_n & 0 \\ n_x\mathcal{U}_n & n_x^2(cz - |\mathcal{U}_n|) + |\mathcal{U}_n| & n_x n_y(cz - |\mathcal{U}_n|) & 0 \\ n_y\mathcal{U}_n & n_x n_y(cz - |\mathcal{U}_n|) & n_y^2(cz - |\mathcal{U}_n|) + |\mathcal{U}_n| & 0 \\ 0 & 0 & 0 & |\mathcal{U}_n| \end{pmatrix}. \tag{2.51}$$

From this modified expression of the original dissipation matrix (2.27), it is worth mentioning that the symmetry of the original Jacobian matrix is lost in the subsonic regime. Moreover, it can be observed

that, in the incompressible limit, this correction corresponds to the following asymptotic behavior of the matrix dissipation

$$|\tilde{\boldsymbol{A}}_{\mathbf{0}}^{\mathbf{Rieper}}| \simeq \begin{pmatrix} \mathcal{O}(\frac{1}{M}) & \mathcal{O}(M) & \mathcal{O}(M) & 0 \\ \mathcal{O}(1) & \mathcal{O}(1) & \mathcal{O}(1) & 0 \\ \mathcal{O}(1) & \mathcal{O}(1) & \mathcal{O}(1) & 0 \\ 0 & 0 & 0 & \mathcal{O}(1) \end{pmatrix}. \tag{2.52}$$

In comparison with the original asymptotic behavior of the original matrix-valued dissipation (2.29), the Rieper's fix reduces the contributions of the velocities in the continuity and momentum equations by one order of magnitude, while maintaining the asymptotic behavior of the first column. This is consistent with the observation that the correction only modifies the normal velocity jump as indicated in (2.50).

The same NACA0012 airfoil test case was considered at inflow Mach number $M = 0.85$ with incidence $\alpha = 1°$. The Rieper's fix shows few differences with original Roe scheme in the transonic regime, as shown in the next Figures 2.2. A similar Fig.2.2a to the previous case illustrates the convergence history of the l^2-norms of the normalized explicit residuals with respect to the evolution of the CFL value. The computation is again initially set to CFL = 6. Then, at iteration 15, the adaptive CFL number starts with a prescribed CFL = 25. Similarly, the CFL value undergoes fluctuations around the 400th iteration, followed by a sudden increase after the 500th iteration. In that case, the CFL number takes values ranging from 30 to 100,000 between the 600th and the 700th iteration, resulting in a quadratic convergence to the zero machine precision.
Figures 2.2b and 2.2c depict the entropy and Mach number distributions at the solid wall. In comparison to the previous results obtained with Roe scheme using the MUSCL extrapolation in Fig.2.1d, Fig.2.2b shows that the Rieper's fix produces slightly lower levels for the spurious entropy S. However, in the case of the first-order scheme, Fig.2.2b illustrates clearly that the Rieper's fix is characterized by much less spurious entropy levels upstream of the shock waves than the original first-order Roe scheme (see Fig. 2.1a). Figure 2.2c also shows that the numerical shock structure of the shock waves computed by the Rieper's fix is very similar to the Roe scheme.

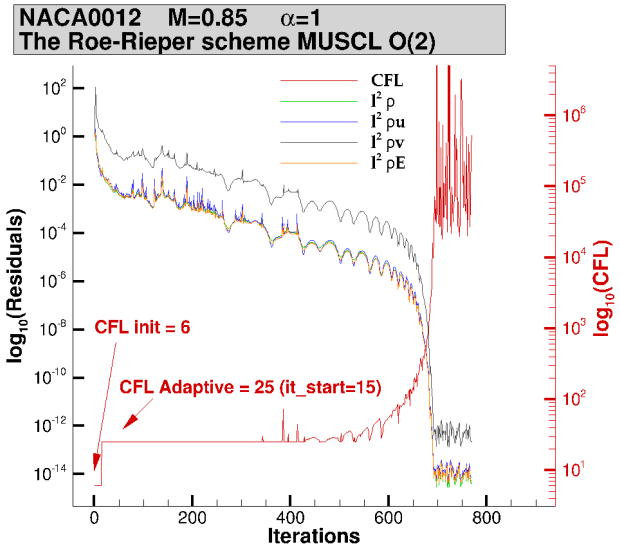

(a) Convergence history for residuals and the CFL

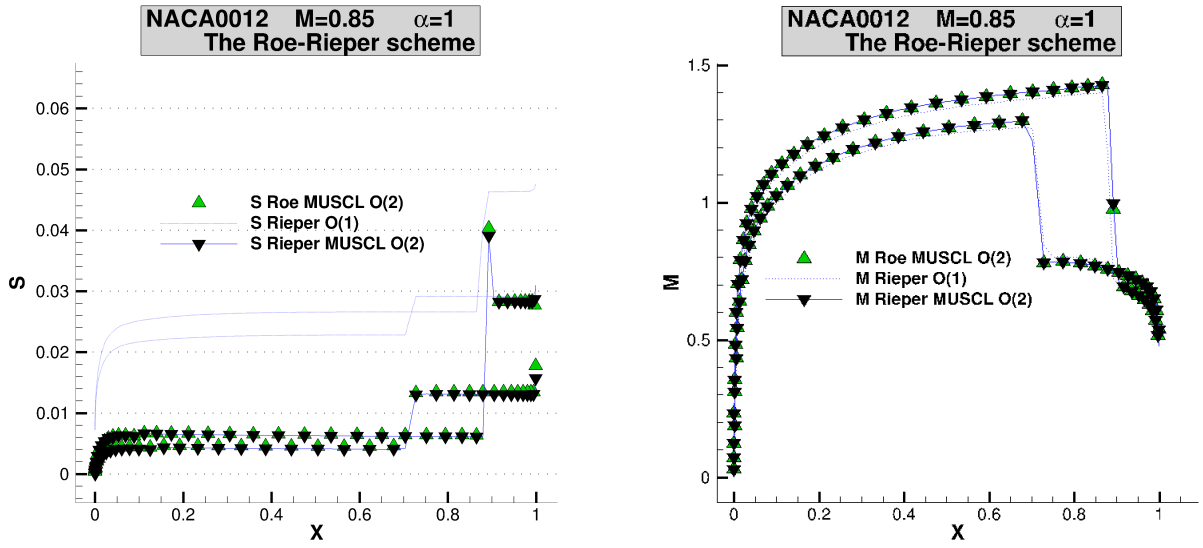

(b) Production of spurious entropy at the wall

(c) Mach number at the wall

Figure 2.2: Roe-Rieper scheme with MUSCL reconstruction O(2), NACA0012 airfoil at $M = 0.85$ $\alpha = 1^\circ$

2.5.3 . The artificial speed of sound approach of Rossow

The Rossow's artificial speed of sound approach [26,27] (also referred to as the Roe-Rossow scheme in the manuscript) represents another type of low Mach number correction applied to the Roe scheme. The formulation of the artificial speed of sound actually corresponds to a modified speed of sound arising from a preconditioning method of the Jacobian matrix investigated by Turkel. This modified speed of sound is also related to the Roe-Turkel scheme introduced in [7]. They are numerical evidence thoroughly validated by Rossow [27], that this correction appears to be a promising candidate for use as a foundation in this Ph-D work. To the best of our knowledge, the discrete properties of this modified Roe scheme have not been derived in the literature. The following chapter 3 addresses in detail the description and the discrete analyses of the Roe-Rossow scheme. Thus, this section only provides a brief reinterpretation of the correction, without further derivations. This correction is also seen as an alternative approach for low-Mach number corrections, formulated from different foundations than the low Mach number fix introduced by Rieper. In the case of the artificial speed of sound approach, the two scalar coefficients arising in the Liu-Vinokur form are given by the following expressions

$$\begin{pmatrix} \delta\mathcal{U}_n \\ \delta p \end{pmatrix} = \begin{pmatrix} \frac{B}{\tilde{c}} & \frac{1}{\tilde{c}'\tilde{c}}\frac{A}{\tilde{\rho}} \\ \frac{\tilde{c}'}{\tilde{c}}A\tilde{\rho} & \frac{B}{\tilde{c}} \end{pmatrix} \begin{pmatrix} \Delta\mathcal{U}_n \\ \Delta p \end{pmatrix} \quad \text{with} \quad \begin{cases} \alpha = \dfrac{1}{2}(1-\beta^2) \\ \beta^2 = \min(\max(M^2, M_{ref}^2), 1) \\ \tilde{c}' = c\sqrt{\alpha^2 M_n^2 + \beta^2} \end{cases} \quad \text{and} \quad \tilde{c}' \leq c \quad , \tag{2.53}$$

with unchanged coefficients A and B given by (2.46), and where c' is a rescaling coefficient corresponding to the artificial speed of sound, substituting the original speed of sound c in $\delta\mathcal{U}_n$, while a ratio between the artificial and the original speed of sound is introduced in δp by this correction. As indicated in (2.53), the articial speed of sound is defined from the directional Mach number, a local Mach number M and a reference Mach number M_{ref}, which is a user-defined parameter in the entire computational domain. This parameter is generally used as a cut-off value to circumvent instabilities occurring near stagnation points [88], and should be defined with care, as it may significantly influence the stability and the accuracy of the discrete solution. In this work, this reference Mach number was set to a much smaller value than the inflow Mach number, and even to the order of magnitude of the machine precision in most cases. Indeed, the definition of this cut-off value prevents singularities from

configurations with a dead zone, which is typically characterized by a local Mach number equals to 0 (see for instance the normal velocity jump in the definition of $\delta\mathcal{U}_n$ in (2.53)). By introducing the normalized form of the vector dissipation, it can be observed that the correction is especially characterized by the amplification of the pressure jumps, as outlined below

$$\textbf{(Rossow)} \quad \delta\check{\mathcal{U}}_n = \frac{1}{\epsilon^2}(1-\epsilon\frac{|\tilde{\mathcal{U}}_n|}{\tilde{c}})\frac{\Delta p}{\tilde{\rho}\tilde{c}'} + \epsilon\frac{\tilde{\mathcal{U}}_n\Delta\mathcal{U}_n}{\tilde{c}}, \qquad \delta\check{p} = \frac{1}{\epsilon}\frac{\tilde{\mathcal{U}}_n\Delta p}{\tilde{c}} + (1-\epsilon\frac{|\tilde{\mathcal{U}}_n|}{\tilde{c}})\tilde{\rho}\tilde{c}'\,\Delta\mathcal{U}_n. \tag{2.54}$$

In comparison with the same coefficients formulated for the Rieper's fix (2.50), in coefficient $\delta\check{\mathcal{U}}_n$, only the pressure jump Δp is amplified by one order of magnitude in ϵ, whereas the normal velocity jump $\Delta\mathcal{U}_n$ remains identical to the original formulation (2.48). Regarding the second coefficient $\delta\check{p}$, the contribution of the pressure jump is unchanged and is identical for the two corrections and the original Roe scheme, whereas the normal velocity jump $\Delta\mathcal{U}_n$ for the two modified Roe schemes exhibits a similarity in the asymptotic order of the first term, and a difference in the asymptotic order of the second term.
As demonstrated in chapter 3, the discrete analysis for the Roe-Rossow scheme shows clear similarities with the Roe-Turkel scheme [7, 21], and the discrete properties of the Roe-Turkel scheme can be also commented here to illustrate the following numerical assessment of the Roe-Rossow scheme. With the rescaling proposed by Rossow, it can be observed from (2.54) that a non-centered pressure gradient for the leading-order $p^{(0)}$ is obtained in the momentum equations at the order $\mathcal{O}(1/\epsilon^2)$. This is related to the fact that the amplification of the pressure jump Δp in coefficient $\delta\check{\mathcal{U}}_n$ accelerates the first occurrence of the leading order pressure jumps in the asymptotic analysis, as previously observed in the discrete analysis of the Roe-Turkel scheme (see equations (52) - (53) in Guillard-Viozat [7]). Therefore, this second approach is fundamentally opposed to the centering of the pressure gradient $p^{(1)}$ at order $\mathcal{O}(1/\epsilon)$, since in that case, no centered pressure gradients in the asymptotic analysis are obtained.

It is also interesting to look at the asymptotic behavior of modified dissipation matrix according to the Roe-Rossow scheme, because as indicated for the Rieper's fix, this behavior provides some insights regarding the effects of the correction on the spectral properties of the modified matrix dissipation in the modified numerical flux

$$\boldsymbol{\mathcal{F}}^{\mathbf{Rossow}}(\boldsymbol{w_l},\boldsymbol{w_r},\boldsymbol{n}) = \frac{\boldsymbol{f}(\boldsymbol{w_l},\boldsymbol{n})+\boldsymbol{f}(\boldsymbol{w_r},,\boldsymbol{n})}{2} - \frac{1}{2}|\boldsymbol{A}^{\mathbf{Rossow}}(\tilde{\boldsymbol{w}},\boldsymbol{n})|\,\Delta\boldsymbol{w}$$

Following the analysis conducted in section 2.3.2, the matrix-valued dissipation formulated for the symmetrizing variables has the following expression

$$|\tilde{\boldsymbol{A}}_{\mathbf{0}}^{\mathbf{Rossow}}| = \begin{pmatrix} \frac{c}{c'}(c-|\mathcal{U}_n|)+|\mathcal{U}_n| & n_x\mathcal{U}_n & n_y\mathcal{U}_n & 0 \\ n_x\mathcal{U}_n & n_x^2\frac{c'}{c}(c-|\mathcal{U}_n|)+|\mathcal{U}_n| & n_xn_y\frac{c'}{c}(c-|\mathcal{U}_n|) & 0 \\ n_y\mathcal{U}_n & n_xn_y\frac{c'}{c}(c-|\mathcal{U}_n|) & n_y^2\frac{c'}{c}(c-|\mathcal{U}_n|)+|\mathcal{U}_n| & 0 \\ 0 & 0 & 0 & |\mathcal{U}_n| \end{pmatrix}. \tag{2.55}$$

In contrast to the Rieper's fix (2.55), the symmetry of the original Jacobian matrix is preserved with the introduction of the artificial speed of sound, and the following asymptotic behavior is found in the

incompressible limit

$$|\tilde{\boldsymbol{A}}_{\mathbf{0}}^{\mathbf{Rossow}}| \simeq \begin{pmatrix} \mathcal{O}(\frac{1}{M^2}) & \mathcal{O}(1) & \mathcal{O}(1) & 0 \\ \mathcal{O}(1) & \mathcal{O}(1) & \mathcal{O}(1) & 0 \\ \mathcal{O}(1) & \mathcal{O}(1) & \mathcal{O}(1) & 0 \\ 0 & 0 & 0 & \mathcal{O}(1) \end{pmatrix}. \tag{2.56}$$

In comparison with the original matrix-valued dissipation of the Roe scheme (2.29), the Roe-Rossow scheme increases by one order of magnitude the contributions of the pressure jumps in the first equation, while the dissipation in velocity equations is reduced by one order of magnitude, similarly to the Rieper's fix.

The same test case as considered in Fig.2.1 and Fig.2.2 was used as a preliminary assessment of the Rossow's artificial speed of sound approach. As observed with the Rieper's fix, the Roe-Rossow scheme also shows few differences with both the original Roe scheme and the Roe-Rieper scheme, as indicated in Fig.2.3. Figure 2.3a illustrates the convergence history of the l^2-norms of the normalized explicit residuals with respect to the evolution of the CFL number. The adaptive CFL methodology is the same as in the two previous cases and results in a similar behavior. The computation was initially set to a CFL = 4.5, as a higher value would also result in an unstable computation. Next, at the iteration 10, the adaptive CFL starts with a CFL = 16. Similarly, the CFL value exhibits fluctuations around the 300th iteration, followed by a sudden increase after the 600th iteration leading to a quadratic convergence to the steady-state solution. In that case, in the quadratic phase of the convergence history, the CFL number increases from 50 to a value exceeding 22,000 in about 100 iterations.
Looking at the entropy distribution in Fig.2.3b, we can see similar trends as previously observed with the original Roe scheme and the Rieper's fix. Note that the Roe-Rossow scheme also globally reduces significantly the spurious entropy levels upstream of the shock waves for the first-order scheme, with respect to the original Roe scheme in the same mesh. When considering the MUSCL extrapolation using the van Albada limiter, we can see that the Roe-Rossow scheme (black symbols) produces almost similar spurious entropy levels than the original Roe scheme (green symbols). The comparison with the Rieper's fix shows that the Roe-Rossow scheme generates somewhat higher spurious entropy levels for both the first-order and the second-order schemes.
Figure 2.3c also shows that the numerical shock structure of the shock waves is also almost identical to the Roe scheme and the Rieper's fix.

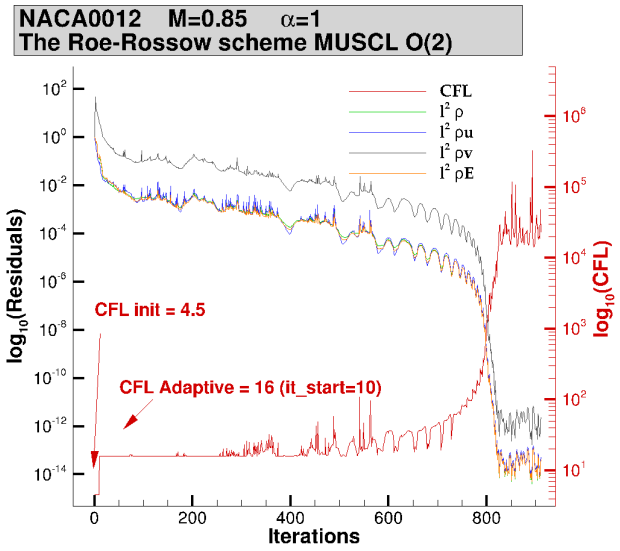

(a) Convergence history for residuals and the CFL

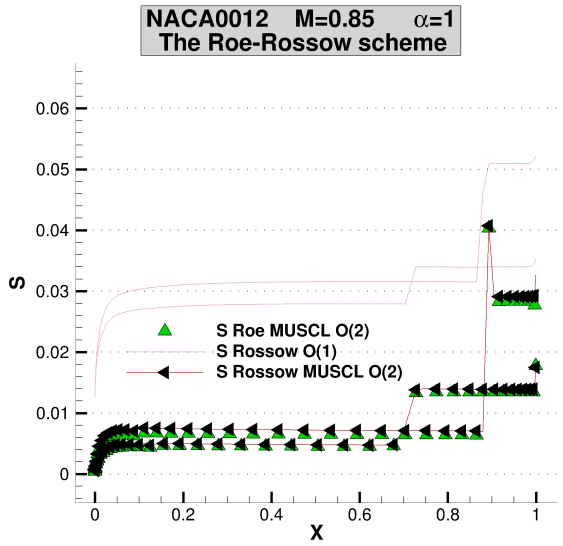

(b) Production of spurious entropy at the wall

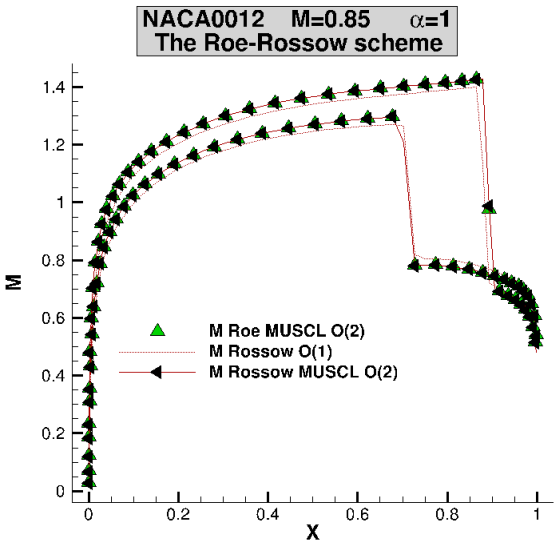

(c) Mach number at the wall

Figure 2.3: Roe-Rossow scheme with MUSCL reconstruction O(2), NACA0012 airfoil at $M = 0.85$ $\alpha = 1°$

2.5.4 . Investigations into a third approach

The following section describes an attempt of formulating a novel low Mach number correction of the Roe scheme, which, upon further analysis, appears interesting to be discussed in this chapter. However, although promising discrete properties can be obtained, the accuracy of the proposed corrections has been found to be less satisfactory than initially anticipated. This may be attributed to the fact that the investigated correction deviates substantially from the theoretical framework proposed in the literature, especially from the framework analysis introduced by Li-Gu [21] based on the Liu-Vinokur decomposition, as shown in the following. Indeed, the modified dissipation vector is formulated using some uncommon practices, which nonetheless turned out to have promising properties according to the asymptotic discrete analysis. This modified dissipation vector ensures the correct pressure fluctuations in the incompressible limit, and even the absence of pressure checkerboard mode problems for the

two initial systems arising at the leading orders in the analysis. Nevertheless, the asymptotic discrete analysis represents only one part of the study of low-Mach number corrections, as it does not address the relations between terms within the dissipation vector.

As previously shown, the Rieper's fix can be associated with an approach based on asymptotically centering the pressure gradient $p^{(1)}$ in the momentum equations, at the order $\mathcal{O}(1/\epsilon)$. In contrast, the alternative approach originally formulated with the Roe-Turkel scheme, can be considered as a discretization avoiding a centered pressure gradient $p^{(0)}$ at the order $O(1/\epsilon^2)$, and consequently, also at the order $O(1/\epsilon)$, for the pressure gradient of $p^{(1)}$. Here, the third approach is inspired by the analysis of Guillard-Viozat (Lemma 3.1 in [7]), which demonstrates that checkerboard modes for $p^{(0)}$ do not exist for the Roe scheme. By reproducing the appropriate asymptotic subsystems at the leading orders $O(1/\epsilon^2)$ and $O(1/\epsilon)$, the accuracy problem is solved while avoiding the existence of spurious pressure checkerboard mode problems in the discrete solutions. To achieve the appropriate subsystems, it is necessary to amplify some of the pressure jumps in the dissipation vector, in an analogous manner to the Roe-Rossow and Roe-Turkel schemes, but here with the objective of centering asymptotically the pressure gradients $p^{(0)}$ and $p^{(1)}$ in the momentum equations, as formulated below. This can be easily achieved by introducing a modified dissipation vector such that:

$$\boldsymbol{d} = |\tilde{\mathcal{U}}_n| \begin{pmatrix} \Delta\rho \\ \Delta\rho u \\ \Delta\rho v \\ \Delta\rho E \end{pmatrix} + \begin{pmatrix} \delta\mathcal{U}_n^{Rossow}\,\tilde{\rho} \\ \delta\mathcal{U}_n^{Roe}\,\tilde{\rho}\tilde{u} \\ \delta\mathcal{U}_n^{Roe}\,\tilde{\rho}\tilde{v} \\ \delta\mathcal{U}_n^{Rossow}\,\tilde{\rho}\tilde{H} \end{pmatrix} + \delta p^{Rossow} \begin{pmatrix} 0 \\ n_x \\ n_y \\ \tilde{\mathcal{U}}_n \end{pmatrix} \quad , \tag{2.57}$$

where the coefficients $(\delta\mathcal{U}_n^{Rossow}, \delta p^{Rossow})$ are given by expressions (2.53), with the original coefficient $\delta\mathcal{U}_n^{Roe}$ in the momentum equations, defined in (2.43). In comparison with the fifteen corrections studied by Li-Gu in [21], the definition of the dissipation vector (2.57) leads to unusual practices, as it decouples the numerical dissipation by introducing two different scalar quantities for the normal interface velocity $\delta\mathcal{U}_n$ according to the equations. Using standard notations adopted by numerous authors for the asymptotic discrete analysis (see chapter 3, section 3.2), the corresponding non-dimension semi-discretized scheme in space for the incompressible limit can be formulated as follows

$$\begin{aligned} h\, d_t\rho_I + \frac{1}{2}\sum_{J\in\mathcal{V}(I)} \Bigg[& \rho_J \mathcal{U}_J \cdot n_{IJ} \\ & - \left\{ |\tilde{\mathcal{U}}_{n_{IJ}}|\Delta_{IJ}\rho + \epsilon\frac{\tilde{\rho}_{IJ}\tilde{\mathcal{U}}_{n_{IJ}}}{\tilde{c}_{IJ}}\Delta_{IJ}\mathcal{U}_n + \frac{1}{\epsilon^2}\frac{\Delta_{IJ}p}{\tilde{c}'_{IJ}}\left(1 - \epsilon\frac{|\tilde{\mathcal{U}}_{n_{IJ}}|}{\tilde{c}_{IJ}}\right) \right\} \Bigg] \quad = 0 \end{aligned} \tag{2.58}$$

$$\begin{aligned} h\, d_t(\rho_I \boldsymbol{\mathcal{U}_I}) + \frac{1}{2}\sum_{J\in\mathcal{V}(I)} \Bigg[& \rho_J \mathcal{U}_J \cdot n_{IJ}\boldsymbol{\mathcal{U}_J} + \frac{1}{\epsilon^2} p_j \boldsymbol{n_{IJ}} \\ & - \Big\{ \tilde{\boldsymbol{\mathcal{U}}}_{\boldsymbol{IJ}} |\tilde{\mathcal{U}}_{n_{IJ}}|\Delta_{IJ}\rho + \tilde{\rho}_{IJ}|\tilde{\mathcal{U}}_{n_{IJ}}|\Delta_{IJ}\boldsymbol{\mathcal{U}} \\ & + \Delta_{IJ}\mathcal{U}_n \left(\epsilon\frac{\tilde{\rho}_{IJ}\tilde{\mathcal{U}}_{n_{IJ}}}{\tilde{c}_{IJ}}\tilde{\boldsymbol{\mathcal{U}}}_{\boldsymbol{IJ}} + \tilde{\rho}_{IJ}\tilde{c}'_{IJ}\boldsymbol{n_{IJ}}\left(1 - \epsilon\frac{|\tilde{\mathcal{U}}_{n_{IJ}}|}{\tilde{c}_{IJ}}\right) \right) \\ & + \Delta_{IJ}p \left(\frac{1}{\epsilon}\frac{\tilde{\boldsymbol{\mathcal{U}}}_{\boldsymbol{IJ}}}{\tilde{c}_{IJ}}\left(1 - \epsilon\frac{|\tilde{\mathcal{U}}_{n_{IJ}}|}{\tilde{c}_{IJ}}\right) + \frac{1}{\epsilon}\frac{\tilde{\mathcal{U}}_{n_{IJ}}}{\tilde{c}_{IJ}}\boldsymbol{n_{IJ}} \right) \Big\} \Bigg] \quad = \boldsymbol{0} \end{aligned} \tag{2.59}$$

$$
\begin{aligned}
h\, d_t(\rho_I E_I) + \frac{1}{2}\sum_{J\in\mathcal{V}(I)}\Bigg[& (\rho_J E_J + p_J)\mathcal{U}_J \cdot n_{IJ} \\
& - \Bigg\{ \epsilon^2 |\tilde{\mathcal{U}}_{n_{IJ}}| \frac{|\tilde{\mathcal{U}}_{IJ}|^2}{2} \Delta_{IJ}\rho + \epsilon^2 \tilde{\rho}_{IJ} |\tilde{\mathcal{U}}_{n_{IJ}}| \tilde{\mathcal{U}}_{IJ} \cdot \Delta_{IJ}\mathcal{U} \\
& + \Delta_{IJ}\mathcal{U}_n \left(\epsilon \tilde{\rho}_{IJ} \tilde{H}_{IJ} \frac{\tilde{\mathcal{U}}_{n_{IJ}}}{\tilde{c}_{IJ}} + \epsilon^2 \tilde{\rho}_{IJ} \tilde{\mathcal{U}}_{n_{IJ}} \tilde{c}'_{IJ} \left(1 - \epsilon \frac{|\tilde{\mathcal{U}}_{n_{IJ}}|}{\tilde{c}_{IJ}}\right) \right) \\
& + \Delta_{IJ}p \left(\frac{|\tilde{\mathcal{U}}_{n_{IJ}}|}{\gamma - 1} + \epsilon \frac{(\tilde{\mathcal{U}}_{n_{IJ}})^2}{\tilde{c}_{IJ}} + \frac{1}{\epsilon^2} \frac{\tilde{H}_{IJ}}{\tilde{c}'_{IJ}} \left(1 - \epsilon \frac{|\mathcal{U}_{n_{IJ}}|}{\tilde{c}_{IJ}}\right) \right) \Bigg\} \Bigg] = 0
\end{aligned}
\tag{2.60}
$$

where the artificial speed of sound used by Rossow $\tilde{c}'_{IJ}$ and its effects in the normalization process are evidenced in blue, and the reference Mach number ϵ is indicated in red. Note that, depending on the initial terms constituting the dissipation vector, there are several possible equivalent formulations for the dissipation, associated with the momentum and energy equations (2.59 - 2.60). The semi-discrete scheme in space presented here is obtained by using the expressions of the Liu-Vinokur decomposition and reformulating the jumps of the conservative variables in the first vector. This is performed using a property of the Roe average for the momentum equations, with the following relation used in the energy equations

$$
\Delta(\rho E) = \frac{1}{\gamma - 1}\Delta p \quad + \quad \frac{|\boldsymbol{\mathcal{U}}|^2 \Delta\rho}{2} \; + \; \rho \boldsymbol{\mathcal{U}} \cdot \Delta \boldsymbol{\mathcal{U}}.
$$

Assuming that the solution can be expanded in power of the Mach number $\varepsilon \ll 1$, and then inserting this expression into the equations, we get the leading-order system at order $\mathcal{O}(1/\epsilon^2)$

$$
\begin{aligned}
& \sum_{J\in\mathcal{V}(I)} \frac{\Delta_{IJ}p^{(0)}}{\tilde{c}'^{(0)}_{IJ}} = 0 \\
& \sum_{J\in\mathcal{V}(I)} p_J^{(0)} \boldsymbol{n_{IJ}} = \mathbf{0} \\
& \sum_{J\in\mathcal{V}(I)} \Delta_{IJ}p^{(0)} \frac{\tilde{H}^{(0)}_{IJ}}{\tilde{c}'^{(0)}_{IJ}} = 0
\end{aligned}
\quad .
\tag{2.61}
$$

The momentum equations in (2.61) entail the existence of spurious pressure checkerboard modes in the solution, as both four-field pressures and a constant pressure $p^{(0)}$ are potential solutions of these equations. However, following the proof given by Guillard-Viozat (Lemma 3.1 in [7]), the uniqueness of a constant pressure in space $p^{(0)}$ can be established through the maximum principle, thereby eliminating the possibility of spurious four-field pressure solutions. As observed in the normalized equations (2.58 - 2.60), all terms involved at the order $\mathcal{O}(1/\epsilon)$ are proportional to the pressure jump Δp. Consequently, the system at the order $\mathcal{O}(1/\epsilon)$ reduces to a previously found result

$$
\begin{aligned}
& \sum_{J\in\mathcal{V}(I)} \frac{\Delta_{IJ}p^{(1)}}{\tilde{c}'^{(0)}_{IJ}} = 0 \\
& \sum_{J\in\mathcal{V}(I)} p_J^{(1)} \boldsymbol{n_{IJ}} = \mathbf{0} \\
& \sum_{J\in\mathcal{V}(I)} \Delta_{IJ}p^{(1)} \frac{\tilde{H}^{(0)}_{IJ}}{\tilde{c}'^{(0)}_{IJ}} = 0
\end{aligned}
\quad .
\tag{2.62}
$$

Then, a similar result can be also obtained for $p^{(1)}$, thus demonstrating that the discrete solution exhibits the correct order of pressure fluctuations in the incompressible limit.
With regard to the asymptotic analyses of the semi-discretized scheme in space, this approach is of interest, as it solves the accuracy problem while also providing a numerical proof that the pressure checkerboard mode problems on $p^{(0)}$ and $p^{(1)}$ do not exist, in accordance with the asymptotic behavior of the vector dissipation.
However, an examination of the numerical results for this modified vector dissipation (2.57) highlights significant discrepancies when compared to the original Roe-Rossow scheme for the same NACA0012 airfoil test-case. Indeed, Fig.2.4b shows a larger increase of spurious entropy produced at the stagnation point. Globally, the modified Roe-Rossow scheme displays higher entropy levels at the wall, in comparison with the Roe scheme at the second-order accuracy in space. The corresponding Mach number distribution is compared in figure 2.4b.

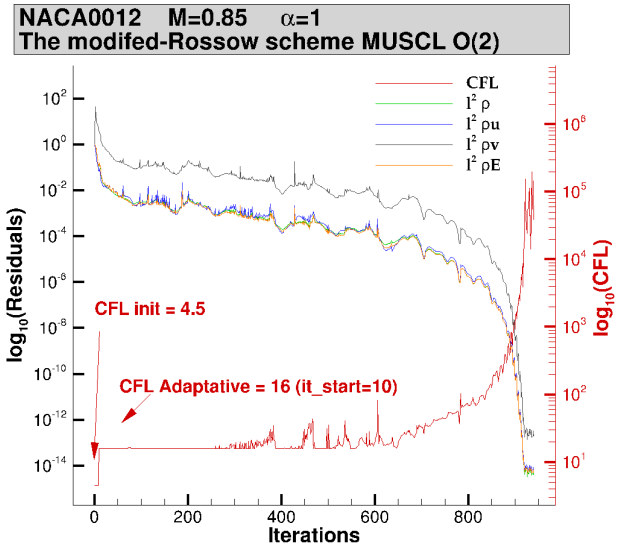

(a) Convergence history for residuals and the CFL

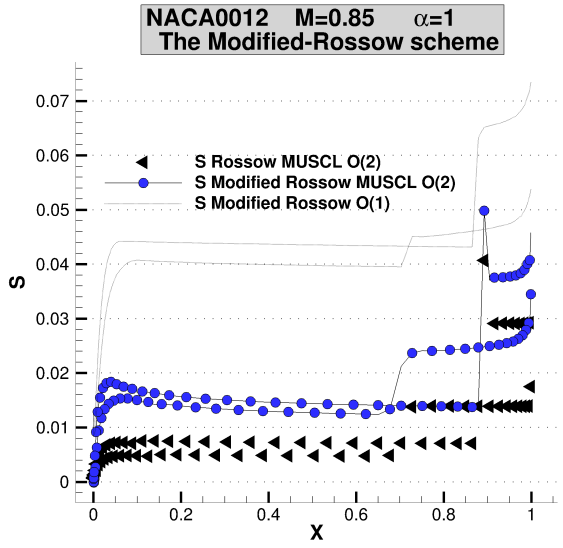

(b) Production of spurious entropy at the wall

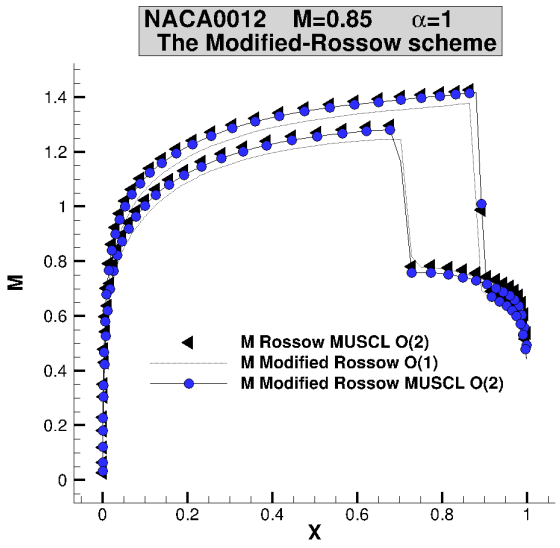

(c) Mach number at the wall

Figure 2.4: Modified Roe-Rossow scheme with MUSCL reconstruction O(2), NACA0012 airfoil at $M = 0.85$ $\alpha = 1^{\circ}$

Additional tests were conducted in order to investigate the behavior of the modified scheme (2.57) for low Mach number flows. The numerical results are not fully satisfactory, as the correction introduces other issues. As an example, looking at the non-lifting cylinder test-case in Fig.2.5 (which is discussed in detail in the next chapter), the discrete solution corresponds to an incorrect approximation of the potential solution upstream of the cylinder. As it can be observed, the symmetry of the solution in the y-direction is lost. The steady-state solution obtained after convergence is characterized by two nonphysical vortices for the inviscid downstream the cylinder.

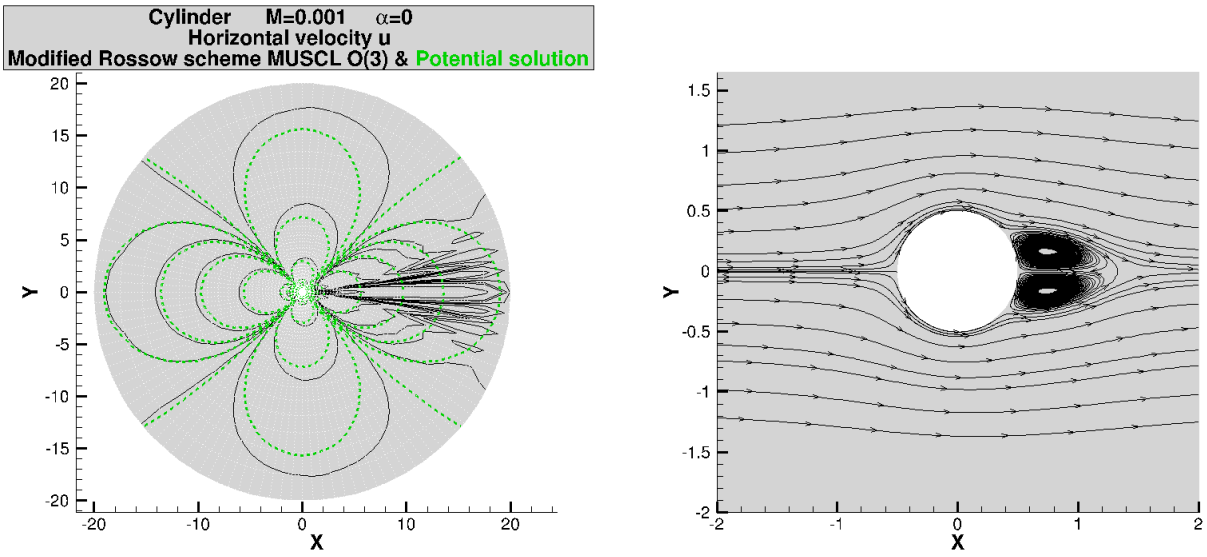

(a) Comparison upstream and downstream

(b) Nonphysical cylinder recirculation bubble for the Euler equations

Figure 2.5: Steady-state solution for the modified Roe-Rossow scheme with MUSCL reconstruction O(3)

This behavior could be explained using the analysis of Turkel in section 2.3.2. Compared to the maximum dissipation allowed for the artificial viscosity matrix in entropic variables (2.35), it is found that the first three entries of the last row of the matrix-valued dissipation of the modified Rossow-scheme are non-zero. Indeed, the simplifications obtained in the final row for the Roe-Rossow scheme are no longer available, as the rescaling is not applied uniformly to all equations in (2.57). This results globally in some unbalanced unbalanced rescaling with too much dissipation introduced, especially in the entropy equation. Without further theoretical developments to correct the spurious production of entropy, no further investigations are presented for this rescaling strategy. In addition, no further interest was found, as this correction is too similar to the second approach consisting in amplifying the pressure jumps in $\delta\mathcal{U}_n$ and could suffers from similar issues.
However, this demonstrates that the accuracy problem for the Roe scheme can be mainly fixed either by centering asymptotically the pressure gradient $p^{(1)}$ in the momentum equations at the order $\mathcal{O}(1/\epsilon)$, or by avoiding a centered pressure gradient $p^{(0)}$ at the order $O(1/\epsilon^2)$, which yields a non-centered pressure gradient of $p^{(1)}$ at the order $O(1/\epsilon)$. These two approaches illustrate two opposite potential corrections, with both having distinct advantages and drawbacks, but also admitting several possible formulations. This discussion is further addressed in the following chapter, providing a detailed analysis of the Roe-Rossow scheme.

3 - Analysis of the Rossow's Artificial Speed of Sound Approach for the Computation of Compressible Flows in the Incompressible Limit

This chapter corresponds to a paper submitted to the Journal of Computational Physics, in which a thorough analysis of the artificial speed of sound approach is carried out.
The novelty of this contribution lies in the asymptotic analysis performed on the modified Roe's approximate Riemann solver according to the artificial speed of sound approach, for the computation of compressible flows in the incompressible limit.
The discrete analysis is formulated in the framework of a standard cell-centered finite-volume method. To our knowledge, the asymptotic discrete properties of this approach, published by C.-C. Rossow more than 20 years ago, are not published in the literature. As mentioned in chapter 2, this approach modifies some entries of the Roe matrix-valued dissipation and especially aims at amplifying the pressure jumps in the incompressible limit.
It is especially shown, within a normalization of the semi-discrete scheme in space, that the discrete solutions are characterized by the correct 2nd order of the pressure disturbances in space at the incompressible time scale, also avoiding enforcing the discrete divergence free constraint of the leading-order velocity. There are numerical evidence illustrating that the Rossow's artificial speed of sound approach is not prone to pressure checkerboard issues in the limit of vanishing Mach numbers.
Results and part of the analysis are compared to the Rieper's low Mach number fix and to the Roe-Turkel scheme. The analysis points out that the artificial speed of sound is very similar to the Roe-Turkel scheme in terms of asymptotic properties.
The contributions of this work are the following:

1 It is demonstrated that the von Neumann stability condition given initially by Rossow has to be completely reformulated in the low speed limit. The resulting stringent stability condition is asymptotically identical to the Roe-Turkel scheme.

2 The analysis also addresses the incompressible-acoustic interactions characterizing the compressible discrete solutions in the incompressible limit. We show that the discrete solutions have permanent acoustic disturbances in the low speed limit, even for the steady-state problem, characterized by acoustic pulses generated at very short times, and dissipated at larger times. The intensity of these acoustic disturbances is related to the modification of the jumps of the normal velocity component at the cell interface.

3 A robust and stable numerical approach is presented, based on modern tools such as Algorithmic Differentiation and fast LU decomposition libraries. This leads to the development of efficient implicit schemes, which remain very stable and overcome the stiffness of the stability constraint in the low Mach number limit. Only a few hundreds of iterations are required to obtain a quadratic convergence to the steady-state solutions, even for very low-Mach number flows decreased up to 10^{-6}.

Moreover, the paper has also 3 appendices, in which are derived the eigenspaces of modified matrix dissipation, a proof regarding the behavior of the spectral radius of the modified matrix-valued dissipation, and the last appendix describes a similar formulation to the Harten-Hyman decomposition for this modified numerical flux. This suggests a careful reformulation of the entropy fix.

Analysis of the Rossow's Artificial Speed of Sound Approach for the Computation of Compressible Flows in the Incompressible Limit

Victor Courtin, Jean-Christophe Boniface*

DAAA, ONERA, Institut Polythechnique de Paris, 92190 Meudon, France

Abstract

We look at a simple modification of the Roe approximate Riemann solver in the incompressible limit, considering the Rossow's artificial speed of sound approach, for compressible flow simulations with inflow Mach numbers decreased up to 10^{-6}. Although published by C.-C. Rossow more than twenty years ago, this approach appears surprisingly to be much less popular than the Roe-Turkel scheme introduced in 1999 by Guillard and Viozat or than the Rieper's low Mach number fix proposed in 2011. In addition, no asymptotic discrete analysis of this modification of the Roe scheme is known in the literature. A common feature of these modified Roe schemes is that they all aimed at introducing a necessary rescaling of the original Roe's matrix-valued dissipation for the computation of low Mach number flows. In this paper, the analysis conducted gives a new insight into the artificial speed of sound approach, with emphasis on properties of the corresponding rescaled dissipation matrix for the solution accuracy, the Von Neumann stability, and the asymptotic behavior of the discrete solutions in the incompressible limit. It is especially shown that, first, the discrete pressure field recovers the proper order of pressure disturbances in space, and second, in opposite to the Rieper's fix, the Rossow's artificial speed of sound is not prone to checkerboard pressure modes. This modification of the Roe scheme has also almost identical discrete asymptotic properties, and the same stringent Von Neumann stability condition, than the Roe-Turkel scheme, although being potentially slightly less dissipative.

Keywords: Euler equations, Low Mach number, Compressible flow, Potential flow, Finite-volume method, Roe scheme, Roe-Turkel scheme, Artificial speed of sound, Low Mach number fix, Incompressible time-scale, Acoustic time-scale, Wave equation, Asymptotic analysis, Checkerboard pressure-velocity decoupling, Von Neumann stability, Implicit scheme

1. Introduction

In the last twenty years, a number of numerical schemes based on the Roe's approximate Riemann solver [1] have been developed in order to compute consistent solutions of the Euler equations with the incompressible limit, while preserving the shock-capturing capability of the original Roe scheme. This is further motivated nowadays, where industry routinely uses CFD in the design process and there are many situations in which industrial flows are characterized by coexisting compressible and nearly incompressible flows. Local low-speed preconditioners became popular in years 90s with the pioneering works of Turkel [2], Choi and Merkel [3], Weiss and Smith [4], Van Leer et al. [5], which were further analyzed and generalized by Turkel et al. [6, 7]. This approach has optimal properties for the convergence of the steady-state problem, improving the conditioning of the flux Jacobian matrix by slowing down the acoustic wave speeds towards the the local velocity, and the accuracy, with a consistent approximation of low Mach number flows. However, the extension to unsteady flows is not trivial and without special care, the time accuracy may be lost [8, 9]. Additionally, low speed preconditioners modify the equations, the flux Jacobian matrix, the stability condition and all boundary conditions based on the characteristic variables or the Riemann invariants must be completely reformulated [10, 11, 12]. Since then, a decreasing interest in the CFD community is observed in the development of local preconditioners for both steady-state and time-dependent problems.

Email address: jean-christophe.boniface@onera.fr ()

In the years 2000, a new density-based approach for compressible flows was considered, aiming at drastically simplifying the extension of compressible schemes to handle incompressible flows. This was initiated with the case of the Roe-Turkel scheme studied by Guillard and Viozat in [13, 14], and followed with the All-Speed Roe-type scheme developed by Li and Gu only modifying the eigenvalues [15, 16], the artificial speed of sound according to Rossow [19, 20, 21, 22], further improved within an implicit time stepping scheme combined to multigrid acceleration techniques [23, 24], and more recently the Rieper's low Mach number fix [25, 26]. The artificial speed of sound and the Roe-Turkel scheme were also compared for high-lift configurations in a recent work by Langer [27]. With this new way of formulating the low speed preconditioning, a clear advantage was found, as the numerical scheme recovers the formulation for compressible flows, with a standard extension to unsteady flows, using usual time-marching algorithms. It is also no longer required to reformulate characteristic-like boundary conditions. All these Roe-type schemes actually aim at providing a more consistent rescaling of the matrix dissipation with the asymptotic behavior of the physical equations in the low speed limit, as pointed out by Turkel et al. [7]. They especially ensure the proper scaling of the pressure field, following the asymptotic discrete analysis developed by Guillard and Viozat [13]. This approach has likely motivated the extension to low Mach number flow of Godunov schemes [28, 29], AUSM-type schemes [30, 31, 32] or more recently to HLL-type Approximate Riemann Solver [33, 34]. However, in modifying the matrix-valued dissipation of the Roe scheme, there are certain features of the numerical procedure that it would also be worth striving for.

First, the proper formulation of the Von Neuman stability condition for the explicit scheme is an essential feature of the numerical procedure, when no preconditioner is applied to the time-derivative. In the formulation of their preconditioned Lax-Friedrichs-Turkel scheme, Birken and Meister [35] have demonstrated that, in the low speed limit, the explicit scheme is stable if the local time-step satisfies a stringent stability condition, given by the spectral radius of the matrix dissipation. This is also the case of the Roe-Turkel scheme reformulated in [36] and with the Rossow's artificial speed of sound, as demonstrated in the paper. In the case of the low Mach number fix for instance, it can be shown that a necessary stability condition is close to the usual Von Neumann condition for compressible flows.

Second, some authors have argued that an accurate extension of the Roe scheme to the incompressible limit should satisfy the discrete divergence-free constraint of the leading order velocity in the asymptotic limit. This is especially the case of the All-Speed Roe scheme developed in [15] and the low Mach number fix [25]. Some other approximate Riemann solvers were also designed to satisfy the discrete divergence-free constraint, see for instance the low Mach correction applied to the all-Mach HLLC scheme developed in [37]. Note that the divergence constraint is not enforced by the Roe-Turkel and by the artificial speed of sound, as shown in the paper. As discussed later, and advocated by Guillard et al. [38], "*they are sound theoretical reasons to prefer a scheme that does not enforce the discrete divergence-free constraint*". Assuming isentropic flow, the functional analysis indicates that two limits of the continuous Euler equations exist, with on one hand the elliptic incompressible system satisfying the divergence-free constraint for the slow incompressible time scale, and on the other hand, an hyperbolic acoustic system for the fast acoustic time scale. Then, the solution of the Euler equations in the incompressible limit is characterized by acoustic-incompressible interactions, in which the incompressible solution is only one component of the solution. This asymptotic behavior with two time scales was well described for instance by Klein for the compressible Euler equations applied to combustion science [39].

In addition, it was also shown that the All-Speed Roe scheme and the low Mach number fix have large inconsistencies in a vertex-centered triangular mesh [38]. This stems from the fact that, from the incompressible theory, using a collocated arrangement for velocity and pressure on unstaggered grids without specific stabilization, undampted spurious pressure modes cannot be ruled out with a cell-centered finite-volume scheme.

As the asymptotic properties of the Rossow's artificial speed of sound approach are not formally derived in the literature, it was found necessary to perform a thorough analysis of this modification of the Roe approximate Riemann solver. The asymptotic and stability analysis especially conducted in this paper gives a new insight into this interesting approach. The scheme introduces simple modifications of the first-order Roe scheme for the computation of low Mach number flows and returns the original Roe scheme at the sonic point according to the local Mach number. Therefore it can also be used for the computation compressible flows with little effort, provided that the entropy fix is formulated carefully at vanishing eigenvalues of the dissipation matrix (see Appendix C).

The following set of independent variables are used throughout the analysis of the compressible Euler equations:

- $\boldsymbol{W} = [\rho, \rho u, \rho v, \rho E]^T$ (conservative variables used for shock-capturing),
- $\boldsymbol{d\tilde{W}_0} = [d\Phi, du, dv, dS\,]^T$ (symmetrizing variables used in the analysis of the asymptotic behavior of the matrix dissipation in the incompressible limit),
- $\boldsymbol{U} = [\rho, u, v, p]^T$ (primitive variables),

where ρ is the density, $\boldsymbol{\mathcal{U}} = [u, v]^T$ are the velocity components, p is the pressure, E is the total energy per unit volume, $H = E + \frac{p}{\rho}$ is the total enthalpy per unit mass, with the differential variables $d\Phi = \frac{dp}{\rho c}$ proportional to the pressure and $dS = \frac{dp - c^2 d\rho}{\rho c}$ proportional to the entropy, c being the speed of sound.

In all the following, we assume that the flowfield satisfies the ideal gas law. So $c^2 = \gamma \frac{p}{\rho}$ and $H = \dfrac{c^2}{(\gamma - 1)} + \dfrac{|\boldsymbol{\mathcal{U}}|^2}{2}$, γ being the ratio of the specific heats.

We consider the Euler equations in integral form on each computational cell Ω of the structured mesh, with boundary $\partial\Omega$ with unit outward normal $\boldsymbol{n} = [n_x, n_y]^T$:

$$\frac{d}{dt} \int_{\Omega} \boldsymbol{W}\, dV + \int_{\partial\Omega} \boldsymbol{F}(\boldsymbol{W}) \cdot \boldsymbol{n}\, dS = \boldsymbol{0} \tag{1}$$

where $\boldsymbol{F}$ is the flux vector. System (1) is discretized using a cell-centered finite-volume method. This leads to the semi-discrete form:

$$V \frac{d}{dt} \boldsymbol{W} + \boldsymbol{R}(\boldsymbol{W}, \boldsymbol{n}) = \boldsymbol{0}, \qquad \text{with} \qquad \boldsymbol{R}(\boldsymbol{W}, \boldsymbol{n}) = \sum_{cell\ boundary} \boldsymbol{F}(\boldsymbol{W}) \cdot \boldsymbol{n}\, S \tag{2}$$

where V denotes the volume of the computational cell and S is the area of the cell interface.

We will consider next modifications in the low-speed limit of the baseline first-order Roe scheme [1], with the numerical flux $\mathcal{F}$ discretizing the physical flux $\boldsymbol{F}$ across the cell interfaces:

$$\mathcal{F} = \frac{1}{2} \left[\boldsymbol{F}(\boldsymbol{W_R}) + \boldsymbol{F}(\boldsymbol{W_L})\right] - \frac{1}{2} |\boldsymbol{A}_{roe}| \, (\boldsymbol{W_R} - \boldsymbol{W_L}) \tag{3}$$

where $\boldsymbol{W_L}$ and $\boldsymbol{W_R}$ are the left and right (usually reconstructed) solution vectors in adjacent cells to the cell interface and $\boldsymbol{A}_{roe}$ is the Roe matrix.

The analysis described in the following focuses on the properties of the modified matrix-valued dissipation in the subsonic regime. For the baseline first-order Roe scheme, the dissipation vector $\boldsymbol{d} = |\boldsymbol{A}_{roe}| \, (\boldsymbol{W_R} - \boldsymbol{W_L}) = |\boldsymbol{A}_{roe}| \Delta \boldsymbol{W}$ leads to large inconsistencies of the discrete solution in the incompressible limit, due to an improper asymptotic behavior of the coefficients of the matrix dissipation $|\boldsymbol{A}_{roe}|$. The artificial speed of sound approach, and many other published corrections of the Roe scheme, modify the matrix dissipation following different ideas. Modifying the matrix dissipation has also a large impact on the numerical stability in the incompressible limit, as shown in [35] for the preconditioned Lax Friedrich scheme and in [36] for the Roe-Turkel scheme. The link between the asymptotic behavior of the numerical scheme and the Von Neumann condition for stability was also described for the SUPG scheme developed in [40], where it is shown that a necessary condition for stability requires that the asymptotic behavior of the entries of the dissipation matrix matches that of the terms of the Euler equations.

This article is organized as follows. The next section 2, the Rossow's artificial speed of sound approach is introduced. The important section 3 is dedicated to the asymptotic analysis of the artificial speed of sound approach in the incompressible limit. Eigenvalues and the spectral radius of the modified matrix dissipation are derived in section 4, and the Von Neumann condition for stability is discussed. Stability considerations are of major importance when computing compressible low Mach number flows. This has motivated the development of an efficient implicit Newton-like scheme described in 5, based on Algorithmic Differentiation (AD) of the flux residual and fast algorithms for the construction and inversion of the corresponding exact Jacobian matrix. This implicit scheme allows using very large CFL numbers for the steady-state problem, in order to overcome the stringent stability condition. Numerical experiments presented in sections 6 and 7 illustrate the main results of the above analysis. Some comments and perspectives are given as concluding remarks in section 8.

2. Rescaling of the Roe Scheme According to Rossow

In the following, we assume the flow subsonic across the cell interface, i.e. $|M_n| \leq 1$, where $M_n = \dfrac{\mathcal{U}_n}{c}$ is the directional Mach number, $\mathcal{U}_n = un_x + vn_y$ being the normal velocity at the cell interface. Then the acoustic eigenvalues of the dissipation matrix according to Roe $|\boldsymbol{A}_{roe}|$ are given by $|\lambda_-| = c - \mathcal{U}_n$ and $|\lambda_+| = c + \mathcal{U}_n$, and the dissipation vector expressed for the jumps of the primitive variables can be formulated explicitly.

In successive works [19, 20, 21, 22], Rossow introduces the interface Mach number $M_0 = sgn(\dfrac{\mathcal{U}_n}{c})\ min(M_n, 1)$ and formulates the dissipation vector for the jumps of the primitive variables, within expansions with terms factored by M_0 and $(1 - |M_0|)$. For subsonic flows, the interface Mach number is then simply defined as $M_0 = M_n$ and the rescaling of the Roe scheme in the incompressible limit was achieved by introducing an artificial speed of sound as described in [19, 22]. This approach was further developed by Rossow in [21] for a blended pressure/density based scheme and in [22] considering a pure density-based approach. We shall consider here this later implementation. The rescaling is obtained by replacing the speed of sound c in the non-vanishing coefficients $(1 - |M_0|)$ with an artificial speed of sound $c^{'}$.

Let $\boldsymbol{d} = [\Delta \boldsymbol{F}_\rho, \Delta \boldsymbol{F}_{\rho V}, \Delta \boldsymbol{F}_{\rho E}]^T$ be the components of the dissipation vector corresponding to the mass, momentum and energy conservation laws. We remind for sake of clarity the dissipation vector corresponding to the rescaled Roe scheme with artificial speed of sound $c^{'}$, introduced in [20] (Table 1) and described in the three-dimensional case in [24]

$$
\begin{array}{lllll}
\Delta \boldsymbol{F}_\rho & = |\mathcal{U}_n|\Delta\rho & + \rho M_0 \Delta \mathcal{U}_n & + \frac{1}{c^{'}}(1 - |M_0|)\Delta p \\
\Delta \boldsymbol{F}_{\rho\mathcal{U}} & = |\mathcal{U}_n|\boldsymbol{\mathcal{U}}\Delta\rho + \rho|\mathcal{U}_n|\Delta\boldsymbol{\mathcal{U}} & + \Big[\rho\boldsymbol{\mathcal{U}}M_0 + \rho c^{'}\boldsymbol{n}(1 - |M_0|)\Big]\Delta\mathcal{U}_n & + \Big[\boldsymbol{n}M_0 + \frac{1}{c^{'}}\boldsymbol{\mathcal{U}}(1 - |M_0|)\Big]\Delta p \\
\Delta \boldsymbol{F}_{\rho E} & = |\mathcal{U}_n|\dfrac{|\boldsymbol{\mathcal{U}}|^2}{2}\Delta\rho + \rho|\mathcal{U}_n|\boldsymbol{\mathcal{U}}.\Delta\boldsymbol{\mathcal{U}} & + \Big[\rho H M_0 + \rho\mathcal{U}_n c^{'}(1 - |M_0|)\Big]\Delta\mathcal{U}_n & + \Big[\frac{1}{(\gamma-1)}|\mathcal{U}_n| + \mathcal{U}_n M_0 + \frac{H}{c^{'}}(1 - |M_0|)\Big]\Delta p.
\end{array}
\tag{4}
$$

So, with this modification of the dissipation vector, only terms factored by $1 - |M_0|$ dominating in the incompressible limit are modified by the correction. The artificial speed of sound is defined from a local diagonal preconditioner:

$$
c^{'} = c\sqrt{\alpha^2 M_n^2 + \beta^2}, \qquad \text{with} \qquad \alpha = \frac{1}{2}(1 - \beta^2) \qquad \text{and} \qquad \beta^2 = \min(\max(M^2, M_{ref}^2), 1), \tag{5}
$$

where M is the Mach number, and M_{ref} is related to a reference Mach number. This formulation actually borrows the modified speed of sound arising from the preconditioning of the Jacobian matrix $\boldsymbol{PA}$, with all eigenvalues slowed down towards the local flow velocity as the Mach number goes to zero (see for instance Turkel et al. for a general form of preconditioners [7]). Then we have:

$$
c^{'} \longrightarrow V_{ref} \qquad \text{as} \qquad M \longrightarrow 0, \tag{6}
$$

where V_{ref} is some reference speed. In order to recover the proper scaling of the matrix dissipation in the incompressible limit, the dominance of the pressure difference terms is strongly amplified, with

$$
\frac{1}{c^{'}}(1 - |M_0|) \simeq O(1) \qquad \text{while} \qquad \frac{1}{c}(1 - |M_0|) \simeq O(M), \tag{7}
$$

whereas the dominance of the jumps of the directional velocity $\Delta\mathcal{U}_n$ is reduced in the momentum and total energy equations. Rossow assessed that a better scaling of the pressure field could be retrieved by simply substituting the speed of the sound by expression (6) in the above expansions and thoroughly demonstrated this statement in [22] (see also [23]) within grid convergence, Reynolds number and Mach number effects. In [41], this idea of artificial speed of sound has been adapted to a preconditioning method, which turned out to be more robust than the standard preconditioning using matrix-dissipation $\boldsymbol{P}^{-1}|\boldsymbol{PA}|$.

However, the Rossow's artificial speed of sound approach does not bring the same modifications to the jumps of the normal velocity, as formulated by the Rieper's fix. The jumps of the normal velocity are strongly related to the

intensity of the acoustic content in the discrete solution, as demonstrated in [29] for the case of the Godunov scheme, which may be hard to damp out in the very incompressible limit considering a steady-state approach, as illustrated later in the paper.

In our implementation, as previously done for the formulation of the Roe-Turkel scheme in [36], the arbitrary reference Mach number M_{ref}, acting as a cut-off value in the definition (5) of the artificial speed of sound, was set to a much smaller value than a reference Mach number, and even to the order of magnitude of the zero-level machine in most of the cases, regardless of the mesh used. Note that in the case of the Roe-Turkel scheme formulated in [13] and the preconditioned Godunov scheme considered in [29], the use of a reference Mach number in the global preconditioning parameter M_{ref} in coefficient β^2 is not always explicitly mentioned.

In the remaining of the paper, the scheme characterized by the dissipation vector (4) with the artificial speed of sound (5) according to Rossow will be simply referred to as the Roe-Rossow scheme.

Next, we shall introduce a more convenient expression of the dissipation vector, i.e. not restricted to subsonic flows. Following a common analysis framework introduced by Li-Gu in [17], the expression of the dissipation vector can be rearranged according to the Liu-Vinokur decomposition [50]. This form has been popularized by the pioneer work of Weiss-Smith [4] regarding the development of local low Mach number preconditioners. According to this decomposition, the modified dissipation vector with the artificial speed of sound can be expressed equivalently as a sum of three vectors:

$$\boldsymbol{d} = |\mathcal{U}_n| \begin{bmatrix} \Delta\rho \\ \Delta(\rho \boldsymbol{U}) \\ \Delta(\rho E) \end{bmatrix} + \delta\mathcal{U}_n \begin{bmatrix} \rho \\ \rho \boldsymbol{U} \\ \rho H \end{bmatrix} + \delta p \begin{bmatrix} 0 \\ \boldsymbol{n} \\ \mathcal{U}_n \end{bmatrix}, \tag{8}$$

where the first vector corresponds to the basic scalar upwind dissipation, and the second and third coefficients $\delta\mathcal{U}_n$ and δp are related to the convected velocity and the pressure at the cell interface, respectively

$$\delta\mathcal{U}_n = \frac{A}{\rho c c'}\Delta p \; + \; \frac{B}{c}\Delta\mathcal{U}_n, \qquad \delta p = \frac{B}{c}\Delta p \; + \; \rho\frac{c'}{c}A\Delta\mathcal{U}_n, \tag{9}$$

with coefficients

$$A = \frac{|\lambda_+| + |\lambda_-|}{2} - |\lambda_0|, \qquad B = \frac{|\lambda_+| - |\lambda_-|}{2}, \tag{10}$$

only depending on the original eigenvalues of the Roe matrix.

3. Asymptotic Analysis in the Incompressible Limit

Different types of asymptotic analysis as presented next allows a better understanding of the behavior characterizing the Roe-Rossow scheme in the incompressible limit. In order to investigate the underlying effects of the artificial speed of sound approach and the discrete properties of the resulting scheme, we shall proceed step by step as indicated in the following.

The analysis starts with the asymptotic behavior of the matrix-valued dissipation, with expected effects on the solution accuracy, for the equations recast in symmetrizing variables. Then, a usual normalization process employed in the low Mach number analysis of the Euler equations is introduced and a preliminary discrete analysis is derived and discussed, using the comprehensive framework proposed by Li-Gu for the Roe scheme.

Finally, a fully discrete asymptotic analysis is conducted, confirming the main trends given by results obtained with the Li-Gu analysis.

3.1. Asymptotic behavior of the matrix-valued dissipation in symmetrizing variables

Turkel [9, 12] suggested to use the symmetrizing variables $d\tilde{\boldsymbol{W}}_{\boldsymbol{0}}$, which greatly simplifies the analysis and a much easier formulation of the dissipation matrix is obtained. In particular, the main results of the stability analysis carried out in section 4 and the two formulations of the entropy fix indicated in Appendix C are derived using this set of symmetrizing variables.

The dissipation vector can be further expanded to be recast in jumps of $\boldsymbol{d\tilde{W}_0}$ variables. Applying the pre-multiplication with $\dfrac{\partial \tilde{\boldsymbol{W}}_{\mathbf{0}}}{\partial \boldsymbol{W}}$ for the change of variables (see Appendix A), we get in matrix dissipation form:

$$\tilde{\boldsymbol{d}}_{\mathbf{0}} = \frac{\partial \tilde{\boldsymbol{W}}_{\mathbf{0}}}{\partial \boldsymbol{W}} \boldsymbol{d} = \tilde{\boldsymbol{D}}_{\mathbf{0}} \, \Delta \tilde{\boldsymbol{W}}_{\mathbf{0}}, \tag{11}$$

with the modified matrix-valued dissipation in $\boldsymbol{d\tilde{W}_0}$ variables:

$$\tilde{\boldsymbol{D}}_{\mathbf{0}} = \begin{pmatrix} r(c - |\mathcal{U}_n|) + |\mathcal{U}_n| & n_x \mathcal{U}_n & n_y \mathcal{U}_n & 0 \\ n_x \mathcal{U}_n & n_x^2 \dfrac{1}{r}(c - |\mathcal{U}_n|) + |\mathcal{U}_n| & n_x n_y \dfrac{1}{r}(c - |\mathcal{U}_n|) & 0 \\ n_y \mathcal{U}_n & n_x n_y \dfrac{1}{r}(c - |\mathcal{U}_n|) & n_y^2 \dfrac{1}{r}(c - |\mathcal{U}_n|) + |\mathcal{U}_n| & 0 \\ 0 & 0 & 0 & |\mathcal{U}_n| \end{pmatrix}, \tag{12}$$

where the dimensionless ratio is introduced

$$r = \frac{c}{c'} = \frac{1}{\sqrt{\alpha^2 M_n^2 + \beta^2}} \geq 1. \tag{13}$$

Note that this ratio is directional, i.e. depending explicitly on the cell face orientation with the directional Mach number M_n. Setting $r = 1$, matrix (12) returns to the original Jacobian matrix, with no rescaling.

In addition, we can see that the approach of Rossow preserves the symmetry property of the original Jacobian matrix for this set of variables.

In the incompressible limit, it can be stated that:

$$\tilde{\boldsymbol{D}}_{\mathbf{0}} \simeq \begin{pmatrix} O(\frac{1}{M^2}) & O(1) & O(1) & 0 \\ O(1) & O(1) & O(1) & 0 \\ O(1) & O(1) & O(1) & 0 \\ 0 & 0 & 0 & O(1) \end{pmatrix} \quad \text{as} \quad M \longrightarrow 0. \tag{14}$$

This has to be compared with the maximum allowed dissipation achieved by the Roe-Turkel scheme, for a consistent rescaling of the matrix dissipation with the asymptotic behavior of the physical portion of the equations, according to the scaling analysis employed by Turkel et al. [7, 12]

$$\tilde{\boldsymbol{P}}_{\mathbf{0}}{}^{-1} |\tilde{\boldsymbol{P}}_{\mathbf{0}} \tilde{\boldsymbol{A}}_{\mathbf{0}}| \simeq \begin{pmatrix} O(\frac{1}{M^2}) & O(\frac{1}{M}) & O(\frac{1}{M}) & 0 \\ O(\frac{1}{M}) & O(1) & O(1) & 0 \\ O(\frac{1}{M}) & O(1) & O(1) & 0 \\ 0 & 0 & 0 & O(1) \end{pmatrix} \quad \text{as} \quad M \longrightarrow 0. \tag{15}$$

So we see that the Roe-Rossow scheme introduces somewhat less dissipation in the incompressible limit in the equations for the pressure and the velocity components. However, in the pressure equation, the leading-order dissipation coefficient behaves identically ($\simeq O(\frac{1}{M^2})$) for both schemes. In practice, this lower amount of dissipation in entropic variables provided by the Roe-Rossow scheme is not clearly reproduced by computations, when compared to solutions obtained with the Roe-Turkel scheme. This asymptotic behavior can also be compared to the matrix dissipation

characterizing the low Mach number fix proposed by Rieper in [25], for which

$$\tilde{\boldsymbol{D}}_{\mathbf{0}} \simeq \begin{pmatrix} O(\frac{1}{M}) & O(M) & O(M) & 0 \\ O(1) & O(1) & O(1) & 0 \\ O(1) & O(1) & O(1) & 0 \\ 0 & 0 & 0 & O(1) \end{pmatrix} \quad \text{as} \quad M \longrightarrow 0. \tag{16}$$

We first note that the symmetry of the original Jacobian matrix is no longer preserved with the Rieper's fix. Second, it can be seen that the low Mach number fix yields a less dissipative scheme, especially in the scaling of the pressure equation, with diminishing dissipation coefficients with an order $O(M)$ compared to the Roe-Rossow scheme and up to $O(M^2)$ compared to the Roe-Turkel scheme.

3.2. Discrete asymptotic analysis

We next introduce the normalized quantities (time, space, flow variables) used in the incompressible normalization of the Euler equations, with successively

$$\tilde{t} = t\frac{v_{ref}}{l_{ref}}, \quad \tilde{x} = \frac{x}{l_{ref}}, \quad \tilde{y} = \frac{y}{l_{ref}}, \quad \tilde{\rho} = \frac{\rho}{\rho_{ref}}, \quad \tilde{u} = \frac{u}{v_{ref}}, \quad \tilde{v} = \frac{v}{v_{ref}}, \quad \tilde{c} = \frac{c}{c_{ref}}, \quad \tilde{p} = \frac{p}{p_{ref}}, \tag{17}$$

where l_{ref} is a reference length scale, ρ_{ref} a reference density, v_{ref} the reference speed, c_{ref} a reference speed of sound and $p_{ref} = \rho_{ref} c_{ref}^2$ a reference pressure. The reference velocity is independent of the reference speed of sound $\sqrt{p_{ref}/\rho_{ref}}$. This ensures that the normalized speed velocity remains of order $O(1)$ in the limit of a vanishing reference Mach number, defined in all the following with

$$\epsilon = \frac{v_{ref}}{c_{ref}}. \tag{18}$$

So, in the normalization process, all above quantities are of the same order of magnitude, around unity. In addition, taking identical reference quantity for the total enthalpy and the total energy $E_{ref} = H_{ref} = p_{ref}/\rho_{ref}$, the total enthalpy is not modified by the normalization $\tilde{H} = \tilde{E} + \tilde{p}/\tilde{\rho}$. However, the equation of state is modified as follows

$$\tilde{p} = (\gamma - 1)[\tilde{\rho}\tilde{E} - \epsilon^2 \frac{\tilde{u}^2 + \tilde{v}^2}{2}]. \tag{19}$$

Note that the above normalization for $\tilde{t}$ corresponds to an incompressible or convective time-scale. An acoustic time-scale can also be defined by replacing the reference velocity v_{ref} by the reference speed of sound c_{ref} in the expression of $\tilde{t}$.

As demonstrated in [13], at the incompressible time-scale, this normalization process applied to the compressible Euler equations indicates that the pressure gradient is the dominating term with factor $1/\epsilon^2$ and that the pressure field is constant in space up to second-order fluctuations

$$\tilde{p}(x, y, t) = \tilde{p}_0(t) + \epsilon \tilde{p}_1(t) + \epsilon^2 \tilde{p}_2(x, y, t) = \tilde{P}_0(t) + \epsilon^2 \tilde{p}_2(x, y, t). \tag{20}$$

In this expression, $\tilde{P}_0$ corresponds to the surrounding ambient pressure, and the pressure disturbance field $\tilde{p}_2$ can be interpreted as the "incompressible" pressure satisfying a Poisson-type equation. This normalization process also shows that the leading order velocity $\boldsymbol{\mathcal{U}}_0$ satisfies a divergence-free constraint $\boldsymbol{\nabla} \cdot \boldsymbol{\mathcal{U}}_{\mathbf{0}} = 0$. However, there are theoretical reasons demonstrating that this property should not be reproduced at the discrete level, as indicated next.

At the acoustic time-scale, the pressure field is constant in space up to first-order fluctuations only and $\tilde{p}_1(x, y, t)$ is solution of a linear wave equation [38].

3.2.1. Preliminary semi-empirical discrete analysis of the dissipation vector

Following the formalism introduced by Li-Gu in [17] for the comparison of fifteen different low-Mach modifications of the dissipation vector, the normalization process of the discrete scheme yields the following normalized form of decomposition (8)

$$\tilde{\boldsymbol{d}} = |\tilde{\mathcal{U}}_n| \begin{bmatrix} 1 & 0 & 0 \\ 0 & 1 & 0 \\ 0 & 0 & 1 \end{bmatrix} \begin{bmatrix} \Delta\tilde{\rho} \\ \Delta(\tilde{\rho}\tilde{\boldsymbol{U}}) \\ \Delta(\tilde{\rho}\tilde{E}) \end{bmatrix} + \delta\check{\mathcal{U}}_n \begin{bmatrix} 1 & 0 & 0 \\ 0 & 1 & 0 \\ 0 & 0 & 1 \end{bmatrix} \begin{bmatrix} \tilde{\rho} \\ \tilde{\rho}\tilde{\boldsymbol{U}} \\ \tilde{\rho}\tilde{H} \end{bmatrix} + \delta\check{p} \begin{bmatrix} 0 & 0 & 0 \\ 0 & 1 & 0 \\ 0 & 0 & \epsilon \end{bmatrix} \begin{bmatrix} 0 \\ \boldsymbol{n} \\ \tilde{\mathcal{U}}_n \end{bmatrix}. \tag{21}$$

In this expression, $(\delta\check{\mathcal{U}}_n, \delta\check{p})$ are some function of the normalized coefficients $(\delta\mathcal{U}_n, \delta p)$ in the low Mach number range. In the case of the Roe-Rossow scheme, when compared to the Roe scheme and the Rieper's fix, we get successively

$$\begin{aligned}
&\text{Rossow:} \quad \delta\check{\mathcal{U}}_n = (1-\epsilon\frac{|\tilde{\mathcal{U}}_n|}{\tilde{c}})\frac{1}{\epsilon^2}\frac{\Delta\tilde{p}}{\tilde{\rho}\tilde{c}'} + \epsilon\frac{\tilde{\mathcal{U}}_n}{\tilde{c}}\Delta\tilde{\mathcal{U}}_n, \qquad \delta\check{p} = \tilde{\mathcal{U}}_n\frac{1}{\epsilon}\frac{\Delta\tilde{p}}{\tilde{c}} + (1-\epsilon\frac{|\tilde{\mathcal{U}}_n|}{\tilde{c}})\tilde{\rho}\tilde{c}'\Delta\tilde{\mathcal{U}}_n, \\
&\text{Roe:} \quad \delta\check{\mathcal{U}}_n = (1-\epsilon\frac{|\tilde{\mathcal{U}}_n|}{\tilde{c}})\frac{1}{\epsilon}\frac{\Delta\tilde{p}}{\tilde{\rho}\tilde{c}} + \epsilon\frac{\tilde{\mathcal{U}}_n}{\tilde{c}}\Delta\tilde{\mathcal{U}}_n, \qquad \delta\check{p} = \tilde{\mathcal{U}}_n\frac{1}{\epsilon}\frac{\Delta\tilde{p}}{\tilde{c}} + \frac{1}{\epsilon}(1-\epsilon\frac{|\tilde{\mathcal{U}}_n|}{\tilde{c}})\tilde{\rho}\tilde{c}\Delta\tilde{\mathcal{U}}_n, \\
&\text{Rieper:} \quad \delta\check{\mathcal{U}}_n = (1-\epsilon\frac{|\tilde{\mathcal{U}}_n|}{\tilde{c}})\frac{1}{\epsilon}\frac{\Delta\tilde{p}}{\tilde{\rho}\tilde{c}} + \epsilon^2\tilde{z}\frac{\tilde{\mathcal{U}}_n}{\tilde{c}}\Delta\mathcal{U}_n, \qquad \delta\check{p} = \tilde{\mathcal{U}}_n\frac{1}{\epsilon}\frac{\Delta\tilde{p}}{\tilde{c}} + (\tilde{z}-\frac{|\tilde{\mathcal{U}}_n|}{\tilde{c}})\tilde{\rho}\tilde{c}\Delta\tilde{\mathcal{U}}_n,
\end{aligned} \tag{22}$$

where $\tilde{z}$ is the normalized Rieper's fix $z = \epsilon\tilde{z}$, with the fix simply defined as a local directional Mach number formulated originally by Rieper $z = \dfrac{|\mathcal{U}_n| + |\mathcal{U}_t|}{c}$, where $\mathcal{U}_t$ the tangential velocity at the cell interface.

These coefficients actually provide a deeper insight into the respective discrete asymptotic properties of these respective corrections of the matrix dissipation. According to the analysis performed by Li-Gu, the asymptotic behavior in the incompressible limit of these coefficients indicates the ability of the modified scheme to compute the correct order of the pressure disturbances (so-called later the physical problem) and to avoid the occurrence of pressure checkerboard modes.

In more details, regarding the pressure coefficient $\delta\check{p}$ in (22), Li-Gu observed that the term $\rho c\Delta\mathcal{U}_n$ must reach the order $O(1)$ to cure the non physical problem. Indeed, this is a common feature of most of the modified Roe-type schemes investigated in [17]. Looking at the corresponding normalized coefficient for the Roe-Rossow scheme, compared to the Rieper's fix, we see from expressions (22) that

$$(\delta\check{\mathbf{p}}) \qquad \text{Rossow:} \quad (1-\epsilon\frac{|\tilde{\mathcal{U}}_n|}{\tilde{c}})\tilde{\rho}\tilde{c}'\Delta\tilde{\mathcal{U}}_n \simeq \tilde{\rho}\tilde{c}'\Delta\tilde{\mathcal{U}}_n \simeq O(1), \qquad \text{Rieper:} \quad (\tilde{z}-\frac{|\tilde{\mathcal{U}}_n|}{\tilde{c}})\tilde{\rho}\tilde{c}\Delta\tilde{\mathcal{U}}_n \simeq O(1). \tag{23}$$

as $\epsilon \longrightarrow 0$. Then both schemes should compute discrete solutions satisfying the proper scaling (20) of the pressure field.

In a series of published works [15, 18], Li-Gu have shown the interest of the Momentum Interpolation Method (MIM) for their All-Speed-Roe scheme to cure checkerboard modes. Such mechanisms, already known for the AUSM+(P) scheme [30, 31, 32], can also be employed to enforce the pressure-velocity coupling in the low Mach-number limit. Regarding the coefficient $\delta\check{\mathcal{U}}_n$, it has been especially stated in [17]-(section 4) that the pressure difference term within has a strong effect to damp out pressure checkerboard modes. Comparing again the Roe-Rossow scheme with the Rieper's fix, we see this time that both schemes yield a different behavior, since for the leading-order term we get

$$(\delta\check{\mathcal{U}}_{\mathbf{n}}) \qquad \text{Rossow:} \quad \frac{1}{\epsilon^2}(1-\epsilon\frac{|\tilde{\mathcal{U}}_n|}{\tilde{c}})\frac{\Delta\tilde{p}}{\tilde{\rho}\tilde{c}'} \simeq O(\frac{1}{\epsilon^2}), \qquad \text{Rieper:} \quad (1-\epsilon\frac{|\tilde{\mathcal{U}}_n|}{\tilde{c}})\frac{1}{\epsilon}\frac{\Delta\tilde{p}}{\tilde{\rho}\tilde{c}} \simeq O(\frac{1}{\epsilon}), \tag{24}$$

as $\epsilon \longrightarrow 0$. It is worth mentioning that Li-Gu have found a similar behavior $O(1/\epsilon^2)$ of this coefficient for the Roe-Turkel scheme. These results show that Roe-Rossow scheme undergoes the same asymptotic behavior as the

Roe-Turkel scheme, and thus should also avoid the occurrence of pressure checkerboard modes. According to the second rule, this correction should not be prone to checkerboard mode problems, in opposition with the Rieper's fix.

Following the analysis of Li-Gu, this asymptotic behavior also indicates that the divergence-free constraint for the leading velocity $\mathcal{U}_0$ should not be satisfied by the Roe-Rossow scheme. Indeed, this discrete property was first established by Li-Gu for the Roe-Turkel scheme in [15]. It has been especially shown that, this condition is one pre-requisite for deriving a Poisson-type equation for the second-order pressure disturbance $p^{(2)}$. Some of these assertions are partially true in the case of the Roe-Rossow scheme, as demonstrated in the next section.

However, in accordance with the conclusions of Li-Gu, we also believe that the pressure checkerboard mode problems are only partially explained in published works. To our experience, in practice, no checkerboard issues could be observed for the Roe-Rossow scheme, even in highly stretched or high density meshes, for all inflow Mach number tested, up to very low Mach numbers considered in this paper. In addition, no such discrete problem seems to have been reported in the literature with the Roe-Turkel scheme, except in a previous work by Li-Gu [15], but no longer mentioned later [17].

On the other hand, regarding the Rieper's fix, the occurrence of pressure checkerboard modes can be easily triggered, as illustrated in the section 6. According to the original paper [25], the discrete solution may encounter some checkerboard mode problem for the first-order disturbance pressure p_1 in conjunction with enforcing the discrete divergence-free property of the leading order velocity. Although, in practice, weak checkerboard modes for the second-order disturbance pressure p_2 are also observed. Thus, with the Rieper's fix, it is well known that in the low Mach number limit, the discrete solution may undergo some transient undamped spurious pressure modes, strongly contaminating the discrete solution.

3.2.2. Asymptotic analysis of the semi-discrete equations in space at the incompressible time scale

Results discussed in the previous sections for the Roe-Rossow scheme are thoroughly demonstrated in this section within a discrete asymptotic analysis of the normalized semi-discrete scheme in space. The underlying idea is to reproduce at the discrete level the continuous analysis carried out for the normalized compressible equations in [39, 45]. This approach was first applied by Guillard-Viozat [13] in the incompressible limit, for the Roe-Turkel scheme. From the normalized space-discretization, significant discrete properties of the asymptotic behavior of the discrete solutions can be recovered, especially for the pressure field, which can be compared with the continuous case. In all the following, the tilde symbol introduced in the previous section in the normalization process is omitted.

Let introduce the space discretization of the Euler equations using a uniform mesh spacing h of some arbitrary cell Ω_I of the computational mesh

$$h\frac{d}{dt}\boldsymbol{W}_I + \sum_{J\in\mathcal{V}(\mathcal{I})} \boldsymbol{\mathcal{F}}^{\boldsymbol{n}}_{\boldsymbol{IJ}} \cdot \boldsymbol{n_{IJ}} = \boldsymbol{0}, \tag{25}$$

where the set of the neighboring cells of Ω_I is denoted $\mathcal{V}(I)$, and $\boldsymbol{n_{IJ}}$ is the unit outward normal vector at the cell interfaces $\partial\Omega_I$ pointed towards the neighboring cells Ω_J. Using standard notations adopted by numerous authors, the Roe average is indicated by index $\cdot_{IJ}$ for $(\boldsymbol{\mathcal{U}}, H)$ at the cell interface, and $\Delta\bullet = (\cdot)_J - (\cdot)_I$ denotes the spatial difference operator. Considering the incompressible time-scale, the normalized semi-discrete equations for the first-order Rossow-Roe scheme write successively for the density, momentum and total energy equations

$$\begin{aligned} h\,\frac{d\rho_I}{dt} + \frac{1}{2}\sum_{J\in\mathcal{V}(I)}\Bigg[\quad & \rho_J \boldsymbol{\mathcal{U}_J}\cdot\boldsymbol{n_{IJ}} \\ & - \left\{ |\mathcal{U}_{n_{IJ}}|\Delta_{IJ}\rho + \epsilon\,\frac{\rho_{IJ}\mathcal{U}_{n_{IJ}}}{c_{IJ}}\Delta_{IJ}\mathcal{U}_n + \frac{1}{\epsilon^2}\frac{\Delta_{IJ}p}{c'_{IJ}}(1-\epsilon\frac{|\mathcal{U}_{n_{IJ}}|}{c_{IJ}}) \right\} \Bigg] = 0, \end{aligned} \tag{26}$$

$$h\,\frac{d\,(\rho_I \boldsymbol{\mathcal{U}_I})}{dt} + \frac{1}{2}\sum_{J\in\mathcal{V}(I)}\Big[\quad \rho_J \boldsymbol{\mathcal{U}_J}\cdot\boldsymbol{n_{IJ}}\boldsymbol{\mathcal{U}_J} + \frac{1}{\epsilon^2}p_j\boldsymbol{n_{IJ}}$$
$$-\Big\{\boldsymbol{\mathcal{U}}_{IJ}|\mathcal{U}_{n_{IJ}}|\Delta_{IJ}\rho + \rho_{IJ}|\tilde{\mathcal{U}}_{n_{IJ}}|\boldsymbol{\Delta_{IJ}\mathcal{U}}$$
$$+\Delta_{IJ}\mathcal{U}_n\Big(\epsilon\,\frac{\rho_{IJ}\mathcal{U}_{n_{IJ}}}{c_{IJ}}\boldsymbol{\mathcal{U}_{IJ}} + \rho_{IJ}c'_{IJ}\boldsymbol{n_{IJ}}\,(1-\epsilon\frac{|\mathcal{U}_{n_{IJ}}|}{c_{IJ}})\Big)$$
$$+\Delta_{IJ}p\Big(\frac{1}{\epsilon^2}\frac{\boldsymbol{\mathcal{U}_{IJ}}}{c'_{IJ}}(1-\epsilon\frac{|\mathcal{U}_{n_{IJ}}|}{c_{IJ}}) + \frac{1}{\epsilon}\frac{\mathcal{U}_{n_{IJ}}}{c_{IJ}}\boldsymbol{n_{IJ}}\Big)\Big\}\quad\Big] \qquad = 0, \tag{27}$$

$$h\,\frac{d(\rho_I E_I)}{dt} + \frac{1}{2}\sum_{J\in\mathcal{V}(I)}\Big[\quad (\rho_J E_J + p_J)\boldsymbol{\mathcal{U}_J}\cdot\boldsymbol{n_{IJ}}$$
$$-\Big\{\epsilon^2\,|\mathcal{U}_{n_{IJ}}|\frac{|\boldsymbol{\mathcal{U}}_{IJ}|^2}{2}\Delta_{IJ}\rho + \epsilon^2\rho_{IJ}|\mathcal{U}_{n_{IJ}}|\boldsymbol{\mathcal{U}_{IJ}}\cdot\boldsymbol{\Delta_{IJ}\mathcal{U}}$$
$$+\Delta_{IJ}\mathcal{U}_n\Big(\epsilon\,\rho_{IJ}H_{IJ}\frac{\mathcal{U}_{n_{IJ}}}{c_{IJ}} + \epsilon^2\,\rho_{IJ}\mathcal{U}_{n_{IJ}}c'_{IJ}\,(1-\epsilon\frac{|\mathcal{U}_{n_{IJ}}|}{c_{IJ}})\Big)$$
$$+\Delta_{IJ}p\Big(\frac{|\mathcal{U}_{n_{IJ}}|}{\gamma-1} + \epsilon\,\frac{(\mathcal{U}_{n_{IJ}})^2}{c_{IJ}} + \frac{1}{\epsilon^2}\frac{H_{IJ}}{c'_{IJ}}(1-\epsilon\frac{|\mathcal{U}_{n_{IJ}}|}{c_{IJ}})\Big)\Big\}\quad\Big] \qquad = 0. \tag{28}$$

So discrete flow variables for the density, velocity and pressure, solutions of system (26)-(28), are some explicit functions of the vanishing Mach number ϵ, and similarly to [39, 45, 13], are assumed to be asymptotic expansions in power of the reference Mach number of the form

$$\phi_I(t) = \phi_I^{(0)}(t) + \epsilon\,\phi_I^{(1)}(t) + \epsilon^2\,\phi_I^{(2)}(t) + O(\epsilon^3) \qquad \text{as} \qquad \epsilon \longrightarrow 0, \tag{29}$$

with normalized coefficients $\phi_I^{(k)} \simeq O(1)$ for all k. Then, inserting these expansions and collecting terms with equal power for the parameter ϵ in (26-28), we get for the leading order equations at *order* $\dfrac{1}{\epsilon^2}$:

$$\sum_{J\in\mathcal{V}(I)}\frac{\Delta_{IJ}p^{(0)}}{c'^{(0)}_{IJ}} = 0, \tag{30}$$

$$\sum_{J\in\mathcal{V}(I)} p_J^{(0)}\boldsymbol{n_{IJ}} - \frac{\Delta_{IJ}p^{(0)}\boldsymbol{\tilde{\mathcal{U}}^{(0)}_{IJ}}}{c'^{(0)}_{IJ}} = 0, \tag{31}$$

$$\sum_{J\in\mathcal{V}(I)}\Delta_{IJ}p^{(0)}\frac{\tilde{H}^{(0)}_{IJ}}{c'^{(0)}_{IJ}} = 0. \tag{32}$$

This discrete system is in close analogy with the same leading order equations found for the Roe-Turkel scheme (see the equations (51)-(54) in [13]). The only difference stems from the coefficient of the pressure jump in the momentum equations (31). This similarity of results is also related to the respective asymptotic behavior of the matrix-valued dissipation, previously observed in (14) for the Roe-Rossow scheme, and in (15) for the Roe-Turkel scheme, which lead to a similar leading-order system in the incompressible limit.

Consequently, the discrete analysis of these two modified Roe-type scheme can be performed using the same proof given in [13] for the Roe-Turkel scheme. Then, with some restrictions on the boundary conditions, it can be shown that the Roe-Rossow scheme also admits a unique constant solution for the "0-state" leading-order pressure

$$p_I^{(0)}(t) = p_J^{(0)}(t)\,, \quad \forall I, J. \tag{33}$$

However, collecting terms at *order* $1/\epsilon$, the Roe-Turkel and Roe-Rossow schemes yield two distinct discrete systems of equations. As observed in [13] for the Roe-Turkel scheme, no term of this order appears explicitly in the normalized

semi-discrete equations. This is not the case for the Roe-Rossow scheme, as it can be seen in system (26)-(28). Nevertheless, inserting a constant pressure $p^{(0)}$ into equations (30)-(32) makes vanishing these terms of order $1/\epsilon$. Hence, the two modified dissipation vectors exhibit an identical behavior and the resulting order $1/\epsilon$ system remains almost identical to the leading order system. The only difference being that the "0-state" pressure $p^{(0)}$ is replaced by $p^{(1)}$ at order $1/\epsilon$. Therefore, assuming that $p^{(0)}$ and $p^{(1)}$ are constant in space at the boundary [13], we find that the discrete solution of the Roe-Rossow scheme undergoes pressure fluctuations of second-order in space for the disturbance pressure $p^{(2)}$, in the whole computational domain

$$p_I(t) = p^{(0)}(t) + p^{(1)}(t)\,\epsilon + p_I^{(2)}(t)\,\epsilon^2 + O(\epsilon^3). \tag{34}$$

This fundamental feature of the continuous solution is then recovered at the discrete level by the Roe-Rossow scheme, indicating its ability to compute accurate discrete solutions for low Mach number flows. Then, inserting pressures $p^{(0)}$ and $p^{(1)}$ constant in space into (26)-(28) yields the following *Order* 1 system

$$h\,\partial_t \rho_I^{(0)} + \frac{1}{2}\sum_{J\in\mathcal{V}(\mathcal{I})}\left[\rho_J^{(0)}\boldsymbol{\mathcal{U}}_J^{(0)}\cdot\boldsymbol{n}_{IJ} - \left\{\quad \frac{\Delta_{IJ}p^{(2)}}{c_{IJ}^{\prime(0)}} \quad\right\}\right] = 0, \tag{35}$$

$$h\,\partial_t\left(\rho_I^{(0)}\boldsymbol{\mathcal{U}}_{\boldsymbol{I}}^{(\mathbf{0})}\right) + \frac{1}{2}\sum_{J\in\mathcal{V}(\mathcal{I})}\left[\rho_J^{(0)}\boldsymbol{\mathcal{U}}_J^{(0)}\cdot\boldsymbol{n}_{IJ}\boldsymbol{\mathcal{U}}_{\boldsymbol{J}}^{(\mathbf{0})} + p_J^{(2)}\boldsymbol{n}_{\boldsymbol{IJ}} - \left\{\quad \rho_{IJ}^{(0)}\left|\boldsymbol{\mathcal{U}}_{\boldsymbol{IJ}}^{(\mathbf{0})}\cdot\boldsymbol{n}_{\boldsymbol{IJ}}\right|\Delta_{IJ}\boldsymbol{\mathcal{U}}^{(\mathbf{0})} + \rho_{IJ}^{(0)}c_{IJ}^{\prime(0)}\boldsymbol{n}_{\boldsymbol{IJ}}\Delta_{IJ}\boldsymbol{\mathcal{U}}_{\boldsymbol{n}}^{(\mathbf{0})} + \frac{\Delta_{IJ}p^{(2)}}{c_{IJ}^{\prime(0)}}\boldsymbol{\mathcal{U}}_{\boldsymbol{IJ}}^{(\mathbf{0})} \quad\right\}\right] = 0, \tag{36}$$

$$h\,\partial_t\left(\rho_I^{(0)}E_I^{(0)}\right) + \frac{1}{2}\sum_{J\in\mathcal{V}(\mathcal{I})}\left[\left(\rho_J^{(0)}E_J^{(0)} + p_J^{(0)}\right)\boldsymbol{\mathcal{U}}_J^{(0)}\cdot\boldsymbol{n}_{IJ} - \left\{\quad \Delta_{IJ}p^{(2)}\frac{H_{IJ}^{(0)}}{c_{IJ}^{\prime(0)}} \quad\right\}\right] = 0. \tag{37}$$

The proper scaling in space of the pressure disturbances has also implications for other physical quantities. It can be seen that, considering the normalized equation of state for the ideal gas law (19), the leading "0-state" total energy must also behave similarly as the '0-state" pressure, since

$$\forall I,J \quad p_I^{(0)}(t) = p_J^{(0)}(t) \quad\Longrightarrow\quad \rho_I^{(0)}(t)\,E_I^{(0)}(t) = \rho_J^{(0)}(t)\,E_J^{(0)}(t). \tag{38}$$

In order to simplify the analysis, the leading "0-state" density is assumed to be constant in space as usually formulated in the low Mach number regime (see for instance [13]), which also yields a constant leading "0-state" enthalpy and thus, for the corresponding Roe average

$$\forall I,J \quad H_I^{(0)}(t) = \frac{1}{\rho_I^{(0)}(t)}[\rho_I^{(0)}(t)E_I^{(0)}(t) + p_I^{(0)}(t)] = H_J^{(0)}(t) \quad\Longrightarrow\quad H_{IJ}^{(0)}(t) = H_I^{(0)}(t) \quad \forall I. \tag{39}$$

Similarly to the continuous analysis, in case of no global compression, the background pressure becomes constant in time, and an incompressible Euler equation can be formally recovered. Then, as

$$p_I(t) = p^{(0)} + p^{(1)}\,\epsilon + p_I^{(2)}(t)\,\epsilon^2 + O(\epsilon^3) = \tilde{P}_0 + p_I^{(2)}(t)\,\epsilon^2 + O(\epsilon^3), \tag{40}$$

with $d\tilde{P}_0/dt = 0$ and results (38) and (39), the time derivative in the energy equation (37) vanishes for the "0-state" total energy, and this discrete equation can be simplified in a more relevant form

$$\sum_{J\in\mathcal{V}(I)}\boldsymbol{\mathcal{U}}_{\boldsymbol{J}}^{(\mathbf{0})}\cdot\boldsymbol{n}_{\boldsymbol{IJ}} = \frac{1}{\rho^{(0)}}\sum_{J\in\mathcal{V}(I)}\frac{\Delta_{IJ}p^{(2)}}{c_{IJ}^{\prime(0)}}. \tag{41}$$

In this equation, the left-hand side of equation (41) is a discrete approximation of a divergence of the leading-order velocity field, whereas the right-hand side corresponds to a discrete Laplacian of the disturbance pressure $p^{(2)}$. This result explicitly demonstrates that the Roe-Rossow scheme does not enforce a divergence-free constraint of the velocity, in contrast to the continuous case. This elliptic Poisson-like equation may be interpreted as a local balance

of incompressible pressure forces according to surrounding local flow compression or expansion. This results is also supported by many published numerical experiments, clearly illustrating that accurate steady-state solutions can be obtained in the low Mach number range using the Roe-Turkel or the Roe-Rossow schemes.

The accuracy of discrete compressible solutions obtained with the Roe-Rossow scheme will be also illustrated in a next section through a direct comparison against an analytic potential solution satisfying the divergence-free constraint. Therefore, from a numerical point of view, it might appear reasonable to question the legitimacy of such property. Indeed, it is well established that numerical schemes enforcing a discrete divergence-free constraint are more prone to pressure-checkerboard mode issues. According to the analysis of Guillard-Nkonga [38], this is especially one possible reason to avoid using schemes enforcing this property of the velocity field at the discrete level. This issue is also mentioned in some works of Li-Gu [17], where the mechanism of pressure-velocity coupling using the MIM interpolation method is, in fact, contributing to the loss of the discrete divergence-free constraint in the asymptotic limit. The behavior of the discrete solution can be significantly affected by spurious pressure modes, resulting in either more challenging convergence to the steady state, or in unsteady flows with the occurrence of transient spurious pressure modes in the solution.

3.2.3. Remarks on the asymptotic analysis of the semi-discrete equations in space at the acoustic time scale

In the preceding section, a discrete analysis based on the convective time scale has shown that the modified Roe scheme with artificial speed of sound appears to be governed by a similar set of discrete sub-systems of equations to the Roe-Turkel scheme. However, the compressible Euler equations are also known to admit another asymptotic limit, describing faster phenomenons based on an acoustic time scale. In more recent works, Bruel et al. [43] and Galie et al. [54] have investigated several modified dissipation vectors (including the Roe-Turkel scheme) to assess their accuracy for acoustic computations in the incompressible limit. In particular, a series of numerical tests and a discrete analysis were performed for the case of barotropic flows, highlighting significant shortcomings with the Roe-Turkel scheme. By introducing an asymptotic discrete analysis with two time scales (see proposition 2.1 in [43]), it has been demonstrated that, for specific boundary conditions, the accuracy of the discrete solution is lost.

To our experience, this phenomenon is also reproduced for the first-order Roe-Rossow scheme, as briefly discussed below. The proof given in [43] is purely related to modified dissipation vectors, aiming at amplifying the contribution of the pressure jump in the continuity equation. At the *order* $1/\epsilon$, the time derivative of leading order density $\rho_I^{(0)}$ is thus linked to the first-order pressure jump of $p^{(1)}$. For the Roe-Rossow scheme, we find exactly the same discrete behavior with

$$h\,\partial_t \rho_I^{(0)} + \frac{1}{2}\sum_{J\in\mathcal{V}(I)} \frac{\Delta_{IJ} p^{(1)}}{c_{IJ}'^{(0)}} = 0.$$

Bruel et al. [43] have observed that the first-order pressure $p^{(1)}$ is necessary constrained to be constant in space in the case of periodic or wall boundary conditions. This is also the case for all boundary conditions extrapolating the pressure in ghost cells for instance. Consequently, the discrete solution results in an incorrect scaling of the pressure fluctuations in the acoustic limit, which may lead to a pathological "physical" evolution. Indeed, as illustrated in their figure 9, an acoustic wave scaled on the reference Mach number ϵ cannot propagate even with positive velocities.

Additionally, it has been stated that, the uniformity in space of $p^{(1)}$ can be a contributing factor in the observed strong damping of the density, as shown in their figures (1-2). Based on our observations from similar unsteady numerical experiments carried out with the Roe-Rossow scheme, it can be thought that the strong damping of the acoustic pulse may also be partially explained by the use of too large CFL numbers. An inappropriate stability criterion in unsteady low Mach number computations could influence the damping of high frequencies present in the acoustic waves. As it will be discussed and demonstrated with numerical evidences in the following sections, the proper formulation of the stability condition for modified compressible density-based schemes is essential in the low Mach number limit. This critical point largely remains an open question insufficiently discussed and documented in the literature.

4. Stability Condition for the Explicit Scheme

The proper formulation of the stability condition for the explicit scheme is an essential feature of the numerical procedure. The stability condition may be strongly concerned with the eigenvalues of the matrix-valued dissipation,

as the rescaling has a major effect on the solution accuracy in the incompressible limit. As shown next, the asymptotic behavior of the modified acoustic eigenvalues may have large consequences on the Von Neumann condition for stability of the explicit scheme in the low Mach-number range. This depends on the way the matrix dissipation is modified.

In the case of the Roe-Rossow scheme, we find that matrix (12) has the following eigenvalues

$$\begin{cases} \mu_0 &= |\mathcal{U}_n| \qquad \text{with multiplicity 2 for the 2D problem} \\ \mu_\pm &= \dfrac{c}{2r}\left[(r^2+1)(1-|M_n|)+2r|M_n| \pm \sqrt{(r^2-1)^2(1-|M_n|)^2+4r^2M_n^2}\right] \quad (r=\dfrac{c}{c'}) \end{cases} \tag{42}$$

with the following properties:

1. The modified acoustic eigenvalues are positive in the subsonic range with $\mu_+ > 0$ and $\mu_+\mu_- = \frac{c^2}{r^2}\left[r^2(1-|M_n|)+r(1+r^2)|M_n|\right](1-|M_n|) \geq 0$ when $|M_n| \leq 1$;
2. Thus the symmetric matrix (12) is positive semi-definite in the subsonic range;
3. The spectral radius is given by $\max(\mu_0, \mu_-, \mu_+) = \mu_+$ (see Appendix B);
4. We find that $\mu_+ \geq |\mathcal{U}_n| + c = \rho(\boldsymbol{A})$ the spectral radius of the original Jacobian matrix, $\forall |M_n| \leq 1$ (see Appendix B);
5. At the sonic line, $c' = c \Rightarrow r = 1$ and $\mu_+ = \rho(\boldsymbol{A})$.

In the incompressible limit, $M_n \longrightarrow 0$ and the acoustic eigenvalues behave as:

$$\mu_\pm \simeq \frac{c'}{2}\left[(r^2+1) \pm |r^2-1|\right]. \tag{43}$$

Since $r \geq 1$:

$$\mu_+ \simeq \frac{c^2}{c'} = O(\frac{1}{M^2}), \qquad \mu_- \simeq c' \simeq V_{ref} = O(1). \tag{44}$$

These above results show that Roe-Rossow scheme is closely related to the rescaling of the Roe scheme reformulated for the Roe-Turkel scheme in [36], with identical stiffness in term of stability constraint. Result (44) is likely related to the fact that the artificial speed of sound is defined from the same local preconditioner and that, in modifying the pressure jumps, the fastest acoustic speed travels at almost infinite speed, with large consequences on the numerical stability. In particular, we see that the stringent stability condition that applies to the Roe-Turkel scheme has to be applied also to the Roe-Rossow scheme in the asymptotic limit, with acoustics waves associated to μ_+ traveling at infinite speed of the order $O(\frac{1}{M^2})$ while acoustic waves associated to μ_- are slowed down to a reference flow velocity.

An important result for the stability in the low speed limit has been given by Birken and Meister, under an essential condition that the fastest wave speed of the dissipation matrix is of order $O(\frac{1}{M^2})$ as $M \to 0$ (see [35], Lemma 4.1 and Theorem 4.2). The proof uses a subordinate matrix norm for the amplification matrix, given in one space-dimension with mesh spacing δx by

$$\boldsymbol{G}(\xi,\sigma) = \boldsymbol{Id} + (cos(\xi)-1)\sigma\boldsymbol{D} - i\ sin(\xi)\sigma\boldsymbol{A}, \tag{45}$$

where $\boldsymbol{Id}$ is the identity matrix, $\boldsymbol{D}$ the dissipation matrix, $\boldsymbol{A}$ the flux Jacobian matrix, ξ the wave number (normalized by $1/\delta x$), $\sigma = \dfrac{\Delta t}{\delta x}$ and $i^2 = -1$. An essential mechanism of this proof relies in the fact that $\rho(\boldsymbol{D}) >> \rho(\boldsymbol{A})$ as $M \to 0$, where $\rho(\boldsymbol{D})$ and $\rho(\boldsymbol{A})$ are the spectral radius of $\boldsymbol{D}$ and $\boldsymbol{A}$, respectively. As $\rho(\boldsymbol{A}) = O(\frac{1}{M})$, this condition is satisfied by the Roe-Rossow scheme with $\rho(\boldsymbol{D}) = \mu_+$ and result (44). Therefore the necessary Von Neumann condition is the same as for the explicit Roe-Turkel scheme reformulated in [36], with for a fixed mesh spacing

$$\Delta t \leq \frac{h}{\mu_+} \simeq O(hM^2) \qquad \text{as} \qquad M \longrightarrow 0, \tag{46}$$

where h represents some characteristic cell distance and μ_+ is given by (42). With the above property 5., the Von Neumann condition (46) returns the standard stability condition at the sonic line

$$\Delta t \leq \frac{h}{|\mathcal{U}_n| + c} \qquad \text{as} \qquad M \longrightarrow 1. \tag{47}$$

The necessary stability condition (46) is well posed and allows the use of very large CFL numbers in the incompressible limit, provided that an efficient implicit scheme is developed accordingly. Note that this condition is much more restrictive than the stability condition used by Rossow, formulated by replacing the speed of sound by the Roe-Rossow scheme in (47) with

$$\Delta t \leq \frac{h}{|\mathcal{U}_n| + c'} \simeq O(h) \qquad \text{as} \qquad M \longrightarrow 0. \tag{48}$$

With this above stability condition, only moderate values of the CFL can be used for the steady-state problem and a prohibitive number of iterations may be required in the very low Mach number range.

A Newton-like implicit scheme described next was especially built for the steady-state problem, ideally so that very large CFL numbers in the incompressible limit could be used, which is not always possible, with typically $CFL \simeq O(\frac{1}{M^2})$ in order to counterbalance the constraint of very small time steps $\Delta t \simeq O(M^2)$.

It is also interesting to look at the case of the Rieper's fix, for which it can be demonstrated that the modified fastest wave speed has a less restrictive asymptotic behavior, with:

$$\mu_+ \simeq c = O(\frac{1}{M}) \quad \text{and} \quad \mu_+ \leq \rho(\boldsymbol{A}) \qquad \text{as} \qquad M \longrightarrow 0. \tag{49}$$

Then the strong stability condition given by Birken and Meister does not applied in that case, and it is expected that the low Mach number fix will not further deteriorate the stability constraint of the original Roe scheme. Although this correction is easy to implement, as the fix only introduces vanishing jumps $\Delta\mathcal{U}_n$ in the acoustic wave strengths for all equations, the eigenspaces and eigenvalues of the dissipation matrix are modified and the proper reformulation of the stability condition following the asymptotic properties (49) is actually not straightforward. One reason is that the modified dissipation matrix by low Mach number corrections is no longer a function of the flux Jacobian matrix, making the Fourier analysis for stability more complex.

5. An implicit Newton-like scheme for the steady-state problem

Even in the case of two-dimensional academic test cases, the computation of steady or unsteady compressible flows can become challenging in the low Mach number limit. The accuracy issue is a crucial point, largely discussed in the previous sections. But it is not the only one. It is well known that, in the low Mach number limit, a much slower convergence rate is generally experienced in which large iteration numbers are required, as it has been again mentioned recently with the JST-scheme in [53]. The information associated with the slowest wave will propagate during a time step at a distance corresponding to $\mu_- \Delta t$, which can also be compared to a fraction of the characteristic cell size h, with the following behavior in the case of low speed flows and the use of standard moderate CFL numbers

$$\mu_- \Delta t \leq CFL \frac{h}{R_c} << h, \tag{50}$$

where R_c is the condition number. As stated above, in the case of the Roe-Rossow scheme (and also for the Roe-Turkel scheme), we see that $R_c \simeq O(1/M^2)$ as $M \longrightarrow 0$, which is strongly related to the stability condition. Therefore, the number of iterations required in order to reach the steady state may become prohibitively large, unless very large CFL number of the order of R_c can be used.

As described in the following section, a robust and stable numerical approach was developed in order to overcome the stability constraints previously mentioned. In this work, a significant effort was dedicated to the development of an efficient implicit scheme, using modern tools such as Algorithmic Differentiation and fast LU decomposition libraries. The construction of an exact Jacobian matrix of the flux balance was performed using acceleration methods, such as coloring mesh techniques. Including these tools and techniques, it is shown in the following how discrete accurate steady-state solutions can be obtained with quadratic convergence in few hundreds or a few thousands of iterations depending on the mesh density, without the use of multigrid acceleration methods, for very low Mach number decreased up to 10^{-6}.

We have considered the following standard linearized backward-Euler time-stepping scheme formulated for a cell-centered finite-volume method on structured mesh

$$\left(\frac{V}{\Delta t}\boldsymbol{\mathcal{I}} + \frac{\partial \boldsymbol{R}^n}{\partial \boldsymbol{W}^n}\right)(\boldsymbol{W}^{n+1} - \boldsymbol{W}^n) = -\boldsymbol{R}^n. \tag{51}$$

The key ingredient for an efficient implicit stage is the construction of the Jacobian matrix of the flux balance $\dfrac{\partial \boldsymbol{R}^n}{\partial \boldsymbol{W}^n}$, required for the time integration. An automatic procedure was designed for the generation of the exact Jacobian matrix of the flux balance $\boldsymbol{R}^n$ by Algorithmic Differentiation, as indicated next. The implicit scheme (51) is then solved using the LU decomposition provided by the Intel library : oneMKL PARDISO - Parallel Direct Sparse Solver Interface [51]. The objective was first to derive a fast and stable implicit scheme, allowing to use large CFL numbers, in order to overcome the stringent stability condition (46). Second, in the case of steady computations, this also has the remarkable advantage of reducing significantly the number of iterations required, since quadratic convergence can be reached when an adaptive CFL number is used. In addition, during the quadratic phase of the convergence history, CFL numbers may reach extremely high values, as it will be also illustrated in section 6.

5.1. Construction of the exact Jacobian matrix

The construction of the exact Jacobian matrix relies on Tapenade [44], an Algorithmic Differentiation tool based on Source Transformation. Over the last ten years, this useful tool has been successfully applied in numerous applications [52, 47] and has demonstrated relevance and efficiency [45, 46]. In our case, it proved to be an powerful tool in simplifying tedious calculations in the differentiation of a modified Roe scheme, accounting for second or third order MUSCL reconstruction, the physical boundary conditions and inner matching boundaries, where the current stencil of the first or higher order scheme is modified. Without Algorithmic Differentiation tool, such types of differentiation are commonly approximated in practice in the formulation of the implicit stage. In the following, we briefly indicate how, in the absence of high-performance computing constraints, a CFD code could easily operate using Tapenade. For the use of Tapenade in an HPC framework, the reader is referred to [46].

5.1.1. Tapenade: an Algorithmic Differentiation tool

First, in general, Tapenade [44] remains independent of the CFD-code and is not used during the run time. The reason is that, upon providing a file that contains a function written in either C or Fortran code, Tapenade generates a differentiated code that must be compiled. Second, Tapenade admits two different modes, which correspond to a matrix-vector product over the Jacobian matrix. For a smooth function denoted $\boldsymbol{g} : \boldsymbol{X} \in \mathcal{R}^n \longrightarrow \mathcal{R}^m$, the differentiated code corresponds to either a tangent mode or a reverse mode

$$\text{Tangent/Forward mode:} \quad \frac{\partial \boldsymbol{g}}{\partial \boldsymbol{X}}\,\boldsymbol{Y}, \quad \forall \boldsymbol{Y} \in \mathcal{R}^n, \qquad \text{Reverse mode:} \quad \boldsymbol{Y}^t\,\frac{\partial \boldsymbol{g}}{\partial \boldsymbol{X}}, \quad \forall \boldsymbol{Y} \in \mathcal{R}^m. \tag{52}$$

Depending on the mode chosen and on the definition of the vector $\boldsymbol{Y}$, either the directional derivatives (tangent mode) or the gradients (reverse mode) of the function can be calculated. Therefore, if the entire exact Jacobian matrix is the query, an iterative algorithm must be considered, consisting in calling the differentiated code several times and storing results in a sparse matrix format. The iterative algorithm will progressively reconstruct the matrix either row by row or column by column.

Note that although both modes are possible for reconstructing a Jacobian matrix, they achieve different performances. Due to an higher complexity, the reverse mode might be more demanding in terms of consumed memory and CPU-time. Nevertheless, in theory, the execution of both differentiated codes are few times longer than the original code.

5.1.2. Accelerating method for the construction of the exact Jacobian matrix: mesh coloring methods

In this work, the construction of the Jacobian matrix $\dfrac{\partial \boldsymbol{R}^n}{\partial \boldsymbol{W}^n}$ was carried out using the tangent mode. In order to optimize the CPU time for the construction of the Jacobian matrix, a mesh coloring method was applied. Such technique consists in constructing a partition of the mesh $\mathcal{M}$ that serves to maximize the information recovered with a single matrix-vector product in (52). For a structured mesh, mesh coloring methods can be easily constructed since they can be spanned with a canonical coloring. For instance, as sketched in the figures below, the number of subsets in the partition (the number of colors) can be determined by taking the full square encompassing the stencil of the scheme.

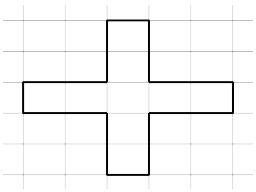

Stencil with MUSCL reconstruction

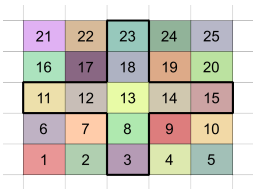

Canonical coloring

The rest of the mesh can then be just spanned by the square in the (x,y) space directions. For every cell sharing the same color, stencils are juxtaposed, while for cells with different colors, stencil are overlaid. This represents a first and easy manner to optimize CPU time for the construction by reducing the number of calls to the differentiated code. The smaller the number of colors involved in the mesh coloring is, the more efficient the construction of the Jacobian matrix will be.

5.2. Adaptive CFD formulation based on a pseudo transient continuation method for the steady-state problem

Some other techniques were introduced for steady flow computations in order to efficiently accelerate the convergence rate to the steady state. A local time stepping method combined with a CFL evolution strategy was developed based on numerical experiments, to enforce a smooth transition from the backward-Euler scheme to a Newton-Raphson method. This is achieved by the use of infinite CFL numbers in (51), resulting in

$$\frac{\partial \boldsymbol{R}^n}{\partial \boldsymbol{W}^n}(\boldsymbol{W}^{n+1} - \boldsymbol{W}^n) = -\boldsymbol{R}^n. \tag{53}$$

Our adaptive CFL formulation is strongly inspired from the pseudo transient continuation technique proposed by Crivellini & Bassi in [48]. Nevertheless, the efficiency of our formulation remains questionable while being an important topic of the literature [49]. As this is not the main attention of the present paper, one might find a better CFL evolution strategy in the literature. The following formulation has been originally designed to achieve a quadratic convergence for low Mach number flows with uniform initial conditions. Attention has been paid to ensure that the strategy is not overly sensitive to the input parameters. In our case, this CFL evolution strategy has been helpful for our test cases with the following formulation

$$\text{CFL} = \min\left(\text{CFL}_{adapt},\ \text{CFL}_{max}\right), \qquad \text{CFL}_{adapt} = \max\left((1 + \frac{1}{r^{\beta}})\text{CFL}_{init},\ \text{CFL}_{min}\right), \tag{54}$$

where $CFL_{init}, CFL_{min}, CFL_{max}$ are input parameters. A desirable behavior of the CFL number should be to smoothly increase as long as the vector of the explicit residuals drop down for all equations. Assuming the adaptive CFL is set at the iteration i_0, the coefficient r is defined with the normalized explicit residuals in the l^2-norm and the l^{∞}-norm

$$\boldsymbol{R}_{\boldsymbol{2}}^{\boldsymbol{n}} = \left(\frac{\| (R^n)_i \|_2}{\| (R^{i_0})_i \|_2} \right)_{i=1,4}, \quad \boldsymbol{R}_{\boldsymbol{\infty}}^{\boldsymbol{n}} = \left(\frac{\| (R^n)_i \|_\infty}{\| (R^{i_0})_i \|_\infty} \right)_{i=1,4}, \quad \text{where } \|\cdot\|_2 = \left(\frac{1}{N_c} \sum_{l=1}^{N_c} \frac{(\cdot)_l^2}{V_l} \right)^{\frac{1}{2}}, \quad \|\cdot\|_\infty = \max_l \left(\frac{|(\cdot)_l|}{V_l} \right), \tag{55}$$

which proved to be numerically efficient. In these above expressions, N_c stands for the total number of cells of volume V_l, and i corresponds to $i = 1, 4$ for the flux balance $(R^n)_i$ of each equation in the two-dimensional case. In opposition to [48], investigations were performed with a fluctuating β coefficient in (54). The underlying idea was to incorporate a criterion that would monitor the different magnitudes of the residuals, with the purpose to either amplify or to reduce the behavior of $1/r$. The following formulation of the coefficients r and β were found within numerical experiments

$$r = \max(\ \|\boldsymbol{R}_{\boldsymbol{2}}^{\boldsymbol{n}}\|_2,\ \|\boldsymbol{R}_{\boldsymbol{\infty}}^{\boldsymbol{n}}\|_\infty\ ) \qquad \beta = \min\left(\left| \log_{10}\left(\frac{\min\limits_i\ (R_2^n)_i}{\max\limits_i\ (R_2^n)_i} \right) \right|,\ \left| \log_{10}\left(\frac{\min\limits_i\ (R_\infty^n)_i}{\max\limits_i\ (R_\infty^n)_i} \right) \right| \right) \tag{56}$$

The optimal scenario considering expression (56), although rarely encountered, would correspond to a decreasing coefficient r, with one of the two ratios in the expression of β approaching unity. In such case, the value of CFL_{adap}

given by expression (54) would be strongly amplified. This formulation turns out to be also robust in the transient phase of the computation, in which numerical instabilities can be triggered and amplified by an excessive CFL number. Consequently, numerical instabilities would propagate to all equations, leading to a change of ratios in (56), and thereby, to an increase of β. In the absence of strict dispersion or concentration of the residuals occurring during the iterations, the only possibility to reach high CFL numbers is given by the behavior of r.

Figure 1 illustrates the convergence history of the l^2-norm (solid curves) and l^∞-norm (dashed curves) of the normalized residuals associated with the Roe-Rossow scheme, for the steady-state solution of the non-lifting cylinder test-case, at inflow Mach number $M = 0.01$. An extreme mesh density was considered in this numerical experiment, in order to illustrate the robustness of this adaptive CFL strategy, using a less dissipative scheme with a third-order MUSCL reconstruction. The evolution of the adaptive CFL according to formulation (54-56) is also indicated in red in the figure.

Due to the extreme high mesh density considered (composed of 1,048,576 cells) and that a uniform initial condition was prescribed, a straightforward computation using a third-order MUSCL reconstruction was found to be insufficiently stable to support CFL numbers greater than $O(1/M^2)$, as required by the stability condition. The initial CFL number could have been set to a smaller value (at least between $O(1/M)$ and $O(1/M^2)$). However, this approach may not be computationally efficient, as the number of required iterations may drastically increase, and also accounting for that the CPU time required by direct solvers for each iteration cannot be neglected. Indeed, a smaller initial CFL number results in the fluctuating CFL requiring more iterations, before the adaptive CFL begins to fluctuate and reach much higher values. This is related to the fact that the evolution of residuals is slowed down, whereas the underlying idea of the formulation was to amplify or to reduce the contribution of the coefficient r defined in (56).

In that specific numerical experiment, in order to minimize the time required to obtain a converged discrete solution with third-order MUSCL reconstruction, the computation has been performed by successively restarting and converging the discrete solution, starting from the first-order scheme in space "O(1)", then using a second-order MUSCL reconstruction "MUSCL O(2)", to finally consider a third-order reconstruction in space "MUSCL O(3)". The initial CFL number was set to $CFL = 10^5 > O(1/M^2)$, which proved to be stable using first the first-order scheme. At quadratic convergence, very large CFL numbers were reached, with $CFL \simeq 10^{15}$ using the first-order scheme and $CFL \simeq 10^9$ considering higher-order MUSCL reconstructions. The input values used in expression (54), corresponding to the successive runs illustrated in Fig. 1, are summarized in table 1.

Note that this situation with 3 successive restarts, using a high density mesh, is not the usual practice for the test cases discussed in the next section 6. In most of the cases, considering standard density meshes, computations using this adaptive CFL formulation could be performed from scratch, starting with the desired space accuracy. In the most difficult cases however, it may be only necessary to start the computations from a few iterations performed with the first-order scheme or more dissipative MUSCL reconstruction.

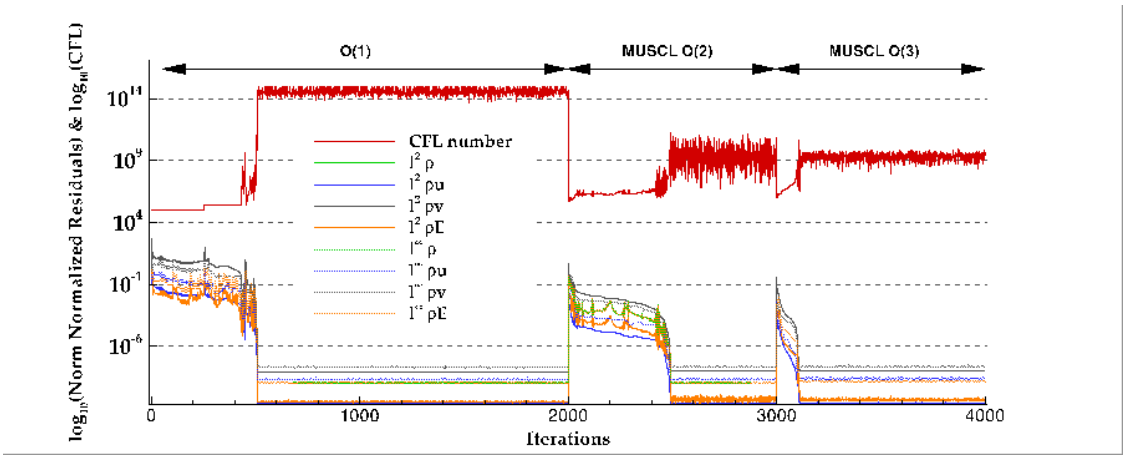

Figure 1: Convergence of the Rossow-Roe scheme for an inviscid flow around the non-lifting cylinder at inflow Mach number 10^{-2}, using a 1025x1025 O-type mesh and three successive space discretizations.

	it_{start}	it_{end}	it_{i_0}	CFL_{init}	CFL_{min}	CFL_{max}
O(1)	1	1999	250	10^5	2.5 x 10^5	10^{15}
MUSCL O(2)	2000	2999	2005	5 x 10^5	5 x 10^5	10^{15}
MUSCL O(3)	3000	3999	3005	10^6	10^6	10^{15}

Table 1: Input parameters for the adaptive CFL numbers used in the successive runs of Fig. (1).

6. Results for the cylinder Problem

This baseline test-case using structured meshes was considered to illustrate the above analysis, assuming inviscid flow. A grid convergence study was carried out and effects of grid stretching on the discrete solutions in the very low speed limit were also investigated. Results are discussed in details and are compared to the potential flow theory. In all the following, the first-order Roe-Rossow scheme will be indicated with *O(1)* in the figures, while the scheme using a second or third-order MUSCL reconstructions will be indicated respectively with *MUSCL O(2)* (Van Albada limiter) and *MUSCL O(3)* (no limiter). No entropy fix needs to be applied in low Mach number flow computations for the model problem considered in this section. The authors are aware that for more complex viscous flows or three-dimensional flows, it is generally not possible to eliminate the entropy fix.

6.1. Test-case description

For this elementary test-case, different types of mesh were considered in order to illustrate the asymptotic behavior and the solution accuracy, for a decreasing inflow Mach number M_∞ in the range 10^{-1} to 10^{-6}. Converged steady-state solutions with such low Mach number flow conditions could only be obtained in a very limited number of iterations with the stability conditions discussed in section 4, and using the implicit scheme with adaptive CFL number described in 5. The meshes used are described in table 2, for basically 3 types of structured mesh: Cartesian, an irregular curvilinear mesh and a standard curvilinear mesh, represented in Fig. 2. A sequence of Cartesian meshes was considered for a grid convergence study with density 65×65, 129×129, 257×257, 513×513 and 1025×1025. The irregular mesh is characterized by a grid refinement in the circumferential direction, downstream of the cylinder only. This yields a highly stretched mesh designed to trigger checkerboard pressure modes. A standard curvilinear mesh was also used and is considered as the baseline mesh. The sequence of Cartesian meshed were defined with a very large extension of the outer boundary with 150 diameters, in order to propagate the acoustic pressure in the farfield, and also avoiding interactions with the farfield boundary condition.

For all meshes, a slip condition was applied at the solid wall. At the outer boundary, a characteristic farfield boundary condition was used. Note that the solution of the potential theory was imposed as external state at the outer boundary for the steady-state case. This analytic solution is defined for a non-lifting flow from a prescribed surrounding "0-state" (ρ_0, V_0, p_0), with constant density $\rho_{pot} = \rho_0$, free divergence velocity $\boldsymbol{V}_{pot} = [V_r, V_\theta]^T$ in cylindrical coordinates (r, θ), with $V_r(r,\theta) = (1 - R^2/r^2)\, cos\theta\, V_0$ and $V_\theta(r,\theta) = -(1 + R^2/r^2)\, sin\theta\, V_0$, R being the cylinder radius. Then, the static pressure is given by the Bernoulli equation for incompressible flows $p_{pot} = p_0 + 0.5\rho_0(V_0^2 - |\boldsymbol{V}_{pot}|^2)$. The prescribed uniform "0-state" is also the initial data in the steady-state computations, and is defined with $V_0 = \sqrt{\gamma p_0/\rho_0}\, M_\infty$ depending on the prescribed inflow Mach number.

Mesh definition	Mesh density (nodes)	Number of cells	Mesh extension (in diameter)
Cartesian mesh : min density	65×65	4096	150
Cartesian mesh : max density	1025×1025	1 048 576	150
Curvilinear irregular mesh	140×40	5421	20
Curvilinear standard mesh	121×40	4680	20

Table 2: Definition of structured meshes used for the cylinder problem (mesh definition = circumferential × radial).

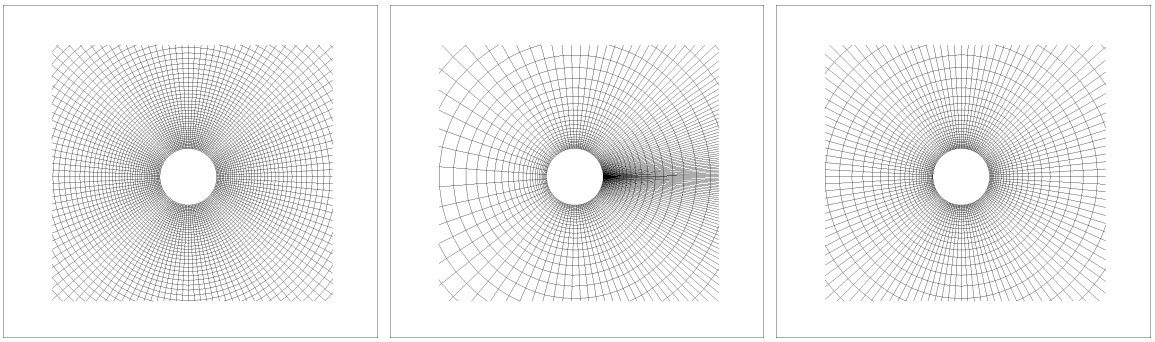

Figure 2: Types of structured meshes used for the cylinder problem. Left: Cartesian, Center: Curvilinear irregular, Right: Curvilinear standard.

6.2. Disturbance pressure consistency

In the incompressible limit, we shall especially consider the proper behavior of the pressure field $p(x, y) = p_0 + p_2(x, y)M_\infty^2$ as $M_\infty \longrightarrow 0$, where p_0 is a reference surrounding pressure and M_∞ is the prescribed inflow Mach number. Therefore, reformulating the normalized pressure field with the following quantity

$$\tilde{p}(x, y) = \frac{p(x, y) - p_{min}}{p_{max} - p_{min}} = \frac{p_2(x, y) - p_{2_{min}}}{p_{2_{max}} - p_{2_{min}}} = \tilde{p}_2(x, y) \in [0, 1] \qquad \text{as} \qquad M_\infty \longrightarrow 0, \tag{57}$$

this expression returns the normalized disturbance pressure field $\tilde{p}_2(x, y)$, which should be independent on the inflow Mach number. The proper behavior of the pressure field in the incompressible limit can also be displayed with the amplitude of the pressure disturbance versus the inflow Mach number

$$\delta\tilde{p} = \frac{p_{max} - p_{min}}{p_{max}} \simeq \left[\frac{p_{2_{max}} - p_{2_{min}}}{p_0}\right] M_\infty^2 \qquad \text{as} \qquad M_\infty \longrightarrow 0, \tag{58}$$

which should be a quadratic function $\delta\tilde{p}(M_\infty)$ of the inflow Mach number. The above quantity $\delta\tilde{p}$ only indicates the consistency of the pressure field, i.e. with the correct amplitude of the disturbance pressure, not the overall accuracy of the computations for the pressure field. The solution accuracy depends obviously on both the mesh definition and the space accuracy of the scheme. The same quantities are also meaningful for the density, when characterized by second-order fluctuations.

Another simple indicator of consistency is the pressure coefficient at the wall, which returns, according to the asymptotic analysis

$$C_p(x, y) = \frac{p_2(x, y)}{\frac{1}{2}\gamma p_0} \qquad \text{as} \qquad M_\infty \longrightarrow 0. \tag{59}$$

Therefore, the C_p coefficient is the non-dimensionalized disturbance pressure at the wall, which should be also independent on the inflow Mach number in the asymptotic limit.

The behavior of the slope of $\delta\tilde{p}$ with the inflow Mach number for the Roe-Rossow scheme is represented in the Fig. 3 left, with logarithmic scales. It can be clearly seen that the computed disturbance pressure returns a quadratic function of the inflow Mach number, thus illustrating that the artificial speed of sound approach reproduces the proper pressure field in the asymptotic limit, as demonstrated in section 3.2.2. As observed by many authors for some other modified Approximate Riemann Solver, the consistency of the pressure field is intrinsically satisfied regardless of the mesh used or the space accuracy considered, as illustrated in the left figure.

Additional computations were performed in the standard curvilinear mesh using a second-order MUSCL reconstruction. The consistency of the corresponding pressure field is again illustrated in Fig. 3 for contours of the normalized pressure field (center) and the pressure coefficient C_p (right), independent of decreasing inflow Mach numbers in the incompressible limit $M_\infty = 10^{-2}$ to 10^{-6}. The C_p coefficient computed with the second-order scheme almost matches exactly with the incompressible C_p coefficient in this coarse mesh, which indicates that the wall pressure for the weakly compressible solution almost fits the incompressible pressure, solution of the Bernoulli equation. This is not exactly achieved with the first-order scheme.

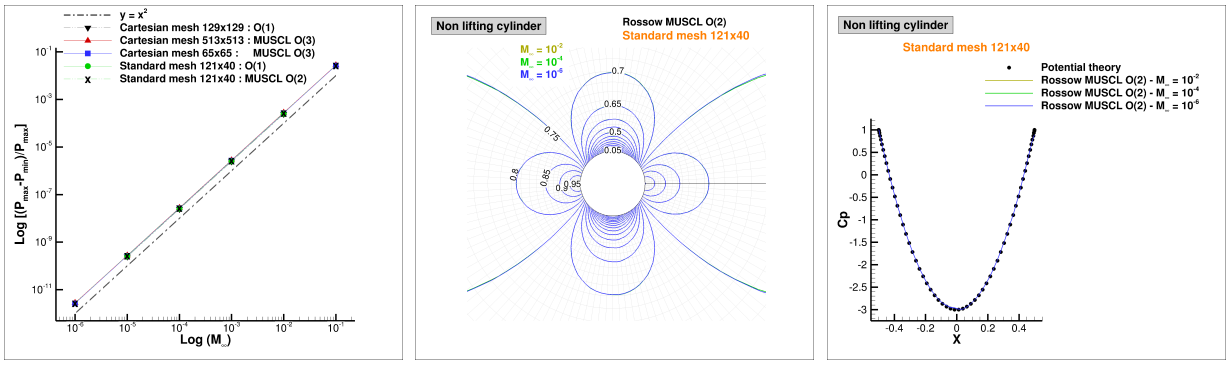

Figure 3: Slope of the amplitude of the pressure disturbance $\delta\tilde{p}$ with the inflow Mach number for different meshes and space discretizations (left), normalized disturbance pressure $\tilde{p}(x, y)$ (center) and pressure coefficient (right) for low inflow Mach numbers computed in the standard curvilinear mesh with the Roe-Rossow MUSCL O(2) scheme.

6.3. Overall solution accuracy at the incompressible time scale

The overall solution accuracy at the incompressible time scale depends essentially on the proper representation of the pressure disturbances in the incompressible limit. However, as for compressible flow simulations, solution accuracy also depends on the mesh definition, the mesh density and space accuracy, even for weakly compressible flows. For this simple steady-state test-case, the exact potential solution provides a valuable reference for the assessment of the accuracy of the compressible solution, for its incompressible component. This is achieved considering the converged CFD solution to the steady-state, using a usual local time-step, corresponding to the incompressible time scale.

The comparison of some converged solutions of the Roe-Rossow scheme with the potential solution is illustrated in the Fig. 4, for 2 different meshes and 2 different MUSCL reconstructions (order 2 in the standard curvilinear mesh and order 3 in the very fine Cartesian mesh). In the left and center figures, the iso-contours of the velocity components in the Cartesian reference frame are compared to the analytic expressions (black dashed lines). It can seen that for the finest mesh density 1025x1025 (green solid line), the weakly compressible solution seems to match perfectly with the potential solution for the velocity components, while using the standard curvilinear mesh, some entropy errors can be observed for the horizontal velocity, downstream of the cylinder (red solid line). The corresponding solutions for the C_p coefficient are plotted in the right figure. We have also plotted the solution of the first-order Roe-Rossow scheme computed in the standard mesh, for comparison. This shows that the first-order accuracy in space is clearly not sufficient to represent the wall pressure with this mesh density, which should closely match with the Bernoulli equation for this test case, as is it the case with the higher order MUSCL reconstructions used.

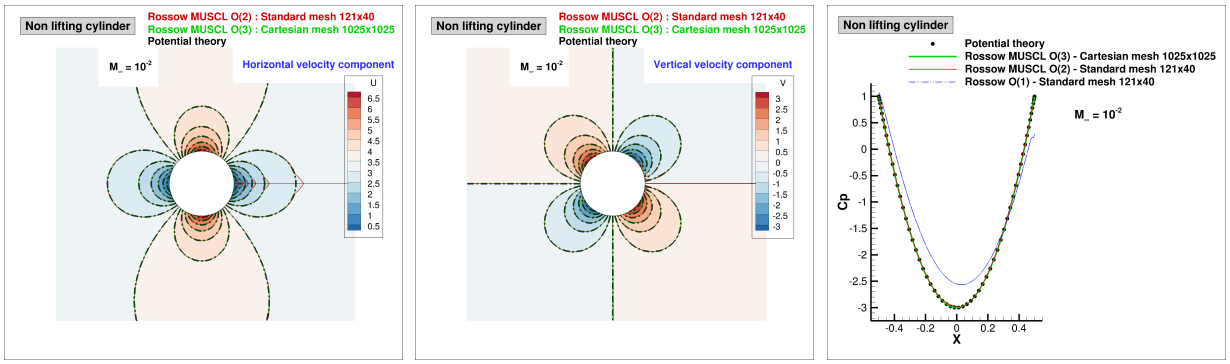

Figure 4: Effect of the mesh density and the space discretization on the solution accuracy for the horizontal (left) and vertical (center) velocity components, and the Cp coefficient (Comparisons with the analytic potential solution).

Some grid-convergence indicators were also defined for solutions computed in the sequence of Cartesian meshes, considering the scheme with third-order reconstruction. We looked at the l^2 norms computed at the cell center of the whole computational domain, for the difference between the compressible and the potential solutions, in terms of pressure $\Delta_{Bernoulli\ pressure} = \|p - p_{pot}\|_2$ and density $\Delta_{Cst\ density} = \|\rho - \rho_{pot}\|_2$. As the potential solution is obtained from a 0-order state depending of the Mach number in our analysis, these 2 indicators are represented for the increasing mesh density in log scale in Fig. 5, for 2 representative low Mach numbers $M_\infty = 10^{-2}$ (left) and $M_\infty = 10^{-4}$ (right).

For a given inflow Mach number, we find that the slope is of second-order with the mesh spacing for the pressure difference indicator $\Delta_{Bernoulli\ pressure}$, while it is only slightly less than first-order for the density difference indicator $\Delta_{Cst\ density}$. Although the scheme has a real space accuracy more than first-order, it is not truly third-order, even in a Cartesian mesh. In addition, as the dissipation matrix behaves differently according to the conservation of mass, momentum and total energy, the scheme accuracy may be different for error indicators applied to different primitive variables. We also see that the slopes are independent on the Mach number (identical in the two figures).

Also note that log scales used for these 2 grid-convergence indicators for $M_\infty = 10^{-4}$ (right) are exactly shifted with a ratio $10^{-2} \times 10^{-2}$ with respect to the scale displayed at $M_\infty = 10^{-2}$ (left), whatever the mesh density. For the pressure difference, it is expected that the difference between the compressible and incompressible pressures lies in the second-order disturbance pressure $p_2(x, y)M_\infty^2$ in expression (20), not represented in the incompressible theory. So $\Delta_{Bernoulli\ pressure} \simeq O(M^2)$ for low Mach numbers, which is reproduced comparing the scales for the pressure difference in the two figures. The same behavior is reproduced in this analysis for the density. These plots also indicate that for the Roe-Rossow scheme applied to this steady test-case, assuming constant 0-order density, the density is also characterized by second-order disturbances in the Mach number of the surrounding density. This asymptotic behavior of the density, also satisfies by the Rieper's fix, could be demonstrated using a similar proof as indicated in [56]. Identical second-order slopes with the decreasing Mach number, as indicated in Fig. 3 left for the pressure, can be plotted for the amplitude of the density fluctuation.

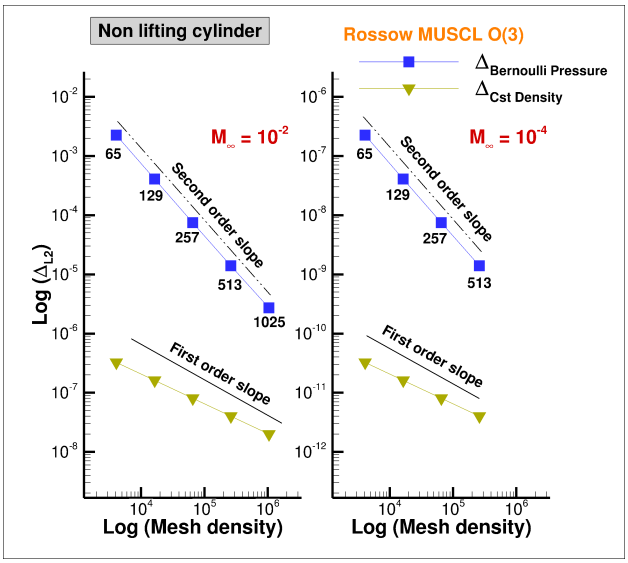

Figure 5: Grid convergence error in l^2 norm between the compressible and incompressible solutions for the pressure and density, at Mach number $M_\infty = 10^{-2}$ (left) and $M_\infty = 10^{-4}$ (right).

6.4. Acoustic-incompressible interactions

The following considerations regarding acoustic-incompressible interactions in the discrete solutions are not configuration dependent and are just discussed here for the cylinder test-case. The presence of an unsteady acoustic pressure at the acoustic time-scale, can be detected, even for the steady-state problem, looking at first the behavior of the convergence history in the incompressible limit.

The convergence history for the normalized density residual, corresponding to different inflow Mach numbers, are compared in the next figures, for decreasing Mach numbers $M_\infty = 10^{-1}$ to $M_\infty = 10^{-6}$ in the fixed standard

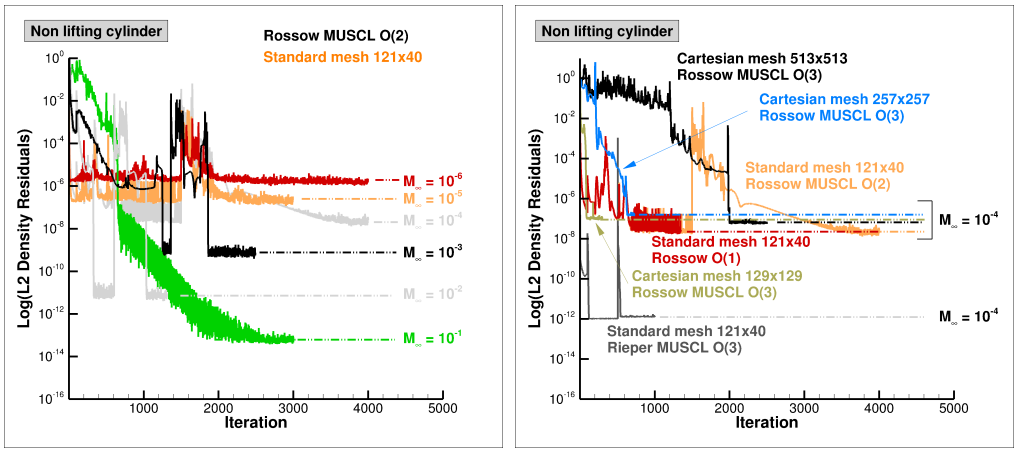

Figure 6: Convergence history for decreasing inflow Mach numbers in the standard mesh (left) and at a fixed $M = 10^{-4}$ with effects on the convergence history of mesh definition and space accuracy (right).

curvilinear mesh (Fig. 6 left) and for a fixed inflow Mach number $M_\infty = 10^{-4}$, with effects on the convergence history of the mesh definition and the order of the space discretization (Fig. 6 right). Large CFL numbers could be used for all calculations, as illustrated in Fig. 1. Most of the computations have required a restart from a more dissipative solution, to reach a quadratic-like convergence to the desired space accuracy, in order to achieve similar residual drops with comparable numbers of iterations, independently of the mesh definition or mesh density used.

As shown in Fig. 6 left for a fixed mesh, a significant shift with the zero-level machine can be observed, especially noticeable when $M_\infty \to 0$. This is illustrated with the dashed lines, highlighting the different levels of the thresholds reached according to the inflow Mach number. Such thresholds are usually not observed for compressible or nearly incompressible flows, where residuals for the steady-state problem can be dropped to the zero-level machine. On the other hand, it can be observed in Fig. 6 right that a similar threshold is reached with residuals dropped with only 6 orders, for $M_\infty = 10^{-4}$, regardless the mesh used or the space accuracy considered. A typical convergence history with a residual dropped with 12 orders obtained with the Rieper's fix at the same Mach number is also plotted for comparison in this figure, illustrating the large shift of the thresholds occurring at low Mach numbers with the Roe-Rossow scheme.

The occurrence of a threshold for the steady-state problem likely originates from an acoustic content in the discrete solution computed with the Roe-Rossow scheme, as it was also observed in the case of the Roe-Turkel scheme [36]. Such pressure fluctuations in the discrete solutions, not completely damped out by the numerical procedure, may result from transient acoustic pressure waves, which can be more easily interpreted from unsteady computations, looking at the dilatation rate, as shown in the following for the divergence of the velocity field. The cancellation problem due to accumulated round-off errors as mentioned sometimes in the literature, cannot explained what is clearly shown in Fig. 6, with very different thresholds found when the Rieper's fix is compared to the Roe-Rossow scheme, at the same inflow Mach number.

An unsteady computation was performed using a third-order MUSCL extrapolation in space and the implicit Backward Euler scheme (51), first-order accurate in time, in the fine Cartesian mesh 513×513. The inflow Mach number was again set to $M_\infty = 10^{-4}$. The initial and farfield conditions are identical to the steady-state problem, except that a uniform flowfield was prescribed as external state at the farfield boundary. An arbitrary time-step $\Delta t = 10^{-4} s$ was used, since no physical frequency can be retrieved from these inviscid flow simulations, using steady boundary conditions. The authors are aware that physically relevant acoustic waves can only result from the interaction of turbulent boundary layers occurring at the trailing edge.

From this numerical experiment, unsteady pressure fluctuations can be visualized from contours of the dilatation rate at different time steps, as illustrated in the next figures (7) to (9). Divergence of velocity is closely tied to the principle of conservation of mass. Positive divergence indicates expansion, leading to the formation of regions of low pressure (white patterns). Conversely, negative divergence suggests compression, resulting in regions of high pressure

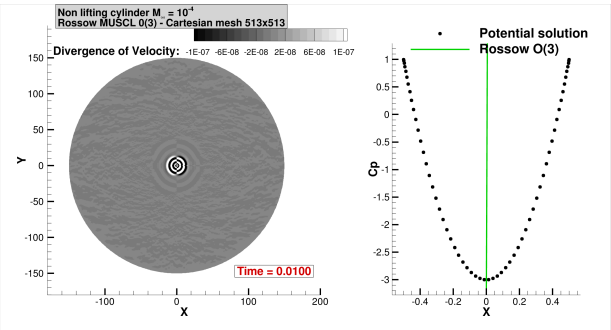

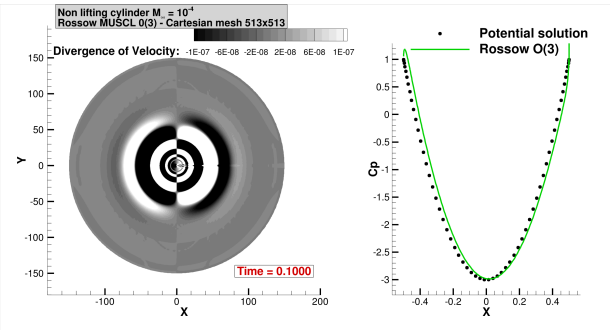

Figure 7: Contours of the dilatation rate for the unsteady solution at different time steps for $M_\infty = 10^{-4}$ in a fine Cartesian grid (left) and corresponding Cp evolution at the wall (right).

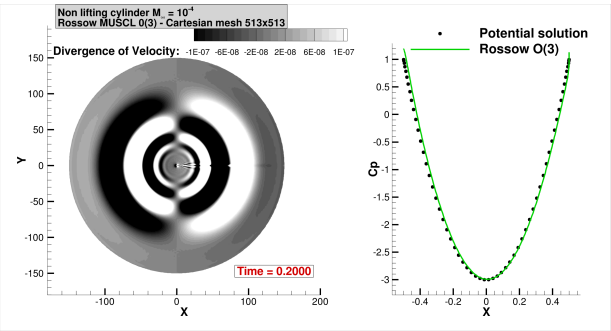

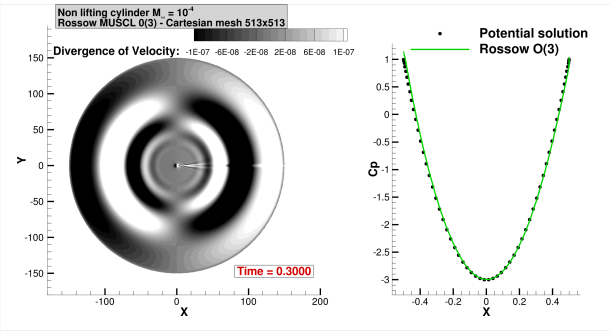

Figure 8: Contours of the dilatation rate for the unsteady solution at different time steps for $M_\infty = 10^{-4}$ in a fine Cartesian grid (left) and corresponding Cp evolution at the wall (right).

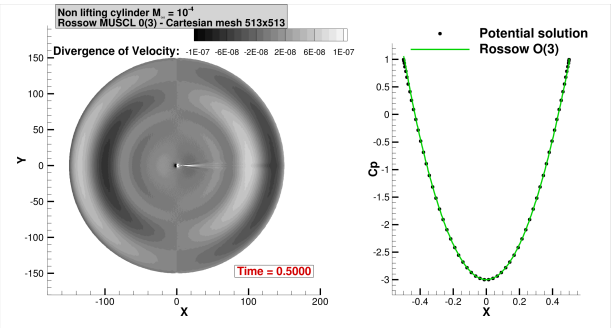

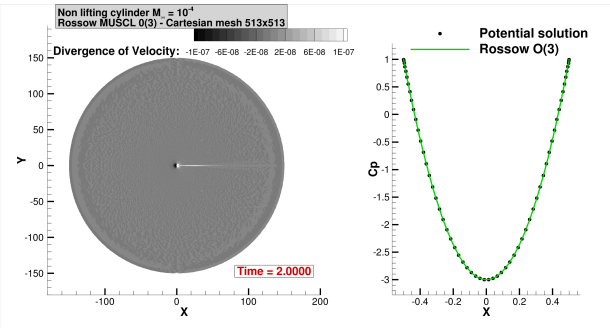

Figure 9: Contours of the dilatation rate for the unsteady solution at different time steps for $M_\infty = 10^{-4}$ in a fine Cartesian grid (left) and corresponding Cp evolution at the wall (right).

(black patterns). The acoustic component is characterized by acoustic pulses immediately generated at very short times, then propagating in the farfield, as illustrated in the figures.

After a transient phase, it can also be noted that the incompressible pressure is well reproduced, from plots of the corresponding C_p evolution with time at the wall, also displayed in the figures. In the long times, the C_p distribution become almost identical to the steady-state case, and independent of the unsteady iterations. So a permanent regime is found near the wall. This behavior illustrates that the incompressible pressure in the discrete solution, corresponding to the incompressible time-scale, is also characterized by the proper behavior with second-order disturbances

$p_2(x, y, t)M_\infty^2$, for the unsteady problem.

As the initial condition consists in prescribing a uniform flowfield over the computational domain, an acoustic wave is generated at the wall boundaries. Acoustic pulses are also related to amplified velocity jumps found in the short times in the discrete solution near the wall, generating pressure waves as shown in [29]. In the case of the Rieper's fix for instance, the cancellation of the jumps of the normal velocity in the low Mach number range seems to strongly reduce the intensity of the acoustic content in the solution. Expansion waves with much lower intensity were found with the Rieper's fix, although pulses reflected back into the computational domain were observed with the low Mach number fix. This is also visible in the steady-state case, with much lower thresholds reached in the convergence history, as indicated in Fig. 6 right, although the Rieper's fix yields a less dissipative scheme than the artificial speed of sound approach.

In addition, looking at in details the patterns for the dilatation rate in the farfield, it can be seen that the unsteady discrete solution has permanent acoustic disturbances in the large times. As the Roe-Rossow scheme does not introduce strong reductions of the intensity of the velocity jumps, and is rather characterized by dominant effects of increased pressure jumps, this may explained the noticeable thresholds characterizing the convergence history, previously illustrated in the case of the steady-state problem.

6.5. Checkerboard pressure modes

In this last section, the discrete asymptotic analysis discussed in section 3.2.1 is illustrated for the pressure checkerboard issue, comparing the Roe-Rossow scheme to the Rieper's fix, with the third-order MUSCL reconstruction for both schemes. Many preliminary tests conducted during this work have clearly shown the occurrence of checkerboard pressure modes, especially in highly stretched grids, when using the Rieper's low Mach number fix. We also illustrate from numerical evidence, that the artificial speed of sound approach is free of any pressure checkerboard modes.

This is first shown in Fig. 10 for the case of the standard curvilinear mesh, with results illustrating the behavior of the normalized pressure field (right) for the inflow Mach number set to $M_\infty = 10^{-4}$. Apparent weak pressure checkerboard modes on p_2 can be seen for the Rieper's fix far from the wall for this mesh (red solid lines), where this regular mesh as larger cells with higher stretching. However, the C_p distribution of both schemes are almost identical and free of any odd-even pressure decoupling at the wall, where the mesh is almost Cartesian.

This is no longer the case in the irregular non-symmetrical mesh, characterized by a high grid stretching in the whole mesh. The same plots are given in the next figure 11 for solutions obtained in this mesh. In that case, pressure checkerboard modes are greatly amplified using the Rieper's fix. In contrast, the Roe-Rossow scheme is not sensitive to the mesh definition, and no checkerboard modes can be observed, even considering lower Mach numbers, decreased up to $M_\infty = 10^{-6}$. This is also the case of the Roe-Turkel scheme, as demonstrated in [38].

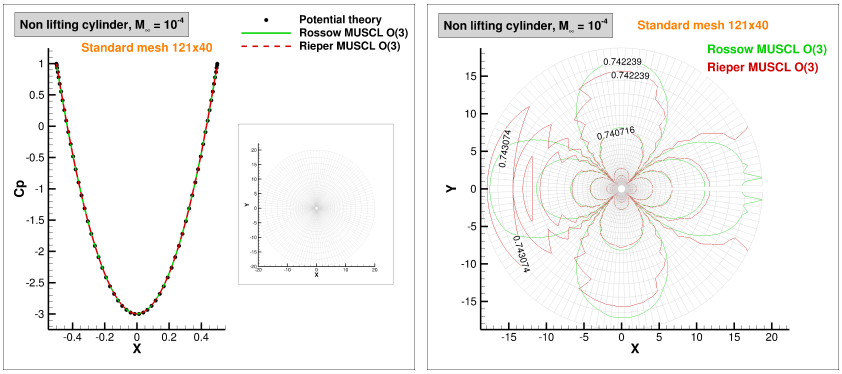

Figure 10: Occurrence of pressure checkerboard issues in the standard mesh with the Roe-Rossow scheme compared to the Rieper's fix at $M_\infty = 10^{-4}$. Pressure coefficient (left), normalized pressure contours (right).

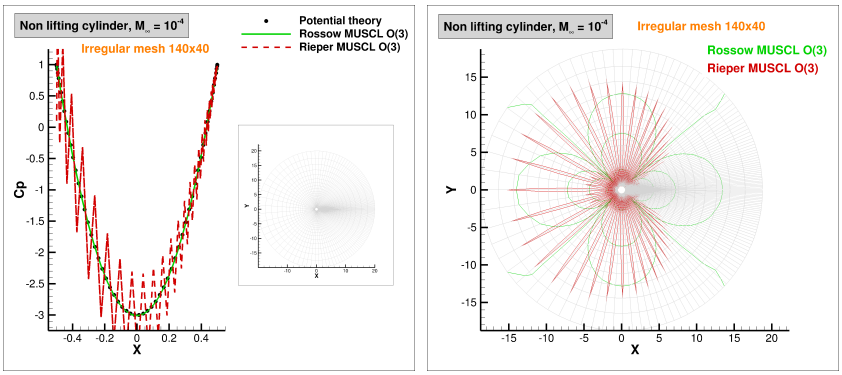

Figure 11: Occurrence of pressure checkerboard issues in the irregular mesh with the Roe-Rossow scheme compared to the Rieper's fix at $M_\infty = 10^{-4}$. Pressure coefficient (left), normalized pressure contours (right).

7. Results for the NACA0012 airfoil

Some additional results are briefly presented for the case of the NACA0012 airfoils, for lifting and non-lifting steady configurations, at different Mach numbers ranging from low speed to supersonic flow conditions. Different meshes were considered as illustrated in Fig. 12, with definition given in table 3.

In this section, we are basically interested in some comparisons with the original Roe scheme and the Roe-Turkel scheme, for accuracy assessment of the artificial speed of sound approach. All results presented in this section were obtained using the *MUSCL O(2)* reconstruction, and an entropy fix was applied for transonic and supersonic test-cases (see Appendix C).

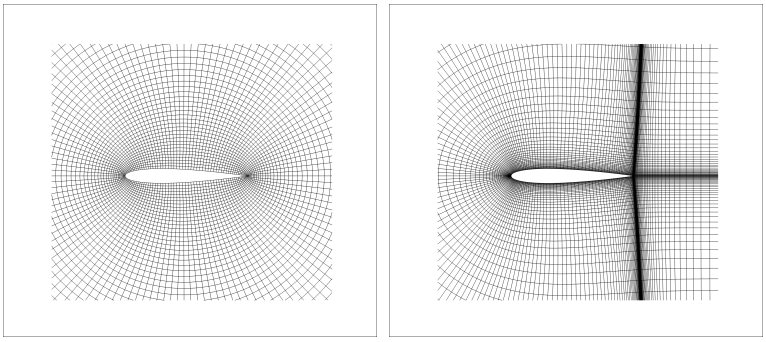

Figure 12: Types of structured meshes used for the NACA0012 airfoil. Left: Cartesian-like Vasseberg-Jameson O-mesh, Right: Curvilinear stretched C-mesh.

Mesh definition	Mesh density (nodes)	Number of cells	Mesh extension (in chord)
"O"-mesh standard	129×129	16 384	150
"O"-mesh medium	257×257	66 049	150
"C"-mesh	279×60	16 402	20

Table 3: Definition of structured meshes used for the NACA0012 airfoil. Cartesian "O"-meshes are Vasseberg-Jameson meshes used in [42].

We first look at the pressure and drag coefficients, together with entropy distributions at the upper and lower sides. Some comparisons are illustrated in the next figures, considering different flow conditions, in the non-lifting case, for solutions computed in the standard "C"-mesh. In the next figures 13, results obtained with the Roe-Rossow scheme

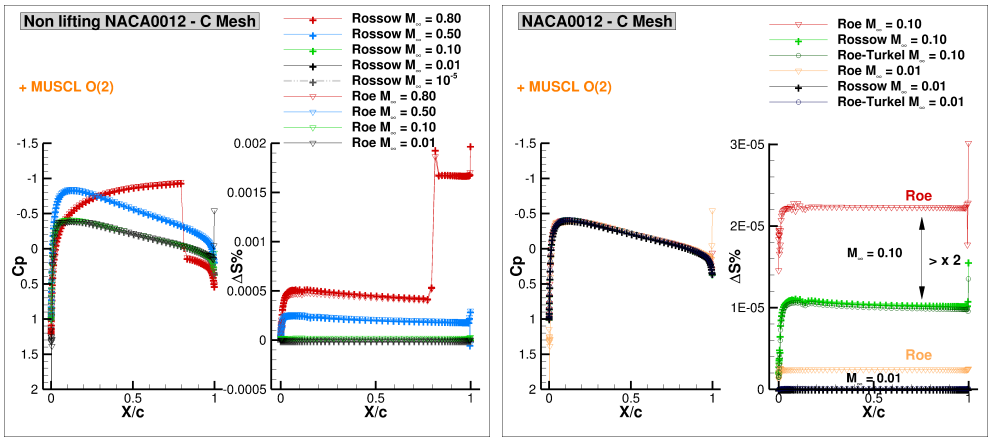

Figure 13: Pressure coefficient and entropy distribution in compressible and low Mach number regimes, for the Roe-Rossow scheme compared to the original Roe scheme (left) and the Roe-Turkel scheme (right) (C-mesh).

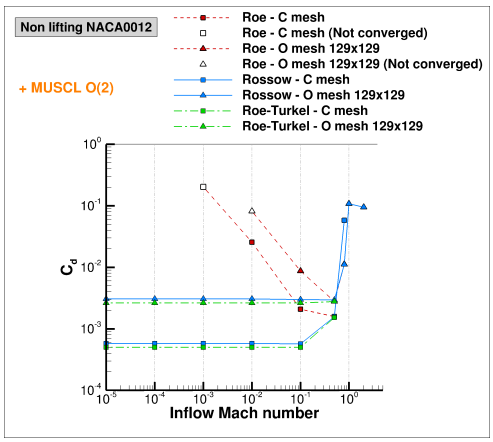

Figure 14: Drag coefficient for the Roe-Rossow scheme compared in different meshes to the original Roe scheme and the Roe-Turkel scheme, in compressible and low Mach number regimes.

are compared to the Roe scheme for compressible and low Mach number regimes (left) and also to the Roe-Turkel scheme for low Mach numbers (right). Note first that in the transonic case $M_\infty = 0.80$, the solution obtained with the Roe-Rossow scheme is characterized by an almost identical numerical shock structure than for the original Roe scheme, with similar spurious entropy levels generated at the stagnation point, upstream the shock wave. Same trends can be observed for the compressible case at $M_\infty = 0.5$. In the low Mach number range however, the Roe scheme exhibits expected inconsistencies with the pressure, especially visible at the leading and trailing edges.

The loss of accuracy of the Roe scheme in the low Mach number range is further highlighted in the right figure, where it can be seen, at decreasing Mach numbers $M_\infty = 0.1$ and $M_\infty = 0.01$ in isentropic flow conditions, that the Roe scheme (red and orange symbols) has more than 50% higher spurious entropy levels than the modified Roe-Rossow and the Roe-Turkel schemes (green and black symbols). It can be also noted that the two modified Roe schemes have a similar accuracy with very close levels of spurious entropy in the low Mach number limit.

The drag coefficient is also a relevant indicator of accuracy, even for inviscid flows. In the next Fig. 14, the evolution of the drag coefficient with the Mach number is plotted from $M_\infty = 10^{-5}$ in the incompressible limit to the supersonic regime at $M_\infty = 2$. All Roe-type schemes compared with theses plots give the same drag coefficient in the compressible regime $M_\infty \geq 0.5$, for a given mesh. Two different meshes were used for these comparisons, with large

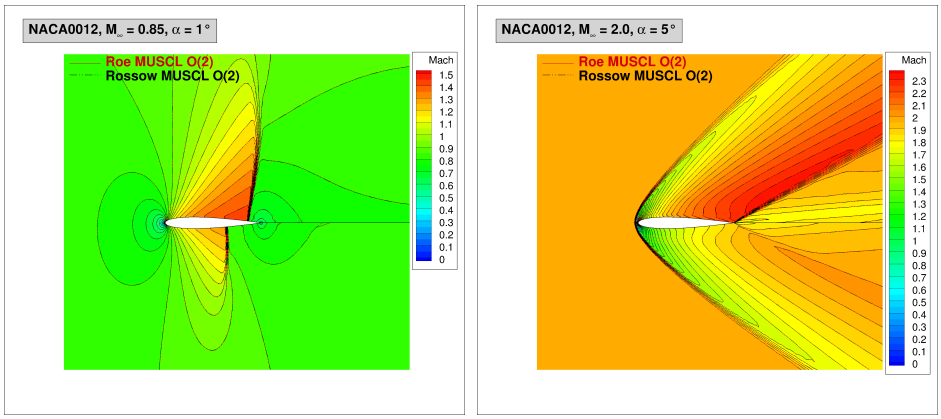

Figure 15: Mach number contours in lifting transonic (left) and supersonic (right) regimes, for the Roe-Rossow scheme compared to the original Roe scheme (medium "O"-mesh).

inconsistencies and even no convergence, observed with the Roe scheme when $M_\infty \leq 0.1$ (red symbols), whatever the mesh definition, Cartesian "O"-mesh or "C"-mesh (with similar density as reported in table 3). We also see that for both mesh definitions, in the limit of vanishing Mach numbers, the Roe-Rossow and Roe-Turkel schemes produce intrinsically an almost constant spurious drag in the incompressible regime. The level of this spurious drag depends only of the mesh density or the mesh definition and the accuracy of the MUSCL reconstruction.

The two last results shown in Fig. 15 for the medium "O"-mesh illustrate the ability of the Roe-Rossow scheme to compute classical compressible transonic and supersonic flows, respectively at $M_\infty = 0.85, \alpha = 1°$ and $M_\infty = 2.0, \alpha = 5°$. Both solutions have similar robustness and accuracy, with slight differences located essentially in the vicinity of the stagnation point, as it can be expected (Roe with red solid contours, Rossow with black dash-dotted contours).

8. Conclusions

The concept of artificial speed of sound was thoroughly validated by Rossow, addressing the analytical stiffness for low Mach number flow, the discrete stiffness for Reynolds number effects and mesh convergence. Our contribution in this work was to emphasize the asymptotic properties, not derived by Rossow, for this rescaling of the Roe scheme, especially aiming at increasing the amplitude of the pressure jump in the matrix-valued dissipation. It has been pointed out that this modified Roe-type scheme is very similar to the Roe-Turkel scheme in terms of asymptotic properties. It has been particularly demonstrated that the modified numerical flux ensures the proper order of pressure disturbances in space, and that the scheme does not enforce the divergence-free constraint of the leading-order velocity. Numerous numerical experiments using different structured meshes and Mach numbers decreased up to $M_\infty = 10^{-6}$ have shown that the scheme is insensitive to the mesh definition and is free of any pressure checkerboard issue. This seems to be a more general behavior, strongly related to the amplification of the pressure jumps. In addition, the Von Neumann analysis for stability shows that a much more restrictive stability condition, than the suggested stability condition considered by Rossow, must be applied in the low speed limit, at least for the steady-state problem, which is asymptotically identical to the Roe-Turkel scheme. This proper Von Neumann condition has motivated the development of an efficient implicit scheme using Algorithmic Differentiation, and allowing a fast convergence to the steady-state, for all low inflow Mach numbers tested.

As shown by many authors, the Euler equations in the incompressible limit are characterized by incompressible-acoustic interactions. One other possible guideline in designing the low Mach number fix is to cancel out numerical acoustics pressure waves arising from the jump of the normal velocity. This correction also corresponds to a reduced scheme truncation error. Unsteady computations carried out in this paper have illustrated that the artificial speed of sound approach contains a much stronger acoustic content in the discrete solution than the Rieper's fix for instance. This was correlated with typical thresholds found in the convergence history for the steady-state problem, also observed in the case of the Roe-Turkel scheme and also visible in some convergence histories given by Rossow. This

may stem from the fact that the Rossow's correction only slightly reduces the velocity jumps, and in the same time, strongly increases the pressure jumps.

It might be tempting to combine the artificial speed of sound and the Rieper's fix, to investigate a possible reduction of the acoustic thresholds observed in steady-state computations. Such scheme can be easily formulated, since different coefficients of the matrix dissipation are affected by the low Mach number fix and the artificial speed of sound. The authors made the experience of blending both corrections into a single numerical flux, rescaling the pressure jumps using the artificial speed of sound, while decreasing the jumps of the normal velocity according to Rieper. However, as the pressure gradient is strongly dominating the velocity field in the low Mach number limit, the resulting scheme turned out to be insensitive to the cancellation of the jumps of the normal velocity and behaves exactly as the Roe-Rossow scheme, with the same asymptotic stability condition.

Moreover, from investigations also carried out in this paper at the acoustic time scale, it was found that the discrete solution computed with the artificial speed of sound is characterized by an incorrect scaling of the pressure fluctuations. Ongoing works by the authors aim at gaining a better understanding of the discrete mechanisms behind the suitable amplification of the pressure jumps, trying to relax the stiffness of the stability constraint, and to recover at the acoustic time-scale a proper pressure fluctuation $p^{(1)}$ in space, not achieved by schemes amplifying the pressure jumps.

9. Acknowledgments

This work was partially supported by the SONICE project which is a France Relance project co-funded by the French Civil Aviation Authority (DGAC). France Relance benefits from EU funding via the NextGenerationEU initiative.

Appendix A.

Results indicated in this appendix are mostly used in Appendix C.

The changes of variables between the symmetrizing $d\tilde{\boldsymbol{W}}_{\mathbf{0}}$ variables and the conservative variables $\boldsymbol{W}$ are given in the two-dimensional case by

$$\frac{\partial \tilde{\boldsymbol{W}}_{\mathbf{0}}}{\partial \boldsymbol{W}} = \begin{pmatrix} \frac{\gamma-1}{2}\frac{|\boldsymbol{\mathcal{U}}|^2}{\rho c} & (1-\gamma)\frac{u}{\rho c} & (1-\gamma)\frac{v}{\rho c} & \frac{(\gamma-1)}{\rho c} \\ \frac{-u}{\rho} & \frac{1}{\rho} & 0 & 0 \\ \frac{-v}{\rho} & 0 & \frac{1}{\rho} & 0 \\ \frac{1}{\rho c}\left(\frac{\gamma-1}{2}|\boldsymbol{\mathcal{U}}|^2 - c^2\right) & (1-\gamma)\frac{u}{\rho c} & (1-\gamma)\frac{v}{\rho c} & \frac{(\gamma-1)}{\rho c} \end{pmatrix}, \quad \frac{\partial \boldsymbol{W}}{\partial \tilde{\boldsymbol{W}}_{\mathbf{0}}} = \begin{pmatrix} \frac{\rho}{c} & 0 & 0 & \frac{-\rho}{c} \\ \frac{\rho u}{c} & \rho & 0 & \frac{-\rho u}{c} \\ \frac{\rho v}{c} & 0 & \rho & \frac{-\rho v}{c} \\ \frac{\rho H}{c} & \rho u & \rho v & \frac{-\rho}{c}\frac{|\boldsymbol{\mathcal{U}}|^2}{2} \end{pmatrix}. \tag{A.1}$$

In practice, the eigenspaces of the matrix valued dissipation can be derived for the conservative variables within the change of variables

$$\boldsymbol{d} = \frac{\partial \boldsymbol{W}}{\partial \tilde{\boldsymbol{W}}_{\mathbf{0}}} \tilde{\boldsymbol{D}}_{\mathbf{0}} \frac{\partial \tilde{\boldsymbol{W}}_{\mathbf{0}}}{\partial \boldsymbol{W}} (\boldsymbol{W}_R - \boldsymbol{W}_L), \tag{A.2}$$

In symmetrizing variables, the modified dissipation matrix (12) can be diagonalized with:

$$\tilde{\boldsymbol{D}}_{\mathbf{0}} = \tilde{\boldsymbol{R}}_{\mathbf{0}} \tilde{\boldsymbol{\Lambda}} \tilde{\boldsymbol{L}}_{\mathbf{0}}, \tag{A.3}$$

where $\tilde{\boldsymbol{\Lambda}} = \mathrm{diag}(\mu_+, \mu_-, \mu_0, \mu_0)$ is the diagonal matrix of the modified eigenvalues and the left and right eigenvector matrix given explicitly in the following.

The dissipation matrix (12) has the following right and left eigenvector matrix in $d\tilde{\boldsymbol{W}}_{\boldsymbol{0}}$ variables:

$$\tilde{\boldsymbol{R}}_{\boldsymbol{0}} = \begin{pmatrix} Q_+ & Q_- & 0 & 0 \\ -n_x\mathcal{U}_n & -n_x\mathcal{U}_n & -n_y & 0 \\ -n_y\mathcal{U}_n & -n_y\mathcal{U}_n & n_x & 0 \\ 0 & 0 & 0 & 1 \end{pmatrix}, \quad \tilde{\boldsymbol{L}}_{\boldsymbol{0}} = \begin{pmatrix} \dfrac{1}{\mu_- - \mu_+} & \dfrac{-n_x\mathcal{U}_n}{(\mu_- - \mu_+)Q_+} & \dfrac{-n_y\mathcal{U}_n}{(\mu_- - \mu_+)Q_+} & 0 \\ \dfrac{-1}{\mu_- - \mu_+} & \dfrac{n_x\mathcal{U}_n}{(\mu_- - \mu_+)Q_-} & \dfrac{n_y\mathcal{U}_n}{(\mu_- - \mu_+)Q_-} & 0 \\ 0 & -n_y & n_x & 0 \\ 0 & 0 & 0 & 1 \end{pmatrix}, \tag{A.4}$$

with eigenvalues $\mu_\pm$ given by (42) and where the following coefficients have been introduced

$$Q_+ = \frac{1}{r}(c - |\mathcal{U}_n|) + |\mathcal{U}_n| - \mu_+, \qquad Q_- = \frac{1}{r}(c - |\mathcal{U}_n|) + |\mathcal{U}_n| - \mu_-, \qquad \text{with} \qquad r = \frac{c}{c^{'}}. \tag{A.5}$$

Note that with the identity

$$Q_+Q_- = -\mathcal{U}_n^2, \tag{A.6}$$

it can be readily shown that the right and left eigenvector matrix are orthogonal. Thus, the rescaling of the Roe scheme according to Rossow preserves in the subsonic range the properties of the original flux Jacobian matrix formulated in symmetrizing variables.

Appendix B.

In this appendix, it is demonstrated that, for eigenvalues (42) of the modified dissipation matrix according to the Rossow's artificial speed of sound approach (12), the following inequalities hold in the subsonic range $|M_n| \leq 1$ (with $c^{'} \leq c$ or else $r \geq 1$):

1. $\mu_+ \geq |\mathcal{U}_n|$ (Then μ_+ is the spectral radius of the dissipation matrix);
2. $\mu_+ \geq |\mathcal{U}_n| + c = \rho(\boldsymbol{A})$ the spectral radius of the flux Jacobian matrix;

Proof 1. Taking advantage of having both

$$\mu_\pm = \frac{c}{2r}\left[(r^2+1)(1-|M_n|) + 2r|M_n| \pm \sqrt{\Delta}\right] \geq 0, \tag{B.1}$$

using identity $\mu_+\mu_- = \frac{c^2}{r^2}\left[r^2(1-|M_n|) + r(1+r^2)|M_n|\right](1-|M_n|)$, we can derive the following expression:

$$(\mu_+ - |\mathcal{U}_n|)\underbrace{(\mu_- + |\mathcal{U}_n|)}_{\geq 0} = \frac{c^2}{r^2}\underbrace{[r^2(1-|M_n|) + r(1+r^2)|M_n|]}_{\geq 0}\underbrace{(1-|M_n|)}_{\geq 0} + \frac{c^2}{r}|M_n|(\sqrt{\Delta} - r|M_n|). \tag{B.2}$$

So the sign of $\mu_+ - |\mathcal{U}_n|$ is also the sign of

$$(\mu_+ - |\mathcal{U}_n|)\underbrace{(\mu_- + |\mathcal{U}_n|)}_{\geq 0}\underbrace{(\sqrt{\Delta} + r|M_n|)}_{\geq 0} = \frac{c^2}{r^2}\underbrace{\left[[r^2(1-|M_n|) + r(1+r^2)|M_n|](1-|M_n|)\right]}_{\geq 0}\underbrace{(\sqrt{\Delta} + r|M_n|)}_{\geq 0} + \frac{c^2}{r}|M_n|(\Delta - r^2|M_n|^2). \tag{B.3}$$

With $\Delta - r^2M_n^2 = (r^2-1)^2(1-|M_n|)^2 + 3r^2M_n^2 \geq 0$, we get $\mu_+ - |\mathcal{U}_n| \geq 0 \ \forall |M_n| \leq 1, \forall r \geq 1$.

Proof 2. Following the same idea, we also derive

$$[\mu_+ - \rho(\boldsymbol{A})]\underbrace{[\mu_- + \rho(\boldsymbol{A})]}_{\geq 0} = \frac{c^2}{r}\underbrace{(1-r)^2|M_n|(1-|M_n|)}_{\geq 0} + \frac{c^2}{r}\underbrace{(1+|M_n|)}_{>0}(\sqrt{\Delta} - 2r|M_n|). \tag{B.4}$$

And the sign of $\mu_+ - \rho(\boldsymbol{A})$ is also the sign of

$$[\mu_+ - \rho(\boldsymbol{A})]\underbrace{[\mu_- + \rho(\boldsymbol{A})]}_{\geq 0}\underbrace{(\sqrt{\Delta} + 2r|M_n|)}_{\geq 0} = \frac{c^2}{r}(1-r)^2\underbrace{|M_n|(1-|M_n|)(\sqrt{\Delta} + 2r|M_n|)}_{\geq 0} + \frac{c^2}{r}\underbrace{(1+|M_n|)}_{>0}(\Delta - 4r^2M_n^2). \quad \text{(B.5)}$$

With $\Delta - 4r^2M_n^2 = (r^2-1)^2(1-|M_n|)^2 \geq 0$, all terms in the RHS of the previous expression are non-negative for $|M_n| \leq 1$ Therefore $\mu_+ - \rho(\boldsymbol{A}) \geq 0 \ \forall |M_n| \leq 1, \ \forall r \geq 1$.

Appendix C.

We show in this appendix that it is possible to derive a decomposition of the modified dissipation vector according to Rossow following the Harten-Hyman decomposition of the Roe scheme (see [55]), in the modified right-eigenvectors basis $(\tilde{\boldsymbol{r}}_{\boldsymbol{0}})_k$ given by columns of matrix $\tilde{\boldsymbol{R}}_{\boldsymbol{0}}$ (A.4). Then, a formulation of a necessary entropy fix for vanishing eigenvalues is suggested based on this decomposition. All derivations indicated above were thoroughly checked numerically and tested by the authors for the test-cases considered in this paper.

A way to proceed is to consider first the following decomposition of the jump $\Delta\tilde{\boldsymbol{W}}_{\boldsymbol{0}}$ in symmetrizing variables in the right eigenvector basis with

$$\Delta\tilde{\boldsymbol{W}}_{\boldsymbol{0}} = \sum_k \tilde{\alpha}_k(\tilde{\boldsymbol{r}}_{\boldsymbol{0}})_k \quad \text{(C.1)}$$

and considering the modified dissipation vector according to Rossow reformulated in jump of the entropic variables

$$\begin{aligned} \boldsymbol{d} &= \frac{\partial \boldsymbol{W}}{\partial \tilde{\boldsymbol{W}}_{\boldsymbol{0}}}\tilde{\boldsymbol{D}}_{\boldsymbol{0}}\frac{\partial \tilde{\boldsymbol{W}}_{\boldsymbol{0}}}{\partial \boldsymbol{W}}(\boldsymbol{W}_R - \boldsymbol{W}_L) \\ &= \frac{\partial \boldsymbol{W}}{\partial \tilde{\boldsymbol{W}}_{\boldsymbol{0}}}\tilde{\boldsymbol{D}}_{\boldsymbol{0}}\Delta\tilde{\boldsymbol{W}}_{\boldsymbol{0}} \\ &= \frac{\partial \boldsymbol{W}}{\partial \tilde{\boldsymbol{W}}_{\boldsymbol{0}}}\tilde{\boldsymbol{D}}_{\boldsymbol{0}}\sum_k \tilde{\alpha}_k(\tilde{\boldsymbol{r}}_{\boldsymbol{0}})_k \\ &= \frac{\partial \boldsymbol{W}}{\partial \tilde{\boldsymbol{W}}_{\boldsymbol{0}}}\sum_k \tilde{\alpha}_k\mu_k(\tilde{\boldsymbol{r}}_{\boldsymbol{0}})_k \end{aligned} \quad \text{(C.2)}$$

with the modified eigenvalues (42). Then in entropic variables, the dissipation vector has the following components

$$\frac{\partial \tilde{\boldsymbol{W}}_{\boldsymbol{0}}}{\partial \boldsymbol{W}}\boldsymbol{d} = \sum_k \tilde{\alpha}_k\mu_k(\tilde{\boldsymbol{r}}_{\boldsymbol{0}})_k \quad \text{(C.3)}$$

and upon projection into the modified left eigenvector basis $(\tilde{\boldsymbol{l}}_{\boldsymbol{0}})_k^T$ given by the rows of matrix $\tilde{\boldsymbol{L}}_{\boldsymbol{0}}$ (A.4), we finally get the following expressions for the unknown $\tilde{\alpha}_k$ coefficients

$$(\tilde{\boldsymbol{l}}_{\boldsymbol{0}})_k^T.\frac{\partial \tilde{\boldsymbol{W}}_{\boldsymbol{0}}}{\partial \boldsymbol{W}}\boldsymbol{d} = \tilde{\alpha}_k\mu_k \qquad \text{as} \qquad (\tilde{\boldsymbol{l}}_{\boldsymbol{0}})_i^T.(\tilde{\boldsymbol{r}}_{\boldsymbol{0}})_j = \delta_{i,j}. \quad \text{(C.4)}$$

Then the idea is to compute the LHS of this previous expressions for all left eigenvectors using the entropic variables

and find the $\tilde{\alpha}_k$ coefficients by direct identification. After some algebra, we get first using the same notations as before

$$\frac{\partial \tilde{\boldsymbol{W}}_{\mathbf{0}}}{\partial \boldsymbol{W}}\boldsymbol{d} = \begin{pmatrix} \mathcal{U}_n \Delta \mathcal{U}_n + \left[\frac{1}{\rho}\frac{c}{c'}(1-\frac{\mathcal{U}_n}{c}) + \frac{|\mathcal{U}_n|}{\rho c}\right]\Delta p \\ |\mathcal{U}_n|\Delta u + c' n_x (1-\frac{|\mathcal{U}_n|}{c})\Delta \mathcal{U}_n + n_x \frac{\mathcal{U}_n}{\rho c}\Delta p \\ |\mathcal{U}_n|\Delta v + c' n_y (1-\frac{|\mathcal{U}_n|}{c})\Delta \mathcal{U}_n + n_y \frac{\mathcal{U}_n}{\rho c}\Delta p \\ \frac{c}{\rho}|\mathcal{U}_n|\Delta\rho - \frac{|\mathcal{U}_n|}{\rho c}\Delta p \end{pmatrix}, \tag{C.5}$$

and using properties of eigenvalues (42) and coefficients $Q_\pm$ (A.5), we see that coefficients $(\tilde{\alpha}_0)_k$ can be successively identified with

1) For $(\tilde{\boldsymbol{l}}_{\mathbf{0}})_1^T = [0,0,0,1]$:

$$(\tilde{\boldsymbol{l}}_{\mathbf{0}})_1^T . \frac{\partial \tilde{\boldsymbol{W}}_{\mathbf{0}}}{\partial \boldsymbol{W}}\boldsymbol{d} = \frac{c}{\rho}\left[\Delta\rho - \frac{\Delta p}{c^2}\right]|\mathcal{U}_n| = \tilde{\alpha}_1\mu_0 \tag{C.6}$$

2) For $(\tilde{\boldsymbol{l}}_{\mathbf{0}})_2^T = [0,-n_y,n_x,0]$:

$$(\tilde{\boldsymbol{l}}_{\mathbf{0}})_2^T . \frac{\partial \tilde{\boldsymbol{W}}_{\mathbf{0}}}{\partial \boldsymbol{W}}\boldsymbol{d} = \left[n_x\Delta v - n_y\Delta u\right]|\mathcal{U}_n| = \tilde{\alpha}_2\mu_0 \tag{C.7}$$

3) For $(\tilde{\boldsymbol{l}}_{\mathbf{0}})_+^T = [\frac{1}{\mu_- - \mu_+}, \frac{-n_x\mathcal{U}_n}{(\mu_- - \mu_+)Q_+}, \frac{-n_y\mathcal{U}_n}{(\mu_- - \mu_+)Q_+}, 0]$:

$$(\tilde{\boldsymbol{l}}_{\mathbf{0}})_+^T . \frac{\partial \tilde{\boldsymbol{W}}_{\mathbf{0}}}{\partial \boldsymbol{W}}\boldsymbol{d} = \frac{1}{(\mu_- - \mu_+)}\left[\frac{\Delta p}{\rho c} - \frac{\mathcal{U}_n}{Q_+}\Delta\mathcal{U}_n\right]\mu_+ = \tilde{\alpha}_+\mu_+ \tag{C.8}$$

4) For $(\tilde{\boldsymbol{l}}_{\mathbf{0}})_-^T = [\frac{-1}{\mu_- - \mu_+}, \frac{n_x\mathcal{U}_n}{(\mu_- - \mu_+)Q_+}, \frac{n_y\mathcal{U}_n}{(\mu_- - \mu_+)Q_+}, 0]$:

$$(\tilde{\boldsymbol{l}}_{\mathbf{0}})_-^T . \frac{\partial \tilde{\boldsymbol{W}}_{\mathbf{0}}}{\partial \boldsymbol{W}}\boldsymbol{d} = -\frac{1}{(\mu_- - \mu_+)}\left[\frac{\Delta p}{\rho c} - \frac{\mathcal{U}_n}{Q_-}\Delta\mathcal{U}_n\right]\mu_- = \tilde{\alpha}_-\mu_-. \tag{C.9}$$

Note that coefficients $\tilde{\alpha}_1$ and $\tilde{\alpha}_2$ for the linear waves are not modified by the artificial speed of sound. So in conservative variables, we see that the dissipation vector according to Rossow can be reformulated as follows

$$\boldsymbol{d} = \sum_k \tilde{\alpha}_k\mu_k \frac{\partial \boldsymbol{W}}{\partial \tilde{\boldsymbol{W}}_{\mathbf{0}}}(\tilde{\boldsymbol{r}}_{\mathbf{0}})_k = \sum_k \tilde{\alpha}_k\mu_k\tilde{\boldsymbol{r}}_k \tag{C.10}$$

with the modified right eigenvectors $\tilde{\boldsymbol{r}}_k$ formulated for the conservative variables. Explicitly, this reads

$$
\begin{aligned}
&\boldsymbol{d} = \Delta \boldsymbol{F}^{\mathbf{1}}_{\mathbf{0}} + \Delta \boldsymbol{F}^{\mathbf{2}}_{\mathbf{0}} + \Delta \tilde{\boldsymbol{F}}_{\mathbf{-}} + \Delta \tilde{\boldsymbol{F}}_{\mathbf{+}} = \\
&\left(\Delta\rho - \frac{\Delta p}{c^2}\right)|\mathcal{U}_n| \begin{bmatrix} 1 \\ u \\ v \\ \dfrac{|\boldsymbol{V}|^2}{2} \end{bmatrix} \quad \text{(Entropy wave)} = \Delta \boldsymbol{F}^{\mathbf{1}}_{\mathbf{0}} \\
&+\rho(n_y \Delta u - n_x \Delta v)|\mathcal{U}_n| \begin{bmatrix} 0 \\ n_y \\ -n_x \\ u n_y - v n_x \end{bmatrix} \quad \text{(Vorticity wave)} = \Delta \boldsymbol{F}^{\mathbf{2}}_{\mathbf{0}} \\
&-\frac{\rho}{c}\frac{\mu_-}{(\mu_- - \mu_+)}\left[\frac{\Delta p}{\rho c} - \frac{\mathcal{U}_n}{Q_-}\Delta \mathcal{U}_n\right] \begin{bmatrix} Q_- \\ uQ_- - n_x a \mathcal{U}_n \\ vQ_- - n_y a \mathcal{U}_n \\ HQ_- - a\mathcal{U}_n^2 \end{bmatrix} \quad \text{(Upstream running acoustic wave)} = \Delta \tilde{\boldsymbol{F}}_{\mathbf{-}} \\
&+\frac{\rho}{c}\frac{\mu_+}{(\mu_- - \mu_+)}\left[\frac{\Delta p}{\rho c} - \frac{\mathcal{U}_n}{Q_+}\Delta \mathcal{U}_n\right] \begin{bmatrix} Q_+ \\ uQ_+ - n_x a \mathcal{U}_n \\ vQ_+ - n_y a \mathcal{U}_n \\ HQ_+ - a\mathcal{U}_n^2 \end{bmatrix} \quad \text{(Downstream running acoustic wave)} = \Delta \tilde{\boldsymbol{F}}_{\mathbf{+}}
\end{aligned}
\tag{C.11}
$$

and it can be clearly seen that the artificial speed of sound only modified the acoustic part of the dissipation vector.

Also note that:

1) If $c^{'} = c$ and so no correction of the speed of sound is applied in the supersonic flow, then we find that $\mu_\pm = c \pm |\mathcal{U}_n|$, $Q_+ = -|\mathcal{U}_n|$, $Q_- = |\mathcal{U}_n|$ and it can be checked that the decomposition (C.11) return the original Roe scheme;

2) In the case $\mathcal{U}_n = 0$ and then the correction applies with $c^{'} \neq c$, no singularity can appear in this previous decomposition.

3) It can also be checked that expanding (C.11) in coefficients M_0 and $1 - |M_0|$ returns exactly expression (4) of the dissipation vector.

The idea behind this later formulation is to further modified the contribution of the acoustic waves so that this modified dissipation vector according to Rossow can be formulated as some explicit correction of the Roe scheme. Using the identities

$$
\begin{aligned}
Q_+\mu_+ - Q_-\mu_- &= [r(c - |\mathcal{U}_n|) + |\mathcal{U}_n|]\,(\mu_- - \mu_+) \\
Q_-\mu_+ - Q_+\mu_- &= \left[\frac{1}{r}(c - |\mathcal{U}_n|) + |\mathcal{U}_n|\right](\mu_- - \mu_+) \\
Q_+Q_- &= -\mathcal{U}_n^2,
\end{aligned}
\tag{C.12}
$$

with $r = \dfrac{c}{c^{`}}$, it is possible to combine the two last acoustic contributions as follows

$$\Delta\tilde{\boldsymbol{F}}_{-} + \Delta\tilde{\boldsymbol{F}}_{+} =$$

$$\frac{\rho}{c}\frac{\mu_{-}}{(\mu_{-}-\mu_{+})}\left[\frac{\Delta p}{\rho c} - \frac{\mathcal{U}_n}{Q_{-}}\Delta\mathcal{U}_n\right]\begin{bmatrix} Q_{-} \\ uQ_{-} - n_x c\mathcal{U}_n \\ vQ_{-} - n_y c\mathcal{U}_n \\ HQ_{-} - c\mathcal{U}_n^2 \end{bmatrix} + \frac{\rho}{c}\frac{\mu_{+}}{(\mu_{-}-\mu_{+})}\left[\frac{\Delta p}{\rho c} - \frac{\mathcal{U}_n}{Q_{+}}\Delta\mathcal{U}_n\right]\begin{bmatrix} Q_{+} \\ uQ_{+} - n_x c\mathcal{U}_n \\ vQ_{+} - n_y c\mathcal{U}_n \\ HQ_{+} - c\mathcal{U}_n^2 \end{bmatrix}$$

$$= \left[\frac{\Delta p}{2c^2}2\left(\frac{c}{c^{`}}(c-|\mathcal{U}_n|)+|\mathcal{U}_n|\right) + \rho c(2\mathcal{U}_n)\frac{\Delta\mathcal{U}_n}{2c^2}\right]\begin{bmatrix} 1 \\ u \\ v \\ H \end{bmatrix} + \left[\frac{\Delta p}{2c^2}(2\mathcal{U}_n) + \rho c 2\left(\frac{c^{`}}{c}(c-|\mathcal{U}_n|)+|\mathcal{U}_n|\right)\frac{\Delta\mathcal{U}_n}{2c^2}\right]\begin{bmatrix} 0 \\ cn_x \\ cn_y \\ c\mathcal{U}_n \end{bmatrix}. \tag{C.13}$$

We see that if $c^{`} = c$ (no correction) then

$$2\left(\frac{c}{c^{`}}(c-|\mathcal{U}_n|)+|\mathcal{U}_n|\right) = 2\left(\frac{c^{`}}{c}(c-|\mathcal{U}_n|)+|\mathcal{U}_n|\right) = 2c = |\lambda_{+}| + |\lambda_{-}| \quad \text{and} \quad 2\mathcal{U}_n = |\lambda_{+}| - |\lambda_{-}|, \tag{C.14}$$

so that $\Delta\tilde{\boldsymbol{F}}_{-} + \Delta\tilde{\boldsymbol{F}}_{+}$ recovers the original Harten-Hyman formulation of the Roe scheme for the acoustic decomposition as pointed out before. At this point, two formulations can be considered for the modified acoustic decomposition.

- **Formulation 1)** We look at modified pseudo acoustic eigenvalues λ_{+}^{*} and λ_{-}^{*} solutions of the 2 conditions:

$$\begin{cases} 2\left(\dfrac{c}{c^{`}}(c-|\mathcal{U}_n|)+|\mathcal{U}_n|\right) &= |\lambda_{+}^{*}| + |\lambda_{-}^{*}| \\ 2\mathcal{U}_n &= |\lambda_{+}^{*}| - |\lambda_{-}^{*}| \end{cases} \tag{C.15}$$

  and we find that the solutions for $|\lambda_{\pm}^{*}|$ are given by

$$|\lambda_{+}^{*}| = c^{*} + \mathcal{U}_n \quad \text{and} \quad |\lambda_{-}^{*}| = c^{*} - \mathcal{U}_n \tag{C.16}$$

  where:

$$c^{*} = \frac{c}{c^{`}}\left[c + (\frac{c^{`}}{c} - 1)|\mathcal{U}_n|\right] = \frac{c}{c^{`}}(c-|\mathcal{U}_n|) + |\mathcal{U}_n| \simeq O(\frac{1}{M^2}) \quad \text{as} \quad M \to 0. \tag{C.17}$$

- **Formulation 2)** We may also consider solutions of conditions

$$\begin{cases} 2\left(\dfrac{c^{`}}{c}(c-|\mathcal{U}_n|)+|\mathcal{U}_n|\right) &= |\lambda_{+}^{*}| + |\lambda_{-}^{*}| \\ 2\mathcal{U}_n &= |\lambda_{+}^{*}| - |\lambda_{-}^{*}| \end{cases} \tag{C.18}$$

  and we find that the solutions for $|\lambda_{\pm}^{*}|$ are given by

$$|\lambda_{+}^{*}| = c^{*} + \mathcal{U}_n \quad \text{and} \quad |\lambda_{-}^{*}| = c^{*} - \mathcal{U}_n \tag{C.19}$$

  where this time

$$c^{*} = \frac{c^{`}}{c}\left[c + (\frac{c}{c^{`}} - 1)|\mathcal{U}_n|\right] = c^{`}(1-|M_0|) + |\mathcal{U}_n| \simeq O(1) \quad \text{as} \quad M \to 0. \tag{C.20}$$

Then, an explicit correction of the Roe scheme clearly appear with both Formulations.

Lets first consider formulation 1. With expressions (C.16)-(C.17) for the pseudo acoustic eigenvalues λ^*_+ and λ^*_-, we find that the dissipation vector can be formulated as follows

$$\begin{aligned}
\boldsymbol{d} = &\left(\Delta\rho - \frac{\Delta p}{c^2}\right)|\mathcal{U}_n|\begin{bmatrix} 1 \\ u \\ v \\ \dfrac{|\boldsymbol{V}|^2}{2} \end{bmatrix} + \rho(n_y\Delta u - n_x\Delta v)|\mathcal{U}_n|\begin{bmatrix} 0 \\ n_y \\ -n_x \\ un_y - vn_x \end{bmatrix} \\
&+\left[\frac{\Delta p - \rho c\Delta\mathcal{U}_n}{2c^2}\right]|\lambda^*_-|\begin{bmatrix} 1 \\ u - cn_x \\ v - cn_y \\ H - c\mathcal{U}_n \end{bmatrix} + \left[\frac{\Delta p + \rho c\Delta\mathcal{U}_n}{2c^2}\right]|\lambda^*_+|\begin{bmatrix} 1 \\ u + cn_x \\ v + cn_y \\ H + c\mathcal{U}_n \end{bmatrix} \\
&\underbrace{+\rho c\left[\frac{(c^{'} - c)(c^{'} + c)}{cc^{'}}\right](c - |\mathcal{U}_n|)\frac{\Delta\mathcal{U}_n}{c^2}\begin{bmatrix} 0 \\ cn_x \\ cn_y \\ c\mathcal{U}_n \end{bmatrix}}_{Correction\ term\ formulation\ 1}
\end{aligned} \tag{C.21}$$

where the last correction term disappears when $c^{'} = c$.

With formulation 2 and expressions (C.19)-(C.20) for the pseudo acoustic eigenvalues λ^*_+ and λ^*_-, we get a similar expression with a different correction term

$$\begin{aligned}
\boldsymbol{d} = &\left(\Delta\rho - \frac{\Delta p}{c^2}\right)|\mathcal{U}_n|\begin{bmatrix} 1 \\ u \\ v \\ \dfrac{|\boldsymbol{V}|^2}{2} \end{bmatrix} + \rho(n_y\Delta u - n_x\Delta v)|\mathcal{U}_n|\begin{bmatrix} 0 \\ n_y \\ -n_x \\ un_y - vn_x \end{bmatrix} \\
&+\left[\frac{\Delta p - \rho c\Delta\mathcal{U}_n}{2c^2}\right]|\lambda^*_-|\begin{bmatrix} 1 \\ u - cn_x \\ v - cn_y \\ H - c\mathcal{U}_n \end{bmatrix} + \left[\frac{\Delta p + \rho c\Delta\mathcal{U}_n}{2c^2}\right]|\lambda^*_+|\begin{bmatrix} 1 \\ u + cn_x \\ v + cn_y \\ H + c\mathcal{U}_n \end{bmatrix} \\
&\underbrace{+\rho c\left[\frac{(c - c^{'})(c + c^{'})}{cc^{'}}\right](c - |\mathcal{U}_n|)\frac{\Delta\mathcal{U}_n}{c^2}\begin{bmatrix} 1 \\ u \\ v \\ H \end{bmatrix}}_{Correction\ term\ formulation\ 2}
\end{aligned} \tag{C.22}$$

where the last correction term also disappears when $c^{'} = c$. Obviously, in that case, decomposition (C.21) is identical to decomposition (C.22) and both collapse into the original Harten-Hyman decomposition. This has also been checked numerically.

Then, using one of these two expressions for the Roe scheme corrected according to Rossow, a general formulation of the modulus of the acoustic eigenvalues can be considered for all Mach number conditions within the following expressions

$$|\lambda_{\pm}^{*}| = \frac{1}{2}\left[(1+\epsilon)|\mathcal{U}_n \pm c| + (1-\epsilon)(c^{*} \pm \mathcal{U}_n)\right] \quad \text{with} \quad \epsilon = sign(1, |M_0| - 1) \tag{C.23}$$

together with a vanishing correction term at the sonic line where in the flowfield $|M_0| \geq 1$. The entropy fix is applied to vanishing eigenvalue $|\lambda_{\pm}^{*}|$ at the sonic line.

Formulation of the entropy fix

The issue of formulating the entropy fix is only relevant for the acoustic eigenvalues modified by the artificial speed of sound approach. Consider for instance formulation 1). A natural way to fit, at a vanishing acoustic eigenvalue, the modified two last acoustic contributions of the dissipation vector with the correction term $\boldsymbol{T}$

$$\Delta\tilde{\boldsymbol{F}}_{-} + \Delta\tilde{\boldsymbol{F}}_{+} + \boldsymbol{T} \tag{C.24}$$

with the original Roe scheme, is to apply the same entropy fix for the original $|\lambda_{\pm}|$ and to the modified eigenvalues $|\lambda_{\pm}^{*}| = c^{*} \pm \mathcal{U}_n$. When the threshold of the entropy fix is reached, the correction term $\boldsymbol{T}$ is not yet suppressed and both numerical fluxes (Roe and Rossow) are still different. This suggests to consider the following formulation of the acoustic portion of the dissipation vector (C.21) with formulation 1

$$\begin{aligned}\Delta\tilde{\boldsymbol{F}}_{-} + \Delta\tilde{\boldsymbol{F}}_{+} + \boldsymbol{T} = {} & \left[\frac{\Delta p - \rho c \Delta\mathcal{U}_n}{2c^2}\right]\Phi(|\lambda_{-}^{*}|)\begin{bmatrix} 1 \\ u - cn_x \\ v - cn_y \\ H - c\mathcal{U}_n \end{bmatrix} + \left[\frac{\Delta p + \rho c \Delta\mathcal{U}_n}{2c^2}\right]\Phi(|\lambda_{+}^{*}|)\begin{bmatrix} 1 \\ u + cn_x \\ v + cn_y \\ H + c\mathcal{U}_n \end{bmatrix} \\ & \underbrace{+\rho c\left[\frac{(c^{`}-c)(c^{`}+c)}{cc^{`}}\right](c - |\mathcal{U}_n|)\frac{\Delta\mathcal{U}_n}{c^2}\begin{bmatrix} 0 \\ cn_x \\ cn_y \\ a\mathcal{U}_n \end{bmatrix}}_{Correction\ term\ formulation\ 1}\end{aligned} \tag{C.25}$$

where we have considered the standard continuously differentiable approximation of $|x|$ according to [55]

$$\begin{cases} \Psi(\mu) = \dfrac{\mu^2 + \delta_h^2}{2\delta_h} & \text{si} \quad \mu < \delta_h \\ \Psi(\mu) = \mu & \text{si} \quad \mu \geq \delta_h \end{cases} \tag{C.26}$$

for any modified acoustic eigenvalue $\mu = |\lambda_{\pm}^{*}|$. We look at different situations of vanishing modified acoustic eigenvalues

- If $|\lambda_{-}^{*}| = c^{*} - \mathcal{U}_n = 0$, then $\mathcal{U}_n = c^{*} > 0$ and:

$$\Psi(|\lambda_{-}^{*}|) = \frac{\delta_h}{2} = \Psi(|\lambda_{-}|)_{|_{\lambda_{-}=0}} \tag{C.27}$$

and with definition (C.17), if $c^{*} = \mathcal{U}_n > 0$ then necessarily $c - |\mathcal{U}_n| = 0$ or $|M_n| = \dfrac{|\mathcal{U}_n|}{c} = 1$.

- If $|\lambda_+^*| = c^* + \mathcal{U}_n = 0$, then $\mathcal{U}_n = -c^* < 0$ and:

$$\Psi(|\lambda_+^*|) = \frac{\delta_h}{2} = \Psi(|\lambda_+|)_{|_{\lambda_+=0}} \tag{C.28}$$

and with definition (C.17), if $\mathcal{U}_n = -c^* < 0$ then $|\mathcal{U}_n| = c^*$ and again $c - |\mathcal{U}_n| = 0$ or $|M_n| = \dfrac{|\mathcal{U}_n|}{c} = 1$.

The same behavior of the entropy fix holds for formulation 2. And for both formulation 1 or 2, we see that the correction term cancels out when $c^* - \mathcal{U}_n = 0$ or $c^* + \mathcal{U}_n = 0$.

Considering again formulation 1, if for instance $c^* - \mathcal{U}_n = 0$ then $|\mathcal{U}_n| = c$ and

$$\Delta\tilde{\boldsymbol{F}}_- + \Delta\tilde{\boldsymbol{F}}_+ + \boldsymbol{T} =$$

$$\left[\frac{\Delta p - \rho c \Delta \mathcal{U}_n}{2c^2}\right]\frac{\delta_h}{2}\begin{bmatrix} 1 \\ u - cn_x \\ v - cn_y \\ H - c\mathcal{U}_n \end{bmatrix} + \left[\frac{\Delta p + \rho c \Delta \mathcal{U}_n}{2c^2}\right](c^* + \mathcal{U}_n)\begin{bmatrix} 1 \\ u + cn_x \\ v + cn_y \\ H + a\mathcal{U}_n \end{bmatrix} + \mathbf{0} \tag{C.29}$$

$$= (\Delta\tilde{\boldsymbol{F}}_- + \Delta\tilde{\boldsymbol{F}}_+)_{Roe}$$

as:

$$c^* + \mathcal{U}_n = 2c^* = 2\frac{c}{c}(c - |\mathcal{U}_n|) + 2|\mathcal{U}_n| = 2|\mathcal{U}_n| = 2c = |\lambda_+|. \tag{C.30}$$

Similarly, if $c^* + \mathcal{U}_n = 0$ then $|\mathcal{U}_n| = c$ and:

$$\Delta\tilde{\boldsymbol{F}}_- + \Delta\tilde{\boldsymbol{F}}_+ + \boldsymbol{T} =$$

$$\left[\frac{\Delta p - \rho c \Delta \mathcal{U}_n}{2c^2}\right](c^* - \mathcal{U}_n)\begin{bmatrix} 1 \\ u - cn_x \\ v - cn_y \\ H - c\mathcal{U}_n \end{bmatrix} + \left[\frac{\Delta p + \rho c \Delta \mathcal{U}_n}{2c^2}\right]\frac{\delta_h}{2}\begin{bmatrix} 1 \\ u + cn_x \\ v + cn_y \\ H + a\mathcal{U}_n \end{bmatrix} + \mathbf{0} \tag{C.31}$$

$$= (\Delta\tilde{\boldsymbol{F}}_- + \Delta\tilde{\boldsymbol{F}}_+)_{Roe}$$

as $\mathcal{U}_n = -c^* < 0$ and so $|\mathcal{U}_n| = c^*$, then $|\mathcal{U}_n| = c$ and

$$c^* - \mathcal{U}_n = -2\mathcal{U}_n = 2|\mathcal{U}_n| = 2c = |\lambda_-|. \tag{C.32}$$

Identical smooth transition with the Roe scheme holds with formulation 2 in case of vanishing modified acoustic eigenvalue $|\lambda_+^*| = c^* + \mathcal{U}_n$.

References

[1] P. L. Roe Approximate Riemann Solvers, Parameter Vectors, and Difference Schemes J. Comput. Phys., 43 (1981) 357-372

[2] Turkel E. Preconditioned Methods For Solving the Incompressible And Low Speed Compressible Equations J. Comput. Phys., 72(2) (1987) 277-298

[3] Choi Y.H. Merkle C.L. The Application of Preconditioning To Viscous Flows J. Comput. Phys., 105 (1993) 207-223

[4] J. M. Weiss and W. A. Smith Preconditioning Applied to Variable and Constant Density Flows AIAA Journal, 33 (1995), 2050-2057

[5] B. Van Leer, W.T. Lee and P. Roe Characteristic Time-Stepping or Local Preconditioning of the Euler Equations AIAA-91-1552-CP (1991)

[6] E. Turkel Review of Preconditioning Methods For Fluid Dynamics Applied Numerical Math 12:257-284, 1993
[7] E. Turkel, A. Fiterman, and B. Van Leer Preconditioning and the limit of the compressible to the incompressible flow equations for finite difference schemes In M. Hafez and D.A. Caughey, editors, Computing the future: Advances and Prospects for Computational Aerodynamics, pp. 215-234, John Wiley ans Sons, 1994
[8] E. Turkel, V.N. Vatsa Choice of Variables and Preconditioning for Time Dependent Problems AIAA paper 2003-3692, 2003
[9] E. Turkel and V.N. Vatsa Local Preconditioners for Steady State and Dual Time Stepping ESAIM: M2AN 39(3), 515-536, 2005
[10] E. Turkel, V.N. Vatsa, R.Radespiel Preconditioning Methods For Low Speed Flows AIAA paper 96-2460, 1996.
[11] E. Turkel, R. Radespiel and N. Kroll Assessment of Preconditioning Methods For Multidimensional Aerodynamics Computers & Fluids, 6 (1997) 613-634
[12] E. Turkel Preconditioned Techniques in Computational Fluid Dynamics Annual Review of Fluid Mechanics (1999) Vol. 31, pp. 385-416
[13] H. Guillard, C. Viozat On The Behaviour of Upwind Schemes in The Low Mach Number Limit Computers & Fluids, 28 (1999) 63-86
[14] C. Viozat Implicit Upwind Schemes for Low Mach Number Compressible Flows INRIA Report No 3084, January 1997, https://hal.inria.fr/inria-00073607
[15] X.S. Li, C.W. Gu An All-Speed Roe-Type Scheme and its Asymptotic Analysis of Low Mach Number Behaviour J. Comput. Phys., 227 (2008) 5144-5159
[16] X.S. Li, C.W. Gu, J.Z. Xu Development of Roe-Type Scheme for All-Speed Flows Based on Preconditioning Method Computers & Fluids, 28 (2009) 810-817
[17] X.S. Li, C.W. Gu Mechanism of Roe-type Schemes for All-Speed Flows and its Application Computers & Fluids, 86 (2013) 56-70
[18] X.S. Li, C.W. Gu The momentum interpolation method based on the time-marching algorithm for All-Speed flows J. Comput. Phys., Volume 229, Issue 20, 1 October 2010, Pages 7806-7818
[19] Cord-Christian Rossow Extension of a Compressible Code Toward the Incompressible Limit AIAA Journal Vol. 41, No. 12, December 2003
[20] C.-C. Rossow A Flux-Splitting Scheme for Compressible and Incompressible Flows J. Comput. Phys., 164 (2000) 104-122
[21] C.-C. Rossow A blended pressure/density based method for the computation of incompressible and compressible flows J. Comput. Phys., 185 (2003) 375-398
[22] C.-C. Rossow Efficient Computation of Compressible and Incompressible Flows J. Comput. Phys., 220 (2007) 879-899
[23] Swanson RC , Rossow C-C. An efficient solver for the RANS equation and a one-equation turbulence model Computers & Fluids, 42 (2011) 13-25
[24] Swanson RC , Turkel E , Rossow C-C . Convergence acceleration of Runge–Kutta schemes for solving the Navier–Stokes equations J. Comput. Phys., 224 (2007) 365-388
[25] F. Rieper A Low Mach Number Fix for Roe's Approximate Riemann Solver J. Comput. Phys., 230 (2011) 5263-5287
[26] K. Oßwald, A. Siegmund, P. Birken, V. Hannemann and A. Meister L2 Roe: a Low Dissipation Version of Roe's Approximate Riemann Solver for Low Mach Numbers Int. J. Numer. Meth. Fluids, (2015), DOI: 10.1002/fld.4175
[27] S. Langer Investigations of a second order finite volume code towards the incompressible limit J. Comput. Phys., 149 (2017) 119-137
[28] S. Dellacherie Analysis of Godunov Type Schemes Applied to The Compressible Euler System at Low Mach Number J. Comput. Phys., 229 (2010) 978-1016
[29] H. Guillard, A. Murrone On the Behaviour of Upwind Schemes in the Low Mach Number Limit: II. Godunov Type Schemes Computers & Fluids, 33 (2004) 655-675
[30] Edwards, J.R., and Liou, M.S. Low-Diffusion Flux-Splitting Methods for Flows at All Speeds AIAA Journal, Vol. 36, No. 9, 1998, pp. 1610-1617
[31] I. Mary, P.Sagaut, M. Deville An Algorithm for Unsteady Viscous Flows at all Speeds Int. J. Numer. Meth. Fluids, Vol. 34 (2000), pp. 371-401
[32] Ivan Mary and Pierre Sagaut Large Eddy Simulation of Flow Around an Airfoil Near Stall AIAA Journal, Vol. 40, No. 6, June 2002
[33] F. Rieper On the dissipation mechanism of upwind-schemes in the low Mach number regime: A comparison between Roe and HLL J. Comput. Phys., 229 (2010) 221-232
[34] M. Pelanti Low Mach number preconditioning techniques for Roe-type and HLLC-type methods for a two-phase compressible flow model Applied Mathematics and Computation 310 (2017) 112-133
[35] P. Birken, A. Meister Stability of Preconditioned Finite-Volume Schemes at Low Mach Number BIT Numerical Mathematics, 45, (2005), 463-480
[36] J.-C. Boniface Rescaling of the Roe Scheme in Low Mach-Number Flow Regions J. Comput. Phys., 328 (2017) 177-199
[37] W. Xie, R. Zhang, J. Lai, H. Li An accurate and robust HLLC-type Riemann solver for the compressible Euler system at various Mach numbers Int. J. Numer. Meth. Fluids. 2018;1-34
[38] Hervé Guillard, Boniface Nkonga On the Behaviour of Upwind Schemes in the Low Mach Number Limit: A Review Rémi Abgrall and Chi-Wang Shu (Eds). Handbook of Numerical Analysis, Volume 18, pp 203-231, Elsevier, 2017
[39] R. Klein Semi-Implicit Extension of Godunov-Type Scheme Based on Low Mach Number Asymptotics I: One-Dimensional Flow J. Comput. Phys., 121 (1995) 213-237
[40] J.S. Wong, D.L. Darmofal and J. Peraire The Solution of the Euler Equations at Low Mach Number Using a Stabilized Finite Element Algorithm Comput. Methods Appl. Mech. Engrg. 190 (2001) 5719-5737
[41] Oren Peles, Eli Turkel Acceleration methods for multi-physics compressible flow Journal of Computational Physics 358 (2018) 201–234
[42] J. Vassberg and A. Jameson In Pursuit of Grid Convergence for Two-Dimensional Euler Solutions Journal of Aircraft, Vol. 47, No. 4, 2010
[43] P. Bruel, S. Delmas, J. Jung, V. Perrier A low Mach correction able to deal with low Mach acoustics J. Comput. Phys., 378 (2019) 723-759
[44] Hascoët, L. and Pascual, V. The Tapenade Automatic Differentiation tool: Principles, Model, and Specification ACM Transactions On Mathematical Software, 39 (2013), 3
[45] J.-D. Müller and P. Cusdin On the performance of discrete adjoint CFD codes using automatic differentiation Int. J. Numer. Meth. Fluids (2005); 47:939–945
[46] B.Maugars, S.Bourasseau, C.Content, B.Michel, B.Berthoul, J.Nunez Ramirez, P.Raud , L.Hascoët Algorithmic Differentiation for an efficient CFD solver ECCOMAS 2022 - 8th European Congress on Computational Methods in Applied Sciences and Engineering,

https://hal.science/hal-03759125
[47] A.Poulain, C.Content, D.Sipp, G.Rigas, E.Garnier BROADCAST: A high-order compressible CFD toolbox for stability and sensitivity using Algorithmic Differentiation Computer Physics Communications, Volume 283, February 2023, 108557
[48] A. Crivellini, F. Bassi An implicit matrix-free Discontinuous Galerkin solver for viscous and turbulent aerodynamic simulations Computers & Fluids, Volume 50, Issue 1, November 2011, Pages 81-93
[49] H. M. Bücker, B. Pollul, A. Rasch On CFL evolution strategies for implicit upwind methods in linearized Euler equations Int. J. Numer. Meth. Fluids 2009; 59:1–18
[50] Y. Liu, M. Vinokur Upwind Algorithms for General Thermo-Chemical Nonequilibrium Flows 27th Aerospace Sciences Meeting; January 1989, https://arc.aiaa.org/doi/abs/10.2514/6.1989-201
[51] Intel Math Kernel Library (Intel MKL) https://www.intel.com/content/www/us/en/developer/tools/oneapi/onemkl.html
[52] C. Dosne, R. Barrier, S. Bourasseau, M. Carini, R. Moretti, J. Peter An adjoint body-force approach for fully-coupled aero-propulsive optimizations 15th ECCOMAS Thematic Conference on Evolutionary and Deterministic Methods for Design, Optimization and Control, June 2023, https://hal.science/hal-04146020
[53] S. Seraj, A. Yildirim, J.L. Anibal, J. R.R.A. Martins Dissipation and time step scaling strategies for low and high Mach number flows J. Comput. Phys, 491 (2023) 112358
[54] T. Galié, J. Jung, I. Lannabi, V. Perrier Extension of an all-Mach Roe scheme able to deal with low Mach acoustics to full Euler system ESAIM: Proceedings and Surveys, 2023, https://univ-pau.hal.science/hal-04164990
[55] A. Harten, J.M. Hyman Self Adjusting Grid Method For One-Dimensional Hyperbolic Conservation Laws J. Comput. Phys., 50, 235-269 (1983)
[56] Bo-Xi Lin, Chao Yan, Shu-Sheng Chen Density enhancement mechanism of upwind schemes for low Mach number flows Acta Mech. Sin. (2018) 34(3):431–445

4 - The HLLC scheme, introduction and review

Contents

The fourth chapter is dedicated to an in-depth examination of the HLL-type schemes, with a special attention given to the framework introduced by Harten, Lax and van Leer [4], establishing the entropy stability, not intrinsically achieved by the Roe scheme. As will be seen later, the construction of these schemes differs fundamentally, as it does not rely on the introduction of a linearized problem. While the primary concern of this chapter is related to the HLLC scheme, the original HLL scheme, and the improved HLLEM scheme, are also addressed. A review of the existing literature is presented, outlining the various approaches employed for the analysis and the necessary modifications of these schemes in the low Mach number limit. From this literature survey, a critical overview is presented, regarding some features such as the wave structure or a common framework analysis, that would need further investigations. A last section is devoted to the analysis conducted by Pelanti, which, along with the discussion in section 2.5, became a major source of inspiration for the investigation of low Mach number corrections, described in the next chapter.

4.1 . HLL-type schemes

This chapter primarily focuses on the HLLC scheme, which serves as a foundation for this work. However, the HLL and HLLEM schemes are also addressed in this section, as the three formulations are relatively similar, and have been extensively discussed together in the literature. The objective of this section is to introduce a second approach for the development of approximate Riemann solvers, which is commonly referred to in the literature as HLL-type schemes. These schemes exhibit some fundamental differences with the Roe-type linearization, as not being derived from a linearized problem, involving an approximated Jacobian matrix. In contrast, the original HLL scheme is based on consistency conditions with the integral form of the conservation laws and entropy inequality. Nevertheless, a common feature between the two approaches is that, they entail the construction of simple wave solvers, as previously discussed with the Roe scheme in the section 2.2.1. The original formulation of the HLL scheme was first introduced in the work of Harten-Lax-van Leer [4], within the formulation

of a unified formalism for upstream difference schemes for hyperbolic conservation laws. This analysis presents a comprehensive framework for upstream difference schemes that enables comparisons between different schemes. A particular attention is paid to the theoretical foundation of Godunov-type schemes, addressing a sufficient condition for the entropy stability of the discrete solution. Through decades, the original HLL scheme has given rise to a multitude of variations in the literature (see for instance the HLL [4, 89], HLLEM [72], HLLC [24, 34], HLL-CPS [90] and HLLS [91] schemes among others) in an effort to express more accurate solvers that are better suited to capturing the features of the solution.

4.1.1 . Definition of the HLL scheme

In the following, for the introduction of the underlying concepts, the analysis is restricted to the one dimensional case ($d = 1$). Let us introduce an initial value problem for the conservative form of the Euler equation with a discontinuous initial condition given by $\boldsymbol{w_0}(x)$

$$\begin{cases} \partial_t \boldsymbol{w} + \partial_x \boldsymbol{f}(\boldsymbol{w}) = \boldsymbol{0} \\ \boldsymbol{w}(0,x) = \boldsymbol{w_0}(x) = \begin{cases} \boldsymbol{w_l} & \text{if } x < 0 \\ \boldsymbol{w_r} & \text{if } x > 0 \end{cases} . \end{cases} \tag{4.1}$$

It is known from the hyperbolic theory that the exact solution is self-similar, and thus can be expressed as follows $\boldsymbol{w}(t,x) = \boldsymbol{\omega}^{\boldsymbol{Godunov}}(x/t; \boldsymbol{w_l}, \boldsymbol{w_r})$. Moreover, the exact solution is characterized by a complex structure which involves up to four constant states $\big(\boldsymbol{w_l},\ \boldsymbol{w_l^*},\ \boldsymbol{w_r^*},\ \boldsymbol{w_r}\big)$, separated by three characteristic curves. These curves are associated with the three characteristic speeds $(\lambda_l,\ \lambda_*,\ \lambda_r)$, indexed here as before in an increasing order, connecting states either through shock or rarefaction waves and through a contact discontinuity for the intermediate wave, as illustrated in Fig.4.1.

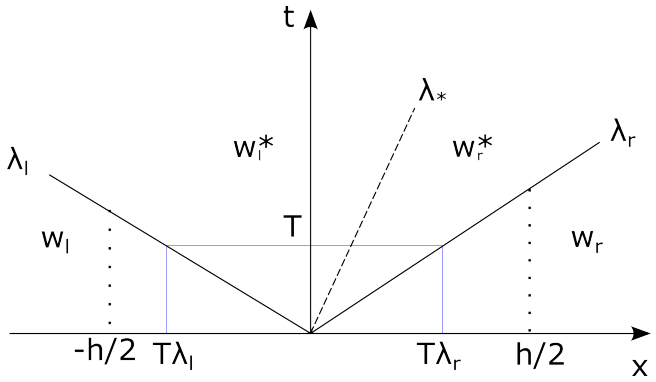

Figure 4.1: Wave structure of the exact solution associated with the Riemann problem (4.1)

By integrating the conservation laws over an arbitrary rectangle $[0,\ T] \times [-h/2,\ h/2]$, with $T > 0$ and $h > 0$, we obtain

$$\begin{aligned} 0 &= \int_0^T \int_{-h/2}^{h/2} \big(\partial_t \boldsymbol{w} + \partial_x \boldsymbol{f}(\boldsymbol{w})\big)\, dx\, dt \\ &= \int_{-h/2}^{h/2} \boldsymbol{w}(T,x)\, dx \ - \ \frac{h}{2}\,(\boldsymbol{w_l} + \boldsymbol{w_r}) + \int_0^T \Big(\boldsymbol{f}\big(\boldsymbol{w}(t,\frac{h}{2})\big) - \boldsymbol{f}\big(\boldsymbol{w}(t,\frac{-h}{2})\big)\Big)\, dt\ . \end{aligned} \tag{4.2}$$

In addition, if T is assumed sufficiently small, then the rectangle domain contains all the signals involved in the fan waves, as depicted in Fig.4.1. Therefore, the integral of the conservation laws (4.2) simplifies and leads to

$$\int_{-h/2}^{h/2} \boldsymbol{w}(T,x)\, dx = \int_{-h/2}^{h/2} \boldsymbol{\omega}^{\boldsymbol{Godunov}}(\frac{x}{T}; \boldsymbol{w_l}, \boldsymbol{w_r})\, dx = \frac{h}{2}(\boldsymbol{w_l} + \boldsymbol{w_r}) - T\big(\boldsymbol{f}(\boldsymbol{w_r}) - \boldsymbol{f}(\boldsymbol{w_l})\big). \tag{4.3}$$

This expression describes a fundamental feature of the exact solution, specifically an integral consistency condition with the conservation laws, which is the cornerstone for the derivation of HLL-type schemes, as discussed next. Similarly, this relation could be also obtained by considering either the left and right halves of rectangle, resulting in

$$\begin{aligned}\int_{-h/2}^{0} \boldsymbol{\omega}^{\boldsymbol{Godunov}}(\frac{x}{T};\boldsymbol{w_l},\boldsymbol{w_r})\,dx &= \frac{h}{2}\boldsymbol{w_l} - \Big(\int_0^T \boldsymbol{f}\big(\boldsymbol{w}(t,0)\big)\,dt - T\boldsymbol{f}(\boldsymbol{w_l})\Big)\\ \int_{0}^{h/2} \boldsymbol{\omega}^{\boldsymbol{Godunov}}(\frac{x}{T};\boldsymbol{w_l},\boldsymbol{w_r})\,dx &= \frac{h}{2}\boldsymbol{w_r} - \Big(T\boldsymbol{f}(\boldsymbol{w_r}) - \int_0^T \boldsymbol{f}\big(\boldsymbol{w}(t,0)\big)\,dt\Big)\end{aligned}, \tag{4.4}$$

where in both cases, the integral on the right-hand side is dependent on the orientation of the fan waves, as it evaluates the exact solution along the initial discontinuity. To circumvent the need of computing the exact solution of $\boldsymbol{\omega}^{\boldsymbol{Godunov}}$ in order to define a numerical flux, Harten-Lax-van Leer in [4] proposed a method based on the construction of an approximate Riemann solution, while keeping the essential properties of the exact solution. Indeed, the HLL scheme relies on the introduction of an approximated Riemann solution $\boldsymbol{\omega}^{\boldsymbol{HLL}}$, characterized by a simpler formulation, composed solely of two simple waves, associated with the wave speed estimates (S_l, S_r)

$$\boldsymbol{\omega}^{\boldsymbol{HLL}}(\frac{x}{t};\boldsymbol{w_l},\boldsymbol{w_r}) = \begin{cases}\boldsymbol{w_l} & \text{if} \quad \frac{x}{t} < S_l(\boldsymbol{w_l},\boldsymbol{w_r}),\\ \boldsymbol{w_*} & \text{if} \quad S_l(\boldsymbol{w_l},\boldsymbol{w_r}) < \frac{x}{t} < S_r(\boldsymbol{w_l},\boldsymbol{w_r}),\\ \boldsymbol{w_r} & \text{if} \quad S_r(\boldsymbol{w_l},\boldsymbol{w_r}) < \frac{x}{t}.\end{cases} \tag{4.5}$$

The expression involves three constant states $(\boldsymbol{w_l}, \boldsymbol{w_*}, \boldsymbol{w_r})$, where $\boldsymbol{w}^*$ represents an average state being the crucial component to be determined. In addition, the simple waves are no longer related with the exact signals (λ_l, λ_r), but are instead associated with two discrete wave speed estimates (S_l, S_r). The structure of the approximate solution $\boldsymbol{\omega}^{\boldsymbol{HLL}}$ is depicted in Fig.4.2.

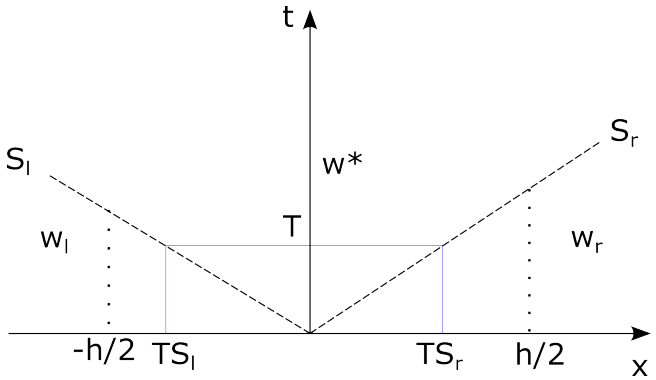

Figure 4.2: Structure of the approximate solution $\boldsymbol{w}^{\boldsymbol{HLL}}$

Assuming that two acoustic wave speed estimates (S_l, S_r) are provided, and introducing h sufficiently large such that

$$\frac{h}{2} > T\max\big(|S_l|,\,|S_r|\big),$$

then, the integral of the approximate solution $\boldsymbol{\omega}^{\boldsymbol{HLL}}$ over $[-\frac{h}{2}, \frac{h}{2}]$ can be formulated as follows

$$\int_{-h/2}^{h/2} \boldsymbol{\omega}^{\boldsymbol{HLL}}(\frac{x}{T};\boldsymbol{w_l},\boldsymbol{w_r})\,dx = (S_l\,T + \frac{h}{2})\,\boldsymbol{w_l} + (S_r\,T - S_l\,T)\,\boldsymbol{w_*} + (\frac{h}{2} - S_r\,T)\,\boldsymbol{w_r}. \tag{4.6}$$

Harten, Lax and van Leer observed that, the expression of the average state $\boldsymbol{w_*}$ could be derived by imposing a consistency condition between the integral of the exact and approximated solutions. This consistency condition can be formulated as follows

$$\int_{-h/2}^{h/2} \boldsymbol{\omega^{Godunov}}(\frac{x}{T}; \boldsymbol{w_l}, \boldsymbol{w_r})\, dx = \int_{-h/2}^{h/2} \boldsymbol{\omega^{HLL}}(\frac{x}{T}; \boldsymbol{w_l}, \boldsymbol{w_r})\, dx. \tag{4.7}$$

Indeed, in the case of overestimated acoustic wave speed estimates (S_l, S_r) (i.e. respectively smaller and larger than the exact signals), this result provides a sufficient condition for h ensuring that the left-hand side of (4.7) satisfies the integral consistency condition with the conservation laws given in (4.3). As a result, applying the integral consistency condition with the conservation laws in the expression (4.7), yields the following definition, once the terms have been rearranged

$$\boldsymbol{w^*(w_l, w_r)} = \frac{S_r \boldsymbol{w_r} - S_l \boldsymbol{w_l} - \big(\, \boldsymbol{f(w_r)} - \boldsymbol{f(w_l)} \,\big)}{S_r - S_l}. \tag{4.8}$$

Then, the formulation of the intermediate numerical flux for the HLL scheme is obtained using the integral consistency over either the left or the right rectangle (4.4), both leading to an equivalent expression, since the condition (4.7) holds. By imposing the equality between the two solutions over the rectangle $[0, T] \times [-\frac{h}{2}, 0]$, this gives

$$\begin{aligned} &\frac{h}{2}\boldsymbol{w_l} - \Big(\textstyle\int_0^T \boldsymbol{f}\big(\boldsymbol{w}(t,0)\big)\, dt - T\boldsymbol{f}(\boldsymbol{w_l})\Big) = T\, S_l(\boldsymbol{w_*} - \boldsymbol{w_l}) + \frac{h}{2}\boldsymbol{w_l} \\ \Leftrightarrow \qquad &\\ &\frac{1}{T}\textstyle\int_0^T \boldsymbol{f}\big(\boldsymbol{w}(t,0)\big)\, dt = \boldsymbol{f}(\boldsymbol{w_l}) + \, S_l(\boldsymbol{w_*} - \boldsymbol{w_l}) \end{aligned},$$

and therefore the intermediate numerical flux is introduced as follows

$$\boldsymbol{f}_* = \boldsymbol{f}(\boldsymbol{w_l}) + \, S_l(\boldsymbol{w_*} - \boldsymbol{w_l}).$$

Similarly, integrating over the right rectangle $[0, T] \times [0, \frac{h}{2}]$, this gives another equivalent formulation of the intermediate flux

$$\boldsymbol{f}_* = \boldsymbol{f}(\boldsymbol{w_r}) - \, S_r(\boldsymbol{w_r} - \boldsymbol{w_*}).$$

The expression of intermediate numerical flux can be equivalently reformulated by inserting the definition of the average state (4.8) into the two above definitions. After some simplifications, the numerical flux associated with the HLL scheme can be for instance formulated as follows

$$\boldsymbol{\mathcal{F}^{HLL}}(\boldsymbol{w_l}, \boldsymbol{w_r}) = \begin{cases} \boldsymbol{f}(\boldsymbol{w_l}) & \text{if } S_l \, > 0 \\ \dfrac{S_r\, \boldsymbol{f}(\boldsymbol{w_l}) - S_l\, \boldsymbol{f}(\boldsymbol{w_r}) + S_l\, S_r\, (\boldsymbol{w_r} - \boldsymbol{w_l})}{S_r - S_l} & \text{if } S_l < 0 < S_r \,, \\ \boldsymbol{f}(\boldsymbol{w_r}) & \text{if } S_r < 0 \end{cases} \tag{4.9}$$

and the expression is fully determined, provided that the wave estimates (S_l, S_r) are defined. A more compact formulation for the numerical flux was introduced by Harten-Lax-van Leer, which is given by

$$\boldsymbol{\mathcal{F}^{HLL}}(\boldsymbol{w_l}, \boldsymbol{w_r}) = \frac{S_r^+ \boldsymbol{f}(\boldsymbol{w_l}) - S_l^- \boldsymbol{f}(\boldsymbol{w_r})}{S_r^+ - S_l^-} + \frac{S_r^+ S_l^-}{S_r^+ - S_l^-} \boldsymbol{\Delta w}, \tag{4.10}$$

4.1.2 . Wave speed estimates

The definition of the wave estimates is crucial in the formulation of the HLL scheme [64, 65, 89], and more generally in the formulation of HLL-type schemes. Depending on these expressions, valuable properties could be enforced into the schemes, including a more accurate capture of shocks, the

positivity-preserving property, but also the entropy stability of the methods. As pointed out by Davis in [89], regardless the choice of the wave speed estimates (S_l, S_r), the Lax-Wendroff theorem remains applicable. Therefore, if the numerical method converges, the discrete solution will converge to a weak solution of the problem. Nevertheless, this does not ensure that the discrete solution will approximate the entropy solution. Harten, Lax and van Leer have provided a sufficient condition, also known as the Harten-Lax theorem (see theorem 3.1 in [4]), demonstrating that, under some assumptions, Godunov-type schemes tend to approximate the entropy solution. Note that, by considering overestimated acoustic wave speed estimates (S_l, S_r), this provides sufficient assumption for satisfying the theorem. This is due to the fact that underestimated estimates result in a loss of the integral consistency condition, as previously mentioned. In such case, the integral consistency condition between the exact and approximate solutions (4.7) is no longer related to the expression (4.3). In opposition, for overestimated wave speed estimates, then, the integral consistency condition (4.7) can be written as

$$\frac{h}{2}(\boldsymbol{w_l} + \boldsymbol{w_r}) - T\big(\boldsymbol{f}(\boldsymbol{w_r}) - \boldsymbol{f}(\boldsymbol{w_l})\big) = \int_{-h/2}^{h/2} \boldsymbol{\omega^{HLL}}(\frac{x}{T}; \boldsymbol{w_l}, \boldsymbol{w_r})\, dx,$$

and using the definition (4.6) for the right-hand side, and performing simple simplifications yields the next relation

$$\boldsymbol{f}(\boldsymbol{w_r}) - \boldsymbol{f}(\boldsymbol{w_l}) = S_l(\boldsymbol{w_*} - \boldsymbol{w_l}) + S_r(\boldsymbol{w_r} - \boldsymbol{w_*}).$$

Therefore, with overestimated wave speed estimates, the integral consistency condition (4.7) equivalently reduces to satisfying the jump conditions. Regarding the second requirement of the Harten-Lax theorem for the HLL scheme related to the integral consistency with the entropy inequality, details can be found in the work of Davis [89].

The literature has mainly exposed two distinct approaches for deriving wave speed estimates (S_l, S_r). On one hand, direct estimates aim at introducing a smallest and fastest wave speed, as discussed in [64, 65, 72, 89]. On the other hand, pressure-velocity based wave speed estimates were proposed in [24,34,92]. Nevertheless, the second approach is generally more sophisticated because the formulation of the acoustic wave speeds (S_l, S_r) relies on a theoretical analysis of the behavior of the exact solution. These formulations generally express better acoustic wave speed estimates, proved to always include the exact signals, as for instance the estimates proposed by Bouchut [92], or Guermond-Popov [93]. For a complete presentation of the pressure-velocity based wave speed estimates, the reader is referred to Toro's works [24, 34, 94], and also to [92, 93, 95], which delve into this topic.

Two popular direct fan wave estimates are commonly employed in the literature, and therefore, are introduced next. The Davis's estimates [89] is one of the simplest formulation, as the smallest and largest wave speed estimates are given by straightforward evaluations of the eigenvalues according to the left and right states

$$\textbf{(Davis's approximations)} \quad \begin{cases} S_l = \min(\, u_l - c_l, \quad u_r - c_r \,) \\ S_r = \max(\, u_l + c_l, \quad u_r + c_r \,) \end{cases}. \tag{4.11}$$

Although this choice has demonstrated robustness and simplicity in practice, it also introduces some issues that are discussed next. Indeed, as originally pointed out by Davis in [89], these wave speed estimates underestimate the exact speed of shocks, and overestimate the speed of expansion waves. Note that, this has been typically illustrated for the case of the speed of shocks in the work of Guermond-Popov [93] (see for instance the appendix B). Consequently, these estimates do not satisfy the assumption of a sufficient condition given by the Harten-Lax theorem and therefore, this leads to a potential loss of the entropy stability for the Godunov-type scheme. However, such simple estimates proved to be robust in practice, as the resulting discrete solution continued to effectively approximate the entropy solution. Nevertheless, another difficulty of the Davis's estimates (4.11) is to produce smeared

shock waves, affecting the overall accuracy and quality of the discrete solution. As argued by Batten et al. [65], a better accuracy is obtained by considering the Einfeldt's estimates, given by the following expressions

$$\textbf{(Einfeldt's approximations)} \qquad \begin{cases} S_l = \min(\, u_l - c_l, \quad \tilde{u} - \tilde{c} \,) \\ S_r = \max(\, \tilde{u} + \tilde{c}, \quad u_r + c_r \,) \end{cases}, \tag{4.12}$$

where $\tilde{u}$ and $\tilde{c}$ are computed from the Roe average, which provides the advantage to exactly resolve isolated shocks. Furthermore, Batten et al. proved that, when expressions (4.12) are used to introduce the HLLC scheme, defined in the next subsections, then, the scheme satisfies the positivity-preserving property for the density and internal energy. However, the expressions (4.12) are also prone to underestimated speeds of shocks, and again, the possibility of a loss of entropy stability cannot be ruled out.

4.1.3 . Definition of the HLLEM scheme

Although, the HLL-scheme is robust and stable for 1D models, such as the shallow water or the isentropic Euler equations, this scheme is not suitable for the compressible Euler equations. The method suffers from a significant inaccuracy, as it considers an approximation based on a two-wave structure, thereby ignoring the contact wave included in the exact solution. As a consequence, this approximation is responsible of an unacceptable smearing of the contact discontinuity, and therefore a loss the overall accuracy and quality of the discrete solution. The literature has reported several papers aiming at improving this scheme, in order to restore the contact discontinuity, see for instance [24,72,90] among others. In the following, the approach proposed by Einfeldt [72] is discussed, as it introduces a formulation to restore the contact wave based on a finer definition of the average state $\boldsymbol{w_*}$, while preserving the initial structure of the approximate solution $\boldsymbol{\omega^{HLL}}$. In that, this work is interesting, since it first enhances the overall accuracy of the method, and additionally, it also illustrates the significance of a common formalism among these schemes. Indeed, Einfeldt noticed that the Roe scheme can be also expressed [72] as follows

$$\boldsymbol{\mathcal{F}^{Roe}} = \frac{\tilde{\lambda}^+_{d+2}\boldsymbol{f}(\boldsymbol{w_l}) - \tilde{\lambda}^-_1\boldsymbol{f}(\boldsymbol{w_r})}{\tilde{\lambda}^+_{d+2} - \tilde{\lambda}^-_1} + \frac{\tilde{\lambda}^+_{d+2}\tilde{\lambda}^-_1}{\tilde{\lambda}^+_{d+2} - \tilde{\lambda}^-_1}\Big(\boldsymbol{\Delta w} - \frac{\tilde{\lambda}_{d+2} - \tilde{\lambda}_1}{\tilde{\lambda}_{d+2} - \tilde{\lambda}_1 + |\tilde{\lambda}_{d+2} + \tilde{\lambda}_1|}\,(\sum_{k=2}^{d+1}\tilde{\alpha}_k\tilde{\boldsymbol{r}}_{\boldsymbol{k}})\Big), \tag{4.13}$$

where the expression for the coordinates of the jumps of the conservative variables $(\tilde{\alpha}_2, \tilde{\alpha}_3)$ and the two right eigenvectors $(\tilde{\boldsymbol{r}}_{\boldsymbol{2}}, \tilde{\boldsymbol{r}}_{\boldsymbol{3}})$ are given in subsection 2.2.1 (for the case $d = 2$). This reformulation of the numerical flux shows a notable disparity between the two schemes, with especially the presence of additional terms in the Roe scheme, not present in the initial expression of the HLL flux (4.10). Einfeldt [72] argued that the information regarding the contact discontinuity was buried in the average state $\boldsymbol{w_*}$, and conducted a theoretical analysis in order to identify the role of these additional terms. As a result, an improved formulation has been developed to recover the contact discontinuity, which relies on the modification of the approximate Riemann solution through the addition of anti-diffusion terms in the definition of the average state. This has led to the formulation of the HLLEM numerical flux [64, 72], given by

$$\boldsymbol{\mathcal{F}^{HLLEM}}(\boldsymbol{w_l}, \boldsymbol{w_r}) = \frac{S^+_r\boldsymbol{f}(\boldsymbol{w_l}) - S^-_l\boldsymbol{f}(\boldsymbol{w_r})}{S^+_r - S^-_l} + \frac{S^+_r S^-_l}{S^+_r - S^-_l}\Big(\boldsymbol{\Delta w} - \frac{\tilde{c}}{\tilde{c} + |\breve{u}|}\,(\sum_{k=2}^{d+1}\tilde{\alpha}_k\tilde{\boldsymbol{r}}_{\boldsymbol{k}})\Big), \tag{4.14}$$

to be compared with (4.13), where the quantity $\breve{u}$ is given by $\breve{u} = (S_r + S_l)/2$ and corresponds to a numerical approximation of the velocity of the contact discontinuity. However, Park-Kwon [96] claimed that the a better accuracy could be achieved if the Roe average $\tilde{u}$ was used instead of $\breve{u}$, leading therefore to a fully-hybridization of the two schemes.

4.1.4 . Definition of the HLLC scheme

The HLLC scheme [24] represents another extended version of the HLL-type scheme, which has been derived with the objective of recovering the missing contact wave. In contrast with the HLLEM scheme, the approach is based on the enhancement of the structure of the approximate Riemann solution, from a two-wave structure to a three-wave structure, similarly to the exact solution. In the following, the derivation of the HLLC scheme is briefly discussed, by initially recalling the original work by Toro et al. in [24]. Then, the improved version proposed by Batten et al. in [65] is introduced. In order to be consistent with the formulation of the Roe scheme introduced in chapter 2, the following expressions are given in the two-dimensional case (i.e. $d = 2$).

Toro et al. in [24] started to investigate a Godunov-type method based on an approximate Riemann solution $\boldsymbol{\omega}^{\boldsymbol{HLLC}}$ formulated as follows

$$\boldsymbol{\omega}^{\boldsymbol{HLLC}}(\frac{\xi}{t};\boldsymbol{w_l},\boldsymbol{w_r},\boldsymbol{n}) = \begin{cases} \boldsymbol{w_l} & \text{if} \quad \frac{\xi}{t} < S_l(\boldsymbol{w_l},\boldsymbol{w_r},\boldsymbol{n}) \\ \boldsymbol{w_l^*}(\boldsymbol{w_l},\boldsymbol{w_r},\boldsymbol{n}) & \text{if} \quad S_l(\boldsymbol{w_l},\boldsymbol{w_r},\boldsymbol{n}) < \frac{\xi}{t} < S_*(\boldsymbol{w_l},\boldsymbol{w_r},\boldsymbol{n}) \\ \boldsymbol{w_r^*}(\boldsymbol{w_l},\boldsymbol{w_r},\boldsymbol{n}) & \text{if} \quad S_*(\boldsymbol{w_l},\boldsymbol{w_r},\boldsymbol{n}) < \frac{\xi}{t} < S_r(\boldsymbol{w_l},\boldsymbol{w_r},\boldsymbol{n}) \\ \boldsymbol{w_r} & \text{if} \quad S_r(\boldsymbol{w_l},\boldsymbol{w_r},\boldsymbol{n}) < \frac{\xi}{t} \end{cases}, \tag{4.15}$$

where the two intermediate states $(\boldsymbol{w_l^*},\boldsymbol{w_r^*})$ are unknown quantities that must be determined, and, the wave speed estimates $(S_l,\ S_*,\ S_r)$ are input parameters that complete the definition, similarly to the HLL scheme (4.5). In the following, generic wave speed estimates $(S_l,\ S_*,\ S_r)$ are first introduced. In addition, in order to ensure the consistency with the Harten-Lax theorem, we assumed that the two acoustic wave speed estimates, namely (S_l, S_r), overestimate the smallest and largest original signals, respectively. As previously discussed in subsection 4.1.2, in such cases, there exists an equivalence between imposing the integral consistency condition (4.7) between the exact and approximate solutions and the jump conditions. For the HLLC scheme, this requires to find the two intermediate states such that the following relationship holds

$$\boldsymbol{f}(\boldsymbol{w_r},\boldsymbol{n}) - \boldsymbol{f}(\boldsymbol{w_l},\boldsymbol{n}) = S_l(\boldsymbol{w_l^*} - \boldsymbol{w_l}) + S_*(\boldsymbol{w_r^*} - \boldsymbol{w_l^*}) + S_r(\boldsymbol{w_r} - \boldsymbol{w_r^*}).$$

Note that, the derivation of the HLLC scheme can therefore be conducted in two equivalent ways: either by first considering the integral consistency condition, as similarly outlined for the HLL scheme and discussed in Toro et al. [24] and Batten et al. [65], or by directly applying the jump conditions across each wave [34]. Here, the derivation of the HLLC scheme is based on the jump conditions. We look for two intermediate states such that the following conditions are satisfied

$$\begin{cases} \boldsymbol{f}(\boldsymbol{w_l^*},\boldsymbol{n}) - \boldsymbol{f}(\boldsymbol{w_l},\boldsymbol{n}) = S_l(\boldsymbol{w_l^*} - \boldsymbol{w_l}) \\ \boldsymbol{f}(\boldsymbol{w_r^*},\boldsymbol{n}) - \boldsymbol{f}(\boldsymbol{w_l^*},\boldsymbol{n}) = S_*(\boldsymbol{w_r^*} - \boldsymbol{w_l^*}) \\ \boldsymbol{f}(\boldsymbol{w_r},\boldsymbol{n}) - \boldsymbol{f}(\boldsymbol{w_r^*},\boldsymbol{n}) = S_r(\boldsymbol{w_r} - \boldsymbol{w_r^*}) \end{cases} \tag{4.16}$$

For the sake of brevity, in order to establish unified expressions for both the right and left intermediate states, a generic index $\cdot_k$ is introduced in the following to refer to either the left or right side. Depending on the value of k, either the first or third equation in (4.16) is analyzed. In addition, this index is also used in the following notations

$$\begin{cases} \delta_{c_l} = S_l - \mathcal{U}_{n_l} \\ \delta_{c_r} = S_r - \mathcal{U}_{n_r} \end{cases} \quad \text{and} \quad \begin{cases} \delta_{S_l} = S_l - S_* \\ \delta_{S_r} = S_r - S_* \end{cases}. \tag{4.17}$$

These notations are introduced in order to simplify the algebra and the presentation of results. Moreover, these notations turned out to be useful in the last chapter for an in-depth analysis of the wave structure of the HLLC scheme.
In the derivation of the HLLC, we proceed step by step, as follows. By extracting the first component from both the first and third equations in (4.16), it can be observed that, two unknown quantities $\mathcal{U}^*_{n_k}$ and ρ^*_k for the intermediate states $\boldsymbol{w^*_k}$ are related through the following relation:

$$\rho^*_k \mathcal{U}^*_{n_k} - \rho_k \mathcal{U}_{n_k} = S_k(\rho^*_k - \rho_k). \tag{4.18}$$

A crucial feature of the original derivation made by Toro et al. [24] consists in associating the intermediate wave speed estimate to the normal velocity of the left and right states, as follows

$$\mathcal{U}^*_{n_l} \quad = \quad S_* \quad = \quad \mathcal{U}^*_{n_r}. \tag{4.19}$$

Thus, expression (4.18) is no longer underdetermined as the information stems from the estimate S_*. Consequently, after rearranging terms in (4.18) and using notations (4.17), we get the left and right intermediate density

$$\rho^*_k = \frac{\rho_k \delta_{c_k}}{\delta_{S_k}}. \tag{4.20}$$

Then, by considering the momentum equations of (4.16), after rearranging terms, we find that

$$\rho^*_k \boldsymbol{\mathcal{U}^*_k} = \frac{\rho_k \boldsymbol{\mathcal{U}_k} \delta_{c_k}}{\delta_{S_k}} + \frac{(p^*_k - p_k)\boldsymbol{n}}{\delta_{c_k}}, \tag{4.21}$$

resulting in a second underdetermined expression. Nevertheless, upon projection of (4.21) onto the normal vector $\boldsymbol{n}$, an expression for the intermediate pressure p^*_k can be obtained. By using the assumption made by Toro et al. (4.19), with the definition of the intermediate density (4.20), and after some simplifications, we obtain

$$p^*_k = \rho_k(\boldsymbol{\mathcal{U}^*_{n_k}} - \boldsymbol{\mathcal{U}_{n_k}})\delta_{c_k} + p_k. \tag{4.22}$$

Next, by inserting the previous definition into expression (4.21), the intermediate velocity vector can be expressed as follows

$$\boldsymbol{\mathcal{U}^*_k} = \boldsymbol{\mathcal{U}_k} + \boldsymbol{n}(\mathcal{U}^*_{n_k} - \mathcal{U}_{n_k}) = \boldsymbol{n}\,\mathcal{U}^*_{n_k} + \boldsymbol{t}\,\mathcal{U}_{t_k}, \tag{4.23}$$

where the tangential vector is given by $\boldsymbol{t} = (-n_y, n_x)^t$. As a consequence of specifying S_* and of enforcing condition (4.19), the above expression becomes fully determined. Regarding the energy equations in (4.16), the following expression is obtained by inserting the definitions of the intermediate density (4.20) and pressure (4.22), with

$$E^*_k = E_k + (S^* - \mathcal{U}_{n_k})(S^* + \frac{p_k}{\rho_k \delta_{c_k}}). \tag{4.24}$$

This completes the definitions of the intermediate states $(\boldsymbol{w^*_l}, \boldsymbol{w^*_r})$, which can be summarized with:

$$\boldsymbol{w^*_k} = \frac{\rho_k \delta_{c_k}}{\delta_{S_k}} \begin{pmatrix} 1 \\ \boldsymbol{n}\, S_* + \boldsymbol{t}\, \mathcal{U}_{t_k} \\ E_k + (S_* - \mathcal{U}_{n_k})(S_* + \dfrac{p_k}{\rho_k \delta_{c_k}}) \end{pmatrix}. \tag{4.25}$$

As shown above, the jump conditions across each wave (4.16) are naturally underdetermined systems for these equations. In order to restore the contact wave, Toro et al. have imposed to the approximate Riemann solution (4.15) to behave similarly as the exact solution, by preserving the normal velocity along the contact wave (4.19). As demonstrated above, provided that an estimate of the speed of the

contact wave S_* is given, assumption (4.19) allows the definition of the approximate Riemann solution $\boldsymbol{\omega}^{\boldsymbol{HLLC}}$ in (4.15). Nevertheless, regarding the behavior of the exact solution along the contact wave, there exist other quantities that are also conserved, including the intermediate pressure, corresponding to Riemann invariants [31, 34]

$$\mathcal{U}_{n_l}^* = \mathcal{U}_{n_r}^* \qquad \text{and} \qquad p_l^* = p_r^*. \tag{4.26}$$

However, the original derivation made by Toro et al. [24] does not satisfy the second condition for intermediate pressures (4.22). As discussed Toro et al. in [24], numerical evidence demonstrated that this condition could be relaxed. Furthermore, it should be noted that not every Riemann solver satisfies these two conditions. This is especially the case for the Roe scheme.
Batten et al. [65] suggested that a more suitable approximate Riemann solution $\boldsymbol{\omega}^{\boldsymbol{HLLC}}$ could be achieved by slightly modifying the initial approach. This second approach only requires the introduction of (S_l, S_r), while retaining the assumption made by Toro et al. As a consequence of not providing an explicit value for S_*, expressions given in (4.20 - 4.22) are therefore underdetermined, as previously discussed, but they remain still relevant. Batten et al. noted that, by directly imposing to the approximate Riemann solution to satisfy conditions (4.26), then estimates for the intermediate normal velocity S_* and pressure p_* could be derived from the expression of the intermediate pressure (4.22). As for instance, the difference between the left and right intermediate pressures leads to, after rearranging terms

$$S_* = \frac{\rho_r \mathcal{U}_{n_r}(S_r - \mathcal{U}_{n_r}) - \rho_l \mathcal{U}_{n_l}(S_l - \mathcal{U}_{n_l}) - \Delta p}{\rho_r(S_r - \mathcal{U}_{n_r}) - \rho_l(S_l - \mathcal{U}_{n_l})} = \frac{\Delta(\rho \mathcal{U}_n \delta_c) - \Delta p}{\Delta(\rho \delta_c)}, \tag{4.27}$$

thereby formulating an intermediate wave speed estimate, defined according to the two initial conservative states $(\boldsymbol{w_l}, \boldsymbol{w_r})$ and the wave speed estimates (S_l, S_r). A similar approach leads to obtain an estimate for the intermediate pressure p_*. Next, estimates $S_* = \mathcal{U}_{n_l}^* = \mathcal{U}_{n_r}^*$ and $p^* = p_l^* = p_r^*$ are used to express the other quantities in (4.20 - 4.22).
Once the two intermediate states $(\boldsymbol{w_l^*}, \boldsymbol{w_r^*})$ have been found, the numerical flux associated with the HLLC scheme is formulated as follows

$$\boldsymbol{\mathcal{F}}^{\boldsymbol{HLLC}}(\boldsymbol{w_l}, \boldsymbol{w_r}, \boldsymbol{n}) = \begin{cases} \boldsymbol{f}(\boldsymbol{w_l}, \boldsymbol{n}) & \text{if } S_l > 0 \\ \boldsymbol{f_l^*} = \boldsymbol{f}(\boldsymbol{w_l}, \boldsymbol{n}) + S_l(\boldsymbol{w_l^*} - \boldsymbol{w_l}) & \text{if } S_l < 0 < S_* \\ \boldsymbol{f_r^*} = \boldsymbol{f}(\boldsymbol{w_r}, \boldsymbol{n}) - S_r(\boldsymbol{w_r} - \boldsymbol{w_r^*}) & \text{if } S_* < 0 < S_r \\ \boldsymbol{f}(\boldsymbol{w_r}, \boldsymbol{n}) & \text{if } S_r < 0 \end{cases}. \tag{4.28}$$

4.2 . State of the art for low Mach number flows and HLL-type schemes

Similarly to the Roe scheme, the HLL-type schemes also suffer from an accuracy problem in computing low Mach number flows, and requires to be modified in order to obtain consistent discrete solutions. The literature still reports numerous recent corrections for these schemes. While our main concern is initially focused on the HLLC scheme, in this section, the scope of the analysis is slightly expanded, by also briefly discussing some extensions proposed in the literature for the HLL, HLLEM and HLLC schemes. This is motivated by the observation that an increasing number of recent papers investigate the possibility of developing a unified framework for correcting these schemes, with a particular interest on transposing a same low Mach correction to these numerical fluxes, or even to other schemes. The objective of this section is to present a concise review of corrections applied to these schemes. As shown is the following, it is noticeable that the HLL-type schemes can embed similar corrections

applied to the Roe scheme in the low Mach number limit, as illustrated in several papers [21, 97–109], and discussed below. In this section, the formulation of HLL-type schemes is discussed for generic wave speed estimates (S_l, S_*, S_r), without any restrictions on these parameters used in the formulation of these schemes.

4.2.1 . A legacy derived from the analyses of the Roe scheme

We first look at publications by Luo et al. [97] and Park et al. [98], introducing preconditioning methods for the HLLC and HLLEM schemes, respectively. These works describe an approximate methodology for transposing the effects of the Weiss-Smith preconditioning matrix [14,15,110] to HLL-type schemes, for which, the expression of the corresponding artificial viscosity matrix is not known, in contrast to the Roe scheme (see section 2.3). Luo et al. in [97] modified the acoustic wave speed estimates (S_l, S_r) in the formulation of the HLLC scheme (4.25), (4.27 - 4.28) using the wave speeds arising from the preconditioned equations. Latter, in the pursuit of investigations initiated by Park et Kwon in [96], Park et al. used a similar approach to derive a correction described in [98], with a slight adjustment to exploit the common formalism between the Roe and HLLEM schemes indicated in (4.13 - 4.14). This correction similarly substitutes the quantities written in blue in the following preconditioned numerical HLLEM flux

$$\boldsymbol{\mathcal{F}^{HLLE+(P)}} = \frac{S_r^+ \boldsymbol{f}(\boldsymbol{w_l}) - S_l^- \boldsymbol{f}(\boldsymbol{w_r})}{S_r^+ - S_l^-} + \frac{S_r^+ S_l^-}{S_r^+ - S_l^-}\Big(\boldsymbol{\Delta w} - \frac{\tilde{c}}{\tilde{c} + |\tilde{u}|}\big(\sum_{k=2}^{d+1} \tilde{\alpha}_k \tilde{\boldsymbol{r}}_{\boldsymbol{k}}\big)\Big),$$

Li-Gu also conducted a series of investigations in [21], following a comprehensive analysis aiming at identifying the mechanisms responsible for the inaccuracy problem for the Roe scheme. The formulation of their P-HLL and A-HLL schemes is not based on standard preconditioned methods, and therefore maintaining time consistency with the equations. The derivation of these schemes follows a similar approach, which is rather based on the preconditioned dissipation matrix investigated by Turkel, also considered by Guillard-Viozat in the formulation of the so-called Roe-Turkel scheme [7]. Numerical experiments conducted with the P-HLL and A-HLL schemes show that both schemes are capable of resolving the accuracy problem, but nevertheless, are prone to significant pressure checkerboard mode problems, typically not encountered with the Roe-Turkel scheme.

This preconditioned dissipation matrix was also used later in the works of Pelanti in [99, 111, 112], in which a novel approach introducing a necessary rescaling of the dissipation is proposed for the HLLC scheme. Through an investigation of the wave structure, Pelanti identified some interesting similarities that have been highlighted, as potential means of mimicking the formalism of the preconditioning dissipation matrix formulated for the Roe scheme. As a result, this has led to the formulation of the HLLC-Turkel scheme, which has been validated for the Euler equations [99], and for a two-phase compressible flow model [111]. As indicated by the author, this scheme also proved to be robust, providing analogous performance in comparison with the original Roe-Turkel scheme. This later point will be especially developed in the following sections.

More recently, the literature has also reported a number of studies based on other approaches for the extension of HLL-type schemes in the low Mach number regime. These investigations either share common features with the analysis of Dellacherie (the Roe-Dellacherie scheme, or the low Mach Godunov framework) [10,86], or are in line with the popular approach proposed by Thornber et al. [85]. For instance, following the approach of Dellacherie aimed at centering asymptotically the pressure gradient in the equations (the reader is referred to section 2.5.2 for more details), we can enumerate the works of Yu et al. [100, 101] for the HLLEM scheme, Sun et al. in [102] with the HLLIM scheme, and Xie et al. in [103] in the case of the Roe scheme expressed with the HLLEM formalism (4.13). The second approach proposed by Thornber et al. in [85], introduces a rescaling of the dissipation based on the following formulation of modified conservative variables for the left and right states, as

depicted in blue

$$\boldsymbol{w_l} = \begin{pmatrix} \rho_l \\ \rho_l \frac{1}{2}(\boldsymbol{\mathcal{U}_l}\,(1+f(M)) + \boldsymbol{\mathcal{U}_r}\,(1-f(M))) \\ \rho_l E_l \end{pmatrix}. \qquad \boldsymbol{w_r} = \begin{pmatrix} \rho_r \\ \rho_r \frac{1}{2}(\boldsymbol{\mathcal{U}_l}(1-f(M)) + \boldsymbol{\mathcal{U}_r}(1+f(M))) \\ \rho_r E_r \end{pmatrix},$$

where $f(M)$ behaves as a local Mach number, with $f(M) \to 1$ when $M \geq 1$. This reconstruction process, which yields a same centered approximation of the velocity in the low Mach number limit for both the right and left states, proved to significantly improve the accuracy in this regime. However, as pointed-out by Thornber et al. [113], its effectiveness is subject of restriction regarding the limiter used in the MUSCL reconstruction. This formulation has been, for instance, incorporated into the unified framework for the extension of HLL-type schemes to hypersonic heating computations of Xie et al. described in [104], with the introduction of the ASHLLC and ASHLLEM schemes. Additionally, more recently, Gogoi-Mandal continued the investigations with the HLL-TNP scheme in [105], presenting a series of analysis using this approach.

4.2.2 . A quest for unified formulations

We now discuss successive works of Chen et al. [106–108] among others on this topic, which have proposed various corrections applied to different schemes, including the Rusanov, Roe, HLL, HLLC, and even AUSM schemes. Chen et al. proposed a unified formulation, called the LD formulation (low dissipation), based on the decomposition of the jumps of conservative variables $\boldsymbol{\Delta w}$ into a density and a rescaled velocity diffusions, as explained by the authors in [106]. For the Roe and HLL schemes, the modified flux are expressed as follows:

$$\begin{aligned} \boldsymbol{\mathcal{F}^{LD-Roe}} &= \frac{\boldsymbol{f}(\boldsymbol{w_l},\boldsymbol{n}) + \boldsymbol{f}(\boldsymbol{w_r},\boldsymbol{n})}{2} - \frac{1}{2}|\boldsymbol{A}^{\boldsymbol{Roe}}(\tilde{\boldsymbol{w}},\boldsymbol{n})| \left[\begin{pmatrix} \Delta\rho \\ \bar{\rho}\Delta\boldsymbol{\mathcal{U}} \\ \dfrac{\Delta p}{\gamma-1} + \dfrac{|\bar{\mathcal{U}}|^2}{2}\Delta\rho \end{pmatrix} + f(M) \begin{pmatrix} 0 \\ \bar{\boldsymbol{\mathcal{U}}}\Delta\rho \\ \bar{\rho}\Delta(\dfrac{|\mathcal{U}|^2}{2}) \end{pmatrix} \right] \\ \boldsymbol{\mathcal{F}^{LD-HLL}} &= \frac{S_r^+\boldsymbol{f}(\boldsymbol{w_l},\boldsymbol{n}) - S_l^-\boldsymbol{f}(\boldsymbol{w_r},\boldsymbol{n})}{S_r^+ - S_l^-} + \frac{S_r^+ S_l^-}{S_r^+ - S_l^-} \left[\begin{pmatrix} \Delta\rho \\ \bar{\rho}\Delta\boldsymbol{\mathcal{U}} \\ \dfrac{\Delta p}{\gamma-1} + \dfrac{|\bar{\mathcal{U}}|^2}{2}\Delta\rho \end{pmatrix} + f(M) \begin{pmatrix} 0 \\ \bar{\boldsymbol{\mathcal{U}}}\Delta\rho \\ \bar{\rho}\Delta(\dfrac{|\mathcal{U}|^2}{2}) \end{pmatrix} \right] \end{aligned} . \quad (4.29)$$

Then, Chen et al. [107] proposed a novel all-speed HLLC-type scheme, so-called HLLC+, and have provided a discrete analysis and numerical experiments to support this development. The modified scheme introduces intermediate fluxes $\boldsymbol{F_k^*}$ in the simple wave form (4.28), by incorporating anti-dissipation terms, as indicated next

$$\boldsymbol{\mathcal{F}^{HLLC+}} = \begin{cases} \boldsymbol{f}(\boldsymbol{w_l},\boldsymbol{n}) & \text{if } S_l > 0 \\ \boldsymbol{F_l^*} & \text{if } S_l < 0 < S_* \\ \boldsymbol{F_r^*} & \text{if } S_r^* < 0 < S_r \\ \boldsymbol{f}(\boldsymbol{w_r},\boldsymbol{n}) & \text{if } S_r < 0 \end{cases} \quad \text{with} \quad \boldsymbol{F_k^*} = \boldsymbol{f_k^*} + \frac{\rho_l(S_l - \mathcal{U}_{n_l})\rho_r(S_r - \mathcal{U}_{n_r})}{(S_r - \mathcal{U}_{n_r}) - (S_l - \mathcal{U}_{n_l})} \begin{pmatrix} 0 \\ (f(M)-1)\Delta\mathcal{U}_n\boldsymbol{n} \\ (f(M)-1)\Delta\mathcal{U}_n S_* \end{pmatrix}.$$

This approach has been further extended in [108] within a unified formalism, called the APC framework (anti-dissipative pressure correction), where low-Mach corrections have been proposed for the Rusanov, Roe, HLL, HLLC and the AUSM schemes. It is nevertheless notable that the expression obtained for the modified Roe-APC scheme shows several similarities with the Roe-Dellacherie scheme, except in the energy equation [114]. This suggests that these corrections are guided by a relative close approach in addressing the accuracy problem, and therefore entail the pursue of a similar analysis.

4.2.3 . New expressions for the HLLC numerical flux

Other recent approaches in deriving low Mach number corrections for the HLLC scheme have also been documented in the literature, and are based on the introduction of a novel form for expressing the

numerical flux $\boldsymbol{\mathcal{F}^{HLLC}}$. For instance, the works of Fleischmann et al. [109,115] provide a particularly unexpected use of this approach, focusing on shock-stable modifications of the numerical scheme for high Mach number flows. Low Mach corrections were considered to cure numerical instabilities induced by strong shocks, such as the carbuncle phenomena, extensively studied by Chauvat in [116]. As pointed-out in these works, the failure of upwind schemes in computing low Mach number flows may be a contributing factor to the emergence of shock instabilities, particularly in the context of grid-aligned shocks, with a vanishing normal Mach number in the transverse fluxes. Indeed, as argued by Zhiqiang et al. [117], only a small inaccuracy in the tangential fluxes is sufficient to trigger shock instabilities in the discrete solution. Then, Fleischmann et al. proposed shock-stable modifications of the Roe scheme in [115], and subsequently attempted to extend the correction to the HLLC scheme in [109]. However, several difficulties were encountered with the direct transposition of the correction, encouraging the authors to develop a novel formulation for the numerical flux $\boldsymbol{\mathcal{F}^{HLLC}}$. This has motivated the derivation of a more compact form, based on the jump conditions, aimed at facilitating the identification of the mechanism, and thus the transposition of the correction from one solver to the other with

$$\boldsymbol{\mathcal{F}^{HLLC-LM}} = \begin{cases} \boldsymbol{f}(\boldsymbol{w_l},\boldsymbol{n}) & \text{if } S_l > 0 \\ \dfrac{\boldsymbol{f}(\boldsymbol{w_l},\boldsymbol{n}) + \boldsymbol{f}(\boldsymbol{w_r},\boldsymbol{n})}{2} + \dfrac{1}{2}(f(M_l)S_l\boldsymbol{\Delta w_l} - |S_*|\boldsymbol{\Delta w_*} - f(M_r)S_r\boldsymbol{\Delta w_r}) & \text{if } S_lS_r < 0 \\ \boldsymbol{f}(\boldsymbol{w_r},\boldsymbol{n}) & \text{if } S_r < 0 \end{cases}, \tag{4.30}$$

where the quantities $\boldsymbol{\Delta w_l} = \boldsymbol{w_l^*} - \boldsymbol{w_l}$, $\boldsymbol{\Delta w_*} = \boldsymbol{w_r^*} - \boldsymbol{w_l^*}$ and $\boldsymbol{\Delta w_r} = \boldsymbol{w_r} - \boldsymbol{w_r^*}$ are the jumps of the conservative states. In the above expression, it can be observed that the numerical flux no longer involves the definitions of intermediate fluxes ($\boldsymbol{f_l^*}$, $\boldsymbol{f_r^*}$), and therefore provides a more compact form, expressed for subsonic flows (ie $S_lS_r < 0$) as a centered scheme stabilized by a numerical dissipation. Note that a similar formulation is considered in the work of Le Touze-Rutard in [118], where an another modified HLLC scheme is used for a 4-equation diffuse interface model, with the following more compact formulation

$$\begin{aligned} \boldsymbol{\mathcal{F}^{HLLC}} = \frac{\boldsymbol{f}(\boldsymbol{w_l},\boldsymbol{n}) + \boldsymbol{f}(\boldsymbol{w_r},\boldsymbol{n})}{2} \\ - \frac{1}{2}\left[\frac{\sigma_l+\sigma_r}{2}\Big(\boldsymbol{f}(\boldsymbol{w_r},\boldsymbol{n}) - \boldsymbol{f}(\boldsymbol{w_l},\boldsymbol{n})\Big)\right. \\ \left. - \frac{\sigma_r-\sigma_l}{2}\Big(S_l\boldsymbol{\Delta w_l} + S_r\boldsymbol{\Delta w_r} - \sigma_*S_*\boldsymbol{\Delta w_*}\Big)\right], \end{aligned} \tag{4.31}$$

where

$$\sigma_l = \text{sign}(S_l) \qquad \sigma_* = \text{sign}(S_*) \qquad \sigma_r = \text{sign}(S_r)\ .$$

These expressions indicate that the HLLC scheme can be interpreted as an artificial viscosity method, as it can be explicitly formulated with a vector dissipation $\boldsymbol{d^{HLLC}}$, as previously discussed in section 2.2.2, with

$$\boldsymbol{\mathcal{F}^{HLLC}}(\boldsymbol{w_l},\boldsymbol{w_r},\boldsymbol{n}) = \frac{\boldsymbol{f}(\boldsymbol{w_l},\boldsymbol{n}) + \boldsymbol{f}(\boldsymbol{w_r},\boldsymbol{n})}{2} - \frac{1}{2}\boldsymbol{d^{HLLC}},$$

and, in analogy with the Roe scheme, the viscosity matrix is hidden in

$$\boldsymbol{d^{HLLC}} = \bar{\sigma}\boldsymbol{\Delta f} - \frac{\Delta\sigma}{2}\Big(S_l\boldsymbol{\Delta w_l} + S_r\boldsymbol{\Delta w_r} - |S_*|\boldsymbol{\Delta w_*}\Big),$$

where $\bar{\cdot}$ denotes the discrete averaging operator. More details regarding this correction can be found in [118]. It is worth noting that there is also a small number of investigations, which, driven by the objective of either transposing a rescaling strategy or for initiating an analysis, have first reinterpreted the numerical flux $\boldsymbol{\mathcal{F}^{HLLC}}$ with the intention of making expressions more easily comparable.

4.2.4 . Reflection and positioning on key trends for correcting the HLLC scheme

Regardless of the analyses performed in all these works to support these developments, several features can be pointed out and are now discussed.

The pursuit of improving either the Roe scheme or HLL-type schemes for low Mach number flows has been numerous times dominated in the existing literature by a large number of published corrections applied to the Roe scheme, and by their techniques of analysis as mentioned in the two previous chapters. With regard to the transposition of a correction from one method to another, although this approach turned out possible and effective in numerous studies, it may also prove to be misleading. Indeed, we could suggest here that the disparate expressions for the numerical flux have also contributed to the difficulty in correcting the same numerical mechanism, since it may induce a potential risk of introducing a slight variation, and thus, may contribute to the large scattering of the formulation of corrections. Therefore , we could inquire whether this is not a consequence of different interpretations of the numerical flux that have contributed to the difficulty in reproducing a common analysis framework. Yet, Godunov-type schemes admit a small number of common expressions, stemming from the linear hyperbolic theory, which appear to be not sufficiently employed for transposing a correction from one scheme to the other as discussed in the following.

For instance, we may wonder whether the modified LD-Roe scheme of Chen et al. has similar properties as the following formulation of the "LD-Roe-2" scheme, which has an identical modification of the jumps of the conservative variables $\Delta \boldsymbol{w}$ (denoted below $\widetilde{\Delta \boldsymbol{w}}$ for brevity) as in expression (4.29). The only difference occurs in the initial expression of the numerical flux before introducing the same rescaling strategy

$$\boldsymbol{\mathcal{F}^{LD-Roe-2}} = \frac{\tilde{\lambda}^+_{d+2}\boldsymbol{f}(\boldsymbol{w_l},\boldsymbol{n}) - \tilde{\lambda}^-_1\boldsymbol{f}(\boldsymbol{w_r},\boldsymbol{n})}{\tilde{\lambda}^+_{d+2} - \tilde{\lambda}^-_1} + \frac{\tilde{\lambda}^+_{d+2}\tilde{\lambda}^-_1}{\tilde{\lambda}^+_{d+2} - \tilde{\lambda}^-_1}\left[\widetilde{\Delta \boldsymbol{w}} - \frac{\tilde{c}}{\tilde{c}+|\tilde{u}|}\left(\sum_{k=2}^{d+1}\left(\tilde{\boldsymbol{l}}_{\boldsymbol{k}}\widetilde{\Delta \boldsymbol{w}}\right)\tilde{\boldsymbol{r}}_{\boldsymbol{k}}\right)\right],$$

where $\tilde{\boldsymbol{l}}_{\boldsymbol{k}}$ are the left eigenvectors. Indeed, in the absence of rescaling of the dissipation vector (i.e. $\widetilde{\Delta \boldsymbol{w}} = \Delta \boldsymbol{w}$), this flux returns the Roe flux (see sections 2.2.1 and 4.1.3). Nevertheless, when the rescaling is applied, this expression raises a question regarding the relation between a correction and the initial formulation of the numerical flux on which it is applied. Also, this raises the point whether a more accurate representation of the correction strategy could be achieved. Here, we refrain from giving a definitive statement for the LD-Roe case, but rather mention a potential risk: similar heuristic approaches applied to different formulations of the numerical flux could lead to modifications that may be slightly different to the original scheme. This latter point has especially been pointed out by Fleischmann et al. in [109], as the modification of the eigenvalues for a Roe-type scheme, developed in [115], turns out to be ineffective when applied to a HLLC-type scheme. As previously mentioned, this has motivated the authors to find a more comparable formalism between these two schemes. Nevertheless, the linear hyperbolic theory [31, 33, 34, 92] already offers a small number of common formalism for Godunov-type schemes, which can be reminded for comparisons. Indeed, the Roe scheme can either be expressed under the simple wave form (see section 2.2), or, the HLLC scheme could be equivalently written as follows

$$\boldsymbol{\mathcal{F}^{HLLC}}(\boldsymbol{w_l},\boldsymbol{w_r},\boldsymbol{n}) = \boldsymbol{f}(\boldsymbol{w_l},\boldsymbol{n}) \quad + \sum_{\{k\in\{l,*,r\}/S_k<0\}} S_k\Delta \boldsymbol{w_k} = \boldsymbol{f}(\boldsymbol{w_r},\boldsymbol{n}) \quad - \sum_{\{k\in\{l,*,r\}/S_k>0\}} S_k\Delta \boldsymbol{w_k}.$$

By averaging both expressions, this yields the following expression for the numerical flux

$$\boldsymbol{\mathcal{F}^{HLLC}}(\boldsymbol{w_l},\boldsymbol{w_r},\boldsymbol{n}) = \frac{\boldsymbol{f}(\boldsymbol{w_l},\boldsymbol{n}) + \boldsymbol{f}(\boldsymbol{w_r},\boldsymbol{n})}{2} \quad - \frac{1}{2}\sum_{k=1}^{3}|S_k|\Delta \boldsymbol{w_k}, \tag{4.32}$$

where $\boldsymbol{\Delta w_1} = \boldsymbol{\Delta w_l}$, $\boldsymbol{\Delta w_2} = \boldsymbol{\Delta w_*}$ and $\boldsymbol{\Delta w_3} = \boldsymbol{\Delta w_r}$. In comparison, the expression of the dissipation vector in the Roe flux could be also written as

$$\boldsymbol{d^{Roe}} = \sum_{k=1}^{4} |\tilde{\lambda}_k| \tilde{\alpha}_k \tilde{\boldsymbol{r}}_{\boldsymbol{k}} = |\tilde{\lambda}_1| \boldsymbol{\Delta w_1} + |\tilde{\lambda}_2| \boldsymbol{\Delta w_2} + |\tilde{\lambda}_4| \boldsymbol{\Delta w_3}.$$

Note that, the jumps of the conservative states obviously differ between the definitions of the HLLC and Roe schemes. Surprisingly, this latter form seems to not be frequently employed in the literature, while it provides an interesting framework for the discrete analysis, including implicitly a viscosity matrix in the dissipation vectors $\boldsymbol{d^{Roe}}$. Modifications of approximate Riemann solvers should be more carefully undertaken, within a unified framework, as there is a significant risk that the previously observed scattering of modifications of the dissipation vector $\boldsymbol{d^{Roe}}$, mentioned in sections 2.4 and 2.5, may also occur in modifying HLL-type schemes.
In addition, the adaptation of the Turkel analysis to HLL-type schemes, introduced in section 2.3 for the Roe scheme, is made difficult in the absence of an explicit expression of a viscosity matrix. Also, the asymptotic analysis introduced by Guillard-Viozat [7] presents several challenges to be applied to HLL-type schemes, as discussed next. Indeed, an increasing number of recent papers attempt to use this asymptotic discrete analysis, but under assumptions, due to necessary definition of fan waves (S_l, S_*, S_r) in evaluating the numerical flux $\boldsymbol{\mathcal{F}^{HLLC}}$. For instance, in the case of the Einfeldt's approximations (4.12), several authors first apply the following assumptions in the low Mach number limit

$$S_l \simeq -\tilde{c} \qquad \text{and} \qquad S_r \simeq \tilde{c}\,, \qquad\qquad \text{when} \qquad M \longrightarrow 0.$$

Moreover, additional complications also arise from the normalization process in the incompressible limit (see Section 1.4.1). This is for instance illustrated next with the normalization of the intermediate wave speed estimate S_*, which, according to the expression on the right-hand side, requires to define a reference quantity s_r such that the following relationships holds

$$\left(s_r\right) S_* = \left(s_r\right) \frac{\Delta\big(\rho\mathcal{U}_n(S-\mathcal{U}_n)\big) - \Delta p}{\Delta\big(\rho(S-\mathcal{U}_n)\big)} = \left(u_r\right) \frac{\Delta\big(\rho\mathcal{U}_n(S-\mathcal{U}_n)\big)}{\Delta\big(\rho(S-\mathcal{U}_n)\big)} \;-\; \left(\frac{p_r}{\rho_r c_r}\right) \frac{\Delta p}{\Delta\big(\rho(S-\mathcal{U}_n)\big)},$$

where all the above quantities are normalized, and the notation $\cdot_r$ denotes reference quantities. As it can be seen, the definition of s_r inevitably leads to the occurrence of a reference Mach number, either in the first or second term, which must be taken into account in a rigorous analysis. Although the results of the discrete analysis might remain relevant, these examples illustrate the difficulties that are typically addressed through assumptions that must be considered for HLL-type schemes, while such assumptions are unusual in the case of the Roe-type schemes.
Nevertheless, according to the discussion of section 2.5, the works of Park et al. [98] and Pelanti [99] turned out to be a source of inspiration for investigating the existence of a unified formalism, allowing a simultaneous analysis of corrected Roe-types and HLLC-types schemes in the low Mach number limit. Indeed, as discussed in the next section, the work of Pelanti in [99] on the HLLC scheme demonstrates notable similarities with the Roe scheme, from which emerges a framework for deeper investigations regarding what is hidden in the dissipation vector $\boldsymbol{d^{HLLC}}$.

4.3 . The wave structure of the HLLC-scheme

In this section, we present an overview of Pelanti's work [99], in which the analysis of the wave structure of the HLLC flux in form (4.32) was carried out. This work is of particular interest as it

shows significant similarities between the waves of the Roe and the HLLC schemes, and entails the construction of a more comprehensive framework. Indeed, the wave structure is an important feature of Riemann solvers since, it provides the expression of the numerical flux, as for instance illustrated in section 2.2.1 for the Roe scheme. This work turned out to be the basis for further developments in the analysis of the dissipation vector $\boldsymbol{d^{HLLC}}$, which will be detailed in the next chapter.

In section 2.2.1, it has been reminded that the derivation of the simple form of the Roe flux $\boldsymbol{\mathcal{F}^{Roe}}(\boldsymbol{w_l}, \boldsymbol{w_r}, \boldsymbol{n})$ can be achieved using the spectral properties $(\tilde{\lambda}_k, \tilde{\boldsymbol{r}}_{\boldsymbol{k}}, \tilde{\boldsymbol{l}}_{\boldsymbol{k}})$ of the approximate Jacobian matrix $\boldsymbol{A}^{Roe}$. In the case of the HLLC flux, the fundamental idea stems from the search for an analogous approach, while the derivation of the numerical flux $\boldsymbol{\mathcal{F}}$ follows a different construction. Therefore, this constrains the analysis to begin with the definitions of the intermediate states $(\boldsymbol{w_l^*},\ \boldsymbol{w_r^*})$ given in the expression (4.25). But, the investigation is somewhat relatively similar, and consists in looking at each jump of the conservative variables $\boldsymbol{\Delta w}_k$ arising in the structure of the Riemann problem, with the aim of finding a potential path connecting conservative states (see for instance the expression (2.8) for the Roe scheme).

$$\begin{array}{rcccccc} \boldsymbol{\Delta w} = & (\boldsymbol{w_l^*} - \boldsymbol{w_l}) & + & (\boldsymbol{w_r^*} - \boldsymbol{w_l^*}) & + & (\boldsymbol{w_r} - \boldsymbol{w_r^*}) \\ = & \boldsymbol{\Delta w_l} & + & \boldsymbol{\Delta w_*} & + & \boldsymbol{\Delta w_r} \end{array}. \tag{4.33}$$

However, the definitions of the wave speed estimates $(S_l,\ S_*,\ S_r)$ add some complexity for conducting an asymptotic analysis, particularly in the light of the minimum and maximum functions as considered for instance in Davis's approximations (4.11). To initiate the analysis of the wave structure, Pelanti proposed a clever reformulation of fan wave estimates (S_l, S_*, S_r).
Let us introduce a generic discrete fan waves, where the acoustic wave speed estimates are formulated as follows

$$S_l = \mathcal{U}_{n_l} - \hat{c}_l \qquad \text{and} \qquad S_r = \mathcal{U}_{n_r} + \hat{c}_r. \tag{4.34}$$

Thus, only the definition of quantities $\hat{c}_k$ are required to determine the choice of discrete fan waves. Upon insertion of these two expressions into the intermediate wave speed given in the section 4.1.4, we get

$$S_* \quad = \quad \frac{\rho_r \mathcal{U}_{n_r} \hat{c}_r + \rho_l \mathcal{U}_{n_l} \hat{c}_l - \Delta p}{\rho_r \hat{c}_r + \rho_l \hat{c}_l} \quad = \quad \frac{\langle \rho \mathcal{U}_n \hat{c} \rangle - \Delta p}{\langle \rho \hat{c} \rangle}, \tag{4.35}$$

where for convenience, the notation previously introduced $\langle \cdot \rangle$ is reminded $\langle a \rangle = 2\bar{a} = a_l + a_r$. Examples of formulation of $\hat{c}_k$ can be found using the Davis's approximations (4.11), such that

$$\hat{c}_l = \max(c_l,\ c_r - \Delta \mathcal{U}_n) \qquad \text{and} \qquad \hat{c}_r = \max(c_r,\ c_l - \Delta \mathcal{U}_n), \tag{4.36}$$

or considering the Einfledt's approximations (4.12), for which the parameters must be slightly adapted for preserving the original definition

$$\hat{c}_l = \max(c_l,\ \tilde{c}\ - \tilde{\mathcal{U}}_n + \mathcal{U}_{n_l}) \qquad \text{and} \qquad \hat{c}_r = \max(c_r,\ \tilde{c}\ + \tilde{\mathcal{U}}_n - \mathcal{U}_{n_r}). \tag{4.37}$$

This idea is of significant relevance, and has the effect of greatly simplifying the algebra in the following. Note that, this reformulation is not limited to these wave speed estimates. Additional approximations could also be readily formulated in a similar manner, including the pressure-velocity based wave speed estimates given by Toro in [34].
Next, entries $\hat{c}_k$ are considered as generic quantities without further consideration of their definitions. In the decomposition (4.33) of $\boldsymbol{\Delta w}$, each local jump of the conservative variables $\boldsymbol{\Delta w_k}$ are next developed, and the reinterpretation of the wave of speed estimates (4.34) leads to the following expressions

$$\delta_{S_l} = S_l - S_* = \frac{\Delta p - \rho_r \hat{c}_r \Delta \mathcal{U}_n - \hat{c}_l \langle \rho \hat{c} \rangle}{\langle \rho \hat{c} \rangle} \qquad \delta_{S_r} = S_r - S_* = \frac{\rho_l \hat{c}_l \Delta \mathcal{U}_n + \hat{c}_r \langle \rho \hat{c} \rangle + \Delta p}{\langle \rho \hat{c} \rangle}. \tag{4.38}$$

Using the previous expression for δ_{S_l} in $\boldsymbol{\Delta w_l}$, and after some algebra, the left jump of the conservative variables can be expressed as follows

$$\begin{aligned}
\rho_l^* - \rho_l &= \left\{ \frac{\rho_l^*}{\langle \rho \hat{c} \rangle} \left[\frac{\Delta p - \rho_r \hat{c}_r \Delta \mathcal{U}_n}{\hat{c}_l} \right] \right\} \\
(\rho \boldsymbol{\mathcal{U}})_l^* - (\rho \boldsymbol{\mathcal{U}})_l &= \left\{ \frac{\rho_l^*}{\langle \rho \hat{c} \rangle} \left[\frac{\Delta p - \rho_r \hat{c}_r \Delta \mathcal{U}_n}{\hat{c}_l} \right] \right\} \quad (\boldsymbol{\mathcal{U}}_l - \hat{c}_l \boldsymbol{n}), \\
(\rho E)_l^* - (\rho E)_l &= \left\{ \frac{\rho_l^*}{\langle \rho \hat{c} \rangle} \left[\frac{\Delta p - \rho_r \hat{c}_r \Delta \mathcal{U}_n}{\hat{c}_l} \right] \right\} \quad (H_l - \hat{c}_l S_*)
\end{aligned} \tag{4.39}$$

where the right-hand side of the above expression highlights a common scalar factor in each component. Similarly, $\boldsymbol{\Delta w_r}$ is expressed in the same form

$$\begin{aligned}
\rho_r - \rho_r^* &= \left\{ \frac{\rho_r^*}{\langle \rho \hat{c} \rangle} \left[\frac{\Delta p + \rho_l \hat{c}_l \Delta \mathcal{U}_n}{\hat{c}_r} \right] \right\} \\
(\rho \boldsymbol{\mathcal{U}})_r - (\rho \boldsymbol{\mathcal{U}})_r^* &= \left\{ \frac{\rho_r^*}{\langle \rho \hat{c} \rangle} \left[\frac{\Delta p + \rho_l \hat{c}_l \Delta \mathcal{U}_n}{\hat{c}_r} \right] \right\} \quad (\boldsymbol{\mathcal{U}_r} + \hat{c}_r \boldsymbol{n}). \\
(\rho E)_r - (\rho E)_r^* &= \left\{ \frac{\rho_r^*}{\langle \rho \hat{c} \rangle} \left[\frac{\Delta p + \rho_l \hat{c}_l \Delta \mathcal{U}_n}{\hat{c}_r} \right] \right\} \quad (H_r + \hat{c}_r S_*)
\end{aligned} \tag{4.40}$$

In the case of the jumps for the intermediate states $\boldsymbol{\Delta w_*}$, we find after some simplifications

$$\begin{aligned}
\rho_r^* - \rho_l^* &= \Delta\rho + \frac{1}{\langle \rho \hat{c} \rangle} \left[-\Delta p \left(\frac{\rho_r^*}{\hat{c}_r} + \frac{\rho_l^*}{\hat{c}_l} \right) + \Delta \mathcal{U}_n \left(\frac{\rho_r \hat{c}_r \rho_l^*}{\hat{c}_l} - \frac{\rho_l \hat{c}_l \rho_r^*}{\hat{c}_r} \right) \right] \\
(\rho \boldsymbol{\mathcal{U}})_r^* - (\rho \boldsymbol{\mathcal{U}})_l^* &= \hat{\alpha} \left(S_* \boldsymbol{n} - \frac{\langle \mathcal{U}_t \rangle}{2} \boldsymbol{t} \right) + \left\{ \frac{\langle \rho^* \rangle}{2} \Delta \mathcal{U}_t \right\} \boldsymbol{t}, \\
(\rho E)_r^* - (\rho E)_l^* &= \Delta E_n^* + \left\{ \frac{\langle \rho^* \rangle}{2} \Delta \mathcal{U}_t \right\} \frac{\langle \mathcal{U}_t \rangle}{2}
\end{aligned} \tag{4.41}$$

where the notations of Pelanti have been introduced for the two scalar quantities $(\hat{\alpha}, \Delta E_n^*)$ defined as follows

$$\begin{aligned}
\hat{\alpha} &= \rho_r^* - \rho_l^* \\
\Delta E_n^* &= (\rho_r^* h_r - \rho_l^* h_l) + \hat{\alpha} \left[\left(\frac{\langle u^2 \rangle}{4} + \frac{\langle S_*^2 \rangle}{4} \right) + \left(\frac{\langle v^2 \rangle}{4} + \frac{\langle S_*^2 \rangle}{4} \right) - S_* \frac{\langle \mathcal{U}_n \rangle}{2} \right] \\
&\quad + \frac{\langle \rho_* \rangle}{2} \left(\Delta \mathcal{U}_n \left(\frac{\langle \mathcal{U}_n \rangle}{2} - S_* \right) \right) - \Delta p
\end{aligned} \tag{4.42}$$

and $h = e + \dfrac{p}{\rho}$ is the specific enthalpy. The previous expressions illustrate that the waves emanating from the jumps of the conservative variables show notable similarities with the Harten-Hyman decomposition of the Roe flux. This can be seen from the left and right jumps (4.39) and (4.40), given that both expressions have a clear analogy with the decomposition of the Roe flux, see section 2.4.1. In the light of these results, Pelanti then used the wave propagation algorithm developed by Leveque in [33, 35], and proposed the following decomposition of the HLLC scheme into simple waves $\boldsymbol{\mathcal{W}_k}$

$$\boldsymbol{\mathcal{W}_1} = \xi_1 \boldsymbol{r_1} \qquad \boldsymbol{\mathcal{W}_2} = \widehat{\boldsymbol{\mathcal{W}_2}} + \xi_{2s} \boldsymbol{r_{2s}} \qquad \boldsymbol{\mathcal{W}_3} = \xi_3 \boldsymbol{r_3},$$

where the detailed expression of this decomposition of the HLLC scheme can be deduced from the form of expressions (4.39 - 4.41), but are not explicitly written herein. While, for the Roe scheme, this form is well-established [33, 35], and is readily written as four simple waves $\tilde{\boldsymbol{\mathcal{W}}}_{\boldsymbol{k}}$

$$\tilde{\boldsymbol{\mathcal{W}}}_{\mathbf{1}} = \tilde{\alpha}_1 \tilde{\boldsymbol{r}}_{\mathbf{1}} \qquad \tilde{\boldsymbol{\mathcal{W}}}_{\mathbf{2}} = \tilde{\alpha}_2 \tilde{\boldsymbol{r}}_{\mathbf{2}} \qquad \tilde{\boldsymbol{\mathcal{W}}}_{\mathbf{3}} = \tilde{\alpha}_3 \tilde{\boldsymbol{r}}_{\mathbf{3}} \qquad \tilde{\boldsymbol{\mathcal{W}}}_{\mathbf{4}} = \tilde{\alpha}_4 \tilde{\boldsymbol{r}}_{\mathbf{4}}.$$

To summarize, the approach of Pelanti offers a common formalism based on the wave structure, revealing similarities between the two approximate Riemann solvers, particularly on the waves $(\boldsymbol{\mathcal{W}}_{\mathbf{1}}, \tilde{\boldsymbol{\mathcal{W}}}_{\mathbf{1}})$ and $(\boldsymbol{\mathcal{W}}_{\mathbf{3}}, \tilde{\boldsymbol{\mathcal{W}}}_{\mathbf{4}})$, through an equivalent reformulation of the wave speed estimates. Based on these similarities, Pelanti investigated a low Mach number correction of the HLLC scheme, by mimicking the effects of the Turkel preconditioner on dissipation vector. The HLLC-Turkel scheme is formulated by modifying the first and third waves $(\boldsymbol{\mathcal{W}}_{\mathbf{1}}, \boldsymbol{\mathcal{W}}_{\mathbf{3}})$ in a similar manner than the formulation of the Roe-Turkel scheme [7], with modified $(\tilde{\boldsymbol{\mathcal{W}}}_{\mathbf{1}}, \tilde{\boldsymbol{\mathcal{W}}}_{\mathbf{4}})$. Further details can be found in the original [99], with especially a unified discrete asymptotic analysis for the two schemes.
This approach raises several notable points that are further discussed next. First, in some sense that must be clearly determined, both of these approximate Riemann solvers can be corrected employing an "identical" formulation of the rescaling of the dissipation vector. Second, although, this latter point has already been formally highlighted in the literature, the similarity raised by Pelanti could be further investigated in order to define a common framework for the formulation and for the asymptotic analysis of low Mach number corrections. Third, as discussed by Pelanti, this analysis also presents some additional insights on what is hidden inside $\boldsymbol{d}^{\boldsymbol{HLLC}}$, and provides a relevant basis for further investigations into the potential relationship between the HLLC scheme and a Riemann problem expressed as follows

$$\begin{cases} \partial_t \boldsymbol{w} + \boldsymbol{A}^{\boldsymbol{HLLC}}(\boldsymbol{w_l}, \boldsymbol{w_r}, \boldsymbol{n}) \partial_\xi \boldsymbol{w} = \mathbf{0} \\ \boldsymbol{w}(0, \xi) = \begin{cases} \boldsymbol{w_l} & \text{If } \xi < 0 \\ \boldsymbol{w_r} & \text{If } \xi > 0 \end{cases} \end{cases}.$$

In the above expression, the definition of the approximate Jacobian matrix $\boldsymbol{A}^{\boldsymbol{HLLC}}(\boldsymbol{w_l}, \boldsymbol{w_r}, \boldsymbol{n})$ is currently unknown at that stage of the analysis, but it can be assumed to exist, since this scheme is a Godunov-type method.

In the next chapter, the analysis of Pelanti is further developed with the objective of providing additional information into the origin of these similarities. This is achieved by deriving a common formalism between the Roe and HLLC schemes, making easier a common formulation of corrections of the dissipation vector. Furthermore, the aim of these investigations is to determine whether these two methods can be corrected with an identical formulation and, if so, to define precisely how this can be achieved. If such work could be done, it would be a valuable cornerstone for a better understanding of the underlying mechanisms used to improve the accuracy of approximate Riemann solvers.

5 - A common formalism for analyzing and correcting the HLLC and Roe schemes

Contents

5.1 . Introduction & motivations

The primary objective of this last chapter is to examine the possibility of establishing a unified formalism for the HLLC and Roe schemes. A such common formalism could provide a common framework analysis for low Mach number corrections of the dissipation vector. To this end, we shall investigate whether the HLLC scheme can be interpreted in a similar manner to the Roe scheme, specifically, as a method that formulates explicitly an approximate Riemann problem at the interface, as indicated next

$$\begin{cases} \partial_t \boldsymbol{w} + \boldsymbol{A^{HLLC}}(\boldsymbol{w_l}, \boldsymbol{w_r}, \boldsymbol{n})\, \partial_\xi \boldsymbol{w} = \boldsymbol{0} \\ \boldsymbol{w}(0,\xi) = \begin{cases} \boldsymbol{w_l} & \text{If } \xi < 0 \\ \boldsymbol{w_r} & \text{If } \xi > 0 \end{cases} \end{cases} . \tag{5.1}$$

Despite the significant discrepancies in the construction of these two methods, which are discussed in sections 2.1 and 4.1 respectively, the jumps of the conservative states highlight similarities in the two wave structures. However, this designation of wave structure for the HLLC scheme, introduced in [99], is somewhat premature as the wave structure is by definition obtained through the spectral properties of the matrix $\boldsymbol{A}^{\boldsymbol{HLLC}}(\boldsymbol{w_l}, \boldsymbol{w_r}, \boldsymbol{n})$. This quantity remains yet unknown unless if another Riemann problem, associated with another system of conservation laws in higher dimension, is introduced and followed with a Siliciu-type relaxation, as demonstrated by Bouchut [92].
Nevertheless, if we assume the existence of this approximate Jacobian matrix for the HLLC scheme, then it follows that similar manipulations to those highlighted in section 2.2 can be performed for both approximate Riemann solvers. Indeed, for the Roe scheme, the conservation and hyperbolicity conditions yield the following relation

$$\boldsymbol{f}(\boldsymbol{w_r}, \boldsymbol{n}) - \boldsymbol{f}(\boldsymbol{w_l}, \boldsymbol{n}) = \boldsymbol{A}^{\boldsymbol{Roe}}(\tilde{\boldsymbol{w}}, \boldsymbol{n})\, \Delta \boldsymbol{w} = \sum_{k=1}^{d+2} \tilde{\alpha}_k \tilde{\lambda}_k \tilde{\boldsymbol{r}}_{\boldsymbol{k}} = \tilde{\lambda}_1 \Delta \boldsymbol{w_1} + \tilde{\lambda}_2 \Delta \boldsymbol{w_2} + \tilde{\lambda}_{d+2} \Delta \boldsymbol{w_3},$$

where $\tilde{\lambda}_2 = ... = \tilde{\lambda}_{d+1}$ are the intermediate eigenvalues with multiplicity d, $\Delta \boldsymbol{w} = \boldsymbol{w_r} - \boldsymbol{w_l}$, and the intermediate jumps of the conservative variables are given by $\Delta \boldsymbol{w_1} = \boldsymbol{w_l^*} - \boldsymbol{w_l}$, $\Delta \boldsymbol{w_2} = \boldsymbol{w_r^*} - \boldsymbol{w_l^*}$ and $\Delta \boldsymbol{w_3} = \boldsymbol{w_r} - \boldsymbol{w_r^*}$. While, for the HLLC scheme, if an approximate Jacobian matrix could be deduced from this decomposition, then, it would follow that

$$\boldsymbol{f}(\boldsymbol{w_r}, \boldsymbol{n}) - \boldsymbol{f}(\boldsymbol{w_l}, \boldsymbol{n}) = S_1 \Delta \boldsymbol{w_1} + S_2 \Delta \boldsymbol{w_2} + S_3 \Delta \boldsymbol{w_3} = \boldsymbol{A}^{\boldsymbol{HLLC}}(\boldsymbol{w_l}, \boldsymbol{w_r}, \boldsymbol{n})\, \Delta \boldsymbol{w},$$

in which the matrix is not interpreted as a direct evaluation of the exact Jacobian matrix through an average state, but is instead directly formulated with the left and right conservative variables, according to the uniqueness of this quantity given by Roe-Pike [62]. Whereas for the dissipation vector, the identification with the Roe scheme highlights an hidden artificial viscosity matrix, within the comparison

$$\boldsymbol{d}^{\boldsymbol{Roe}} = |\boldsymbol{A}^{\boldsymbol{Roe}}(\tilde{\boldsymbol{w}}, \boldsymbol{n})|\, \Delta \boldsymbol{w} = \sum_{k=1}^{d+2} \tilde{\alpha}_k |\tilde{\lambda}_k| \tilde{\boldsymbol{r}}_{\boldsymbol{k}} \quad \text{and} \quad \boldsymbol{d}^{\boldsymbol{HLLC}} = \sum_{k=1}^{3} |S_k| \Delta \boldsymbol{w_k} = |\boldsymbol{A}^{\boldsymbol{HLLC}}(\boldsymbol{w_l}, \boldsymbol{w_r}, \boldsymbol{n})|\, \Delta \boldsymbol{w},$$

which provides additional information regarding the HLLC scheme. Although all of the above manipulations are founded upon the assumption of the existence of an approximate Riemann problem of the form (5.1), this remains a valid assumption according to the definition of Godunov-type method. The formulation of the dissipation vector with a matrix-valued dissipation plays, for instance, a crucial role in the Fourier analysis for the explicit scheme in the case of low Mach number flows, as shown in chapter 3. For the HLLC scheme, the Fourier analysis is hardly feasible due to the absence of knowledge of a corresponding artificial viscosity matrix. Furthermore, it could be also interesting to examine the relationship between the two approximate Jacobian matrices $\boldsymbol{A}^{\boldsymbol{Roe}}$ and $\boldsymbol{A}^{\boldsymbol{HLLC}}$, with the objective of unifying the discrete asymptotic analysis. Therefore, this motivates further in-depth research.

We shall start the following analysis based on similarities identified by Pelanti in [99], discussed in detail in section 4.3. The present chapter pertains to a pursuit of this analysis for the two-dimensional case (i.e. $d = 2$), with a special attention given:

1. To identify the origin of the similarities between the HLLC and Roe schemes, and thus, to determine whether this method can actually be interpreted as implicitly constructing an approximate Jacobian matrix (5.1).

2. To examine the existence of global corrections for both schemes, especially corrections that are not clearly formulated for a HLLC type of scheme. To illustrate this point, we show how to precisely apply the Rossow's artificial speed of sound approach to the HLLC scheme.

It should be noted that, although this work focuses on low-Mach number flows, the validity of the following investigation is not restricted to this regime, unless explicitly stated otherwise. Therefore, any modifications of the dissipation vector can be similarly investigated, regardless of the flow regime. Let us introduce the following generic expression for the numerical flux

$$\boldsymbol{\mathcal{F}^X}(\boldsymbol{w_l}, \boldsymbol{w_r}, \boldsymbol{n}) = \frac{\boldsymbol{f}(\boldsymbol{w_l}, \boldsymbol{n}) + \boldsymbol{f}(\boldsymbol{w_r}, \boldsymbol{n})}{2} - \frac{1}{2}\,\boldsymbol{d^X} \quad ,$$

where X denotes either the Roe or HLLC schemes, and only the dissipation vector $\boldsymbol{d^X}$ differs between the two schemes, as indicated next

$$\boldsymbol{d^{Roe}} = |\boldsymbol{A^{Roe}}(\tilde{\boldsymbol{w}}, \boldsymbol{n})|\,\Delta \boldsymbol{w} \qquad \text{and} \qquad \boldsymbol{d^{HLLC}} = \sum_{k=1}^{3} |S_k| \Delta \boldsymbol{w_k}.$$

5.2 . The HLLC scheme written as a four simple wave solver

We shall first introduce generic definitions for the acoustic wave speed estimates (S_l, S_r), formulated as follows

$$S_l = \mathcal{U}_{n_l} - \hat{c}_l \qquad \text{and} \qquad S_r = \mathcal{U}_{n_r} + \hat{c}_r,$$

where, the definitions of $\hat{c}_k$ are related to fan wave estimates, not yet explicitly defined here. Furthermore, the estimate for the intermediate wave speed is assumed to be deduced from $(S_l,\ S_r)$, and is expressed as

$$S_* \quad = \quad \frac{\langle \rho \mathcal{U}_n \hat{c} \rangle - \Delta p}{\langle \rho \hat{c} \rangle},$$

in which operator $\langle \cdot \rangle$ is defined for any scalar quantity a as the sum of the right and left states $\langle a \rangle = 2\bar{a} = a_l + a_r$. More details regarding these expressions can be found in section 4.3. To further highlight the similarities between the Roe and HLLC schemes, the two dissipation vectors are reformulated in a similar manner. This is achieved by expressing the two approximate Riemann solvers as a four simple wave solver, thereby enabling an easier and straightforward comparison between the dissipation mechanisms of both approaches. The following expression of the HLLC scheme is obtained from results derived in [99].

Let us first recall the expression of the dissipation vector $\boldsymbol{d^{Roe}}$ for the Roe scheme according to the Harten-Hyman decomposition, using the eigenspaces of the approximate Jacobian matrix $\boldsymbol{A^{Roe}}$

$$\boldsymbol{d^{Roe}} = |\boldsymbol{A^{Roe}}(\tilde{\boldsymbol{w}}, \boldsymbol{n})| \Delta \boldsymbol{w} = \sum_{k=1}^{4} |\tilde{\lambda_k}| \tilde{\alpha_k} \tilde{\boldsymbol{r_k}}$$

$$\tilde{\alpha}_1 = \frac{\Delta p - \tilde{\rho}\tilde{c}\Delta \mathcal{U}_n}{2\tilde{c}^2} \qquad \tilde{\alpha}_2 = \Delta \rho - \frac{\Delta p}{\tilde{c}^2} \qquad \tilde{\alpha}_3 = \tilde{\rho}\Delta \tilde{\mathcal{U}_t} \qquad \tilde{\alpha}_4 = \frac{\Delta p + \tilde{\rho}\tilde{c}\Delta \mathcal{U}_n}{2\tilde{c}^2}$$

$$\tilde{\boldsymbol{r_1}} = \begin{pmatrix} 1 \\ \tilde{u} - \tilde{c} n_x \\ \tilde{v} - \tilde{c} n_y \\ \tilde{H} - \tilde{c}\tilde{\mathcal{U}_n} \end{pmatrix} \qquad \tilde{\boldsymbol{r_2}} = \begin{pmatrix} 1 \\ \tilde{u} \\ \tilde{v} \\ \frac{|\tilde{\boldsymbol{\mathcal{U}}}|^2}{2} \end{pmatrix} \qquad \tilde{\boldsymbol{r_3}} = \begin{pmatrix} 0 \\ -n_y \\ n_x \\ \tilde{\mathcal{U}_t} \end{pmatrix} \qquad \tilde{\boldsymbol{r_4}} = \begin{pmatrix} 1 \\ \tilde{u} + \tilde{c} n_x \\ \tilde{v} + \tilde{c} n_y \\ \tilde{H} + \tilde{c}\tilde{\mathcal{U}_n} \end{pmatrix}, \tag{5.2}$$

where $\mathcal{U}_n$ and $\mathcal{U}_t$ are respectively the directional and tangential velocity components, the operator $\tilde{\cdot}$ stands for the Roe average, and the speed of sound is defined as $\tilde{c} = \sqrt{(\gamma - 1)(\tilde{H} - \frac{|\tilde{\boldsymbol{\mathcal{U}}}|^2}{2})}$.

In the case of the HLLC scheme, in order to obtain a comparable decomposition for the dissipation vector $\boldsymbol{d^{HLLC}}$, the following wave speed estimates are introduced explicitly $S_1 = S_l$, $S_2 = S_* = S_3$, $S_4 = S_r$. Then, it follows that these wave speed estimates are interpreted as eigenvalues of an approximate Jacobian matrix $\boldsymbol{A^{HLLC}}$, which remains unknown yet. In addition, coefficients α_k and right eigenvectors $\boldsymbol{r_k}$ can be explicitly derived for the HLLC scheme, with the following expressions

$$\alpha_1 = \frac{\rho_l^*}{\langle \rho \hat{c} \rangle} \left[\frac{\Delta p - \rho_r \hat{c}_r \Delta \mathcal{U}_n}{\hat{c}_l} \right] \qquad \alpha_2 = 1 \qquad \alpha_3 = \bar{\rho^*} \Delta \mathcal{U}_t \qquad \alpha_4 = \frac{\rho_r^*}{\langle \rho \hat{c} \rangle} \left[\frac{\Delta p + \rho_l \hat{c}_l \Delta \mathcal{U}_n}{\hat{c}_r} \right]$$

$$\boldsymbol{r_1} = \begin{pmatrix} 1 \\ u_l - \hat{c}_l n_x \\ v_l - \hat{c}_l n_y \\ H_l - \hat{c}_l S_* \end{pmatrix} \quad \boldsymbol{r_2} = \begin{pmatrix} \Delta \rho^* \\ \Delta \rho^* \left(n_x S_* - n_y \bar{\mathcal{U}_t} \right) \\ \Delta \rho^* \left(n_y S_* + n_x \bar{\mathcal{U}_t} \right) \\ \Delta E_n^* \end{pmatrix} \quad \boldsymbol{r_3} = \begin{pmatrix} 0 \\ -n_y \\ n_x \\ \overline{\mathcal{U}_t} \end{pmatrix} \quad \boldsymbol{r_4} = \begin{pmatrix} 1 \\ u_r + \hat{c}_r n_x \\ v_r + \hat{c}_r n_y \\ H_r + \hat{c}_r S_* \end{pmatrix}, \tag{5.3}$$

where the mean operator $\bar{a} = \dfrac{\langle a \rangle}{2}$ has been used, and ΔE_n^* is defined as

$$\begin{aligned} \Delta E_n^* = (\rho_r^* h_r - \rho_l^* h_l) + \Delta \rho^* \Bigg[\left(\frac{\langle u^2 \rangle}{4} + \frac{\langle S_*^2 \rangle}{4} \right) + \left(\frac{\langle v^2 \rangle}{4} + \frac{\langle S_*^2 \rangle}{4} \right) - S_* \frac{\langle \mathcal{U}_n \rangle}{2} \Bigg] \\ + \frac{\langle \rho^* \rangle}{2} \left(\Delta \mathcal{U}_n \left(\frac{\langle \mathcal{U}_n \rangle}{2} - S_* \right) \right) - \Delta p \end{aligned}, \tag{5.4}$$

where h is the specific enthalpy $h = e + \dfrac{p}{\rho}$, and e the internal energy. More details concerning the derivation of these quantities can be found in section 4.3.

As it can be seen by comparing the above expressions (5.2 - 5.3), significant similarities appear in the first, third and fourth waves (i.e. $\boldsymbol{\mathcal{W}_k} = \alpha_k \boldsymbol{r_k}$). However, notable discrepancies emerge from the second wave, as particularly evidenced by the last component of $\boldsymbol{r_2}$ with especially the definition of ΔE_n^*. Using the previous expressions (5.2 - 5.3), the two dissipation vectors are derived in a similar form, as indicated next

$$\boldsymbol{d^{Roe}} = \sum_{k=1}^{4} |\tilde{\lambda_k}| \tilde{\alpha_k} \tilde{\boldsymbol{r_k}} \qquad\qquad \boldsymbol{d^{HLLC}} = \sum_{k=1}^{4} |S_k| \alpha_k \boldsymbol{r_k}. \tag{5.5}$$

This formulation for the Roe scheme is characterized by the spectral properties of the approximate Jacobian matrix, and thus, by the wave structure of the Riemann problem. However, for the HLLC scheme, this form represents only a formal interpretation of the dissipation vector, as the associated approximate Riemann problem has not yet been determined. The precise origins of these similarities remain unidentified and are not addressed in the literature, motivating therefore further investigations described in the next section.

5.2.1 . Investigation on the origins of the similarities

The primary concern of this section is to examine the origin of the similarities highlighted in expressions (5.2 - 5.3). These similarities have been for instance used by Pelanti as a valuable cornerstone in order to mimick the effects of the Turkel preconditioner matrix applied to the HLLC scheme. By investigating the origins of these similarities, a common formalism between the two dissipation vectors $\boldsymbol{d^X}$ is derived, as indicated next. A special attention is given to identify the limitations of this analysis for these two approximate Riemann solvers.

Due to their conciseness, expressions in (5.5) are not the best candidate for this analysis. Indeed, notable discrepancies emerge primarily from the second wave $\boldsymbol{\mathcal{W}_2} = \alpha_2 \boldsymbol{r_2}$, and the reasons of such discrepancies are not simple to investigate. To provide a better understanding, a more detailed formulation is obtained by expanding the dissipation vector into a matrix form, as defined by the next

matrix-vector product

$$\boldsymbol{d^X}(\boldsymbol{w_l},\boldsymbol{w_r},\boldsymbol{n}) = \boldsymbol{\mathcal{M}^X}(\boldsymbol{w_l},\boldsymbol{w_r},\boldsymbol{n}) \begin{pmatrix} \Delta\rho \\ \boldsymbol{\Delta\mathcal{U}} \\ \Delta\mathcal{U}_n \\ \Delta p \end{pmatrix} \qquad \text{with } \boldsymbol{\mathcal{M}^X} \in \mathbb{R}^{(d+2)\times(d+3)}, \tag{5.6}$$

which entails the extraction of all terms hidden in the dissipation vector. Note that this choice of dependent variables on the right-hand side of (5.6) is based on the initial definitions of the coordinates $\tilde{\boldsymbol{\alpha}} = (\tilde{\alpha}_k)_k$, from which arising naturally all these distinct jumps. To this end, the first step is to derive explicitly the associated matrix $\boldsymbol{\mathcal{M}^{HLLC}}$ of the HLLC scheme, by further expanding expression (5.5). To simplify the expressions, the previous notations used in the definition of coefficients $(\delta_{c_k}, \delta_{S_k}, \delta_{|S_k|})$ are reminded below

$$\left\{ \begin{array}{l} \delta_{c_l} = S_l - \mathcal{U}_{n_l} \\ \delta_{c_r} = S_r - \mathcal{U}_{n_r} \end{array} \right. \qquad \left\{ \begin{array}{l} \delta_{S_l} = S_l - S^* \\ \delta_{S_r} = S_r - S^* \end{array} \right. \qquad \left\{ \begin{array}{l} \delta_{|S_l|} = |S_l| - |S^*| \\ \delta_{|S_r|} = |S_r| - |S^*| \end{array} \right. .$$

Definitions introduced in (5.3) are used to formulate the dissipation vector $\boldsymbol{d^{HLLC}} = (d_k^{HLLC})_{k=1,4}$, given in (5.5). After some algebra, we get the following components of the dissipation vector

$$d_1^{HLLC} = \Delta\rho \Big[\ |S_*|\ \Big] + \Delta\mathcal{U}_n \left[\frac{\rho_l\rho_r}{\langle\rho\hat{c}\rangle} \left(\frac{\delta_{c_r}}{\delta_{S_l}}\delta_{|S|_l} - \frac{\delta_{c_l}}{\delta_{S_r}}\delta_{|S|_r} \right) \right] + \Delta p \left[\frac{1}{\langle\rho\hat{c}\rangle} \left(-\frac{\rho_l}{\delta_{S_l}}\delta_{|S|_l} + \frac{\rho_r}{\delta_{S_r}}\delta_{|S|_r} \right) \right], \tag{5.7}$$

$$\begin{aligned} \boldsymbol{d_{2/3}^{HLLC}} = \quad & \Delta\rho \left[\ |S_*|\,\overline{\boldsymbol{\mathcal{U}^*}}\ \right] + \boldsymbol{\Delta\mathcal{U}}\left[\bar{\rho^*}|S_*|\right] \\ & + \Delta\mathcal{U}_n \left[\frac{\rho_l\rho_r}{\langle\rho\hat{c}\rangle} \left(\frac{\delta_{c_r}}{\delta_{S_l}} \left\{ |S_l|(\boldsymbol{\mathcal{U}_l} - \hat{c}_l\boldsymbol{n}) - \overline{\boldsymbol{\mathcal{U}^*}}|S_*| \right\} \right.\right. \\ & \qquad \left.\left. - \frac{\delta_{c_l}}{\delta_{S_r}} \left\{ |S_r|(\boldsymbol{\mathcal{U}_r} + \hat{c}_r\boldsymbol{n}) - \overline{\boldsymbol{\mathcal{U}^*}}|S_*| \right\} \right) \quad - \bar{\rho^*}|S_*|\boldsymbol{n} \right] \\ & + \Delta p \left[\frac{1}{\langle\rho\hat{c}\rangle} \left(-\frac{\rho_l}{\delta_{S_l}} \left\{ |S_l|(\boldsymbol{\mathcal{U}_l} - \hat{c}_l\boldsymbol{n}) - \overline{\boldsymbol{\mathcal{U}^*}}|S_*| \right\} \right.\right. \\ & \qquad \left.\left. + \frac{\rho_r}{\delta_{S_r}} \left\{ |S_r|(\boldsymbol{\mathcal{U}_r} + \hat{c}_r\boldsymbol{n}) - \overline{\boldsymbol{\mathcal{U}^*}}|S_*| \right\} \right) \right] \end{aligned} \tag{5.8}$$

$$
\begin{aligned}
d_4^{HLLC} = \quad & \Delta\rho\Bigg[\left(\bar{H} + S_*(S_* - \bar{\mathcal{U}}_n - \frac{\bar{\rho^*}\gamma}{\rho_l\rho_r(\gamma-1)}\bar{p}\right)|S_*|\Bigg] + \Delta u\Bigg[\bar{\rho^*}\bar{u}|S_*|\Bigg] + \Delta v\Bigg[\bar{\rho^*}\bar{v}|S_*|\Bigg] \\
& + \Delta\mathcal{U}_n\Bigg[\frac{\rho_l\rho_r}{\langle\rho\hat{c}\rangle}\Bigg(\frac{\delta_{c_r}}{\delta_{S_l}}\Big\{|S_l|\,(H_l - \hat{c}_l S_*) - |S_*|\,\Big(\overline{H} + S_*(S_* - \bar{\mathcal{U}}_n)\Big)\Big\} \\
& \qquad - \frac{\delta_{c_l}}{\delta_{S_r}}\Big\{|S_r|(H_r + \hat{c}_r S_*) - |S_*|\Big(\overline{H} + S_*(S_* - \bar{\mathcal{U}}_n)\Big)\Big\}\Bigg) \\
& \qquad - \overline{\rho^*}S_*|S_*|\Bigg] \qquad . \quad (5.9) \\
& + \Delta p\Bigg[\frac{1}{\langle\rho\hat{c}\rangle}\Bigg(-\frac{\rho_l}{\delta_{S_l}}\Big\{|S_l|\Big(H_l - \hat{c}_l S_*\Big) - |S_*|\Big(\overline{H} + S_*(S_* - \bar{\mathcal{U}}_n)\Big)\Big\} \\
& \qquad + \frac{\rho_r}{\delta_{S_r}}\Big\{|S_r|(H_r + \hat{c}_r S_*) - |S_*|\Big(\overline{H} + S_*(S_* - \bar{\mathcal{U}}_n)\Big)\Big\}\Bigg) \\
& \qquad + \Big(\frac{\bar{\rho^*}\bar{\rho}\gamma}{\rho_l\rho_r(\gamma-1)} - 1\Big)|S_*|\Bigg]
\end{aligned}
$$

Then, from expressions (5.7 - 5.9), the corresponding matrix $\boldsymbol{\mathcal{M}^{HLLC}}(\boldsymbol{w_l}, \boldsymbol{w_r}, \boldsymbol{n})$ can be readily extracted, with

$$
\boldsymbol{d^{HLLC}} = \boldsymbol{\mathcal{M}^{HLLC}} \begin{pmatrix} \Delta\rho \\ \boldsymbol{\Delta\mathcal{U}} \\ \Delta\mathcal{U}_n \\ \Delta p \end{pmatrix} \qquad \text{with } \boldsymbol{\mathcal{M}^{HLLC}} \in \mathbb{R}^{(d+2)\times(d+3)}, \tag{5.10}
$$

but, its definition is not explicitly given here for the sake of brevity. Instead, in order to elucidate the origin of the similarities between $\boldsymbol{d^{HLLC}}$ and $\boldsymbol{d^{Roe}}$, a specific decomposition of the matrix $\boldsymbol{\mathcal{M}^{HLLC}}$ is introduced. This expression was initially intended to simplify the interpretation and to reinforce the link between the dissipation vectors of these two approximate Riemann solvers. In the following, two matrices $\boldsymbol{\mathcal{M}_c}$ and $\boldsymbol{\mathcal{M}_d}$ are introduced, with the aim of decomposing the matrix $\boldsymbol{\mathcal{M}^{HLLC}}$ into two parts, as indicated below

$$
\boldsymbol{\mathcal{M}^{HLLC}}(\boldsymbol{w_l}, \boldsymbol{w_r}, \boldsymbol{n}) = \boldsymbol{\mathcal{M}_c}(\boldsymbol{w_l}, \boldsymbol{w_r}, \boldsymbol{n}) + \boldsymbol{\mathcal{M}_d}(\boldsymbol{w_l}, \boldsymbol{w_r}, \boldsymbol{n}), \tag{5.11}
$$

where indexes used in notations stand for '**c**ommon' or '**d**eviation'. These two matrices are given by the following expressions

$$\boldsymbol{\mathcal{M}_c} = \left(\begin{array}{c|c|c|c|c} |S_*| & 0 & 0 & \frac{\rho_l\rho_r}{\langle\rho\hat{c}\rangle}\left(\frac{\delta_{c_r}}{\delta_{S_l}}\delta_{|S|_l} - \frac{\delta_{c_l}}{\delta_{S_r}}\delta_{|S|_r}\right) & \frac{1}{\langle\rho\hat{c}\rangle}\left(\frac{\rho_r}{\delta_{S_r}}\delta_{|S|_r} - \frac{\rho_l}{\delta_{S_l}}\delta_{|S|_l}\right) \\ |S_*|\,\overline{u^*} & \overline{\rho^*}|S_*| & 0 & \begin{array}{c}\frac{\rho_l\rho_r}{\langle\rho\hat{c}\rangle}\Big(\frac{\delta_{c_r}|S_l|}{\delta_{S_l}}(u_l - \hat{c}_l n_x) \\ -\frac{\delta_{c_l}|S_r|}{\delta_{S_r}}(u_r + \hat{c}_r n_x)\Big) \\ -n_x\overline{\rho^*}|S_*|\end{array} & \begin{array}{c}\frac{1}{\langle\rho\hat{c}\rangle}\Big(\frac{\rho_r|S_r|}{\delta_{S_r}}(u_r + \hat{c}_r n_x) \\ -\frac{\rho_l|S_l|}{\delta_{S_l}}(u_l - \hat{c}_l n_x) \\ +\overline{u^*}|S_*|(\frac{\rho_l}{\delta_{S_l}} - \frac{\rho_r}{\delta_{S_r}})\Big)\end{array} \\ |S_*|\,\overline{v^*} & 0 & \overline{\rho^*}|S_*| & \begin{array}{c}\frac{\rho_l\rho_r}{\langle\rho\hat{c}\rangle}\Big(\frac{\delta_{c_r}|S_l|}{\delta_{S_l}}(v_l - \hat{c}_l n_y) \\ -\frac{\delta_{c_l}|S_r|}{\delta_{S_r}}(v_r + \hat{c}_r n_y)\Big) \\ -n_y\overline{\rho^*}|S_*|\end{array} & \begin{array}{c}\frac{1}{\langle\rho\hat{c}\rangle}\Big(\frac{\rho_r|S_r|}{\delta_{S_r}}(v_r + \hat{c}_r n_y) \\ -\frac{\rho_l|S_l|}{\delta_{S_l}}(v_l - \hat{c}_l n_y) \\ +\overline{v^*}|S_*|(\frac{\rho_l}{\delta_{S_l}} - \frac{\rho_r}{\delta_{S_r}})\Big)\end{array} \\ \begin{array}{c}|S_*|\Big(\overline{H} \\ -\frac{\bar{\rho^*}\bar{p}}{\rho_l\rho_r}(1 + \frac{1}{\gamma-1})\Big)\end{array} & \overline{\rho^*}\bar{u}|S_*| & \overline{\rho^*}\bar{v}|S_*| & \begin{array}{c}\frac{\rho_l\rho_r}{\langle\rho\hat{c}\rangle}\Big(\frac{\delta_{c_r}|S_l|}{\delta_{S_l}}(H_l - \hat{c}_l S_*) \\ -\frac{\delta_{c_l}|S_r|}{\delta_{S_r}}(H_r + \hat{c}_r S_*)\Big) \\ -\overline{\rho^*}S_*|S_*|\end{array} & \begin{array}{c}\frac{1}{\langle\rho\hat{c}\rangle}\Big(\frac{\rho_r}{\delta_{S_r}}(H_r|S_r| - \overline{H}|S_*| + \hat{c}_r S_*|S_r|) \\ -\frac{\rho_l}{\delta_{S_l}}(H_l|S_l| - \overline{H}|S_*| - \hat{c}_l S_*|S_l|)\Big) \\ +\Big(\frac{\overline{\rho^*}\bar{\rho}\gamma}{\rho_l\rho_r(\gamma-1)} - 1\Big)|S_*|\end{array} \end{array}\right) \tag{5.12}$$

$$\boldsymbol{\mathcal{M}_d} = \left(\begin{array}{c|c|c|c|c} 0 & 0 & 0 & 0 & 0 \\ 0 & 0 & 0 & \frac{\rho_l\rho_r}{\langle\rho\hat{c}\rangle}|S_*|\bar{u^*}\left(\frac{\delta_{c_l}}{\delta_{S_r}} - \frac{\delta_{c_r}}{\delta_{S_l}}\right) & 0 \\ 0 & 0 & 0 & \frac{\rho_l\rho_r}{\langle\rho\hat{c}\rangle}|S_*|\bar{v^*}\left(\frac{\delta_{c_l}}{\delta_{S_r}} - \frac{\delta_{c_r}}{\delta_{S_l}}\right) & 0 \\ |S_*|S_*(S_* - \overline{\mathcal{U}_n}) & 0 & 0 & \frac{\rho_l\rho_r}{\langle\rho\hat{c}\rangle}|S_*|\Big[\bar{H} + S_*(S_* - \overline{\mathcal{U}_n})\Big]\left(\frac{\delta_{c_l}}{\delta_{S_r}} - \frac{\delta_{c_r}}{\delta_{S_l}}\right) & \frac{1}{\langle\rho\hat{c}\rangle}|S_*|\Big[S_*(S_* - \overline{\mathcal{U}_n})\Big]\Big(\frac{\rho_l}{\delta_{S_l}} - \frac{\rho_r}{\delta_{S_r}}\Big) \end{array}\right) \tag{5.13}$$

The purpose of the decomposition (5.11) is to illustrate a very specific feature of the dissipation vector $\boldsymbol{d^{HLLC}}$.

Proposition 5.2.1 (*Consistency relations for the matrices $\boldsymbol{\mathcal{M}}$*) *Let the initial condition of the Riemann problem be continuous, then, there exists a matrix $\boldsymbol{\mathcal{M}}(\boldsymbol{w},\boldsymbol{n}) \in \mathbb{R}^{(d+2)\times(d+3)}$ such that:*

$$\boldsymbol{\mathcal{M}}(\boldsymbol{w},\boldsymbol{n}) = \boldsymbol{\mathcal{M}^{HLLC}}(\boldsymbol{w},\boldsymbol{w},\boldsymbol{n}) = \boldsymbol{\mathcal{M}^{Roe}}(\boldsymbol{w},\boldsymbol{n}).$$

In particular, the decomposition (5.11) of the matrix $\boldsymbol{\mathcal{M}^{HLLC}}$ satisfies the following relations

$$\begin{cases} \boldsymbol{\mathcal{M}_c}(\boldsymbol{w},\boldsymbol{w},\boldsymbol{n}) = \boldsymbol{\mathcal{M}^{Roe}}(\boldsymbol{w},\boldsymbol{n}) \\ \boldsymbol{\mathcal{M}_d}(\boldsymbol{w},\boldsymbol{w},\boldsymbol{n}) = \boldsymbol{0} \in \mathbb{R}^{(d+2)\times(d+3)} \end{cases}. \tag{5.14}$$

The above expression highlights that the two matrices $\boldsymbol{\mathcal{M}^{HLLC}}$ and $\boldsymbol{\mathcal{M}^{Roe}}$ are consistent with respect to the same matrix $\boldsymbol{\mathcal{M}(w,n)}$.

Remark 1 *Obviously if* $\boldsymbol{w_l = w_r = w}$*, then, the intermediates states* $(\boldsymbol{w_l^*, w_r^*})$ *characterizing the HLLC scheme are equal to* $\boldsymbol{w}$*. In addition, the following relations are also satisfied:*

$$\begin{array}{llll} \hat{c}_l = c & S_l = \lambda_1(\boldsymbol{w}) & \delta_{c_l} = -c & \delta_{S_l} = -c \\ \hat{c}_r = c & S_r = \lambda_4(\boldsymbol{w}) & \delta_{c_r} = c & \delta_{S_r} = c \\ & S_* = \lambda_2(\boldsymbol{w}) & & \end{array} ,$$

and by using these relations into the two matrices $\boldsymbol{\mathcal{M}_c}$ *and* $\boldsymbol{\mathcal{M}_d}$*, this leads to (5.14).*

The current question that now arises is: how to interpret this quantity $\boldsymbol{\mathcal{M}(w,n)}$? This question proved to be more challenging than anticipated, as we could only determine the answer with formal observations. This can be heuristically explained with the Roe flux in a simple case, as this method describes explicitly the relation between the approximate Riemann problem and the definition of its matrix-valued dissipation. Indeed, the dissipation vector for the Roe scheme can be equivalently expressed with several forms, as indicated next

$$\boldsymbol{d^{Roe}} = \boldsymbol{\mathcal{M}^{Roe}}(\tilde{\boldsymbol{w}}, \boldsymbol{n}) \begin{pmatrix} \Delta\rho \\ \boldsymbol{\Delta\mathcal{U}} \\ \Delta\mathcal{U}_n \\ \Delta p \end{pmatrix} \quad = \quad |\boldsymbol{A^{Roe}}(\tilde{\boldsymbol{w}}, \boldsymbol{n})|\, \Delta\boldsymbol{w} \quad = \quad \sum_{k=1}^{d+2} |\tilde{\lambda}_k| \tilde{\alpha}_k \tilde{\boldsymbol{r}}_{\boldsymbol{k}}, \tag{5.15}$$

where in order to obtain a consistent numerical flux, the dissipation vector must obviously satisfy the necessary condition given by

$$\boldsymbol{d^{Roe}}(\tilde{\boldsymbol{w}}(\boldsymbol{w},\boldsymbol{w}), \boldsymbol{n}) = 0.$$

However, it is also well-established for the Roe scheme that, the above condition specifically hides another property of the Roe scheme, previously mentioned in section 2.1. This is the consistency condition of the approximate Jacobian matrix, as reminded below

$$\boldsymbol{d^{Roe}}(\tilde{\boldsymbol{w}}(\boldsymbol{w},\boldsymbol{w}), \boldsymbol{n}) = 0 \qquad \text{and additionally} \qquad \boldsymbol{A^{Roe}}(\tilde{\boldsymbol{w}}(\boldsymbol{w},\boldsymbol{w}), \boldsymbol{n}) = \boldsymbol{A}(\boldsymbol{w}, \boldsymbol{n}).$$

Assuming now very small discontinuities in the initial condition, and a smooth solution $\boldsymbol{w}$ such as generally assumed for subsonic flows, then, the linearized Riemann problem could be introduced, in a similar manner as Toro in [119] and [34, Sec. 9.3]. In particular we shall assume that the left and right conservative states and the solution of the Riemann problem are close to a constant state $\hat{\boldsymbol{w}}$. Under these assumptions, the solution of the linearized Riemann problem, formulated as follows

$$\begin{cases} \partial_t \boldsymbol{w} + \boldsymbol{A}(\hat{\boldsymbol{w}}, \boldsymbol{n}) \partial_\xi \boldsymbol{w} = \boldsymbol{0} \\ \boldsymbol{w}(0,\xi) = \begin{cases} \boldsymbol{w_l} & \text{If } \xi < 0 \\ \boldsymbol{w_r} & \text{If } \xi > 0 \end{cases} \end{cases},$$

could be assumed as an appropriate approximation of the exact solution $\boldsymbol{w}$, in which we especially see that

$$|\boldsymbol{A}(\hat{\boldsymbol{w}}, \boldsymbol{n})|\, \Delta\boldsymbol{w} \;=\; \sum_{k=1}^{d+2} |\lambda_k(\hat{\boldsymbol{w}}, \boldsymbol{n})| \alpha_k(\hat{\boldsymbol{w}}, \boldsymbol{w_l}, \boldsymbol{w_r}, \boldsymbol{n}) \boldsymbol{r_k}(\hat{\boldsymbol{w}}, \boldsymbol{n}) \;=\; \boldsymbol{\mathcal{M}}(\hat{\boldsymbol{w}}, \boldsymbol{n}) \begin{pmatrix} \Delta\rho \\ \boldsymbol{\Delta\mathcal{U}} \\ \Delta\mathcal{U}_n \\ \Delta p \end{pmatrix}.$$

Under a few assumptions regarding the validity of the linearized Riemann problem, which appears not important to be discussed here, this simple manipulation clearly identifies the relation between the dissipation vector, the matrix quantity $\boldsymbol{\mathcal{M}}(\hat{\boldsymbol{w}}, \boldsymbol{n})$, and the approximate Riemann problem for a linear hyperbolic system with constant coefficients. Indeed, as it can be seen in the above expression, for a vanishing discontinuity in the initial condition, we then have

$$\boldsymbol{A}(\hat{\boldsymbol{w}}, \boldsymbol{n}) \xrightarrow[\boldsymbol{w_l} \to \boldsymbol{w_r}]{} \boldsymbol{A}(\boldsymbol{w}, \boldsymbol{n}) \qquad \text{and additionally} \qquad \boldsymbol{\mathcal{M}}(\hat{\boldsymbol{w}}, \boldsymbol{n}) \xrightarrow[\boldsymbol{w_l} \to \boldsymbol{w_r}]{} \boldsymbol{\mathcal{M}}(\boldsymbol{w}, \boldsymbol{n}).$$

In the context of the Roe scheme, the above conditions are also satisfied, as these could be expressed as follows

$$\boldsymbol{d}^{\boldsymbol{Roe}}(\tilde{\boldsymbol{w}}, \boldsymbol{n}) = \underset{\boldsymbol{w_l} \to \boldsymbol{w_r}}{\underset{\downarrow}{|\boldsymbol{A}(\boldsymbol{w}, \boldsymbol{n})|}} \; \Delta \boldsymbol{w} = \underset{\boldsymbol{w_l} \to \boldsymbol{w_r}}{\underset{\downarrow}{\boldsymbol{\mathcal{M}}(\boldsymbol{w}, \boldsymbol{n})}} \begin{pmatrix} \Delta\rho \\ \boldsymbol{\Delta \mathcal{U}} \\ \Delta \mathcal{U}_n \\ \Delta p \end{pmatrix} \xrightarrow[\boldsymbol{w_l} \to \boldsymbol{w_r}]{} 0 \; .$$

In opposition, the situation with regard to the HLLC scheme is less clear, given the lack of available information regarding the approximate Riemann problem and the definition of $\boldsymbol{A}^{\boldsymbol{HLLC}}$. Thus, the identical process is open to question. However, the missing information for the HLLC scheme can be compensated with proposition 5.2.1, as the consistency condition for $\boldsymbol{A}^{\boldsymbol{Roe}}$ provides insights that could be also potentially reproduced by the HLLC scheme. Indeed, assuming that $\boldsymbol{A}^{\boldsymbol{HLLC}}(\boldsymbol{w_l}, \boldsymbol{w_r}, \boldsymbol{n})$ exists, then, the consistency of the approximate Jacobian matrix could be deduced from the analysis of the two numerical dissipations, as for instance a particularly consequence of the relation

$$\boldsymbol{\mathcal{M}}(\boldsymbol{w}, \boldsymbol{n}) = \boldsymbol{\mathcal{M}}^{\boldsymbol{HLLC}}(\boldsymbol{w}, \boldsymbol{w}, \boldsymbol{n}) = \boldsymbol{\mathcal{M}}^{\boldsymbol{Roe}}(\boldsymbol{w}, n),$$

and the consistency condition given for the Roe matrix $\boldsymbol{A}^{\boldsymbol{Roe}}$. Thus, the observed similarities between the formulation of $\boldsymbol{d}^{\boldsymbol{HLLC}}$ and $\boldsymbol{d}^{\boldsymbol{Roe}}$ could be explained as a direct consequence of the consistency conditions for the approximate Jacobian matrix $\boldsymbol{A}^{\boldsymbol{X}}$ with respect to the exact Jacobian matrix.

5.3 . A generalization of corrected numerical dissipation for the Roe and HLLC schemes

This section aims at determining how the two approximate Riemann solvers can be modified by implementing an "identical" formulation for a corrected dissipation vector. The objective is to propose a step-by-step approach to first identify the numerical mechanism introduced by the correction, and then, generalize the correction from one Riemann solver to the other using a common formalism for both schemes. It should be noted that, the following approach represents an extension of Pelanti's methodology mimicking preconditioning methods, but in the case of corrections modifying terms that are not readily comparable. Indeed, in [99], Pelanti's original derivation for transposing the X-Turkel correction takes into advantage the similarities in the first and third waves (in our notations in (5.2 - 5.3), these waves correspond to the first and fourth waves), which are specifically modified in the case of the Roe-Turkel scheme. In contrast, we propose here to generalize this methodology, as this condition is now relaxed, and is therefore formulated even in the absence of similarities between terms of these two approximate Riemann solvers.

Let us first introduce a generic modified vector-dissipation, which could be either related to a low-Mach number or a high-Mach number correction. The cornerstone for identifying and transposing the correction is given by the consistency property in Prop. 5.2.1. We shall first state a definition, for the purpose of a well-identified correction and therefore avoiding a potential scattering of corrections. Introducing the following definition:

Definition 5.3.1 (Schemes corrected with an identical strategy of rescaling) *The Roe scheme and the HLLC scheme are identically corrected by a correction X if only if:*

$$\boldsymbol{\mathcal{M}^{X}}(\boldsymbol{w},\boldsymbol{n}) = \boldsymbol{\mathcal{M}^{Roe-X}}(\boldsymbol{w},\boldsymbol{n}) = \boldsymbol{\mathcal{M}^{HLLC-X}}(\boldsymbol{w},\boldsymbol{w},\boldsymbol{n})$$

---

then corrections are characterized according to the modifications made to the initial quantity $\boldsymbol{\mathcal{M}}(\boldsymbol{w},\boldsymbol{n})$.

5.3.1 . Transposition of a correction from the Roe scheme to HLLC scheme

First of all, considering a correction X for the Roe scheme, the numerical flux $\boldsymbol{\mathcal{F}^{Roe-X}}$ can be expressed as follows

$$\boldsymbol{\mathcal{F}^{Roe-X}}(\boldsymbol{w_l},\boldsymbol{w_r},\boldsymbol{n}) = \frac{\boldsymbol{f}(\boldsymbol{w_l},\boldsymbol{n}) + \boldsymbol{f}(\boldsymbol{w_r},\boldsymbol{n})}{2} \quad - \quad \frac{1}{2}\,\boldsymbol{d^{Roe-X}}(\tilde{\boldsymbol{w}},\boldsymbol{n}),$$

in which the numerical dissipation $\boldsymbol{d^{Roe-X}}$ can be equivalently written under the matrix form:

$$\boldsymbol{d^{Roe-X}} = \boldsymbol{\mathcal{M}^{Roe-X}} \begin{pmatrix} \Delta\rho \\ \boldsymbol{\Delta\mathcal{U}} \\ \Delta\mathcal{U}_n \\ \Delta p \end{pmatrix} \qquad \text{with } \boldsymbol{\mathcal{M}^{Roe-X}} \in \mathbb{R}^{(d+2)\times(d+3)}.$$

According to the definition 5.3.1, a matrix $\boldsymbol{\mathcal{M}^{HLLC-X}}$ must be identified and built such that

$$\begin{cases} \boldsymbol{\mathcal{M}^{HLLC-X}}(\boldsymbol{w_l},\boldsymbol{w_r},\boldsymbol{n}) \xrightarrow[M\to 1]{} \boldsymbol{\mathcal{M}^{HLLC}}(\boldsymbol{w_l},\boldsymbol{w_r},\boldsymbol{n}) \\ \boldsymbol{\mathcal{M}^{HLLC-X}}(\boldsymbol{w},\boldsymbol{w},\boldsymbol{n}) = \boldsymbol{\mathcal{M}^{Roe-X}}(\boldsymbol{w},\boldsymbol{n}) \end{cases}. \tag{5.16}$$

Actually, the existence of $\boldsymbol{\mathcal{M}^{HLLC-X}}$ is ensured by proposition 5.2.1, as it only requires to modify the initial formulation of $\boldsymbol{\mathcal{M}^{HLLC}}$ in order to satisfy the above conditions. Nevertheless, its uniqueness is not ensured, and can be easily explained by the decomposition (5.11) together with the consistency relation (5.14)

$$\boldsymbol{\mathcal{M}^{HLLC-X}}(\boldsymbol{w_l},\boldsymbol{w_r},\boldsymbol{n}) = \boldsymbol{\mathcal{M}_c^{HLLC-X}}(\boldsymbol{w_l},\boldsymbol{w_r},\boldsymbol{n}) + \boldsymbol{\mathcal{M}_d^{HLLC-X}}(\boldsymbol{w_l},\boldsymbol{w_r},\boldsymbol{n})$$
$$\text{with} \quad \boldsymbol{\mathcal{M}_c}(\boldsymbol{w},\boldsymbol{w},\boldsymbol{n}) = \boldsymbol{\mathcal{M}^{Roe}}(\boldsymbol{w},n) \quad \text{and} \quad \boldsymbol{\mathcal{M}_d}(\boldsymbol{w},\boldsymbol{w},\boldsymbol{n}) = \mathbf{0} \in \mathbb{R}^{(d+2)\times(d+3)}$$

.

One possible approach to readily find a matrix that satisfies conditions (5.16) is to only modify the first matrix $\boldsymbol{\mathcal{M}_c}(\boldsymbol{w},\boldsymbol{w},\boldsymbol{n})$ while letting the second part $\boldsymbol{\mathcal{M}_d}(\boldsymbol{w},\boldsymbol{w},\boldsymbol{n})$ unchanged. Indeed, the deviation matrix $\boldsymbol{\mathcal{M}_d}$ appears to be non-crucial to the consistency relation as being vanishing. Therefore, this provides a sufficient condition for constructing a matrix that satisfies the consistency condition (5.14), but this should not be the only way to proceed. Indeed, we cannot rule out the possibility of also incorporating the correction in $\boldsymbol{\mathcal{M}_d^{HLLC-X}}$, provided that it is a vanishing matrix when $\boldsymbol{w_l} = \boldsymbol{w_r}$. Nevertheless, the influence of this matrix on the discrete properties of the method remains unclear, and further investigations are needed.

In the next section, this approach is applied for generalizing the artificial speed of sound approach of Rossow [26], as discussed in detail in chapter 3, thus deriving the HLLC-Rossow scheme.

5.3.2 . Transposition of a correction from the HLLC scheme to Roe scheme (conjecture)

Conversely, in order to determine the identical rescaling formulation considered for the Roe scheme, from a corrected numerical flux $\boldsymbol{\mathcal{F}^{HLLC-X}}$, two steps are needed. First of all, it is required to recover the matrix form (5.6), corresponding to a lengthy computation, yielding

$$\boldsymbol{d^{HLLC-X}} = \boldsymbol{\mathcal{M}^{HLLC-X}} \begin{pmatrix} \Delta\rho \\ \boldsymbol{\Delta\mathcal{U}} \\ \Delta\mathcal{U}_n \\ \Delta p \end{pmatrix} \qquad \text{with } \boldsymbol{\mathcal{M}^{HLLC-X}} \in \mathbb{R}^{(d+2)\times(d+3)}.$$

However, this step is a prerequisite to ensure the accurate transposition of the original rescaling formulation of the dissipation vector. On the characterization of the correction is completed, the easiest step follows and consists in deriving the associated corrected matrix $\boldsymbol{\mathcal{M}_d^{Roe-X}}$ from the consistency relation (5.2.1). In this case, the resulting matrix $\boldsymbol{\mathcal{M}_d^{Roe-X}}(\tilde{\boldsymbol{w}}, \boldsymbol{n})$ is unique.
It should be noted that, in the absence of further elaborations and proofs to support this second strategy, it remains a conjecture and serves as a basis to formulate an appropriate approach. Further investigations were not possible due to the time constraints during the Ph-D program, as well as the need to select a relevant correction for the HLLC scheme, that would have required an additional algebraic effort.

5.4 . Derivation of the HLLC-Rossow scheme

The following section aims at briefly recalling the formulation of the artificial speed of sound approach according to Rossow. This correction has been discussed in detail in chapter 3, and also more concisely in section 2.5.3. Then, the approach described in section 5.3.1 is considered to extend the X-Rossow correction to the HLLC scheme, according to definition 5.3.1.

5.4.1 . Initial definition of the Roe-Rossow scheme

The modified vector dissipation associated with the Roe-Rossow scheme, denoted with the shorthand notation in the following as $\boldsymbol{d^{R-R}}$, can be expressed for any flow regime using the following definition

$$\boldsymbol{\mathcal{M}^{R-R}} = \begin{pmatrix} |\tilde{\mathcal{U}}_n| & 0 & 0 & \frac{\tilde{\rho}B}{\tilde{c}} & \frac{A}{\tilde{c}'c} \\ |\tilde{\mathcal{U}}_n|\tilde{u} & |\tilde{\mathcal{U}}_n|\tilde{\rho} & 0 & \frac{\tilde{\rho}\tilde{u}B}{\tilde{c}} + \frac{\tilde{c}'}{\tilde{c}}A\tilde{\rho}n_x & \frac{Bn_x}{\tilde{c}} + \frac{A\tilde{u}}{\tilde{c}'\tilde{c}} \\ |\tilde{\mathcal{U}}_n|\tilde{v} & 0 & |\tilde{\mathcal{U}}_n|\tilde{\rho} & \frac{\tilde{\rho}\tilde{v}B}{\tilde{c}} + \frac{\tilde{c}'}{\tilde{c}}A\tilde{\rho}n_y & \frac{Bn_y}{\tilde{c}} + \frac{A\tilde{v}}{\tilde{c}'\tilde{c}} \\ \frac{|\tilde{\mathcal{U}}_n||\tilde{\mathcal{U}}|^2}{2} & |\tilde{\mathcal{U}}_n|\tilde{\rho}\tilde{u} & |\tilde{\mathcal{U}}_n|\tilde{\rho}\tilde{v} & \frac{\tilde{\rho}\tilde{H}B}{\tilde{c}} + \frac{\tilde{c}'}{\tilde{c}}A\tilde{\rho}\tilde{\mathcal{U}}_n & \frac{B\tilde{\mathcal{U}}_n}{\tilde{c}} + \frac{A\tilde{H}}{\tilde{c}'\tilde{c}} + \frac{|\tilde{\mathcal{U}}_n|}{\gamma-1} \end{pmatrix}, \tag{5.17}$$

with coefficients A and B given by

$$\begin{cases} A = \dfrac{|\tilde{\lambda}_1| + |\tilde{\lambda}_4|}{2} - |\tilde{\lambda}_2| \\ B = \dfrac{|\tilde{\lambda}_4| - |\tilde{\lambda}_1|}{2} \end{cases} \quad \text{where for subsonic flows, these coefficients reduced to} \quad \begin{cases} A = \tilde{c} - |\tilde{\mathcal{U}}_n| \\ B = |\tilde{\mathcal{U}}_n| \end{cases}.$$

Note that in expression (5.17), matrix $\boldsymbol{\mathcal{M}^{R-R}}$ returns to the original definition of $\boldsymbol{\mathcal{M}^{Roe}}$ when $\tilde{c}' = \tilde{c}$. The definition of the artificial speed of sound $\tilde{c}'$ requires to introduce a cut-off value M_{ref} for low-speed flows, assumed to take a small value, as indicated next

$$\begin{cases} \beta^2 = \min(\max(M^2, M_{ref}^2), 1) & \in & [M_{ref}^2,\ 1] \\ \alpha = \dfrac{1}{2}(1 - \beta^2) & \in & [0,\ \dfrac{1 - M_{ref}^2}{2}] \\ \tilde{c}' = \tilde{c}\sqrt{\alpha^2 M_n^2 + \beta^2} & \in & [\tilde{c}\left(M_{ref}^2 + (\dfrac{1 - M_{ref}^2}{2})^2\, M_n^2\right)^{1/2},\ \tilde{c}] \end{cases}. \tag{5.18}$$

In this Ph-D work, the user parameter M_{ref} was always set to the zero-level machine precision. In our experience, depending on the flow configuration, the Roe-Rossow scheme can be implemented with or without the introduction of this cut-off value. In the following, we shall adopt a notation for the HLLC-Rossow scheme that, depending on its definition, can either enable or disable the use of such a cut-off value for low Mach number flows. For more details on this rescaling approach, the reader is referred to section 2.5.3 or to chapter 3.

5.4.2 . Formulation of the artificial speed of sound and of the fan wave estimates

The first step in deriving the HLLC-Rossow scheme relies on the introduction of artificial speeds of sound. Nevertheless, unlike the Roe-Rossow scheme, the modified dissipation vector is obtained by introducing the same rescaling approach through entries $\hat{c}_k$, embedded in the definitions of wave speed estimates $(S_l,\ S_r)$, arising in some terms of the matrix. Regarding the generic definitions of the acoustic wave speed estimates, reminded below

$$S_l = \mathcal{U}_{n_l} - \hat{c}'_l \qquad \text{and} \qquad S_r = \mathcal{U}_{n_r} + \hat{c}'_r,$$

this implies to introduce a number of artificial speeds of sound c'_k, which must match the number of speeds of sound c_k used in the definition of $\hat{c}_k$. Then, only a few substitutions in the initial formulation are required to formulate the modified matrix $\boldsymbol{\mathcal{M}_d^{H-R}}$, as discussed in the next section.
Considering Davis's approximations (4.11), two artificial speeds of sound must be introduced, respectively $\hat{c}'_l$ and $\hat{c}'_r$, which are used to formulate the following quantities

$$\hat{c}'_l = \max\Big(c'_l,\ c'_r - \Delta\mathcal{U}_n\Big) \qquad \text{and} \qquad \hat{c}'_r = \max\Big(c'_r,\ c'_l - \Delta\mathcal{U}_n\Big). \tag{5.19}$$

The definitions of the left and right artificial speeds of sound c'_l and c'_r, respectively, are formulated with slight variation of the artificial speed of sound, by possibly removing the cut-off value, as indicated next

$$\text{For } k \in \{l, r\} \qquad \begin{cases} \beta_k^2 = \min(\mathcal{K}_k, 1) \\ \zeta_k = \dfrac{1}{2}(1 - \beta_k^2) \\ c'_k = c_k\sqrt{{M_{n_k}}^2\zeta_k^2 + \beta_k^2} \end{cases} \qquad \text{with } \mathcal{K}_k = M_k^2. \tag{5.20}$$

In the above expression, the definition of the quantity $\mathcal{K}_k$ determines whether the cut-off value is included or excluded from the scheme. By setting $\mathcal{K}_k = \max(M_k^2, M_{ref}^2)$, then this cut-off value is incorporated into the scheme. There are several reasons to always incorporate a cut-off value into the scheme, while opting to adjust the user parameter M_{ref} to circumvent any potential interaction with the flow. Indeed, this cut-off especially avoids, for instance, singularities for flows where the Mach number is equal to zero in a part of the domain (see for instance (5.17) and its last column where singularities may occur).
Considering Einfeldt's approximates (4.12), an additional third artificial speed of sound must be introduced, corresponding to the initial formulation of $\tilde{c}$ in the expression (5.18), as indicated in the following

$$\hat{c}_l' = \max\Big(c_l',\, \tilde{c}' - (\tilde{\mathcal{U}}_n - \mathcal{U}_{n_l})\Big) \qquad \text{and} \qquad \hat{c}_r' = \max\Big(c_r',\, \tilde{c}' - (\mathcal{U}_{n_r} - \tilde{\mathcal{U}}_n)\Big) \tag{5.21}$$

5.4.3 . Definition of the vector dissipation of the HLLC-Rossow scheme

Regardless of the choice of acoustic wave speed estimates (S_l, S_r) and therefore the number of artificial speeds of sound required, the following step for deriving the HLLC-Rossow scheme requires to determine the matrix satisfying the consistency property (5.2.1). One possible and readily manner for formulating an appropriate matrix $\boldsymbol{\mathcal{M}^{HLLC-Rossow}}$, simply denoted as $\boldsymbol{\mathcal{M}^{H-R}}$ in the following, consists in only searching for a consistent common matrix $\boldsymbol{\mathcal{M}_c^{H-R}}$

$$\boldsymbol{d^{H-R}}(\boldsymbol{w_l}, \boldsymbol{w_r}, \boldsymbol{n}) = \boldsymbol{\mathcal{M}^{H-R}}(\boldsymbol{w_l}, \boldsymbol{w_r}, \boldsymbol{n}) \begin{pmatrix} \Delta\rho \\ \boldsymbol{\Delta\mathcal{U}} \\ \Delta\mathcal{U}_n \\ \Delta p \end{pmatrix} \quad \text{with} \quad \boldsymbol{\mathcal{M}^{H-R}} = \boldsymbol{\mathcal{M}_c^{H-R}} + \boldsymbol{\mathcal{M}_d}, \tag{5.22}$$

and thus, the deviation matrix $\boldsymbol{\mathcal{M}_d}$ is unmodified and given by (5.13). As a result, this leads to the formulation of a modified dissipation vector $\boldsymbol{d^{H-R}}$ that directly satisfies the definition 5.3.1 through the following consistency condition

$$\boldsymbol{\mathcal{M}_c^{H-R}}(\boldsymbol{w}, \boldsymbol{w}, \boldsymbol{n}) = \boldsymbol{\mathcal{M}^{R-R}}(\boldsymbol{w}, \boldsymbol{n}). \tag{5.23}$$

Therefore, after some simple algebra, this yields the following common matrix for the HLLC-Rossow scheme

$$\boldsymbol{\mathcal{M}_c^{H-R}} = \left(\begin{array}{c|c|c|c|c}
|S_*| & 0 & 0 & \frac{\rho_l\rho_r}{\langle\rho\hat{c}\rangle}\left(\frac{\delta_{c_r}}{\delta_{S_l}}\delta_{|S|_l} - \frac{\delta_{c_l}}{\delta_{S_r}}\delta_{|S|_r}\right) & \frac{1}{\langle\rho\hat{c}'\rangle}\left(\frac{\rho_r}{\delta_{S_r}}\delta_{|S|_r} - \frac{\rho_l}{\delta_{S_l}}\delta_{|S|_l}\right) \\
|S_*|\,\overline{u^*} & \overline{\rho^*}|S_*| & 0 & \begin{array}{l}\frac{\rho_l\rho_r}{\langle\rho\hat{c}\rangle}\Big(\frac{\delta_{c_r}|S_l|}{\delta_{S_l}}(u_l - \hat{c}'_l n_x) \\ \quad -\frac{\delta_{c_l}|S_r|}{\delta_{S_r}}(u_r + \hat{c}'_r n_x) \\ \quad -n_x\overline{\rho^*}|S_*|\frac{\langle\rho\hat{c}'\rangle}{\rho_l\rho_r}\Big)\end{array} & \begin{array}{l}\frac{1}{\langle\rho\hat{c}'\rangle}\Big(\frac{\rho_r}{\delta_{S_r}}(u_r|S_r| - \overline{u^*}|S_*|) \\ \quad -\frac{\rho_l}{\delta_{S_l}}(u_l|S_l| - \overline{u^*}|S_*|)\Big) \\ +\frac{n_x}{\langle\rho\hat{c}\rangle}\Big(\frac{\rho_l}{\delta_{S_l}}\hat{c}_l|S_l| + \frac{\rho_r}{\delta_{S_r}}\hat{c}_r|S_r|\Big)\end{array} \\
|S_*|\,\overline{v^*} & 0 & \overline{\rho^*}|S_*| & \begin{array}{l}\frac{\rho_l\rho_r}{\langle\rho\hat{c}\rangle}\Big(\frac{\delta_{c_r}|S_l|}{\delta_{S_l}}(v_l - \hat{c}'_l n_y) \\ \quad -\frac{\delta_{c_l}|S_r|}{\delta_{S_r}}(v_r + \hat{c}'_r n_y) \\ \quad -n_y\overline{\rho^*}|S_*|\frac{\langle\rho\hat{c}'\rangle}{\rho_l\rho_r}\Big)\end{array} & \begin{array}{l}\frac{1}{\langle\rho\hat{c}'\rangle}\Big(\frac{\rho_r}{\delta_{S_r}}(v_r|S_r| - \overline{v^*}|S_*|) \\ \quad -\frac{\rho_l}{\delta_{S_l}}(v_l|S_l| - \overline{v^*}|S_*|)\Big) \\ +\frac{n_y}{\langle\rho\hat{c}\rangle}\Big(\frac{\rho_l}{\delta_{S_l}}\hat{c}_l|S_l| + \frac{\rho_r}{\delta_{S_r}}\hat{c}_r|S_r|\Big)\end{array} \\
\begin{array}{l}|S_*|\Big(\overline{H} \\ -\frac{\bar{\rho}^*\bar{p}}{\rho_l\rho_r}(1+\frac{1}{\gamma-1})\end{array} & \overline{\rho^*}\overline{u}|S_*| & \overline{\rho^*}\overline{v}|S_*| & \begin{array}{l}\frac{\rho_l\rho_r}{\langle\rho\hat{c}\rangle}\Big(\frac{\delta_{c_r}|S_l|}{\delta_{S_l}}(H_l - \hat{c}'_l S_*) \\ \quad -\frac{\delta_{c_l}|S_r|}{\delta_{S_r}}(H_r + \hat{c}'_r S_*) \\ \quad -\overline{\rho^*}S_*|S_*|\frac{\langle\rho\hat{c}'\rangle}{\rho_l\rho_r}\Big)\end{array} & \begin{array}{l}\frac{1}{\langle\rho\hat{c}'\rangle}\Big(\frac{\rho_r}{\delta_{S_r}}(H_r|S_r| - \overline{H}|S_*|) \\ \quad -\frac{\rho_l}{\delta_{S_l}}(H_l|S_l| - \overline{H}|S_*|)\Big) \\ +\frac{S_*}{\langle\rho\hat{c}\rangle}\Big(\frac{\rho_l}{\delta_{S_l}}\hat{c}_l|S_l| + \frac{\rho_r}{\delta_{S_r}}\hat{c}_r|S_r|\Big) \\ \quad +\Big(\frac{\bar{\rho}^*\bar{p}\gamma}{\rho_l\rho_r(\gamma-1)} - 1\Big)|S_*|\end{array}
\end{array}\right). \quad (5.24)$$

For the reader's convenience, a Fortran routine is provided in Appendix A, which merely only requires the adaptation of the input variables according to its own code, facilitating the challenging implementation step. It is also worth noting that, by proceeding to a few straightforward modifications of some variables in the Fortran routine, the code returns the original HLLC scheme, expressed in the matrix form.

5.4.4 . Validation of the HLLC-Rossow scheme

Comparison with the original HLLC scheme

For validation purpose and a first assessment of the HLLC-Rossow scheme, the same test case as described in section 2.5.3 was considered for the NACA0012 airfoil . The original and modified HLLC schemes are first compared in the transonic regime ($M = 0.85$, $\alpha = 1$), using the Einfeldt's approximations for the wave speed estimates. Computations were performed using the same structured C-type mesh with 279x60 nodes, as depicted in Fig.5.2a, with 151 nodes discretizing the solid wall. The boundary conditions are the same as previously described in chapter 2 for this transonic test case. Computations were performed using a second-order MUSCL reconstruction, with van Albada limiter, referred to as "O(2)" in figures 5.2. Figure 5.2b illustrates the convergence history of the l^2-norms of the normalized explicit residuals and the evolution of the CFL value. Considering the same uniform initial condition, a local time stepping method combined with an adaptive CFL is applied in order to quickly converge to the steady-state solution in a few hundreds of iterations. More details regarding the description of the adaptive CFL can be found in chapter 3. As it can be observed in Fig.5.2b, the computation is initially set to CFL = 5, then, at a prescribed iteration 5, the adaptive CFL starts with

a minimum value CFL = 12. In the following iterations, the normalized residuals decrease, resulting in a smooth increase in the CFL value around the 50th iteration, which then begins to fluctuate. At the 500th iteration, the CFL value is characterized by a sharp increase, rising from 30 to 1, 000, 000 at the 700th iteration, resulting in a quadratic convergence to the zero machine precision.

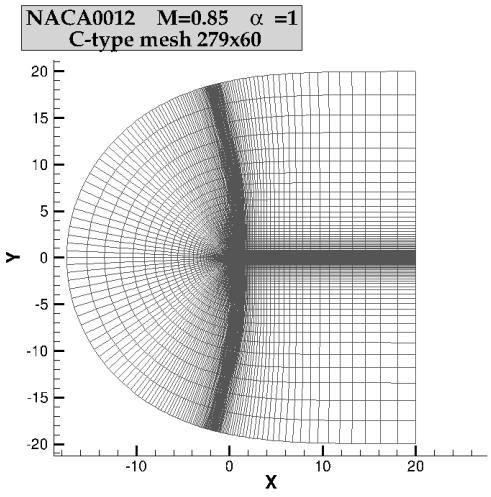

(a) C-type mesh for the NACA0012

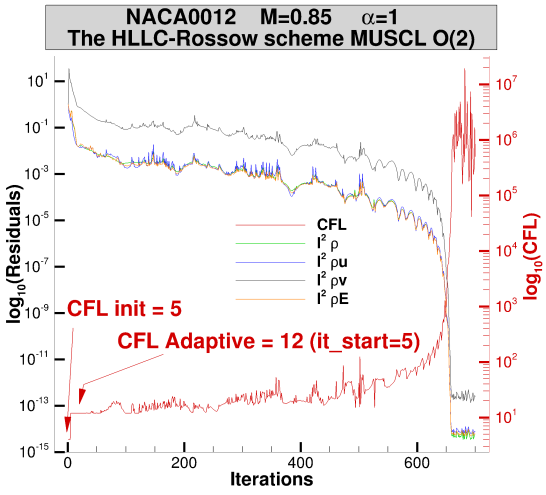

(b) Convergence history for residuals and the CFL number HLLC-Rossow scheme

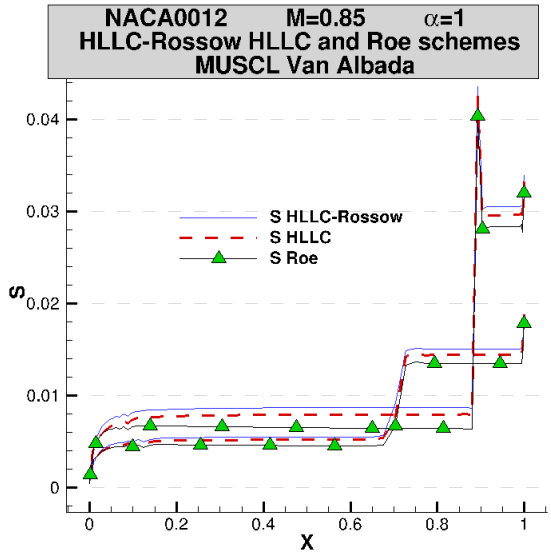

(d) Production of spurious entropy at the wall

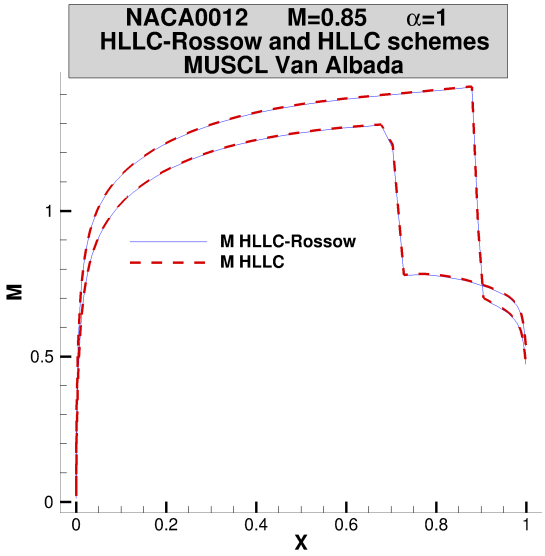

(c) Mach number at the wall

Figure 5.2: The HLLC-Rossow scheme with MUSCL reconstruction O(2), NACA0012 airfoil at $M = 0.85$, $\alpha = 1^\circ$

Next Fig. 5.2c and 5.2d depict the entropy S and the Mach number distributions at the solid wall. For the second-order accuracy in space, the modified HLLC-Rossow scheme produces slightly more spurious entropy than the original HLLC scheme at stagnation points, as shown in Fig. 5.2c. Moreover, when the Einfeldt's approximations are employed, the HLLC scheme exhibits slightly higher levels of spurious entropy in comparison to the Roe scheme indicated by the green triangles. It should be mentioned that, these trends for the original and modified HLLC schemes are consistent with the observations

made in section 2.5.3, when comparing the original and modified Roe schemes. In addition, Fig. 5.2d demonstrates that the numerical shock structure are almost identical for both schemes, as also previously observed in the case of the modified Roe-Rossow scheme. Accordingly, the modified HLLC scheme returns the original scheme in the vicinity of the sonic point, and shows a comparable discrete solution as obtained when the correction is applied to the Roe scheme.

To illustrate the fact that the modified HLLC-Rossow scheme is effective in the low Mach number regime, additional computations were performed for decreasing inflow Mach numbers $M = 0.1$ and $M = 0.001$ in non-lifting conditions, using a third-order MUSCL reconstruction (indicated as MUSCL O(3) in the figures). Stability considerations in the low Mach number limit are discussed in detail for the Roe-Rossow scheme in chapter 3 and are reminded next for the cylinder test-case considering the HLLC-Rossow scheme. The comparison illustrated in the two next figures for $M = 0.1$ demonstrates that the original and modified HLLC schemes display different steady discrete solution. In particular, as shown in Fig. 5.3a, the normalized pressure contours, defined as

$$\frac{p - p_{\min}}{p_{\max} - p_{\min}} \in [0, 1],$$

indicates notable differences especially away from the solid wall. However, it should be noted that the differences in the levels are characterized by small variations, as indicated with few boxed levels in the legend. Additionally, near the wall, it can be observed that the normalized pressure contours for these two schemes almost match, as illustrated in Fig. 5.3b.

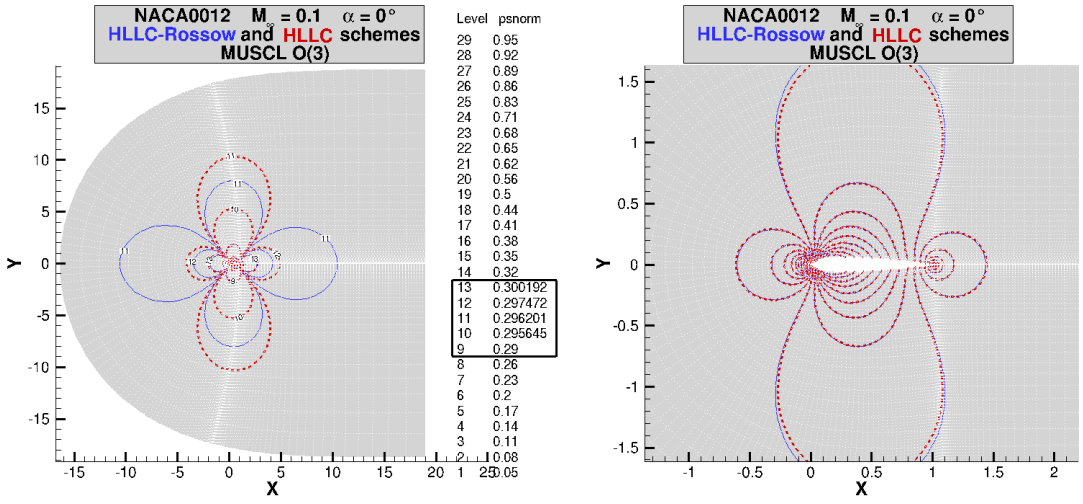

(a) Normalized pressure contours (a) Normalized pressure contours (zoom)

Figure 5.3: The HLLC-Rossow scheme with MUSCL reconstruction O(2), NACA0012 airfoil at $M = 0.1$, $\alpha = 0°$

As the Mach number decreases, the previously observed results no longer manifest, as evidenced by the two figures that follow. Figure 5.4a for the Mach number contours illustrates that in the low Mach number limit, the HLLC scheme has large errors, even when a third-order MUSCl reconstruction is used. This is especially visible for the normalized pressure contours in the vincinity of the wall, which are no longer similar to those calculated by the modified HLLC-Rossow scheme. Moreover, downstream the airfoil oscillations are also observed in the discrete solution, thus demonstrating significant inconsistencies with the original HLLC scheme.

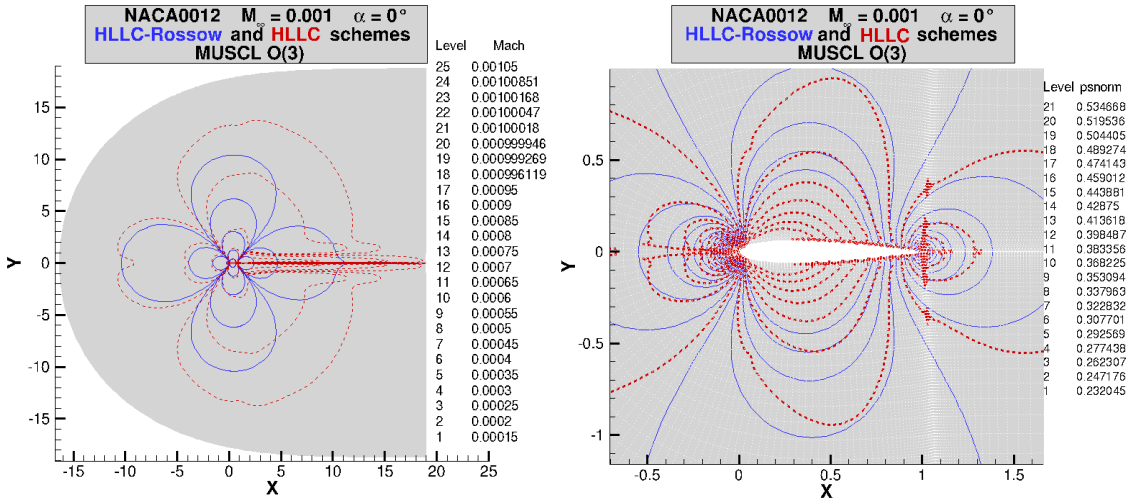

(b) Mach number countours (a) Normalized pressure contours (zoom)

Figure 5.4: The HLLC-Rossow scheme with MUSCL reconstruction O(2), NACA0012 airfoil at $M = 0.001$, $\alpha = 0°$

Comparison with the Roe-Rossow scheme for very low Mach number flows

In was also found interesting to investigate in details the overall accuracy of the discrete steady-state solution in the low Mach number limit, comparing the HLLC-Rossow and Roe-Rossow schemes. The non-lifting cylinder test-case introduced previously in chapter 3 was considered, for an inflow Mach number $M = 0.0001$. For this comparison, a highly stretched mesh downstream of the cylinder was used, with 140 nodes discretizing the solid wall and a mesh extension of 20 diameters, as depicted in Fig. 5.5c. This is one of the most relevant test cases examined, as this irregular mesh was especially design to trigger significant pressure checkerboard modes for low Mach number corrections, such as the Rieper's fix, contaminating the overall accuracy of the discrete solution. In contrast, it has been also shown in chapter 3 that the Roe-Rossow scheme remains notably accurate in this mesh, and is not prone to any pressure checkerboard modes. To further validate the HLLC-Rossow scheme, a third-order MUSCL reconstruction was used (denoted as "O(3)" in the figures), as done previously for the NACA0012 test-case. The discrete solution is then compared with the Roe-Rossow scheme, and with the analytic potential solution given in chapter 3.
Moreover, considering the argumentation on the origins of the similarities with the wave structure of the Roe scheme presented in section 5.2.1, as well as the derivation based on definition 5.3.1, the same stability condition is applied to both schemes in the low Mach number limit. Therefore, as previously discussed in the Chapter 3, the stability condition is defined in the low Mach number limit using the spectral radius of the modified viscosity matrix, as demonstrated by Birken-Meister [29].
Figures 5.5a and 5.5b show the convergence history of the l^2-norms of the normalized explicit residuals and the evolution of the CFL value for both modified schemes. As it can be clearly observed, a similar convergence is found for both schemes, especially with identical convergence thresholds reached. In addition, as illustrated in Fig. 5.5d, the respective pressure coefficients C_p are in good agreement with the incompressible solution, provided that schemes are formulated with a second or third-order MUSCL reconstruction, due to the mesh density and the mesh extension. This highlights that, at the wall, the pressure for these two weakly compressible solutions almost matches the incompressible pressure, solution of the Bernoulli equation. Looking at the horizontal velocity u contours in the field depicted in Fig. 5.5e, it can be seen that the overall accuracy of the discrete solutions is also nearly identical between the two modified schemes. These results show that both compressible schemes provide relevant

approximations of the potential solution, with the exception of the downstream region, where a larger spurious entropy is produced due to the poor mesh quality. Next Figs. 5.5f and 5.5g represent the patterns of the normalized pressure field, obtained with the compressible solutions and compared to the potential theory. The two compressible schemes clearly exhibit similar patterns for the normalized pressure field. However, when compared to the potential solution, significant discrepancies become clearly visible away from cylinder wall, whereas Fig. 5.5e demonstrated that comparable distributions are found for the normalized pressure near the solid wall. Nevertheless, it can be seen that these pressure disturbances are proportional to the Mach number, and far from the wall, weak compressible effects can not be ruled out, even in low Mach number flows, explaining the expected discrepancies found with the incompressible potential solution.

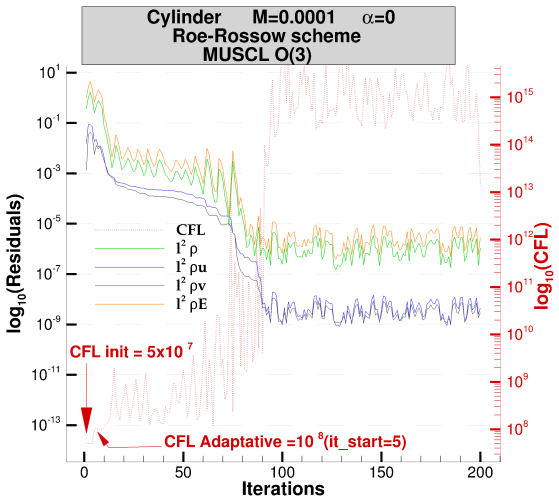

(a) Convergence history for residuals and the CFL number Roe-Rossow scheme

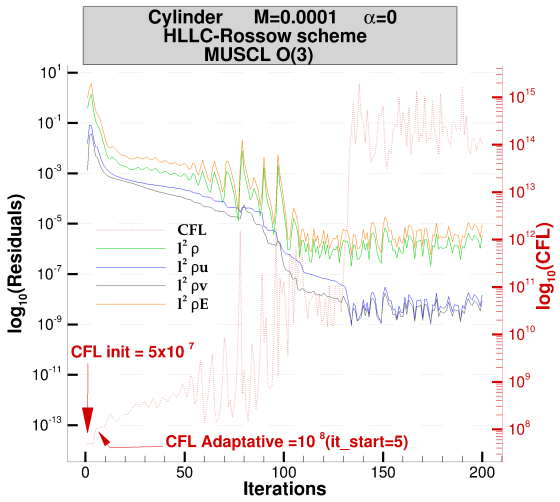

(b) Convergence history for residuals and the CFL number HLLC-Rossow scheme

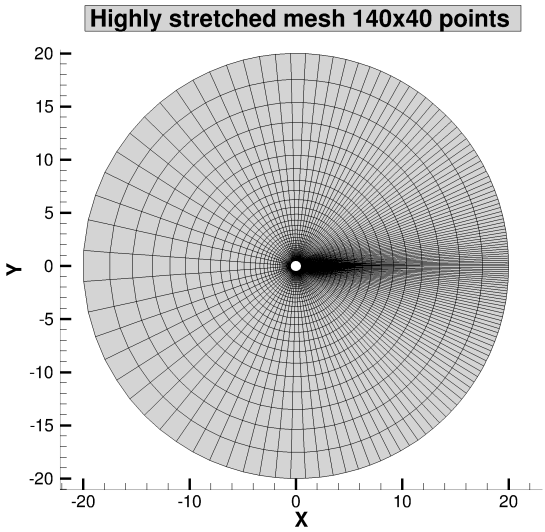

(c) O-type mesh for cylinder mesh triggering pressure checkerboard modes

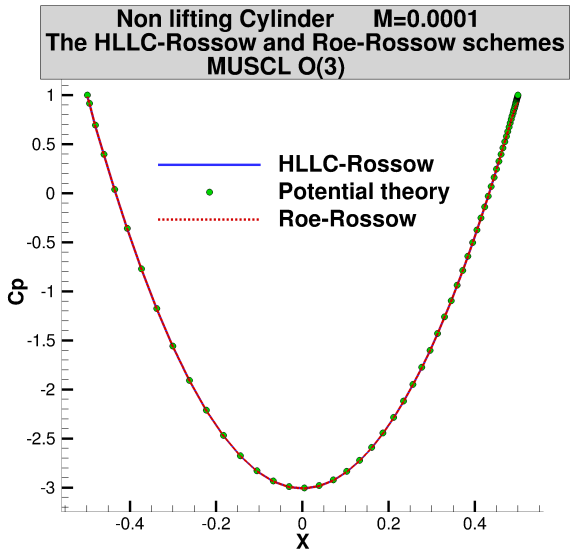

(d) Pressure coefficients at the wall

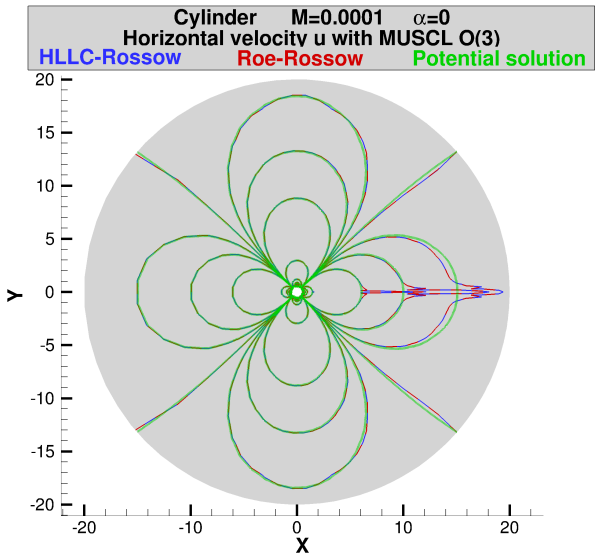

(e) Vertex-centered contours of the horizontal velocity u

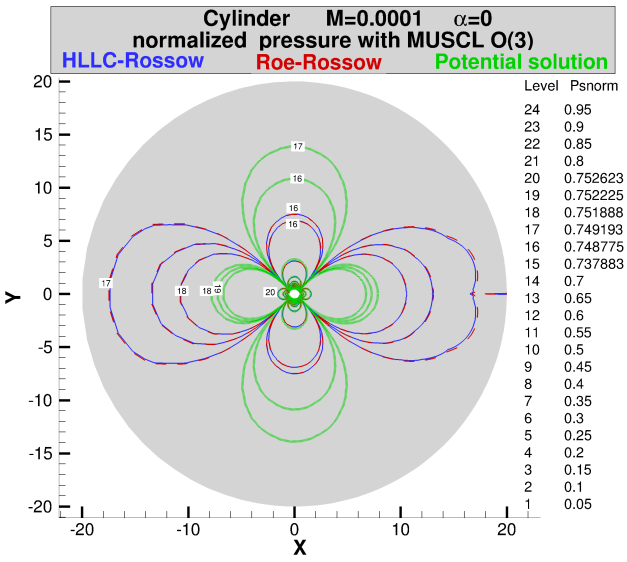

(f) Vertex-centered contours of the normalized pressure

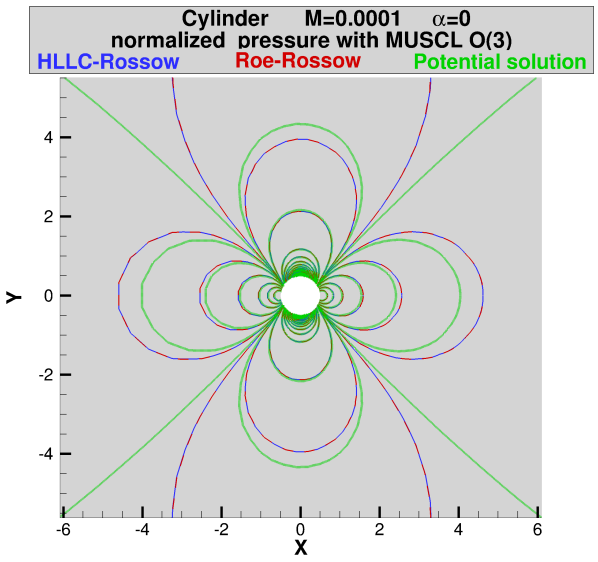

(g) Vertex-centered contours of the normalized pressure (zoom)

Figure 5.5: Comparisons of the Rossow's correction for the HLLC and Roe schemes

In conclusion, these results show that the HLLC-Rossow scheme has a similar behavior compared to the Roe-Rossow scheme, particularly in terms of the overall accuracy of the steady discrete solution, and the convergence history. Both schemes are especially characterized by the absence of spurious pressure checkerboard mode issues in this challenging test case.

5.5 . The Liu-Vinokur form

Further investigations were considered with the objective of simplifying the expression of the dissipation vector $\boldsymbol{d}^{\boldsymbol{HLLC-Rossow}}$, in order to facilitate the implementation in a Fortran routine. To this end, an extension of the Liu-Vinokur form was derived for the HLLC scheme, thereby providing a compact

expression. Furthermore, this form also highlights the significant connection with the analysis made by Li-Gu in [21] and the dozen of low Mach number corrections studied for the Roe scheme, all formulated in a unified formalism of the dissipation vector.

5.5.1 . The initial Liu-Vinokur form for the Roe-Rossow scheme

We shall first begin by briefly recalling the original Liu-Vinokur form, given in [63], formulated for the Roe-Rossow scheme. Additional details regarding this vector dissipation form can be found in section 2.4.2 and chapter 3. We make use of an important property of the Roe average, allowing to easily decompose the discrete space difference operator $\Delta\cdot$, as indicated next

$$\forall a_l, a_r, \rho_l, \rho_r \in \mathbb{R} \quad \Delta(\rho a) = \tilde{a}\Delta\rho + \tilde{\rho}\Delta a \quad \text{with} \quad \tilde{a} = \frac{\sqrt{\rho_l}\, a_l + \sqrt{\rho_r}\, a_r}{\sqrt{\rho_l} + \sqrt{\rho_r}} \quad \text{and} \quad \tilde{\rho} = \sqrt{\rho_l\, \rho_r}. \tag{5.25}$$

Using this property, the dissipation vector associated with the Roe-Rossow scheme can be equivalently expressed as follows

$$\boldsymbol{d^{R-R}} = |\tilde{\mathcal{U}_n}| \begin{pmatrix} \Delta\rho \\ \tilde{\rho}\Delta u + \tilde{u}\Delta\rho \\ \tilde{\rho}\Delta v + \tilde{v}\Delta\rho \\ \tilde{\rho}\Delta E + \tilde{E}\Delta\rho \end{pmatrix} + \delta\mathcal{U}_n^{R-R} \begin{pmatrix} \tilde{\rho} \\ \tilde{\rho}\tilde{u} \\ \tilde{\rho}\tilde{v} \\ \tilde{\rho}\tilde{H} \end{pmatrix} + \delta p^{R-R} \begin{pmatrix} 0 \\ n_x \\ n_y \\ \tilde{\mathcal{U}_n} \end{pmatrix}, \tag{5.26}$$

$$\begin{pmatrix} \delta\mathcal{U}_n^{R-R} \\ \delta p^{R-R} \end{pmatrix} = \begin{pmatrix} \frac{B}{\tilde{c}} & \frac{1}{\tilde{c}'\tilde{c}}\frac{A}{\tilde{\rho}} \\ \frac{\tilde{c}'}{\tilde{c}}A\tilde{\rho} & \frac{B}{\tilde{c}} \end{pmatrix} \begin{pmatrix} \Delta\mathcal{U}_n \\ \Delta p \end{pmatrix} \qquad \text{with} \qquad \begin{cases} A = \dfrac{|\tilde{\lambda_4}| + |\tilde{\lambda_1}|}{2} - |\tilde{\lambda_2}| \\ B = \dfrac{|\tilde{\lambda_4}| - |\tilde{\lambda_1}|}{2} \end{cases},$$

where the definition of the artificial speed of sound $\tilde{c}'$ is given by expression (5.18). Note that, upon substituting $\tilde{c}'$ for the original speed of sound $\tilde{c}$, the above expression returns the formulation of the dissipation vector corresponding to the Roe scheme.

5.5.2 . The Liu-Vinokur form for the HLLC scheme

Starting from the fully-expanded formulation of the vector dissipation written in (5.7 - 5.9), and performing a lengthy algebra, a novel equivalent form is derived by extending the Liu-Vinokur form to the HLLC scheme, as formulated next

$$\begin{aligned} \boldsymbol{d^{HLLC}} = |S_*| & \begin{pmatrix} \Delta\rho \\ \overline{\rho^*}\Delta u + \overline{u^*}\Delta\rho \\ \overline{\rho^*}\Delta v + \overline{v^*}\Delta\rho \\ \overline{\rho^*}\Delta E + \overline{E}\Delta\rho - \left(\overline{\rho^*} - \overline{\rho}\right)\Delta\left(\dfrac{p}{\rho}\right) \end{pmatrix} + \delta\mathcal{U}_n^{HLLC} \begin{pmatrix} \tilde{\rho} \\ \tilde{\rho}\,\overline{u^*} \\ \tilde{\rho}\,\overline{v^*} \\ \tilde{\rho}\,\overline{H} \end{pmatrix} + \delta p^{HLLC} \begin{pmatrix} 0 \\ n_x \\ n_y \\ S_* \end{pmatrix} \\ & + \delta_l^{HLLC} \begin{pmatrix} 0 \\ \overline{u^*} - u_l \\ \overline{v^*} - v_l \\ \overline{H} - H_l \end{pmatrix} + \delta_r^{HLLC} \begin{pmatrix} 0 \\ \overline{u^*} - u_r \\ \overline{v^*} - v_r \\ \overline{H} - H_r \end{pmatrix} + \delta_*^{HLLC} \begin{pmatrix} 0 \\ 0 \\ 0 \\ S_*(S_* - \overline{\mathcal{U}_n}) \end{pmatrix}. \end{aligned} \tag{5.27}$$

As it can be observed, this expression clearly highlights several significant similarities between the two dissipation vectors $\boldsymbol{d^{HLLC}}$ and $\boldsymbol{d^{Roe}}$, while also indicating a notable discrepancy that arises from the last three vectors. It should also be noted that, these expressions exhibit some substitutions occurring between the two schemes. As for instance, the normal velocity $\tilde{\mathcal{U}}_n$, which is replaced by S_* in the first and third terms, as well as the vector $\tilde{\boldsymbol{\mathcal{U}}}$ being substituted by the averaged intermediate velocities $\bar{\boldsymbol{\mathcal{U}}}^*$,

among others. The five scalar coefficients expressed in the Liu-Vinokur form (5.27) are given by the following expressions

$$\begin{cases} \delta\mathcal{U}_n^{HLLC} = \dfrac{\tilde{\rho}}{\langle\rho\hat{c}\rangle}\Delta\mathcal{U}_n\left[\dfrac{\delta_{c_r}\delta_{|S|_l}}{\delta_{S_l}} - \dfrac{\delta_{c_l}\delta_{|S|_r}}{\delta_{S_r}}\right] & + \dfrac{\tilde{\rho}}{\langle\rho\hat{c}\rangle}\Delta p\left[\dfrac{\delta_{|S|_r}}{\rho_l\delta_{S_r}} - \dfrac{\delta_{|S|_l}}{\rho_r\delta_{S_l}}\right] \\ \delta p^{HLLC} = -\dfrac{\rho_l\rho_r}{\langle\rho\hat{c}\rangle}\Delta\mathcal{U}_n\left[\dfrac{\hat{c_l}|S_l|\delta_{c_r}}{\delta_{S_l}} + \dfrac{\hat{c_r}|S_r|\delta_{c_l}}{\delta_{S_r}} + \dfrac{\langle\rho\hat{c}\rangle\overline{\rho^*}|S_*|}{\rho_l\rho_r}\right] & + \dfrac{\Delta p}{\langle\rho\hat{c}\rangle}\left[\rho_r^*|S_r| - \rho_l^*|S_l|\right] \\ \delta_l^{HLLC} = -\dfrac{\rho_l\rho_r}{\langle\rho\hat{c}\rangle}\Delta\mathcal{U}_n\left[\dfrac{\delta_{c_r}|S_l|}{\delta_{S_l}}\right] & + \dfrac{\Delta p}{\langle\rho\hat{c}\rangle}\left[\dfrac{\rho_l|S_l|}{\delta_{S_l}}\right] \\ \delta_r^{HLLC} = \dfrac{\rho_l\rho_r}{\langle\rho\hat{c}\rangle}\Delta\mathcal{U}_n\left[\dfrac{\delta_{c_l}|S_r|}{\delta_{S_r}}\right] & - \dfrac{\Delta p}{\langle\rho\hat{c}\rangle}\left[\dfrac{\rho_r|S_r|}{\delta_{S_r}}\right] \\ \delta_*^{HLLC} = \dfrac{\rho_l\rho_r}{\langle\rho\hat{c}\rangle}|S_*|\Delta\mathcal{U}_n\left[\dfrac{\delta_{c_l}}{\delta_{S_r}} - \dfrac{\delta_{c_r}}{\delta_{S_l}}\right] & + \dfrac{|S_*|}{\langle\rho\hat{c}\rangle}\Delta p\left[\dfrac{\rho_l}{\delta_{S_l}} - \dfrac{\rho_r}{\delta_{S_r}}\right] + |S_*|\Delta\rho \end{cases} . \quad (5.28)$$

The fourth and fifth vectors in decomposition (5.27) were derived as a direct consequence of matching with the second vector in the decomposition (5.26) for the Roe scheme. Indeed, a straightforward reformulation of the scalar quantities $(\delta_l^{HLLC}, \delta_r^{HLLC})$ results in the formulation of a similar vector as the second term. Therefore, in a manner analogous to the Roe scheme, as presented in [14, 21, 83], all these terms involving the scalar quantities $(\delta\mathcal{U}_n^{HLLC},\ \delta_l^{HLLC},\ \delta_r^{HLLC})$ are related to modifications of the convective velocity at the interface.
The last vector in the expression (5.27) globally arises from the last row of the deviation matrix $\boldsymbol{\mathcal{M}_f}$ expressed with (5.13), where the term $S_*(S_* - \overline{\mathcal{U}_n})$ is almost present in each component.

Remark 2 *Freezing the jump quantities in the dissipation vector, and taking* $\boldsymbol{w_l} = \boldsymbol{w_r} = \boldsymbol{w}$ *in the other terms, the following expressions reduce to*

$$\begin{array}{lllll} \hat{c}_l = c & S_l = \lambda_1(\boldsymbol{w}) & \delta_{c_l} = -c & \delta_{S_l} = -c & \delta_{|S_l|} = |\lambda_1(\boldsymbol{w})| - |\lambda_2(\boldsymbol{w})| \\ \hat{c}_r = c & S_r = \lambda_4(\boldsymbol{w}) & \delta_{c_r} = c & \delta_{S_r} = c & \delta_{|S_r|} = |\lambda_4(\boldsymbol{w})| - |\lambda_2(\boldsymbol{w})| \\ & S_* = \lambda_2(\boldsymbol{w}) & & & \end{array} .$$

Then, it can be observed that, the definitions of the scalar quantities simplify to

$$\begin{cases} \delta\mathcal{U}_n^{HLLC} = \Delta\mathcal{U}_n\left[\dfrac{|\lambda_4(\boldsymbol{w})| - |\lambda_1(\boldsymbol{w})|}{2}\right] & + \Delta p\left[\dfrac{1}{\rho c^2}\Big(\dfrac{|\lambda_1(\boldsymbol{w})| + |\lambda_4(\boldsymbol{w})|}{2} - |\lambda_2(\boldsymbol{w})|\Big)\right] \\ \delta p^{HLLC} = \Delta\mathcal{U}_n\left[\rho\Big(\dfrac{|\lambda_1(\boldsymbol{w})| + |\lambda_4(\boldsymbol{w})|}{2} - |\lambda_2(\boldsymbol{w})|\Big)\right] & + \Delta p\left[\dfrac{1}{c}\Big(\dfrac{|\lambda_4(\boldsymbol{w})| - |\lambda_1(\boldsymbol{w})|}{2}\Big)\right] \\ \delta_l^{HLLC} = \Delta\mathcal{U}_n\left[\dfrac{\rho}{c}\dfrac{|\lambda_1(\boldsymbol{w})|}{2}\right] & - \Delta p\left[\dfrac{1}{c^2}\dfrac{|\lambda_1(\boldsymbol{w})|}{2}\right] \\ \delta_r^{HLLC} = -\Delta\mathcal{U}_n\left[\dfrac{\rho}{c}\dfrac{|\lambda_4(\boldsymbol{w})|}{2}\right] & - \Delta p\left[\dfrac{1}{c^2}\dfrac{|\lambda_4(\boldsymbol{w})|}{2}\right] \\ \delta_*^{HLLC} = 0 & - \Delta p\left[\dfrac{|\lambda_2(\boldsymbol{w})|}{c^2}\right] + |\lambda_2(\boldsymbol{w})|\Delta\rho \end{cases} ,$$

in which, the two first coefficients recovered the identical pattern to those documented for the Roe scheme in section 5.5.1 (i.e. when $\tilde{c}' = \tilde{c}$*). Similarly, using these relations in the definition of the intermediate states* $\boldsymbol{w_k^*}$ *makes vanishing the three last vectors in (5.28).*

5.5.3 . The Liu-Vinokur form of the HLLC-Rossow scheme

Considering the Liu-Vinokur decomposition in (5.27), the vector dissipation associated with the HLLC-Rossow scheme (in the sense of the definition 5.3.1) can be equivalently written as

$$\begin{aligned}\boldsymbol{d^{H-R}} = |S_*| \begin{pmatrix} \Delta\rho \\ \overline{\rho^*}\Delta u + \overline{u^*}\Delta\rho \\ \overline{\rho^*}\Delta v + \overline{v^*}\Delta\rho \\ \overline{\rho^*}\Delta E + \overline{E}\Delta\rho - \left(\overline{\rho^*} - \overline{\rho}\right)\Delta\left(\dfrac{p}{\rho}\right) \end{pmatrix} + \delta\mathcal{U}_n^{H-R} \begin{pmatrix} \tilde{\rho} \\ \tilde{\rho}\,\overline{u^*} \\ \tilde{\rho}\,\overline{v^*} \\ \tilde{\rho}\,\overline{H} \end{pmatrix} + \delta p^{H-R} \begin{pmatrix} 0 \\ n_x \\ n_y \\ S_* \end{pmatrix} \\ + \delta_l^{H-R} \begin{pmatrix} 0 \\ \overline{u^*} - u_l \\ \overline{v^*} - v_l \\ \overline{H} - H_l \end{pmatrix} + \delta_r^{H-R} \begin{pmatrix} 0 \\ \overline{u^*} - u_r \\ \overline{v^*} - v_r \\ \overline{H} - H_r \end{pmatrix} + \delta_*^{HLLC} \begin{pmatrix} 0 \\ 0 \\ 0 \\ S_*(S_* - \overline{\mathcal{U}_n}) \end{pmatrix}.\end{aligned} \tag{5.29}$$

As it can be seen, this decomposition yields a significant simplification of the original definition given by the matrix form (5.22) with the two matrices (5.24) and (5.13). Indeed, the formulation of the dissipation vector $\boldsymbol{d^{H-R}}$ only requires to modify fourth out of the five scalar coefficients, as indicated in the following

$$\cdot \begin{cases} \delta\mathcal{U}_n^{H-R} = & \dfrac{\tilde{\rho}}{\langle\rho\hat{c}\rangle}\Delta\mathcal{U}_n\left[\dfrac{\delta_{c_r}\delta_{|S|_l}}{\delta_{S_l}} - \dfrac{\delta_{c_l}\delta_{|S|_r}}{\delta_{S_r}}\right] & + & \dfrac{\tilde{\rho}}{\langle\rho\hat{c}'\rangle}\Delta p\left[\dfrac{\delta_{|S|_r}}{\rho_l\delta_{S_r}} - \dfrac{\delta_{|S|_l}}{\rho_r\delta_{S_l}}\right] \\ \delta p^{H-R} = & -\dfrac{\rho_l\rho_r}{\langle\rho\hat{c}\rangle}\Delta\mathcal{U}_n\left[\dfrac{\hat{c_l}'|S_l|\delta_{c_r}}{\delta_{S_l}} + \dfrac{\hat{c_r}'|S_r|\delta_{c_l}}{\delta_{S_r}} + \dfrac{\langle\rho\hat{c}'\rangle\overline{\rho^*}|S_*|}{\rho_l\rho_r}\right] & + & \dfrac{\Delta p}{\langle\rho\hat{c}\rangle}\left[\rho_r^*|S_r| - \rho_l^*|S_l|\right] \\ \delta_l^{H-R} = & -\dfrac{\rho_l\rho_r}{\langle\rho\hat{c}\rangle}\Delta\mathcal{U}_n\left[\dfrac{\delta_{c_r}|S_l|}{\delta_{S_l}}\right] & + & \dfrac{\Delta p}{\langle\rho\hat{c}'\rangle}\left[\dfrac{\rho_l|S_l|}{\delta_{S_l}}\right] \\ \delta_r^{H-R} = & \dfrac{\rho_l\rho_r}{\langle\rho\hat{c}\rangle}\Delta\mathcal{U}_n\left[\dfrac{\delta_{c_l}|S_r|}{\delta_{S_r}}\right] & - & \dfrac{\Delta p}{\langle\rho\hat{c}'\rangle}\left[\dfrac{\rho_r|S_r|}{\delta_{S_r}}\right] \\ \delta_*^{HLLC} = & \dfrac{\rho_l\rho_r}{\langle\rho\hat{c}\rangle}|S_*|\Delta\mathcal{U}_n\left[\dfrac{\delta_{c_l}}{\delta_{S_r}} - \dfrac{\delta_{c_r}}{\delta_{S_l}}\right] & + & \dfrac{|S_*|}{\langle\rho\hat{c}\rangle}\Delta p\left[\dfrac{\rho_l}{\delta_{S_l}} - \dfrac{\rho_r}{\delta_{S_r}}\right] + |S_*|\Delta\rho \end{cases}, \tag{5.30}$$

where the different artificial speeds of sound $\hat{c}'_k$ are expressed according to the fan wave speed estimates, as previously discussed in section 5.4.2.

Remark 3 *Freezing the jump quantities in the dissipation vector, and taking* $\boldsymbol{w_l} = \boldsymbol{w_r} = \boldsymbol{w}$*, it can be observed that* $(\mathcal{U}_n^{H-R}, \delta p^{H-R})$ *are consistent with expressions of* $(\mathcal{U}_n^{R-R}, \delta p^{R-R})$

For the reader's convenience, a Fortran routine is also provided here in Appendix B, to make easier the implementation step in its own code. Furthermore, it should be also noted that the original HLLC scheme can be simply retrieved by making straightforward modifications to certain variables within the routine.

Although the Liu-Vinokur form establishes a comprehensive formalism, particularly suitable for extending the framework analysis of Li-Gu [21], it does not provide a sufficient expression to avoid a potential scattering of formulations of corrections. Indeed, without a special attention paid to the matrix form in formulating a possible correction, an approximated and inexact characterization of the correction could be achieved by only considering the Liu-Vinokur form, resulting in deviations in the transposition of corrections. This is primary related to the fact that terms are mixed up between the two formulations, as for instance observed with the three last terms in (5.29) that are partially derived from the common matrix $\boldsymbol{\mathcal{M}_c}$. It can be seen here, by a direct comparison with the HLLC-Rossow scheme, that the Liu-Vinokur form does not provide a sufficient expression in accordance with definition 5.3.1.
Further research work could prove beneficial in reinterpreting the definition 5.3.1 and the property 5.2.1 for the Liu-Vinokur form, thereby avoiding the need for this preliminary identification step with the matrix form.

5.6 . Perspectives: the approximate Riemann problem for the HLLC method

In this section, we examine whether the HLLC scheme can be actually interpreted as a method that implicitly builds an approximate Riemann problem, similarly to the Roe scheme

$$\begin{cases} \partial_t \boldsymbol{w} + \boldsymbol{A^{HLLC}}(\boldsymbol{w_l}, \boldsymbol{w_r}, \boldsymbol{n})\, \partial_\xi \boldsymbol{w} = \boldsymbol{0} \\ \boldsymbol{w}(0,\xi) = \begin{cases} \boldsymbol{w_l} & \text{If } \xi < 0 \\ \boldsymbol{w_r} & \text{If } \xi > 0 \end{cases} \end{cases},$$

where $\boldsymbol{A^{HLLC}}$ is related to a discrete approximation of the Jacobian matrix, also satisfying the jump conditions

$$\Delta \boldsymbol{f}(\boldsymbol{w}, \boldsymbol{n}) = \boldsymbol{A^{HLLC}}(\boldsymbol{w_l}, \boldsymbol{w_r}, \boldsymbol{n}) \Delta \boldsymbol{w}.$$

In the following, we shall present some additional investigations carried out during this Ph-D program, offering some insights into the existence and definition of $\boldsymbol{A^{HLLC}}$ and, finally, into the viscosity matrix of the HLLC scheme. Nevertheless, the approach and results presented in this section are open to further investigations, as the requisite algebra remains somewhat opaque and therefore enigmatic. In light of this situation, we refrain from providing a definitive answer, but instead, demonstrate tendencies that may guide further research.

5.6.1 . The direct inversion of the right eigenvectors R

A standard approach for deriving the expressions of these two matrices would be to follow the theory of linear hyperbolic systems with constant coefficients, as previously discussed in section 2.2 for the Roe scheme. This approach relies on determining the invert matrix of the right eigenvectors $\boldsymbol{R}$, assuming that the vectors $(\boldsymbol{r_k})_k$ for the HLLC scheme form a basis. Indeed, as observed in the case of the Roe scheme, the approximate Jacobian matrix can be readily identified through the jump conditions using the spectral properties of the matrix, as indicated next

$$\Delta \boldsymbol{f}(\boldsymbol{w}, \boldsymbol{n}) = \boldsymbol{A^{Roe}}(\tilde{\boldsymbol{w}}, \boldsymbol{n}) \Delta \boldsymbol{w} = \left[\tilde{\boldsymbol{R}}\ \mathbf{diag}\ (\tilde{\lambda}_k) \tilde{\boldsymbol{L}} \right] \Delta \boldsymbol{w} = \sum_{k=1}^{4} \tilde{\alpha}_k \tilde{\lambda}_k \tilde{\boldsymbol{r}}_{\boldsymbol{k}} \quad \text{with} \quad \Delta \boldsymbol{w} = \tilde{\boldsymbol{R}} \tilde{\boldsymbol{\alpha}} \quad \text{and} \quad \tilde{\boldsymbol{L}} \tilde{\boldsymbol{R}} = \tilde{\boldsymbol{R}} \tilde{\boldsymbol{L}} = \boldsymbol{I_4},$$

whereas, for the HLLC scheme, this chapter has previously outlined in section 5.2 expressions aimed at decomposing the jump conditions, according to

$$\Delta \boldsymbol{f}(\boldsymbol{w}, \boldsymbol{n}) = S_1 \Delta \boldsymbol{w_1} + S_2 \Delta \boldsymbol{w_2} + S_4 \Delta \boldsymbol{w_3} = \sum_{k=1}^{4} \alpha_k S_k \boldsymbol{r_k} \quad \text{with} \quad \Delta \boldsymbol{w} = \boldsymbol{R} \boldsymbol{\alpha}.$$

However, this approach was found inefficient when applied to the HLLC scheme, due to significant constraints arising from complex algebraic expressions, leading to overly tedious calculations and results that are not readily manipulable. These difficulties are typically encountered even for the one-dimensional case, where inverting the matrix $\boldsymbol{R}(\boldsymbol{w_l}, \boldsymbol{w_r}, \boldsymbol{n})$ is not a trivial task, also when symbolic calculus is employed such as Mathematica or Maple. The true challenge should be understood as stemming from the parameters employed in evaluating the right eigenvectors. These vectors for the Roe and HLLC schemes are reminded below

$$\textbf{\textit{(Roe)}} \quad \tilde{\boldsymbol{r}}_{\mathbf{1}} = \begin{pmatrix} 1 \\ \tilde{u} - \tilde{c} n_x \\ \tilde{v} - \tilde{c} n_y \\ \tilde{H} - \tilde{c}\tilde{\mathcal{U}}_n \end{pmatrix} \qquad \tilde{\boldsymbol{r}}_{\mathbf{2}} = \begin{pmatrix} 1 \\ \tilde{u} \\ \tilde{v} \\ \frac{|\tilde{\mathcal{U}}|^2}{2} \end{pmatrix} \qquad \tilde{\boldsymbol{r}}_{\mathbf{3}} = \begin{pmatrix} 0 \\ -n_y \\ n_x \\ \tilde{\mathcal{U}}_t \end{pmatrix} \qquad \tilde{\boldsymbol{r}}_{\mathbf{4}} = \begin{pmatrix} 1 \\ \tilde{u} + \tilde{c} n_x \\ \tilde{v} + \tilde{c} n_y \\ \tilde{H} + \tilde{c}\tilde{\mathcal{U}}_n \end{pmatrix}$$

$$\textbf{\textit{(HLLC)}} \quad \boldsymbol{r}_{\mathbf{1}} = \begin{pmatrix} 1 \\ u_l - \hat{c}_l n_x \\ v_l - \hat{c}_l n_y \\ H_l - \hat{c}_l S_* \end{pmatrix} \qquad \boldsymbol{r}_{\mathbf{2}} = \begin{pmatrix} \Delta\rho^* \\ \Delta\rho^* \, \overline{u^*} \\ \Delta\rho^* \, \overline{v^*} \\ \Delta E_n^* \end{pmatrix} \qquad \boldsymbol{r}_{\mathbf{3}} = \begin{pmatrix} 0 \\ -n_y \\ n_x \\ \overline{\mathcal{U}_t} \end{pmatrix} \qquad \boldsymbol{r}_{\mathbf{4}} = \begin{pmatrix} 1 \\ u_r + \hat{c}_r n_x \\ v_r + \hat{c}_r n_y \\ H_r + \hat{c}_r S_* \end{pmatrix} \tag{5.31}$$

and where the quantity ΔE_n^* in the last component of the vector $\boldsymbol{r_2}$ was defined as follows

$$\Delta E_n^* = (\rho_r^* h_r - \rho_l^* h_l) + \Delta\rho^* \left[\left(\frac{\langle u^2 \rangle}{4} + \frac{\langle S_*^2 \rangle}{4} \right) + \left(\frac{\langle v^2 \rangle}{4} + \frac{\langle S_*^2 \rangle}{4} \right) - S_* \overline{\mathcal{U}}_n \right] + \overline{\rho^*} \left(\Delta\mathcal{U}_n \left(\overline{\mathcal{U}}_n - S_* \right) \right) - \Delta p \quad .$$

Once the expressions have been adapted for the one-dimensional case (i.e. for the case $d = 1$), this provides a typical example of a 3x3 matrix that presents a significant challenge to be inverted, even for a symbolic computation software. This is due to the fact that, the manipulations of contributions originating from the left and right states ($\boldsymbol{w_l}$, $\boldsymbol{w_r}$) cannot be readily combined, resulting in gradients that must be then handled with care. In contrast, similar manipulations on the matrix $\tilde{\boldsymbol{R}}(\tilde{\boldsymbol{w}})$ for the Roe scheme do not yield gradient terms, as the eigenvectors are evaluated using a common average state $\tilde{\boldsymbol{w}}$. Furthermore, a second difficulty arises from a choice made in section 5.2, regarding the definition of the second wave $\boldsymbol{\mathcal{W}_2} = \alpha_2 \boldsymbol{r_2} = \boldsymbol{r_2}$, which is subject to question. Indeed, as observed in the above expressions, a better matching between the two schemes could be achieved by reformulating the definition of the second wave as follows

$$\alpha_2 = \Delta\rho^* \qquad \text{and} \qquad \boldsymbol{r_2} = \begin{pmatrix} \frac{1}{\overline{u^*}} \\ \overline{v^*} \\ \frac{1}{\Delta\rho^*} \Delta E_n^* \end{pmatrix}, \tag{5.32}$$

in which, the coordinates α_2 can be also equivalently expressed as

$$\Delta\rho^* = \Delta\rho + \frac{1}{\langle \rho\hat{c} \rangle} \left[\left(\frac{\rho_r \hat{c}_r \rho_l^*}{\hat{c}_l} - \frac{\rho_l \hat{c}_l \rho_r^*}{\hat{c}_r} \right) \Delta\mathcal{U}_n - \left(\frac{\rho_r^*}{\hat{c}_r} + \frac{\rho_l^*}{\hat{c}_l} \right) \Delta p \right] \quad \text{while} \quad \tilde{\alpha}_2 = \Delta\rho - \frac{\Delta p}{\tilde{c}^2},$$

highlighting therefore significant similarities, except in the last component of the vector $\boldsymbol{r_2}$ (energy equation). Nevertheless, these definitions result in a singular expression for the dissipation vector $\boldsymbol{d^{HLLC}}$, occurring for instance in the case of a continuous initial conditions (i.e. $\boldsymbol{w_l} = \boldsymbol{w_r}$). In the absence of further investigation into a crucial factorization for the coefficient ΔE_n^*, provided it exists, these expressions are not suitable for the general case, and should not be considered. Consequently, the original definitions, as formulated in section 5.2, are retained in the following, with particularly $\alpha_2 = 1$.

5.6.2 . Using the similarities as a cornerstone for deriving the matrix L

For these reasons, instead of directly attempting to invert the matrix $\boldsymbol{R}$ for deriving the approximate Jacobian matrix $\boldsymbol{A^{HLLC}}(\boldsymbol{w_l}, \boldsymbol{w_r}, \boldsymbol{n})$, an alternative approach is proposed to circumvent this challenging step. In the following, the matrix $\boldsymbol{L}$ is extracted from the vector of coordinates $\boldsymbol{\alpha}$ by preserving the key relations outlined by the theory of linear hyperbolic systems with constant coefficients. This is especially achieved using the similarities as a valuable cornerstone for the formulation of the left eigenvectors $\boldsymbol{l_k}$, as indicated below. Indeed, since notable similarities have been observed in the first, third and fourth waves $(\boldsymbol{\mathcal{W}_k})_{k=1,3,4} = (\alpha_k \boldsymbol{r_k})_{k=1,3,4}$, we shall investigate their existence also in the definitions of the left eigenvectors $(\boldsymbol{l_k}, \tilde{\boldsymbol{l}}_{\boldsymbol{k}})_{k=1,3,4}$. Therefore, by specifically performing slight adjustments into the original expressions of $(\tilde{\boldsymbol{l}}_{\boldsymbol{k}})_{k=1,3,4}$, as those previously observed in the definitions of the coordinates $(\alpha_k)_k$ for instance, the matrix $\boldsymbol{L}$ is deduced from the matrix-vector product

$$\boldsymbol{L}\Delta\boldsymbol{w} = \boldsymbol{\alpha} \quad \Longleftrightarrow \quad \boldsymbol{l_k}\Delta\boldsymbol{w} = \alpha_k \quad \text{for} \quad k \in \{1,2,3,4\}, \tag{5.33}$$

The requisite algebraic investigations entail a sequence of elementary operations, which once performed, leads to the following definitions for the three common fields

(Roe)	**(HLLC)**
$\tilde{\boldsymbol{l}}_{\boldsymbol{1}} = \begin{pmatrix} \frac{\tilde{\mathcal{U}}_n}{2\tilde{c}} + \frac{\gamma-1}{4}\frac{\lvert\tilde{\mathcal{U}}\rvert^2}{\tilde{c}^2} \\ -\frac{\boldsymbol{n}}{2\tilde{c}} - \frac{\gamma-1}{2}\frac{\tilde{\boldsymbol{\mathcal{U}}}}{\tilde{c}^2} \\ \frac{\gamma-1}{2\tilde{c}^2} \end{pmatrix}^t$	$\boldsymbol{l_1} = \frac{\rho_l^*}{\hat{c}_l\langle\rho\hat{c}\rangle} \begin{pmatrix} \hat{c}_r\,\mathcal{U}_{n_l} + \frac{\gamma-1}{2}\boldsymbol{\mathcal{U}_l}\cdot\boldsymbol{\mathcal{U}_r} \\ -\hat{c}_r\boldsymbol{n} - (\gamma-1)\,\overline{\boldsymbol{\mathcal{U}}} \\ \gamma-1 \end{pmatrix}^t$
$\tilde{\boldsymbol{l}}_{\boldsymbol{2}} = \begin{pmatrix} 1 - \frac{\gamma-1}{2}\frac{\lvert\tilde{\mathcal{U}}\rvert^2}{\tilde{c}^2} \\ (\gamma-1)\frac{\tilde{\boldsymbol{\mathcal{U}}}}{\tilde{c}^2} \\ -\frac{\gamma-1}{\tilde{c}^2} \end{pmatrix}^t$	$\boldsymbol{l_2} = \begin{pmatrix} 1 - \frac{1}{\langle\rho\hat{c}\rangle}\Big[\frac{\gamma-1}{2}(\frac{\rho_l^*}{\hat{c}_l} + \frac{\rho_r^*}{\hat{c}_r})\boldsymbol{\mathcal{U}_l}\cdot\boldsymbol{\mathcal{U}_r} + (\frac{\rho_l^*\hat{c}_r\mathcal{U}_{n_l}}{\hat{c}_l} - \frac{\rho_r^*\hat{c}_l\mathcal{U}_{n_r}}{\hat{c}_r})\Big] \\ \frac{1}{\langle\rho\hat{c}\rangle}\Big[(\gamma-1)(\frac{\rho_l^*}{\hat{c}_l} + \frac{\rho_r^*}{\hat{c}_r})\overline{\boldsymbol{\mathcal{U}}} - \boldsymbol{n}(\frac{\rho_r^*\hat{c}_l}{\hat{c}_r} - \frac{\rho_l^*\hat{c}_r}{\hat{c}_l})\Big] \\ -\frac{1}{\langle\rho\hat{c}\rangle}(\gamma-1)(\frac{\rho_l^*}{\hat{c}_l} + \frac{\rho_r^*}{\hat{c}_r}) \end{pmatrix}^t$
$\tilde{\boldsymbol{l}}_{\boldsymbol{3}} = \begin{pmatrix} -\tilde{\mathcal{U}}_t \\ \boldsymbol{t} \\ 0 \end{pmatrix}^t$	$\boldsymbol{l_3} = \frac{\overline{\rho^*}}{\overline{\rho}} \begin{pmatrix} -\overline{\mathcal{U}_t} \\ \boldsymbol{t} \\ 0 \end{pmatrix}^t$
$\tilde{\boldsymbol{l}}_{\boldsymbol{4}} = \begin{pmatrix} -\frac{\tilde{\mathcal{U}}_n}{2\tilde{c}} + \frac{\gamma-1}{4}\frac{\lvert\tilde{\mathcal{U}}\rvert^2}{\tilde{c}^2} \\ \frac{\boldsymbol{n}}{2\tilde{c}} - \frac{\gamma-1}{2}\frac{\tilde{\boldsymbol{\mathcal{U}}}}{\tilde{c}^2} \\ \frac{\gamma-1}{2\tilde{c}^2} \end{pmatrix}^t$	$\boldsymbol{l_4} = \frac{\rho_r^*}{\hat{c}_r\langle\rho\hat{c}\rangle} \begin{pmatrix} -\hat{c}_l\,\mathcal{U}_{n_r} + \frac{\gamma-1}{2}\boldsymbol{\mathcal{U}_l}\cdot\boldsymbol{\mathcal{U}_r} \\ \hat{c}_l\boldsymbol{n} - (\gamma-1)\,\overline{\boldsymbol{\mathcal{U}}} \\ \gamma-1 \end{pmatrix}^t$

(5.34)

In the above expression, the second left eigenvector $\boldsymbol{l_2}$ has been derived through a simple manipulation, detailed below. By looking at the decomposition of the density jump into a sum of waves, it can be observed that

$$\begin{aligned} \Delta\rho = &\quad \alpha_1(\boldsymbol{r_1})_1 &+ &\quad \alpha_2(\boldsymbol{r_2})_1 &+ &\quad \alpha_4(\boldsymbol{r_4})_1 \\ \Delta\rho = &\quad \alpha_1 &+ &\quad \alpha_2\,\Delta\rho_* &+ &\quad \alpha_4 \\ \boldsymbol{e_1}^t\Delta\boldsymbol{w} = &\Big[\quad \boldsymbol{l_1} &+ &\quad \Delta\rho_*\,\boldsymbol{l_2} &+ &\quad \boldsymbol{l_4} \quad\Big]\Delta\boldsymbol{w} \end{aligned},$$

where $\boldsymbol{e_1}$ denotes the first vector of the canonical basis of $\mathbb{R}^4$. Since the first and fourth vectors are now determined, the expression simplifies and after rearranging terms, we get

$$\Delta\rho_*\,\boldsymbol{l_2} = \boldsymbol{e_1}^t - \boldsymbol{l_1} - \boldsymbol{l_4}, \tag{5.35}$$

It should be noted that, in (5.34), the definition of the second vector $\boldsymbol{l_2}$ corresponds to the above expression (5.35). Consequently, all of these vectors $(\boldsymbol{l_k})_k$ written in (5.34) for the HLLC scheme, satisfy the following conditions

$$\boldsymbol{l_1}\Delta\boldsymbol{w} = \alpha_1 \qquad \boldsymbol{l_2}\Delta\boldsymbol{w} = \Delta\rho^* \qquad \boldsymbol{l_3}\Delta\boldsymbol{w} = \alpha_3 \qquad \boldsymbol{l_4}\Delta\boldsymbol{w} = \alpha_4,$$

in which, all the definitions of the coordinates $\boldsymbol{\alpha} = (\alpha_k)_k$ show globally similarities with the Roe scheme, except the second field, since

$$\alpha_1 = \frac{\rho_l^*}{\langle\rho\hat{c}\rangle}\left[\frac{\Delta p - \rho_r\hat{c}_r\Delta\mathcal{U}_n}{\hat{c}_l}\right] \qquad \alpha_2 = 1 \qquad \alpha_3 = \overline{\rho^*}\Delta\mathcal{U}_t \qquad \alpha_4 = \frac{\rho_r^*}{\langle\rho\hat{c}\rangle}\left[\frac{\Delta p + \rho_l\hat{c}_l\Delta\mathcal{U}_n}{\hat{c}_r}\right].$$

This discrepancy is a direct consequence of the choice made in (5.31) for preventing a singular definition for the vector $\boldsymbol{r_2}$. Consequently, a singularity is unavoidably produced, either in the definition of the vector $\boldsymbol{r_2}$, as illustrated in (5.32), or in the definition of the second left eigenvector $\boldsymbol{l_2}$ due to the setting of $\alpha_2 = 1$, as this implies

$$\boldsymbol{l_2} = \frac{1}{\Delta\rho^*}\Big[\boldsymbol{e_1} - \boldsymbol{l_1} - \boldsymbol{l_4}\Big].$$

In the following, we shall assume that the two initial states $(\boldsymbol{w_l},\ \boldsymbol{w_r})$ are distinct (i.e. $\boldsymbol{w_l} \neq \boldsymbol{w_r}$). Then, it follows that the approximate Jacobian matrix $\boldsymbol{A^{HLLC}}(\boldsymbol{w_l}, \boldsymbol{w_r}, \boldsymbol{n})$ is identified through the decomposition of the jump conditions, as indicated next

$$\Delta\boldsymbol{f}(\boldsymbol{w},\boldsymbol{n}) = \sum_{k=1}^{3} S_k\Delta_k\boldsymbol{w} = \sum_{k=1}^{d+2}\alpha_k S_k\boldsymbol{r_k} = \sum_{k=1}^{d+2}\big(\boldsymbol{R}\ \mathbf{diag}\ (S_k)\big)_k\,[\,(\boldsymbol{L}\ \Delta\boldsymbol{w})_k\,] = \underbrace{\Big[\boldsymbol{R}\ \mathbf{diag}(S_k)\ \boldsymbol{L}\Big]}_{\boldsymbol{A^{HLLC}}(\boldsymbol{w_l},\boldsymbol{w_r},\boldsymbol{n})}\ \Delta\boldsymbol{w}. \quad (5.36)$$

Actually, an identical manipulation can be also performed for the vector dissipation

$$\boldsymbol{d^{HLLC}} = \sum_{k=1}^{3}|S_k|\Delta_k\boldsymbol{w} = \sum_{k=1}^{d+2}\alpha_k|S_k|\boldsymbol{r_k} = \sum_{k=1}^{d+2}\big(\boldsymbol{R}\ \mathbf{diag}\ (|S_k|)\big)_k\,[\,(\boldsymbol{L}\ \Delta\boldsymbol{w})_k\,] = \underbrace{\Big[\boldsymbol{R}\ \mathbf{diag}(|S_k|)\ \boldsymbol{L}\Big]}_{\boldsymbol{D^{HLLC}}(\boldsymbol{w_l},\boldsymbol{w_r},\boldsymbol{n})}\ \Delta\boldsymbol{w}. \quad (5.37)$$

Nevertheless, while explicit formulas are now obtained in the case of distinct $(\boldsymbol{w_l}, \boldsymbol{w_r})$, this approach also demonstrates that matrix $\boldsymbol{L}$ is not identified as the invert of $\boldsymbol{R}$ since

$$\boldsymbol{LR} \neq \boldsymbol{I_4},$$

although the matrix $\boldsymbol{L}$ has been built in order to maintain the decomposition of the jumps of conservative variables, and satisfies the following condition

$$\Delta\boldsymbol{w} = \boldsymbol{R\alpha} = \boldsymbol{RL}\Delta\boldsymbol{w}.$$

Additionally, it can be demonstrated that the left and right vectors are not orthogonal, as for instance

$$\boldsymbol{l_1 r_4} = \frac{\rho_l^*}{\langle\rho\hat{c}\rangle}\Big[-(\gamma-1)(\bar{\mathcal{U}}_n - S_*) - \hat{c}\Delta\mathcal{U}_n\Big] \qquad \boldsymbol{l_4 r_1} \neq 0 \qquad \text{and} \qquad \boldsymbol{l_3 r_k} = 0 \text{ for } k = 1, 2, 4,$$

and moreover, these vectors are also not normalized

$$\boldsymbol{l_1 r_1} = \frac{\rho_l^*}{\langle\rho\hat{c}\rangle}\Big[(\gamma-1)(\bar{\mathcal{U}}_n - S_*) - \Delta\hat{c}\Big] \qquad \text{and} \qquad \boldsymbol{l_3 r_3} = \frac{\overline{\rho^*}}{\overline{\rho}}.$$

Introducing a normalization of these vectors $\boldsymbol{l_k}$ implies to also modify the coordinates α_k, as indicated next for the third vector

$$\boldsymbol{l_3} = \frac{\overline{\rho}}{\overline{\rho^*}}\begin{pmatrix} -\overline{\mathcal{U}_t} \\ \boldsymbol{t} \\ 0 \end{pmatrix}^t \qquad \alpha_3 = \overline{\rho}\,\Delta\mathcal{U}_t$$

However, for others vectors, such as $\boldsymbol{l_1}$, the similar process leads to derive a new singular expression in the case of $\boldsymbol{w_l} = \boldsymbol{w_r}$ as the two gradient terms vanish in such case

$$S_*(\boldsymbol{w}, \boldsymbol{w}, \boldsymbol{n}) = \frac{\langle \rho \mathcal{U}_n \hat{c} \rangle - \Delta p}{\langle \rho \hat{c} \rangle} = \mathcal{U}_n.$$

Finally, although the expressions of the approximate Jacobian matrix and the artificial viscosity matrix have been derived (5.36 - 5.37), and clearly exhibits strong similarities with the expression of the Roe scheme, it can be observed that these expressions do not match the usual definitions for a linear hyperbolic system with constant coefficients.

Conclusion and perspectives

Concluding remarks

The Ph-D work has primarily focused on the formulation of low-Mach number corrections for the Roe and HLLC finite volume schemes, with the aim of enhancing these two numerical methods for simulating compressible flows in various regimes from low Mach number to transonic flows. The purpose was to demonstrate that the formulation of these numerical methods can be modified and generalized without compromising performance in the compressible regime, while preserving the overall accuracy of the compressible discrete solutions for nearly incompressible flows. The objective of this thesis was twofold: first, to contribute to the numerical analysis of these methods, by providing new insights into the formulation of numerically stable low Mach number corrections; second, to propose a robust and efficient correction for these schemes.

In this context, we developed a methodology based on an in-depth examination of the various rescaling approaches proposed in the literature, with a particular focus on the Roe scheme. The review of existing approaches in the literature, along with their analysis using various techniques, provides a critical overview of this challenging research topic, as mainly discussed in the first part of this thesis. Despite decades of active research, this topic remains partially open to further investigation, with some aspects still requiring additional inquiry nowadays. One of the underlying difficulties lies in the simultaneous presence of two acoustic and incompressible time scales, characterizing compressible solutions in the low Mach number limit. The inherent challenges rely in the formulation of a modified matrix-valued dissipation that enables the discrete solution to accurately approximate the solution in the two time scale limits, while circumventing the introduction of side issues such as checkerboard mode problems.

By focusing on the modifications of the dissipation vector of the Roe scheme in the general case (i.e. without considering the mesh or element types), chapter 2 has revealed that there are two distinct approaches to address the accuracy problem in the low Mach number limit. These two approaches are highlighted in this thesis with the Rieper's fix and Rossow's artificial speed of sound approach, which either asymptotically centers the first order pressure gradient in the equations, or in contrast, avoids asymptotically centering the pressure gradients. Both highlight distinct advantages and different drawbacks in the general case.
As demonstrated in the last section of the second chapter, the development of another third approach, which is based on asymptotically centering the leading and first order pressure gradients, turns out insufficiently robust and therefore ineffective, as it introduces more significant side issues compared to the two others. It has been shown that this correction yields excessively large spurious entropy levels at stagnation points, leading to severely deteriorate the overall accuracy of the discrete solution. Moreover, the asymptotic analysis of the third approach highlights common features with the Rossow's correction, indicating that this type of corrections is also subject to similar inconsistencies in the acoustic time scale limit. One could consider these investigations on a third approach as evidence that it is hardly possible to do better than the two approaches already found in the literature.

In chapter 3, we carried out the asymptotic analysis for the modified Roe scheme according to the artificial speed of sound approach of Rossow and we conducted a detailed analysis of this correction.

It is proved that the discrete solutions are characterized by the correct 2nd order of the pressure disturbances in space at the incompressible time scale, and also do not enforce the discrete divergence free constraint of the leading-order velocity. We also demonstrated that the Rossow correction is not prone to spurious pressure checkerboard mode problems. The scheme remains accurate even on highly stretched mesh, in opposition to the Rieper's fix.
Moreover, we show that the von Neumann stability analysis of this scheme results in a more stringent stability condition in the low Mach number limit than initially predicted by Rossow, this correction behaves as the Roe-Turkel scheme. Thus, the time step is constrained to be exceedingly small in the low Mach number limit, which makes it penalized for some CFD applications.
In order to circumvent the stiffness of the stability constraint, a robust and stable numerical approach is presented, based on an implicit time marching with a linearized backward Euler scheme. The key aspects of this approach are Algorithmic Differentiation, fast LU decomposition libraries, a novel numerical stability condition, and the formulation of a pseudo continuation method in a quasi-Newton method. This leads to the development of very stable implicit schemes that allow the use of large CFL numbers, and which remarkably require only a few hundreds of iterations to obtain a quadratic convergence to the steady-state solutions, even for very low-Mach number flows up to 10^{-6}.
This work also addresses the incompressible-acoustic interactions characterizing the compressible discrete solutions in the incompressible limit. We show that the discrete solutions have persistent acoustic disturbances in the low speed limit, even for the steady-state problem, characterized by acoustic pulses generated at very short times, and dissipated at larger times. We found that the intensity of these acoustic disturbances is related to the modification of the jumps of the normal velocity component at the cell interface.

The second part of this thesis was devoted to the HLLC scheme. The in-depth examination of the existing approaches highlights numerous similarities between the corrections applied to the HLLC and Roe schemes. In order to generalize the analysis conducted in the first part regarding the Roe scheme to the HLLC scheme, we propose a pursuit of the analysis carried out by Pelanti focusing on the similarities between the two wave structures of both Riemann solvers. This investigation has resulted in the formulation of a common formalism aimed at analyzing and simplifying the derivation of corrections applied to the two dissipation vectors. Indeed, we established a novel form for the dissipation vector associated with the HLLC scheme that could be readily interpreted as a generalization of the Liu-Vinokur form for the Roe scheme, also known in the literature as the Weiss-Smith decomposition, to the HLLC scheme.
As an application, two approaches were proposed for deriving "identical" low Mach corrections for these two schemes. These approaches are characterized by considering the similarities between the two schemes as a valuable cornerstone for transposing a correction from a the dissipation vector of one method to the other.
In particular, this has notably resulted in the generalization of the artificial speed of sound approach of Rossow to the HLLC scheme, denoted as the HLLC-Rossow scheme. It is shown by numerical evidence that this HLLC-Rossow scheme recovers exactly the same discrete properties as the Roe-Rossow scheme. Accurate discrete solutions are obtained in the low-Mach number limit, and the scheme does not undergo the pressure checkerboard mode problems that could be frequently observed for other corrections. Even by considering a highly stretched mesh, we could not manage to trigger this numerical issue, thereby proving a robust behavior of the proposed scheme.

Perspectives

In light of the results presented above, several limitations and perspectives for further investigation were identified and are now discussed.
First, the numerical approach developed in this work is crucial component in this thesis, as it has significantly allowed investigations by simplifying the acquisition of results with the use exact implicit stage. Nevertheless, this approach is limited to a certain mesh density since direct solvers become prohibitively expensive in terms of memory as the number of cells increases. A first perspective would be to reproduce this approach by considering iterative solvers such as a GMRES solver. Doing so would be valuable to evaluate the difficulties that arise from these ill-conditioned problems, particularly in regard to the need for an accurate resolution of the system to solve the very stiff linear system obtained in the low Mach number limit.
Second, this work mainly focused on the formulation of corrections of the dissipation vector regarding the incompressible time-scale. Nevertheless, it corresponds only to one side of the accuracy problem encountered in low Mach number flows. The acoustics limit cannot be ruled out in the formulation of low Mach number corrections. Nowadays, to the best of our knowledge, the definition of a correction that resolve the accuracy problems in the two asymptotic limits remains an important inquiry of the literature, which requires further investigations. This is related to the fact that, on one hand the first approach turns out effective but suffers from severe pressure checkerboard mode problems, while on the other hand, the second approach leads to inconsistencies in the acoustic limit, while avoiding this pressure-velocity decoupling problem. Then, we could suggest that these two significant issues cannot be easily circumvented, either the pressure checkerboard modes problems or the inconsistencies in the acoustic limit has to be faced and resolved to obtain a compressible scheme remaining accurate in the general case, such as unsteady low Mach number flows.
Third, the common formalism introduced for the HLLC and Roe schemes is open to further investigations for an in-depth examination. The interest lies in the derivation of modified numerical dissipation vectors, and in the investigation of a common asymptotic analysis between the two approximate Riemann solvers. In chapter 5, numerical evidence show that the correction applied to the Roe or HLLC schemes exhibits exactly the same behavior regarding the stability condition, the accuracy of the discrete solution but also the pressure checkerboard mode problem. Although not illustrated in this thesis, it can be pointed out here for further investigations that the inconsistencies in the acoustic limit have also been observed numerically for the HLLC-Rossow scheme. It should also be noted that, identical similar tendencies are also observed by Pelanti, who extended the correction of the Roe-Turkel scheme to the HLLC scheme, since the differences between the two discrete solutions are hardly visible. The answer to all these behaviors can be found in the asymptotic analysis, and a few elements are provided below as interesting leads for further investigations. In opposition to the standard approach applied to the Roe scheme, the asymptotic analysis for the HLLC is lengthy and requires to make a series of choices in the dimensional analysis, as previously discussed in section 4.2.4, with for instance the definition of S_*. Moreover, this requires to performed several Taylor expansions for simplifying expressions. However, a key insight could be easily deduced from the decomposition of the matrix $\boldsymbol{\mathcal{M}}^{\boldsymbol{HLLC}}$ into a common and a deviation matrices ($\boldsymbol{\mathcal{M}}_c$, $\boldsymbol{\mathcal{M}}_d$). This highlights that in the dissipation vector associated with the HLLC scheme, there exists a part which is common and readily related to terms present in the dissipation vector of the Roe scheme, plus some additional terms. The missing details describing the role of these additional terms would be a valuable information for a unified formalism, that are worthy of further research.
Fourth, it would be beneficial to also examine potential close connections with other existing works for the purpose of extending the analysis. For example, the AUSM-like expression of HLLC scheme proposed by Kitamura-Shima in [30], or the JST scheme, which are both schemes commonly used for industrial flows.

To conclude, the formulation of a low Mach correction for the Roe or HLLC schemes remains an active subject that remains open to further research. Nevertheless, it should be investigated simultaneously for avoiding the scattering of the formulations, with a direct attention paid to limiting the introduction of side issues.

A - Fortran source code of $\mathcal{F}^{HLLC-Rossow}$ under the matrix form

```
! ================================================================================
  SUBROUTINE FLUX_HLLC_ROSSOW_Einfeldt_full_dissip(W_L,W_R,P_L,P_R,T_L,T_R,xn1,xn2,gamma,num_flux)
! ================================================================================
  IMPLICIT NONE

  REAL*8, DIMENSION(4),INTENT(in)       :: W_L,W_R,P_L,P_R        !Conservative + Primitive variables
  REAL*8, DIMENSION(3),INTENT(in)       :: T_L,T_R                ![p,H_L,c_L]
  REAL*8,              INTENT(in)       :: xn1,xn2,gamma
  REAL*8, DIMENSION(4),INTENT(inout)    :: num_flux

  REAL*8, DIMENSION(4)                  :: deltaVarW,deltaVarP,xlambda  ! xlambda <=> |S_k|
  REAL*8, DIMENSION(4)                  :: diss_vec,Flx_L,Flx_R

  REAL*8                                :: t1,t2                    !tangential component
  REAL*8                                :: UnL,UnR,UtL,UtR
  REAL*8                                :: DeltaUn

  REAL*8                                :: ro_sqrd_L,ro_sqrd_R
  REAL*8, DIMENSION(4)                  :: Q_L,Q_R,Avg_roe               !\sqrt{rho}[1 u v H] + Roe average[4]

  REAL*8                                :: rho_star_L,rho_star_R
  REAL*8                                :: u_star_l,u_star_r,v_star_l,v_star_r
  REAL*8                                :: rho_star_moy,u_star_moy,v_star_moy

  REAL*8                                :: H_L,H_R,c_L,c_R              !Total Enthalpy + speed of sound (for a better readability)
  REAL*8                                :: rho_moy,u_moy,v_moy,Un_moy,H_moy,p_moy


  REAL*8                                :: Norm_U2_L,M_L,Mn_L,tilde_c_L                      !Left side
  REAL*8                                :: Norm_U2_R,M_R,Mn_R,tilde_c_R                      !Right side
  REAL*8                                :: Norm_Avg_U2,Avg_M,Avg_Mn,tilde_Avg_c              !For Roe average
  REAL*8                                :: Avg_c,Avg_c2,Avg_Un
  REAL*8                                :: alpha, beta2                                      !Coefficients artificial speed of sound


  REAL*8                                :: lambda_m,lambda_mid,lambda_p                      ! S_k
  REAL*8                                :: hat_c_L,hat_c_R,left_arti_speed,right_arti_speed
  REAL*8                                :: dS_R,dS_L,d_absS_R,d_absS_L,dc_R,dc_L             ! Notations in chapter 4-5

  REAL*8                                :: rhoLrhoR,rhoc_sum,rhoc_arti_sum                   !Useful variables for Liu-Vinokur


        ! ---- For a better readability ----
          ! ---- Total Enthalpy and speed of sound ----
        H_L = T_L(2) ; c_L = T_L(3)
        H_R = T_R(2) ; c_R = T_R(3)

       ! ---- Euler's fluxes ----
        ! ---- Left Euler flux----
    Flx_L(1) =  W_L(2) * xn1                    +  W_L(3) * xn2
    Flx_L(2) = (W_L(2) * P_L(2) + P_L(4) )*xn1 + (W_L(2) * P_L(3))*xn2
    Flx_L(3) = (W_L(2) * P_L(3))*xn1            + (W_L(3) * P_L(3) + P_L(4))*xn2
    Flx_L(4) = (W_L(2) * H_L )*xn1           + (W_L(3) * H_L  )*xn2
        ! ---- Right Euler flux ----
    Flx_R(1) =  w_R(2) * xn1                    +  w_R(3) * xn2
    Flx_R(2) = (w_R(2) * P_R(2) + P_R(4) )*xn1 + (w_R(2) * P_R(3))*xn2
    Flx_R(3) = (w_R(2) * P_R(3))*xn1            + (w_R(3) * P_R(3) + P_R(4))*xn2
    Flx_R(4) = (w_R(2) * H_R )*xn1           + (w_R(3) * H_R)*xn2

      ! ---- Directionnal velocity ----
    UnL = P_L(2)*xn1 + P_L(3)*xn2
    UnR = P_R(2)*xn1 + P_R(3)*xn2

      ! ---- Tangeantial vector -----
    t1 = -xn2 ; t2 = xn1
    UtL    = P_L(2)*t1 + P_L(3)*t2
    UtR    = P_R(2)*t1 + P_R(3)*t2

      ! ---- Jump var ----
    deltaVarW(1:4) = W_R(1:4) - W_L(1:4) !ro  rou rov roe
    deltaVarP(1:4) = P_R(1:4) - P_L(1:4) !ro  u   v   ps
    deltaUn        = UnR - UnL

      ! ---- Moyenne de Roe ----
    ro_sqrd_L = SQRT(W_L(1)) ; ro_sqrd_R = SQRT(W_R(1))

    Q_L(:)    = (/ ro_sqrd_L, ro_sqrd_L*P_L(2), ro_sqrd_L*P_L(3), ro_sqrd_L*H_L /) !parameter vector
    Q_R(:)    = (/ ro_sqrd_R, ro_sqrd_R*P_R(2), ro_sqrd_R*P_R(3), ro_sqrd_R*H_R /)

    Avg_roe(1)=  Q_L(1)*Q_R(1)                                                  !\sqrt{rho}( 1 u v H)
    Avg_roe(2)=( Q_L(2)+Q_R(2) )/( Q_L(1)+Q_R(1) )
    Avg_roe(3)=( Q_L(3)+Q_R(3) )/( Q_L(1)+Q_R(1) )
    Avg_roe(4)=( Q_L(4)+Q_R(4) )/( Q_L(1)+Q_R(1) )

    ! ---- Compute Artificial speed of sound -----
       ! ---- Left state ----
    Norm_U2_L = P_L(2)*P_L(2) + P_L(3)*P_L(3)
    M_L       = sqrt(Norm_U2_L)/c_L
```

```
      Mn_L      = UnL/c_L

      beta2     = min(M_L*M_L,1.0_8) ! Without reference Mach number
      alpha     = 0.5*(1.-beta2)
      tilde_c_L = c_L*sqrt( Mn_L*Mn_L*alpha**2 + beta2 ) !artifical speed of sound

          ! ---- Interface state ----
      Norm_Avg_U2 = Avg_roe(2)*Avg_roe(2) + Avg_roe(3)*Avg_roe(3)
      Avg_c2      = (gamma-1)*(Avg_roe(4) - 0.5*(Norm_Avg_U2))
      Avg_c       = sqrt( Avg_c2 )
      Avg_Un      = Avg_roe(2)*xn1 + Avg_roe(3)*xn2

      Avg_M       = sqrt(Norm_Avg_U2)/Avg_c
      Avg_Mn      = Avg_Un/Avg_c

      beta2       = min(Avg_M*Avg_M,1.0_8) ! Without reference Mach number
      alpha       = 0.5*(1.-beta2)
      tilde_Avg_c = Avg_c*sqrt( Avg_Mn*Avg_Mn*alpha**2 + beta2) !artifical speed of sound

          ! ---- Right state ----
      Norm_U2_R = P_R(2)*P_R(2) + P_R(3)*P_R(3)
      M_R       = sqrt(Norm_U2_R)/c_R
      Mn_R      = UnR/c_R

      beta2        = min(M_R*M_R,1.0_8) ! Without reference Mach number
      alpha        = 0.5*(1.-beta2)
      tilde_c_R    = c_R*sqrt( Mn_R*Mn_R*alpha**2 + beta2) !artifical speed of sound

        ! ---- Generaziled speed of sounds ----
      hat_c_L          = max(c_L,Avg_c - Avg_Un + UnL)
      left_arti_speed  = max(tilde_c_L,tilde_Avg_c - Avg_Un + UnL)
      hat_c_R          = max(c_R,Avg_c + Avg_Un - UnR)
      right_arti_speed = max(tilde_c_R,tilde_Avg_c + Avg_Un - UnR)

        !---- Wave speed estimate -----
      lambda_m    = UnL - hat_c_L
        ! ---- Directionnal density is presered in star region ----
      lambda_mid = (W_L(1)*UnL*hat_c_L + W_R(1)*UnR*hat_c_R - deltaVarP(4))/(W_L(1)*hat_c_L + W_R(1)*hat_c_R)
      lambda_p    = UnR + hat_c_R

            ! ---- Eigenvalues ----
      xlambda(1) = abs(lambda_m)
      xlambda(2) = abs(lambda_mid)
      xlambda(3) = xlambda(2)
      xlambda(4) = abs(lambda_p)

             ! ---- delta coefficients ----
      dS_R     = lambda_p - lambda_mid
      dS_L     = lambda_m - lambda_mid
      d_absS_R = xlambda(4) - xlambda(2)
      d_absS_L = xlambda(1) - xlambda(2)
      dc_R     = lambda_p - UnR
      dc_L     = lambda_m - UnL

      ! ============================
      !      ---- Star Region ----
      ! ============================
          ! ---- Left interm State ----
      rho_star_L= W_L(1)*dc_L/dS_L
      u_star_l= lambda_mid*xn1 + UtL*t1
      v_star_l= lambda_mid*xn2 + UtL*t2

        ! ---- Right interm State ----
      rho_star_R= W_R(1)*dc_R/dS_R
      u_star_r= lambda_mid*xn1 + UtR*t1
      v_star_r= lambda_mid*xn2 + UtR*t2

      ! ============================
      !      ---- Mean Values ----
      ! ============================
      rho_moy      = 0.5*(P_L(1)+P_R(1))
      rho_star_moy = 0.5*(rho_star_L+rho_star_R)
      u_star_moy   = 0.5*(u_star_l+u_star_r)
      v_star_moy   = 0.5*(v_star_l+v_star_r)
      u_moy        = 0.5*(P_L(2)+P_R(2)) ! average
      v_moy        = 0.5*(P_L(3)+P_R(3)) ! average
      Un_moy       = xn1*u_moy + xn2*v_moy
      H_moy        = 0.5*(H_L + H_R)
      p_moy        = 0.5*(P_L(4)+P_R(4))


        ! ---- Useful variables ----
      rhoLrhoR     = (W_L(1)*W_R(1))
      rhoc_sum       = P_L(1)*hat_c_L + P_R(1)*hat_c_R
      rhoc_arti_sum  = P_L(1)*left_arti_speed + P_R(1)*right_arti_speed

  ! ================================== Return to the HLLC scheme if ==================================
                                     ! tilde_c_L         = c_L             !Left artifical speed of sound
                                     ! tilde_c_R         = c_R             !Right artifical speed of sound
                                     ! tilde_Avg_c       = Avg_c           !interface artifical speed of sound
                                     ! rhoc_arti_sum     = rhoc_sum
                                     ! left_arti_speed   = hat_c_L
                                     ! right_arti_speed  = hat_c_R
  ! ============================================================================================

    ! ---- Numerical dissipation ----

  diss_vec(1)=  deltaVarW(1)*xlambda(2)            & !End Delta rho
```

```
188             + deltaUn*(rhoLrhoR/rhoc_sum)*(      &
189                   (dc_R/dS_L)*d_absS_L           &
190                 - (dc_L/ds_R)*d_absS_R           &
191                                       )      & !Delta Un
192             + deltaVarP(4)*(1./rhoc_arti_sum)*(  &
193                 + (W_R(1)/dS_R)*d_absS_R         &
194                 - (W_L(1)/dS_L)*d_absS_L         &
195                                           )   !End Delta P
196
197   diss_vec(2)=                                                          &
198         deltaVarW(1)*xlambda(2)*u_star_moy                              & !End Delta Un
199       + deltaVarP(2)*xlambda(2)*rho_star_moy                            & !End Delta u
200       + deltaUn*( (rhoLrhoR/rhoc_sum)*(                                 &
201             (dc_R/dS_L)*(                                               &
202                   xlambda(1)*(P_L(2) - left_arti_speed*xn1)             &
203                         )                                               &
204           - (dc_L/dS_R)*(                                               &
205                   xlambda(4)*(P_R(2) + right_arti_speed*xn1)            &
206                         )                                               &
207           - xn1*rho_star_moy*xlambda(2)*rhoc_arti_sum/rhoLrhoR          &
208           + xlambda(2)*u_star_moy*(dc_L/dS_R - dc_R/dS_L )              &
209                                   )                                     &
210                 )                                                       & !End Delta Un
211       + deltaVarP(4)*(                                                  &
212             (1./rhoc_arti_sum)*(                                        &
213                 (W_R(1)/dS_R)*(P_R(2)*xlambda(4) - u_star_moy*xlambda(2)) &
214               - (W_L(1)/dS_L)*(P_L(2)*xlambda(1) - u_star_moy*xlambda(2)) &
215                                 )                                       &
216           + (xn1/rhoc_sum)*(                                            &
217                 (W_L(1)/dS_L)*hat_c_L*xlambda(1)                        &
218               + (W_R(1)/dS_R)*hat_c_R*xlambda(4)                        &
219                         )                                               &
220                     )                                                     !End Delta P
221
222
223   diss_vec(3)=                                                          &
224         deltaVarW(1)*xlambda(2)*v_star_moy                              & !End Delta rho
225       + deltaVarP(3)*xlambda(2)*rho_star_moy                            & !End Delta v
226       + deltaUn*( (rhoLrhoR/rhoc_sum)*(                                 &
227             (dc_R/dS_L)*(                                               &
228                   xlambda(1)*(P_L(3) - left_arti_speed*xn2)             &
229                         )                                               &
230           - (dc_L/dS_R)*(                                               &
231                   xlambda(4)*(P_R(3) + right_arti_speed*xn2)            &
232                         )                                               &
233           - xn2*rho_star_moy*xlambda(2)*rhoc_arti_sum/rhoLrhoR          &
234           + xlambda(2)*v_star_moy*(dc_L/dS_R - dc_R/dS_L )              &
235                                   )                                     &
236                 )                                                       &  !End Delta Un
237       + deltaVarP(4)*(                                                  &
238             (1./rhoc_arti_sum)*(                                        &
239                 (W_R(1)/dS_R)*(P_R(3)*xlambda(4) - v_star_moy*xlambda(2)) & ! Ce terme peut se simplifier
240               - (W_L(1)/dS_L)*(P_L(3)*xlambda(1) - v_star_moy*xlambda(2)) &
241                                 )                                       &
242           + (xn2/rhoc_sum)*(                                            &
243                 (W_L(1)/dS_L)*hat_c_L*xlambda(1)                        &
244               + (W_R(1)/dS_R)*hat_c_R*xlambda(4)                        &
245                         )                                               &
246                     )                                                     !End Delta P
247
248   diss_vec(4)=                                                           &
249         deltaVarW(1)*(                                                   &
250           + xlambda(2)*(                                                 &
251                 H_moy                                                    &
252               - rho_star_moy*p_moy*gamma/(rhoLrhoR*(gamma-1))            &
253               + lambda_mid*(lambda_mid-Un_moy)                           &
254                       )                                                  &
255                 )                                                        & !End Delta rho
256       + deltaVarP(2)*rho_star_moy*u_moy*xlambda(2)                       & !End Delta u
257       + deltaVarP(3)*rho_star_moy*v_moy*xlambda(2)                       & !End Delta v
258       + deltaUn*(                                                        &
259           (rhoLrhoR/rhoc_sum)*(                                          &
260               (dc_R/dS_L)*(                                              &
261                     xlambda(1)*(H_L - left_arti_speed*lambda_mid)          &
262                           )                                              &
263             - (dc_l/dS_R)*(                                              &
264                     xlambda(4)*(H_R + right_arti_speed*lambda_mid)         &
265                           )                                              &
266             - rho_star_moy*lambda_mid*xlambda(2)*rhoc_arti_sum/rhoLrhoR   &
267             +(dc_l/dS_R - dc_R/dS_L)*(                                   &
268                     xlambda(2)*(lambda_mid*(lambda_mid-Un_moy) + H_moy )  &
269                                 )                                        &
270                           )                                              &
271               )                                                          & !End Delta Un
272       + deltaVarP(4)*(                                                   &
273             (1./rhoc_arti_sum)*(                                         &
274                     (W_R(1)/dS_R)*(                                      &
275                       H_R*xlambda(4) - H_moy*xlambda(2)                  &
276                                   )                                      &
277                   - (W_L(1)/dS_L)*(                                      &
278                       H_L*xlambda(1) - H_moy*xlambda(2)                  &
279                                   )                                      &
280                                 )                                        &
281             + (lambda_mid/rhoc_sum)*(                                    &
282                   (W_L(1)/dS_L)*hat_c_L*xlambda(1)                       &
283                 + (W_R(1)/dS_R)*hat_c_R*xlambda(4)                       &
284                                 )                                        &
285             + xlambda(2)*(                                               &
286                 -1 + (rho_star_moy*rho_moy*gamma)/(rhoLrhoR*(gamma-1))   &
```

```
287                     )                                                   &
288          + (xlambda(2)/rhoc_sum)*(                                      &
289                (W_L(1)/dS_L  - W_R(1)/dS_R)*(                           &
290                    lambda_mid*(lambda_mid-Un_moy)                       &
291                                        )                                &
292                                 )                                       &
293                     )                                                    !End Delta p
294
295       num_flux(1:4)=0.5*( Flx_R(1:4) + Flx_L(1:4) - diss_vec(1:4) )
296
297   ! ============================================================================
298     END SUBROUTINE FLUX_HLLC_ROSSOW_Einfeldt_full_dissip
299   ! ============================================================================
```

B - Fortran source code of $\mathcal{F}^{HLLC-Rossow}$ under the Liu-Vinokur form

```
! ================================================================================
  SUBROUTINE FLUX_HLLC_ROSSOW_LV_FORM(W_L,W_R,P_L,P_R,T_L,T_R,xn1,xn2,gamma,Num,num_flux)
! ================================================================================

  IMPLICIT NONE
  TYPE(DataNum),       INTENT(inout)    :: Num
  REAL*8, DIMENSION(4),INTENT(in)       :: W_L,W_R,P_L,P_R                          !Conservative + Primitive variables
  REAL*8, DIMENSION(3),INTENT(in)       :: T_L,T_R                                  ![p,H_L,c_L]
  REAL*8,              INTENT(in)       :: xn1,xn2,gamma
  REAL*8, DIMENSION(4),INTENT(inout)    :: num_flux

  REAL*8, DIMENSION(4)                  :: deltaVarW,deltaVarP,xlambda
  REAL*8, DIMENSION(4)                  :: diss_vec,Flx_L,Flx_R

  REAL*8                                :: t1, t2                                   !tangential component
  REAL*8                                :: UnL,UnR,UtL,UtR
  REAL*8                                :: DeltaUn,DeltaE
  REAL*8                                :: Un_moy,rho_moy,rho_star_moy,E_moy,H_moy

  REAL*8                                :: ro_sqrd_L,ro_sqrd_R
  REAL*8, DIMENSION(4)                  :: Q_L,Q_R,Avg_roe                        !\sqrt{rho}[1 u v H] + Roe average[4]

  REAL*8                                :: H_L,H_R,c_l,c_R                        !Total Enthalpy + speed of sound (for a better readabil

  REAL*8                                :: Norm_U2_L,M_L,Mn_L,tilde_c_L             !Left side
  REAL*8                                :: Norm_U2_R,M_R,Mn_R,tilde_c_R             !Right side
  REAL*8                                :: Norm_Avg_U2,Avg_M,Avg_Mn,tilde_Avg_c     !For Roe average
  REAL*8                                :: Avg_c,Avg_c2,Avg_Un
  REAL*8                                :: alpha, beta2                             !Coefficients artificial speed of sound

  REAL*8                                :: lambda_m,lambda_mid,lambda_p           ! S_k
  REAL*8                                :: hat_c_L,hat_c_R,left_arti_speed,right_arti_speed
  REAL*8                                :: dS_R,dS_L,dc_R,dc_L,d_absS_R,d_absS_L  ! Notations in chapter 4-5

  REAL*8                                :: rho_star_L,rho_star_R
  REAL*8                                :: u_star_l,u_star_r,v_star_l,v_star_r
  REAL*8                                :: u_star_moy,v_star_moy

  REAL*8                                :: rhoLrhoR,rhoc_sum,rhoc_arti_sum          !Useful variables for Liu-Vinokur
  REAL*8                                :: d_p,d_Un,d_moy_l,d_moy_r,d_moy_C         !5 scalars coefficients
  REAL*8,DIMENSION(4)                   :: upwind,f_vel,f_pres,cor_left,cor_right,cor_inter   !6 vectors of Liu-Vinokur


        ! ---- For a better readability ----
          ! ---- Total Enthalpy and speed of sound ----
        H_L = T_L(2) ; c_l = T_L(3)
        H_R = T_R(2) ; c_r = T_R(3)

    ! ---- Euler's fluxes ----
        ! ---- Left Euler flux----
    Flx_L(1) =  W_L(2) * xn1                    +  W_L(3) * xn2
    Flx_L(2) = (W_L(2) * P_L(2) + P_L(4) )*xn1 + (W_L(2) * P_L(3))*xn2
    Flx_L(3) = (W_L(2) * P_L(3))*xn1            + (W_L(3) * P_L(3) + P_L(4))*xn2
    Flx_L(4) = (W_L(2) * H_L )*xn1           + (W_L(3) * H_L  )*xn2
        ! ---- Right Euler flux ----
    Flx_R(1) =  w_R(2) * xn1                    +  w_R(3) * xn2
    Flx_R(2) = (w_R(2) * P_R(2) + P_R(4) )*xn1 + (w_R(2) * P_R(3))*xn2
    Flx_R(3) = (w_R(2) * P_R(3))*xn1            + (w_R(3) * P_R(3) + P_R(4))*xn2
    Flx_R(4) = (w_R(2) * H_R )*xn1           + (w_R(3) * H_R)*xn2

       ! ---- Directionnal velocity ----
    UnL      = P_L(2)*xn1 + P_L(3)*xn2
    UnR      = P_R(2)*xn1 + P_R(3)*xn2
    deltaUn = UnR - UnL

      ! ---- Tangeantial velocity -----
    t1 = -xn2;     t2 = xn1
    UtL = P_L(2)*t1 + P_L(3)*t2
    UtR = P_R(2)*t1 + P_R(3)*t2

        ! ---- Jump var ----
    deltaVarW(1:4) = W_R(1:4) - W_L(1:4) !rho  rou rov roe
    deltaVarP(1:4) = P_R(1:4) - P_L(1:4) !rho  u   v   ps
    DeltaE         = W_R(4)/W_R(1) - W_L(4)/W_L(1)



      ! ---- Roe Average  ----
    ro_sqrd_L = SQRT(W_L(1)) ; ro_sqrd_R = SQRT(W_R(1))
    Q_L(:)    = (/ ro_sqrd_L, ro_sqrd_L*P_L(2), ro_sqrd_L*P_L(3), ro_sqrd_L*H_L /) !\sqrt{rho}( 1 u v H)
    Q_R(:)    = (/ ro_sqrd_R, ro_sqrd_R*P_R(2), ro_sqrd_R*P_R(3), ro_sqrd_R*H_R /) !\sqrt{rho}( 1 u v H)

    Avg_roe(1)=  Q_L(1)*Q_R(1)
    Avg_roe(2)=( Q_L(2)+Q_R(2) )/( Q_L(1)+Q_R(1) )
    Avg_roe(3)=( Q_L(3)+Q_R(3) )/( Q_L(1)+Q_R(1) )
    Avg_roe(4)=( Q_L(4)+Q_R(4) )/( Q_L(1)+Q_R(1) )

    ! ---- Compute Artificial speed of sound -----
```

```
89          ! ---- Left state ----
90        Norm_U2_L = P_L(2)*P_L(2) + P_L(3)*P_L(3)
91        M_L       = sqrt(Norm_U2_L)/c_l
92        Mn_L      = UnL/c_l
93
94        ! beta2     = min(M_L*M_L,1.0_8)                          ! Without the cut-off strategy
95        beta2     = min(max(M_L*M_L,Num%delta_precond**2),1.0_8) ! With reference Mach number
96        alpha     = 0.5*(1.-beta2)
97        tilde_c_L = c_l*sqrt( Mn_L*Mn_L*alpha**2 + beta2 ) !artifical speed of sound
98
99          ! ---- Interface state ----
100       Norm_Avg_U2 = Avg_roe(2)*Avg_roe(2) + Avg_roe(3)*Avg_roe(3)
101       Avg_c2      = (gamma-1)*(Avg_roe(4) - 0.5*(Norm_Avg_U2))
102       Avg_c       = sqrt( Avg_c2 )
103       Avg_Un      = Avg_roe(2)*xn1 + Avg_roe(3)*xn2
104
105       Avg_M       = sqrt(Norm_Avg_U2)/Avg_c
106       Avg_Mn      = Avg_Un/Avg_c
107
108       ! beta2       = min(Avg_M*Avg_M,1.0_8)                        ! Without the cut-off strategy
109       beta2     = min(max(Avg_M*Avg_M,Num%delta_precond**2),1.0_8) ! With reference Mach number
110
111       alpha       = 0.5*(1.-beta2)
112       tilde_Avg_c = Avg_c*sqrt( Avg_Mn*Avg_Mn*alpha**2 + beta2) !artifical speed of sound
113
114          ! ---- Right state ----
115       Norm_U2_R = P_R(2)*P_R(2) + P_R(3)*P_R(3)
116       M_R       = sqrt(Norm_U2_R)/c_r
117       Mn_R      = UnR/c_r
118
119       ! beta2        = min(M_R*M_R,1.0_8)                          ! Without the cut-off strategy
120       beta2        = min(max(M_R*M_R,Num%delta_precond**2),1.0_8) ! With reference Mach number
121       alpha        = 0.5*(1.-beta2)
122       tilde_c_R    = c_r*sqrt( Mn_R*Mn_R*alpha**2 + beta2) !artifical speed of sound
123
124         ! ---- Generaziled speed of sounds ----
125       hat_c_L           = max(c_l,Avg_c - Avg_Un + UnL)
126       hat_c_R           = max(c_r,Avg_c + Avg_Un - UnR)
127       left_arti_speed  = max(tilde_c_L,tilde_Avg_c - Avg_Un + UnL)
128       right_arti_speed = max(tilde_c_R,tilde_Avg_c + Avg_Un - UnR)
129
130
131         !---- Wave speed estimates -----
132       lambda_m    = UnL - hat_c_L
133          ! ---- normal directionnal speed in star region  ---
134       lambda_mid = (W_L(1)*UnL*hat_c_L + W_R(1)*UnR*hat_c_R - deltaVarP(4))/(W_L(1)*hat_c_L + W_R(1)*hat_c_R)
135       lambda_p    = UnR + hat_c_R
136
137           ! ---- ABS Eigenvalues ----
138       xlambda(1) = abs(lambda_m)
139       xlambda(2) = abs(lambda_mid)
140       xlambda(3) = xlambda(2)
141       xlambda(4) = abs(lambda_p)
142
143           ! ---- delta coefficients ----
144       dS_R     = lambda_p - lambda_mid
145       dS_L     = lambda_m - lambda_mid
146       d_absS_R = xlambda(4) - xlambda(2)
147       d_absS_L = xlambda(1) - xlambda(2)
148       dc_R     = lambda_p - UnR
149       dc_L     = lambda_m - UnL
150
151       ! ============================
152       !     ---- Star Region ----
153       ! ============================
154       rho_star_L= W_L(1)*dc_L/dS_L
155       rho_star_R= W_R(1)*dc_R/dS_R
156             ! ---- velocities ----
157       u_star_l= lambda_mid*xn1 + UtL*t1
158       v_star_l= lambda_mid*xn2 + UtL*t2
159
160       u_star_r= lambda_mid*xn1 + UtR*t1
161       v_star_r= lambda_mid*xn2 + UtR*t2
162
163       ! ============================
164       !     ---- Mean Values ----
165       ! ============================
166       rho_star_moy = 0.5*(rho_star_L+rho_star_R)
167       rho_moy      = 0.5*(P_L(1)+P_R(1))
168       u_star_moy   = 0.5*(u_star_l+u_star_r)
169       v_star_moy   = 0.5*(v_star_l+v_star_r)
170       E_moy        = 0.5*(W_L(4)/P_L(1) + W_R(4)/P_R(1))
171       H_moy         = 0.5*(H_L+H_R)
172       Un_moy       = 0.5*(UnL+UnR)
173
174              ! ---- Useful terms ----
175       rhoc_sum       = P_L(1)*hat_c_L + P_R(1)*hat_c_R
176       rhoc_arti_sum  = P_L(1)*left_arti_speed + P_R(1)*right_arti_speed
177       rhoLrhoR       = (W_L(1)*W_R(1))
178
179       ! ============================
180       !
181       !        Liu-Vinokur Form
182       !
183       ! ============================
184
185           ! ====================================
186           !             Scalar coeff
187           ! ====================================
```

```
188
189       d_Un = (Avg_roe(1)/rhoc_sum)*DeltaUn*(                                          &
190                                           d_absS_L*dc_R/dS_L - d_absS_R*dc_L/dS_R   &
191                                           ) & !End Delta Un
192            +(Avg_roe(1)/rhoc_arti_sum)*deltaVarP(4)*(                                                  &
193                                                     d_absS_R/(W_L(1)*dS_R) -  d_absS_L/(W_R(1)*dS_L) &
194                                                     )!End Delta P
195
196       d_p = (rhoLrhoR/rhoc_sum)*DeltaUn*(                                              &
197                                         - left_arti_speed*xlambda(1)*dc_R/dS_l         &
198                                         - right_arti_speed*xlambda(4)*dc_l/dS_r        &
199                                         - rhoc_arti_sum*rho_star_moy*xlambda(2)/rhoLrhoR &
200                                         ) & !End Delta Un
201           + (deltaVarP(4)/rhoc_sum)*(                                                &
202                                     rho_star_R*xlambda(4) - rho_star_L*xlambda(1)    &
203                                     )  !End Delta P
204
205             ! ---- Deviation Terms ----
206       d_moy_l = (rhoLrhoR/rhoc_sum)*DeltaUn*(                          &
207                                             - xlambda(1)*dc_R/dS_L     &
208                                             ) & !End Delta Un
209                 + (deltaVarP(4)/rhoc_arti_sum)*(                       &
210                                                 W_L(1)*xlambda(1)/ds_l &
211                                                 )  !End Delta P
212
213       d_moy_r = (rhoLrhoR/rhoc_sum)*DeltaUn*(                          &
214                                             xlambda(4)*dc_L/dS_R       &
215                                             ) & !End Delta Un
216               - (deltaVarP(4)/rhoc_arti_sum)*(                         &
217                                               W_R(1)*xlambda(4)/ds_r &
218                                               )  !End Delta P
219
220       d_moy_C = (rhoLrhoR/rhoc_sum)*DeltaUn*xlambda(2)*(                                &
221                                                        - dc_R/dS_L + dc_L/dS_R         &
222                                                       ) & !End Delta Un
223                   - (deltaVarP(4)/rhoc_sum)*xlambda(2)*(                              &
224                                                         - W_L(1)/ds_l  +  W_R(1)/ds_R &
225                                                         ) & !End Delta P
226                     + deltaVarW(1)*xlambda(2) !End Delta rho
227
228           ! ====================================
229           !              Vectors
230           ! ====================================
231       upwind(1)= deltaVarW(1)
232       upwind(2)= u_star_moy*deltaVarW(1) + rho_star_moy*deltaVarP(2)
233       upwind(3)= v_star_moy*deltaVarW(1) + rho_star_moy*deltaVarP(3)
234       upwind(4)= E_moy*deltaVarW(1) + rho_star_moy*DeltaE &
235                  + (rho_star_moy-rho_moy)*(P_R(4)/P_R(1) - P_L(4)/P_L(1))
236
237       f_vel(1)=Avg_roe(1)
238       f_vel(2)=Avg_roe(1)*u_star_moy
239       f_vel(3)=Avg_roe(1)*v_star_moy
240       f_vel(4)=Avg_roe(1)*H_moy
241
242       f_pres(1)= 0
243       f_pres(2)= xn1
244       f_pres(3)= xn2
245       f_pres(4)= lambda_mid
246
247       cor_left(1)= 0
248       cor_left(2)= u_star_moy - P_L(2)
249       cor_left(3)= v_star_moy - P_L(3)
250       cor_left(4)= H_moy - H_L
251
252       cor_right(1)= 0
253       cor_right(2)= u_star_moy - P_R(2)
254       cor_right(3)= v_star_moy - P_R(3)
255       cor_right(4)= H_moy - H_R
256
257       cor_inter(1)= 0
258       cor_inter(2)= 0
259       cor_inter(3)= 0
260       cor_inter(4)= lambda_mid*(lambda_mid - Un_moy)
261
262           ! ---- Numerical Dissipation ----
263       diss_vec(1:4)= xlambda(2)*upwind(1:4) + d_Un*f_vel(1:4) + d_p*f_pres(1:4) &
264                      + d_moy_l*cor_left(1:4) + d_moy_r*cor_right(1:4) + d_moy_C*cor_inter(1:4)
265
266           ! ---- Numerical Flux ----
267       num_flux(1:4)=0.5*( Flx_R(1:4) + Flx_L(1:4) - diss_vec(1:4) )
268
269
270   ! ================================================================================
271     END SUBROUTINE FLUX_HLLC_ROSSOW_LV_FORM
272   ! ================================================================================
```

Bibliography

[1] Richard Courant, Eugene Isaacson, and M. D. Rees. On the solution of nonlinear hyperbolic differential equations by finite differences. Communications on Pure and Applied Mathematics, 5:243–255, 1952.

[2] Sergei K. Godunov and I. Bohachevsky. Finite difference method for numerical computation of discontinuous solutions of the equations of fluid dynamics. Matematičeskij sbornik, 47(89)(3):271–306, 1959. Publisher: Steklov Mathematical Institute of Russian Academy of Sciences.

[3] P. L Roe. Approximate Riemann solvers, parameter vectors, and difference schemes. Journal of Computational Physics, 43(2):357–372, October 1981.

[4] Amiram Harten, Peter D. Lax, and Bram van Leer. On upstream differencing and godunov-type schemes for hyperbolic conservation laws. SIAM Review, 25(1):35–61, 1983.

[5] Eli Turkel. Preconditioned methods for solving the incompressible and low speed compressible equations. Journal of Computational Physics, 72(2):277–298, October 1987.

[6] G. Volpe. Performance of compressible flow codes at low Mach numbers. AIAA Journal, 31(1):49–56, 1993. Publisher: American Institute of Aeronautics and Astronautics _eprint: https://doi.org/10.2514/3.11317.

[7] Hervé Guillard and Cécile Viozat. On the behaviour of upwind schemes in the low Mach number limit. Computers & Fluids, 28(1):63–86, January 1999.

[8] A. Majda. Compressible Fluid Flow and Systems of Conservation Laws in Several Space Variables. Springer, New York, softcover reprint of the original 1st ed. 1984 édition edition, October 2013.

[9] H. Guillard and B. Nkonga. Chapter 8 - On the Behaviour of Upwind Schemes in the Low Mach Number Limit: A Review. In Rémi Abgrall and Chi-Wang Shu, editors, Handbook of Numerical Analysis, volume 18 of Handbook of Numerical Methods for Hyperbolic Problems, pages 203–231. Elsevier, January 2017.

[10] Stéphane Dellacherie. Analysis of Godunov type schemes applied to the compressible Euler system at low Mach number. Journal of Computational Physics, 229(4):978–1016, February 2010.

[11] E. Turkel. Preconditioning Techniques in Computational Fluid Dynamics. Annual Review of Fluid Mechanics, 31(1):385–416, 1999. _eprint: https://doi.org/10.1146/annurev.fluid.31.1.385.

[12] F. Miczek, F. K. Röpke, and P. V. F. Edelmann. New numerical solver for flows at various Mach numbers. Astronomy & Astrophysics, 576:A50, April 2015. Publisher: EDP Sciences.

[13] Jean-Christophe Boniface. Rescaling of the Roe scheme in low Mach-number flow regions. Journal of Computational Physics, 328:177–199, January 2017.

[14] Jonathan M. Weiss and Wayne A. Smith. Preconditioning applied to variable and constant density flows. AIAA Journal, 33(11):2050–2057, November 1995. Publisher: American Institute of Aeronautics and Astronautics.

[15] Hiroaki Nishikawa. Weiss-Smith Local-Preconditioning Matrix is a Diagonal Matrix in the Symmetric Form of the Euler Equations. July 2021.

[16] Y. Colin, H. Deniau, and J. F. Boussuge. A robust low speed preconditioning formulation for viscous flow computations. Computers & Fluids, 47(1):1–15, August 2011.

[17] François Bouchut, Christophe Chalons, and Sébastien Guisset. An entropy satisfying two-speed relaxation system for the barotropic Euler equations: application to the numerical approximation of low Mach number flows. Numerische Mathematik, 145(1):35–76, May 2020.

[18] Christophe Chalons, Mathieu Girardin, and Samuel Kokh. An all-regime Lagrange-Projection like scheme for the gas dynamics equations on unstructured meshes. Communications in Computational Physics, 20(1):188–233, 2016. Publisher: Cambridge University Press.

[19] Jeffrey Haack, Shi Jin, and Jian-guo Liu. An All-Speed Asymptotic-Preserving Method for the Isentropic Euler and Navier-Stokes Equations. Communications in Computational Physics, 12, October 2010.

[20] Stéphane Dellacherie. Checkerboard modes and wave equation. pages 71–80, 2009.

[21] Xue-song Li and Chun-wei Gu. Mechanism of Roe-type schemes for all-speed flows and its application. Computers & Fluids, 86:56–70, November 2013.

[22] Pascal Bruel, Simon Delmas, Jonathan Jung, and Vincent Perrier. A low Mach correction able to deal with low Mach acoustics. Journal of Computational Physics, 378:723–759, February 2019.

[23] Thomas Galié, Jonathan Jung, Ibtissem Lannabi, and Vincent Perrier. Extension of an all-Mach Roe scheme able to deal with low Mach acoustics to full Euler system. ESAIM: Proceedings and Surveys, July 2023.

[24] E. F. Toro, M. Spruce, and W. Speares. Restoration of the contact surface in the HLL-Riemann solver. Shock Waves, 4(1):25–34, July 1994.

[25] Felix Rieper. A low-Mach number fix for Roe's approximate Riemann solver. Journal of Computational Physics, 2011.

[26] Cord-Christian Rossow. A Flux-Splitting Scheme for Compressible and Incompressible Flows. Journal of Computational Physics, 164(1):104–122, October 2000.

[27] Cord-Christian Rossow. Efficient computation of compressible and incompressible flows. Journal of Computational Physics, 220(2):879–899, January 2007.

[28] L. Hascoët and V. Pascual. The Tapenade Automatic Differentiation tool: Principles, Model, and Specification. ACM Transactions On Mathematical Software, 39(3), 2013.

[29] Philipp Birken and Andreas Meister. Stability of Preconditioned Finite Volume Schemes at Low Mach Numbers. BIT Numerical Mathematics, 45:463–480, January 2005.

[30] Keiichi Kitamura and Eiji Shima. Ausm-like expression of hllc and its all-speed extension. International Journal for Numerical Methods in Fluids, 92(4):246–265, 2020.

[31] Godlewski and Raviart. Numerical Approximation of Hyperbolic Systems of Conservation Laws | Edwige Godlewski | Springer. 1996.

[32] Bruno Després. Lois de Conservations Eulériennes, Lagrangiennes et Méthodes Numériques. Mathématiques et Applications. Springer-Verlag, Berlin Heidelberg, 2010.

[33] Leveque. Finite Volume Methods for Hyperbolic Problems. Cambridge University Press, 2002.

[34] Eleuterio F. Toro. Riemann Solvers and Numerical Methods for Fluid Dynamics: A Practical Introduction. Springer-Verlag, Berlin Heidelberg, 3 edition, 2009.

[35] Randall J. LeVeque. Wave propagation algorithms for multidimensional hyperbolic systems. Journal of computational physics, 131(2):327–353, 1997. Publisher: Elsevier.

[36] Peter D. Lax. 1. Hyperbolic Systems of Conservation Laws and the Mathematical Theory of Shock Waves, pages 1–48. 1973.

[37] Jonathan Goodman and Zhouping Xin. Viscous limits for piecewise smooth solutions to systems of conservation laws. Archive for Rational Mechanics and Analysis, 121(3):235–265, September 1992.

[38] S. Schochet. Fast Singular Limits of Hyperbolic PDEs. Journal of Differential Equations, 114(2):476–512, December 1994.

[39] G. Métivier and S. Schochet. The Incompressible Limit of the Non-Isentropic Euler Equations:. Archive for Rational Mechanics and Analysis, 158(1):61–90, May 2001.

[40] Steven Schochet. The mathematical theory of low Mach number flows. ESAIM: Mathematical Modelling and Numerical Analysis, 39(3):441–458, 2005. Publisher: EDP Sciences.

[41] Radyadour Kh. Zeytounian. The Many Faces of the Asymptotics of Low-Mach-Number Flows, pages 27–43. Springer Berlin Heidelberg, Berlin, Heidelberg, 2006.

[42] Thomas Alazard. A minicourse on the low Mach number limit. Discrete and Continuous Dynamical Systems - Series S, 1(3):365–404, 2008. Publisher: American Institute of Mathematical Sciences.

[43] CECILE VIOZAT. Calcul d'ecoulements stationnaires et instationnaires a petit nombre de mach, et en maillages etires. These de doctorat, Nice, January 1998.

[44] Pijush K. Kundu, Ira M. Cohen, and David R. Dowling. Fluid Mechanics. Academic Press, 2012. Google-Books-ID: iUo_4tsHQYUC.

[45] John David Anderson. Fundamentals of aerodynamics. McGraw-Hill series in aeronautical and aerospace engineering. McGraw-Hill Education, New York, NY, sixth edition edition, 2017.

[46] Luigi Ambrosio and Alessio Figalli. Lecture notes on variational models for incompressible Euler equations, page 5871. London Mathematical Society Lecture Note Series. Cambridge University Press, 2014.

[47] R. Klein. Semi-implicit extension of a godunov-type scheme based on low mach number asymptotics I: One-dimensional flow. Journal of Computational Physics, 121(2):213–237, October 1995.

[48] Bertil Gustafsson. Unsymmetric hyperbolic systems and the Euler equations at low Mach numbers. Journal of Scientific Computing, 2(2):123–136, June 1987.

[49] Bram van Leer. Towards the ultimate conservative difference scheme. V. A second-order sequel to Godunov's method. Journal of Computational Physics, 32(1):101–136, July 1979.

[50] SEOKKWAN YOON and ANTHONY JAMESON. An LU-SSOR scheme for the Euler and Navier-Stokes equations. 25th AIAA Aerospace Sciences Meeting, 1986. _eprint: https://arc.aiaa.org/doi/pdf/10.2514/6.1987-600.

[51] Seokkwan Yoon and Antony Jameson. Lower-upper symmetric-gauss-seidel method for the euler and navier-stokes equations. AIAA Journal, 26(9):1025–1026, 1988.

[52] P. Batten, M.A. Leschziner, and U.C. Goldberg. Average-state jacobians and implicit methods for compressible viscous and turbulent flows. Journal of Computational Physics, 137(1):38–78, 1997.

[53] Gang WANG, Yuewen JIANG, and Zhengyin YE. An improved lu-sgs implicit scheme for high reynolds number flow computations on hybrid unstructured mesh. Chinese Journal of Aeronautics, 25(1):33–41, 2012.

[54] Evelyn Otero and Peter Eliasson. Improving the performance of the cfd code edge using lu-sgs and line-implicit methods. 09 2013.

[55] Bram van Leer, Wen-Tzong Lee, and Philip Roe. Characteristic Time-stepping or Local Preconditioning of the Euler equations. volume 1552, June 1991.

[56] Joaquim R.R.A. Martins. Aerodynamic design optimization: Challenges and perspectives. Computers & Fluids, 239:105391, 2022.

[57] A. Crivellini and F. Bassi. An implicit matrix-free Discontinuous Galerkin solver for viscous and turbulent aerodynamic simulations. Computers & Fluids, 50(1):81–93, November 2011.

[58] Arthur Poulain. Optimal linear and non-linear solutions in hypersonic boundary layers : stability and open-loop control. PhD thesis, 2023. Thèse de doctorat dirigée par Sipp, Denis Mécanique des fluides et des solides, acoustique Institut polytechnique de Paris 2023.

[59] Yousef Saad. Iterative Methods for Sparse Linear Systems. Other Titles in Applied Mathematics. Society for Industrial and Applied Mathematics, January 2003.

[60] E. Turkel. Review of preconditioning methods for fluid dynamics. Applied Numerical Mathematics, 12(1):257–284, May 1993.

[61] E. Turkel, A. Fiterman, and B. Vanleer. Preconditioning and the limit to the incompressible flow equations. Technical Report NAS 1.26:191500, July 1993. NTRS Author Affiliations: NASA Langley Research Center NTRS Document ID: 19940009244 NTRS Research Center: Legacy CDMS (CDMS).

[62] Philip Roe and Jack Pike. Efficient Construction and Utilisation of Approximate Riemann Solutions. pages 499–518, June 1985.

[63] Marcel Vinokur. An analysis of finite-difference and finite-volume formulations of conservation laws. Journal of Computational Physics, 81(1):1–52, March 1989.

[64] B. Einfeldt, C.D. Munz, P.L. Roe, and B. Sjögreen. On Godunov-type methods near low densities. Journal of Computational Physics, 1991.

[65] P. Batten, N. Clarke, C. Lambert, and D. M. Causon. On the Choice of Wavespeeds for the HLLC Riemann Solver. SIAM Journal on Scientific Computing, 18(6):1553–1570, November 1997. Publisher: Society for Industrial and Applied Mathematics.

[66] Ami Harten and James M Hyman. Self adjusting grid methods for one-dimensional hyperbolic conservation laws. Journal of Computational Physics, 50(2):235–269, May 1983.

[67] Marica Pelanti, Luigi Quartapelle, L Vigevano, and Luigi Vigevano. A review of entropy fixes as applied to roe's linearization. the Aerospace and Aeronautics Department of Politecnico, page 31, 2001.

[68] J. VonNeumann and R. D. Richtmyer. A Method for the Numerical Calculation of Hydrodynamic Shocks. Journal of Applied Physics, 21(3):232–237, March 1950.

[69] L. G. Margolin and N. M. Lloyd-Ronning. Artificial viscosity—then and now. Meccanica, 58(6):1039–1052, June 2023.

[70] R. Swanson, R. Radespiel, and E. Turkel. Comparison of several dissipation algorithms for central difference schemes. In 13th Computational Fluid Dynamics Conference. American Institute of Aeronautics and Astronautics, August 2023. _eprint: https://arc.aiaa.org/doi/pdf/10.2514/6.1997-1945.

[71] Eitan Tadmor. Numerical viscosity and the entropy condition for conservative difference schemes. Mathematics of Computation, 43(168):369–381, 1984.

[72] Bernd Einfeldt. On godunov-type methods for gas dynamics. SIAM Journal on Numerical Analysis, 25(2):294–318, 1988.

[73] R. F Warming and B. J Hyett. The modified equation approach to the stability and accuracy analysis of finite-difference methods. Journal of Computational Physics, 14(2):159–179, February 1974.

[74] Felix Rieper. On the dissipation mechanism of upwind-schemes in the low Mach number regime: A comparison between Roe and HLL - ScienceDirect. Journal of Computational Physics, 2009.

[75] Joshua Hope-Collins and Luca di Mare. Artificial diffusion for convective and acoustic low Mach number flows I: Analysis of the modified equations, and application to Roe-type schemes. Journal of Computational Physics, 475:111858, February 2023.

[76] D L Darmofal and P J Schmid. The Importance of Eigenvectors for Local Preconditioners of the Euler Equations.

[77] Bram Va, Wen-Tzong Lee, and Philip Roe. Characteristic time-stepping or local preconditioning of the Euler equations. In 10th Computational Fluid Dynamics Conference, Fluid Dynamics and Co-located Conferences. American Institute of Aeronautics and Astronautics, June 1991.

[78] Xue-song Li and Chun-wei Gu. An All-Speed Roe-type scheme and its asymptotic analysis of low Mach number behaviour. Journal of Computational Physics, 227(10):5144–5159, May 2008.

[79] Kai Oßwald, A. Siegmund, Philipp Birken, Volker Hannemann, and Andreas Meister. L2Roe: A low-dissipation version of Roe's approximate Riemann solver for low Mach numbers. International Journal for Numerical Methods in Fluids, 81, September 2015.

[80] Shu-sheng Chen, Chao Yan, Shuai Lou, and Bo-xi Lin. An improved entropy-consistent Euler flux in low Mach number. Journal of Computational Science, 27:271–283, July 2018.

[81] Friedemann Kemm. Numerical investigation of Mach number consistent Roe solvers for the Euler equations of gas dynamics. Journal of Computational Physics, 477:111947, March 2023.

[82] Stefan Langer. Investigations of a compressible second order finite volume code towards the incompressible limit. Computers & Fluids, 149:119–137, June 2017.

[83] YEN LIU and MARCEL VINOKUR. Upwind algorithms for general thermo-chemical nonequilibrium flows.

[84] Hervé Guillard and Angelo Murrone. On the behavior of upwind schemes in the low Mach number limit: II. Godunov type schemes. Computers & Fluids, 33(4):655–675, May 2004.

[85] B. Thornber, A. Mosedale, D. Drikakis, D. Youngs, and R.J.R. Williams. An improved reconstruction method for compressible flows with low Mach number features. Journal of Computational Physics, 227(10):4873–4894, 2008.

[86] Stéphane Dellacherie, Jonathan Jung, Pascal Omnes, and Pierre-Arnaud Raviart. Construction of modified Godunov type schemes accurate at any Mach number for the compressible Euler system. Mathematical Models and Methods in Applied Sciences, November 2016.

[87] Jonathan Jung and Vincent Perrier. Steady low Mach number flows: Identification of the spurious mode and filtering method. Journal of Computational Physics, 468:111462, November 2022.

[88] Sankaran Venkateswaran, Ding Li, and Charles Merkle. Influence of Stagnation Regions on Preconditioned Solutions at Low Speeds. In 41st Aerospace Sciences Meeting and Exhibit, Reno, Nevada, January 2003. American Institute of Aeronautics and Astronautics.

[89] S. F. Davis. Simplified Second-Order Godunov-Type Methods. SIAM Journal on Scientific and Statistical Computing, 9(3):445–473, May 1988. Publisher: Society for Industrial and Applied Mathematics.

[90] J. C. Mandal and V. Panwar. Robust HLL-type Riemann solver capable of resolving contact discontinuity. Computers & Fluids, 63:148–164, June 2012.

[91] Zhijun Shen, Wei Yan, and Guangwei Yuan. A robust HLLC-type Riemann solver for strong shock. Journal of Computational Physics, 309:185–206, March 2016.

[92] François Bouchut. Nonlinear Stability of Finite Volume Methods for Hyperbolic Conservation Laws and Well-Balanced Schemes for Sources, volume 2/2004. January 2004. Journal Abbreviation: Frontiers in Mathematics Publication Title: Frontiers in Mathematics.

[93] Jean-Luc Guermond and Bojan Popov. Fast estimation from above of the maximum wave speed in the Riemann problem for the Euler equations. Journal of Computational Physics, 321:908–926, September 2016.

[94] E. F. Toro, L. O. Müller, and A. Siviglia. Bounds for Wave Speeds in the Riemann Problem: Direct Theoretical Estimates. Computers & Fluids, 209:104640, September 2020.

[95] Nico Fleischmann, Stefan Adami, and Nikolaus A. Adams. On an inconsistency of the arithmetic-average signal speed estimate for HLL-type Riemann solvers. Journal of Computational Physics: X, 8:100077, September 2020.

[96] Soo Hyung Park and Jang Hyuk Kwon. On the dissipation mechanism of Godunov-type schemes. Journal of Computational Physics, 188(2):524–542, July 2003.

[97] Hong Luo, Joseph D. Baum, and Rainald Lohner. Extension of Harten-Lax-van Leer Scheme for Flows at All Speeds. AIAA Journal, 43(6):1160–1166, June 2005. Publisher: American Institute of Aeronautics and Astronautics.

[98] Soo Hyung Park, Jae Eun Lee, and Jang Hyuk Kwon. Preconditioned HLLE Method for Flows at All Mach Numbers. AIAA Journal, 44(11):2645–2653, November 2006.

[99] Marica Pelanti. Wave Structure Similarity of the HLLC and Roe Riemann Solvers: Application to Low Mach Number Preconditioning. SIAM Journal on Scientific Computing, 40(3):A1836–A1859, January 2018.

[100] Hang Yu, Hua Li, Jianqi Lai, and Ye Zhang. A Simple Modification of HLLEM Approximate Riemann Solver Applied to the Compressible Euler System at Low Mach Number. IOP Conference Series: Materials Science and Engineering, 751(1):012002, January 2020. Publisher: IOP Publishing.

[101] H. Yu, Z. Tian, F. Yang, and H. Li. On Asymptotic Behavior of HLL-Type Schemes at Low Mach Numbers. Mathematical Problems in Engineering, 2020, 2020.

[102] Di Sun, Feng Qu, and Junqiang Bai. An effective all-speed Riemann solver with self-similar internal structure for Euler system. Computers & Fluids, 239:105392, May 2022.

[103] W. Xie, Y. Zhang, Q. Chang, and H. Li. Towards an accurate and robust roe-type scheme for all Mach number flows. Advances in Applied Mathematics and Mechanics, 11(1):132–167, 2019.

[104] Wenjia Xie, Zhengyu Tian, Ye Zhang, Hang Yu, and Weijie Ren. A unified construction of all-speed HLL-type schemes for hypersonic heating computations. Computers & Fluids, 233:105215, January 2022.

[105] A. Gogoi and J. C. Mandal. A simple HLLE-type scheme for all Mach number flows. European Journal of Mechanics - B/Fluids, 103:145–162, January 2024.

[106] Shu-sheng Chen, Chao Yan, and Xing-hao Xiang. Effective low-Mach number improvement for upwind schemes. Computers & Mathematics with Applications, 75(10):3737–3755, May 2018.

[107] Shusheng Chen, Boxi Lin, Yansu Li, and Chao Yan. HLLC+: Low-Mach Shock-Stable HLLC-Type Riemann Solver for All-Speed Flows. SIAM Journal on Scientific Computing, 42(4):B921–B950, January 2020.

[108] Shu-sheng Chen, Jin-ping Li, Zheng Li, Wu Yuan, and Zheng-hong Gao. Anti-dissipation pressure correction under low Mach numbers for Godunov-type schemes. Journal of Computational Physics, 456:111027, May 2022.

[109] Nico Fleischmann, Stefan Adami, and Nikolaus A. Adams. A shock-stable modification of the HLLC Riemann solver with reduced numerical dissipation. Journal of Computational Physics, 423:109762, December 2020.

[110] Y. H. Choi and C. L. Merkle. The Application of Preconditioning in Viscous Flows. Journal of Computational Physics, 105(2):207–223, April 1993.

[111] Marica Pelanti. Low Mach number preconditioning techniques for Roe-type and HLLC-type methods for a two-phase compressible flow model. Applied Mathematics and Computation, 310:112–133, October 2017.

[112] Marica Pelanti. A Roe-like reformulation of the HLLC Riemann solver and applications. April 2019.

[113] B. Thornber, D. Drikakis, R. J. R. Williams, and D. Youngs. On entropy generation and dissipation of kinetic energy in high-resolution shock-capturing schemes. Journal of Computational Physics, 227(10):4853–4872, May 2008.

[114] B.-X. Lin, C. Yan, and S.-S. Chen. Density enhancement mechanism of upwind schemes for low Mach number flows. Acta Mechanica Sinica/Lixue Xuebao, 34(3):431–445, 2018.

[115] Nico Fleischmann, Stefan Adami, Xiangyu Y. Hu, and Nikolaus A. Adams. A low dissipation method to cure the grid-aligned shock instability. Journal of Computational Physics, 401:109004, January 2020.

[116] Yann Chauvat. Le phénomène de "carbuncle" : analyse d'une pathologie des schémas numériques à capture de choc. These de doctorat, École nationale supérieure de l'aéronautique et de l'espace (Toulouse ; 1972-2007), January 2005.

[117] Chen Zhiqiang, Xudong Huang, Yu-Xin Ren, Zhifeng Xie, and Ming Zhou. Mechanism Study of Shock Instability in Riemann-Solver-Based Shock-Capturing Scheme. AIAA Journal, 56:1–16, July 2018.

[118] Clement Le Touze and Nicolas Rutard. Numerical methods for diffuse interface multifluid models. In ECCOMAS 2022-8th European Congress on Computational Methods in Applied Sciences and Engineering, 2022.

[119] E. F. Toro. A linearized riemann solver for the time-dependent euler equations of gas dynamics. Proceedings of the Royal Society of London. Series A: Mathematical and Physical Sciences, 434(1892):683–693, 1991.